Fermilab

FERMILAB-THESIS-1993-29

UNIVERSITY OF CALIFORNIA

IRVINE

The Charmonium $^1\mathbf{P}_1$ State (h_c) Produced in Antiproton-Proton Annihilations

DISSERTATION

submitted in partial satisfaction of the requirements for the degree of

DOCTOR OF PHILOSOPHY

in Physics

by

Keith Edwin Gollwitzer

Dissertation Committee:

Professor Jonas Schultz, Chair

Professor Mark Mandelkern

Professor Dennis Silverman

1993

The dissertation of Keith Edwin Gollwitzer is approved,

and is acceptable in quality and form

for publication on microfilm:

_____

_____

_____

Committee Chair

University of California, Irvine

1993

To

Sarah

and
my Parents

Contents

List of Figures

List of Tables

Acknowledgements

I would like to thank all members of the E760 collaboration for the work they have done. The search for and first observation of the charmonium $^1P_1$ state has been a part of the very successful experimental program of E760. Everyone has made contributions to the different aspects of the experiment.

I am grateful to Professors Jonas Schultz and Mark Mandelkern, my advisors, for their time and efforts in discussions of analyses and preparation of this thesis. I would like to acknowledge Professor Rosanna Cester for the outstanding job guiding the collaboration to such successful results.

There are numerous other thanks to people involved with E760. Instead of listing the entire collaboration, I want to thank the people who have helped me pursue some aspect of the experiment: Dr. Alan Hahn, Dr. Schultz and Dr. Mandelkern for the many suggestions involving the development of the single central calorimeter counter Monte Carlo; Dr. Petros Rapidis, Dr. Stephen Pordes and Larry Bartoszek for their work during the construction of the central calorimeter; Steve Trokenheim, Dr. Rapidis and Dr. Pordes for their contributions in modifying the spectrophotometer for the transmittance and radiation damage studies; Dr. Hahn for the online processing code involving the calorimeters, which I learned much from when he made me its caretaker, and for also encouraging development of code to collect punch through particles to be used for relative calibration of counters and monitoring; Dr. Michael Church for asking a seemingly innocent question about whether there were extra central calorimeter clusters present in the data, and his follow-up question of whether the extra clusters can be identified; and lastly, everyone who has provided feedback on the pile-up routines.

I am very grateful to my wife, Sarah, for the encouragement and support she has given as well as enduring numerous schedules. I am very thankful to my parents for providing motivation through out my education.

The US Department of Energy under grant DE-FG03-91ER40679 task B has funded this work.

Curriculum Vitae

1986	B.S. in Physics, Harvey Mudd College
1986–1988	Teaching Assistant, Department of Physics, University of California, Irvine
1987–1993	Research Assistant, Department of Physics, University of California, Irvine
1989	M.S. in Physics University of California, Irvine
1993	Ph.D. in Physics, University of California, Irvine Dissertation: *The Charmonium* $^1P_1$ *State* (h_c) *Produced in Antiproton-Proton Annihilations* Professor Jonas Schultz, Chair

Publications

L. Bartoszek et al., The E-760 Lead-glass Central Calorimeter: Design and Initial Test Results, Nucl. Instr. and Meth. **A301** (1991) 47.

T.A. Armstrong et al., Precision Measurements of Charmonium States Formed in $\bar{p}p$ Annihilation, Phys. Rev. Lett. **68** (1992) 1468.

T.A. Armstrong et al., Study of the χ_1 and χ_2 Charmonium States Formed in $\bar{p}p$ Annihilations, Nucl. Phys. **B373** (1992) 35.

T.A. Armstrong et al., Observation of the $^1P_1$ State of Charmonium, Phys. Rev. Lett. **69** (1992) 2337.

T.A. Armstrong et al., Measurement of the J/ψ and ψ' Resonance Parameters in $\bar{p}p$ Annihilation, Phys. Rev. **D47** (1993) 772.

T.A. Armstrong et al., Proton Electromagnetic Form Factors in the Time-like Region form 8.9 to 13.0 GeV^2, Phys. Rev. Lett. **70** (1993) 1212.

E760 Collaboration, Measurement of the $\gamma\gamma$ Partial Width of the χ_2 Charmonium Resonance, Phys. Rev. Lett., to be published.

E760 Collaboration, Study of the Angular Distribution of the Reaction $\bar{p}p \to J/\psi\gamma \to e^+e^-\gamma$, Phys. Rev. D, to be submitted.

E760 Collaboration, Evidence for $\eta\eta$ Resonances in Antiproton-Proton Annihilations at $2950 < \sqrt{s} < 3620$ MeV, Phys. Lett., to be submitted.

E760 Collaboration, Production of the $f_2(1520)$ Resonance in Antiproton-Proton Annihilations at $2980 < \sqrt{s} < 3526$ MeV, Phys. Lett., to be submitted.

E760 Collaboration, Exclusive Decays of the ψ' Formed in $\bar{p}p$ Annihilations, in preparation.

E760 Collaboration, Two Photon Decays of the $^1S_0$ Charmonium Resonances Formed in $\bar{p}p$ Annihilation, in preparation.

E760 Collaboration, $\bar{p}p$ Annihilation into $\pi^o\pi^o$ and $\gamma\pi^o$, in preparation.

E760 Collaboration, Search for Charmonium $^1P_1$ in $\bar{p}p$ Annihilation, in preparation.

E760 Collaboration, Antiproton-Proton Elastic Scattering, in preparation.

The Large Čerenkov Detector Project Collaboration, A Proposal for a Precision Test of the Standard Model by Neutrino-Electron Scattering, LA–11300–P.

Abstract of the Dissertation

The Charmonium $^1\mathrm{P}_1$ State (h_c) Produced in Antiproton-Proton Annihilations

by

Keith Edwin Gollwitzer

Doctor of Philosophy in Physics

University of California, Irvine, 1993

Professor Jonas Schultz, Chair

A search for the charmonium $^1\mathrm{P}_1$ state (h_c) has been performed in $\bar{p}p$ annihilations close to the spin weighted center of gravity of the triplet P states. A statistically significant enhancement in the $\bar{p}p \rightarrow J/\psi\pi^o$ cross section has been observed with characteristics consistent with the expected mass, total width, and production cross section of the singlet P wave state. The resonance is centered at $\sqrt{s} \simeq 3526.15 \pm 0.15 \pm 0.19$ MeV, greater than the center of gravity of the triplet P states by 0.88 ± 0.47 MeV. The upper limit (90% CL) for the total width is ≤ 1.1 MeV. No candidates for the reactions $\bar{p}p \rightarrow J/\psi\pi^o\pi^o$ and $\bar{p}p \rightarrow J/\psi\pi^+\pi^-$ have been observed; the upper limit (90% CL) $B(^1\mathrm{P}_1 \rightarrow \bar{p}p) \times B(^1\mathrm{P}_1 \rightarrow J/\psi\pi\pi) \leq 3.2 \times 10^{-8}$ is set. Searches to observe the expected dominant decay mode $^1\mathrm{P}_1 \rightarrow \eta_c\gamma$ ($\eta_c \rightarrow \gamma\gamma$ or $\eta_c \rightarrow \pi\pi\eta, \pi\pi\eta' \rightarrow 6\gamma$) show no evidence of a resonance; the upper limit (90% CL) $B(^1\mathrm{P}_1 \rightarrow \bar{p}p) \times B(^1\mathrm{P}_1 \rightarrow \eta_c\gamma) \leq 2.6 \times 10^{-5}$ is set.

Chapter 1

Motivation

Experiment 760 located at Fermi National Accelerator Laboratory (Fermilab) has studied charm antiquark-quark ($\bar{c}c$) bound states, which are called charmonium. E760 was designed not only to study known $\bar{c}c$ resonances, but was also designed to search for and discover new $\bar{c}c$ states. In particular, the experiment's principal purpose is to discover the charmonium $^1\mathrm{P}_1$ (h_c) state. The mass of the $^1\mathrm{P}_1$ is important to understanding the hyperfine structure of bound states in quantum chromodynamics (QCD).

Described in this thesis is the search for the $^1\mathrm{P}_1$ through decays to lower charmonium states:

$$\bar{p}p \rightarrow {}^1\mathrm{P}_1 \rightarrow \quad J/\psi + X \tag{1.1}$$

$$\bar{p}p \rightarrow {}^1\mathrm{P}_1 \rightarrow \quad \eta_c + \gamma. \tag{1.2}$$

The J/ψ and η_c are identified by electromagnetic decay products. In general, E760 searches for charmonium by

$$\bar{p}p \rightarrow \bar{c}c \rightarrow \quad e^+e^- + X \tag{1.3}$$

$$\bar{p}p \rightarrow \bar{c}c \rightarrow \quad \gamma\gamma + X \tag{1.4}$$

where the $e^+e^-(\gamma\gamma)$ invariant mass reconstructs to a $\bar{c}c$ state J/ψ or ψ' (η_c or χ_2) and X can be η, $\pi\pi$, π^o, a gamma ray, or nothing. The $^1\mathrm{P}_1$ radiative decay is also searched for by the η_c decaying to three neutral mesons, which then all subsequently decay to pairs of gamma rays resulting in a 7 gamma ray final state. A further search has involved:

$$\bar{p}p \rightarrow {}^1\mathrm{P}_1 \rightarrow \quad \eta + \gamma, \tag{1.5}$$

$$\bar{p}p \rightarrow {}^1\mathrm{P}_1 \rightarrow \quad \eta' + \gamma, \tag{1.6}$$

where the η and η' decay to three neutral mesons and the final state is 7 gamma rays.

The history of charmonium, theoretical expectations for the $^1\mathrm{P}_1$, and previous experimental spectroscopy results are discussed in this chapter. A description of the experimental apparatus is given in chapter 2. A detailed description of the design and construction of the central calorimeter is presented in chapter 3. The trigger system and procedure for data collection are outlined in chapter 4. The central calorimeter's calibration and monitoring are given in chapter 5. Chapter 6 describes the data filtering, reduction and event selection. Efficiencies and acceptances are contained in chapter 7. The results and conclusions are presented in chapter 8. Some of the descriptions (central calorimeter construction, attempted calibration methods, data acquisition procedure and the pile-up routines) are included to provide essentially the only written detailed documentation of these aspects of the experiment.

$$\begin{pmatrix} e \\ \nu_e \end{pmatrix} \begin{pmatrix} \mu \\ \nu_\mu \end{pmatrix} \begin{matrix} -1 \\ 0 \end{matrix}$$

$$\begin{pmatrix} u \\ d \end{pmatrix} \begin{pmatrix} ? \\ s \end{pmatrix} \begin{matrix} +\frac{2}{3} \\ -\frac{1}{3} \end{matrix}$$

Figure 1.1: The quark and lepton doublets before the discovery of the charm quark and the electrical charges of the members.

1.1 History of the Charm Quark

During the 1960's, a fairly successful model of mesons and baryons was based upon the existence of three quarks (u, d, and s representing respectively up, down and strange flavors). The quarks have fractional charge of $+\frac{2}{3}$ (u) or $-\frac{1}{3}$ (d and s). The quarks can be combined to form complimentary doublets to the then known lepton doublets as shown in figure 1.1. From the aesthetical point of view, a fourth quark of charge $+\frac{2}{3}$ would complete the doublets as pointed out by Bjorken and Glashow [1]; a quark-lepton symmetry would exist and if each quark flavor has three colors (see the next section), then the total charge of the doublets would be zero.

1.1.1 The Expectation of a Fourth Quark

A fourth quark to just fill the last doublet and balance the total fundamental charge was not in itself satisfying. However, arguments arising from the observed weak interactions and experimental results compared to first order QCD calculations suggested a fourth quark.

Figure 1.2: The experimental ratio R as a function of E_{cm} (from reference [3]). R is the ratio of electron–positron annihilation into hadrons and $\mu^+\mu^-$ pairs. For three quarks flavors and three quark colors, $R = 2$; the addition of a fourth quark of charge $+\frac{2}{3}$ increases R to $\frac{10}{3}$ for $E_{cm} > 3$ GeV.

A new quantum number for the quarks, color, was needed to understand the ground states of baryons consisting of three identically flavored quarks without abandoning Fermi-Dirac statistics [2]. One of the early indications that quarks have three colors, came from the experimental ratio of electron–positron annihilation into hadrons and $\mu^+\mu^-$ pairs:

$$R = \frac{\sigma(e^+e^- \rightarrow hadrons)}{\sigma(e^+e^- \rightarrow \mu^+\mu^-)}. \tag{1.7}$$

To lowest order, $R = N \sum q_i^2$ where q_i is the electric charge of the quark flavor, the sum is over quark flavors which satisfy $2m_i \leq E_{cm}$, and N is the number of quark colors. For the three known quarks, the ratio R was expected to be $\frac{2}{3}$ or 2 depending upon whether there are 1 or 3 quark colors. The experiments [4] found R to be closer to 2 for $E_{cm} \leq 3$ GeV/c^2 and therefore the number of quark colors is 3. This ratio

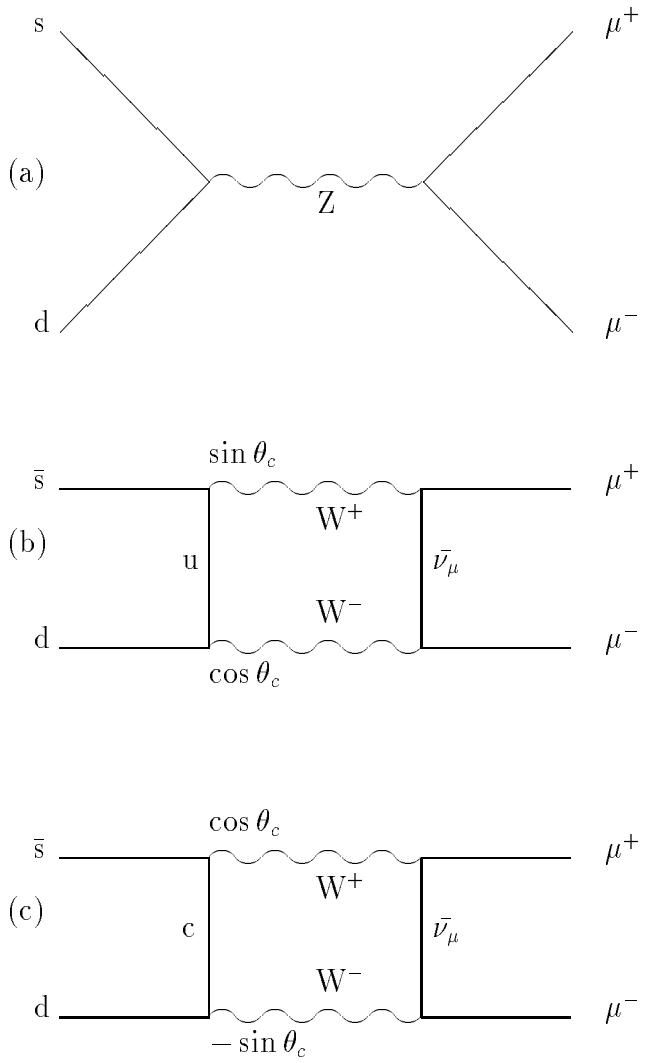

Figure 1.3: Feynman diagrams for $K_L^o \to \mu^+\mu^-$: (a) unacceptable strangeness changing neutral current, and second order contributions without (b) and with (c) the existence of the charm quark (θ_c is the Cabbibo angle).

can also be used as an indication of the number of quark flavors. Experiments also showed an increase in R above E_{cm} of 3-4 GeV. A fourth quark of $+\frac{2}{3}$ charge increases the expected R to $\frac{10}{3}$. Figure 1.2[1] shows the ratio R as a function of E_{cm}.

The existence of a fourth quark was proposed in 1970 by Glashow, Iliopoulos and Maiani in the "GIM mechanism" [5] to explain the absence of strangeness changing weak neutral currents. The strangeness changing neutral current Feynman diagram shown in figure 1.3a is not acceptable for describing $K_L^o \rightarrow \mu^+\mu^-$. The rate from second order Feynman diagrams, one is shown in figure 1.3b, is too large for the very suppressed $K_L^o \rightarrow \mu^+\mu^-$ branching ratio $\approx 10^{-8}$; the d and s quarks have been Cabbibo mixed [6] ($d\cos\theta_c + s\sin\theta_c$) and along with the u quark form a doublet. A new quark, in a doublet with ($s\cos\theta_c - d\sin\theta_c$), introduces second order strangeness changing charged currents, one such Feynman diagram is shown in figure 1.3c. Pairs of second order diagrams, one such pair is the diagrams shown in figure 1.3, do not entirely cancel due to the difference of masses of the up and charm quarks, resulting in the small $B(K_L^o \rightarrow \mu^+\mu^-)$.

1.1.2 Discovery of the J/ψ

The first charmonium state was seen in November 1974 by two experiments. At Brookhaven National Laboratory, the e^+e^-invariant mass in $p + \mathrm{Be} \rightarrow e^+e^- + X$ showed a peak about 3.1 GeV/c^2 [7], figure 1.4; the experimenters named the

[1] A further increase in R as E_{cm} increases comes from $e^+e^- \rightarrow \tau^+\tau^- \rightarrow hadrons$.

Figure 1.4: The e^+e^- invariant mass that constitutes the Brookhaven experiment's J signal (from reference [7]).

new resonance J. Meanwhile researchers at SPEAR (SLAC) [8], saw an energy dependence of the cross section for $e^+e^- \rightarrow hadrons$; a resonance was also identifiable in $e^+e^-$and $\mu^+\mu^-$ final states, figure 1.5, and was named ψ by the experimenters. A third experiment at Frascati [9], was able to immediately reproduce the signal for the particle, which now has the combined name J/ψ.

Immediately it was noticed that the resonance is exceedingly narrow $\ll 1$ MeV, which was much less than the experimental resolutions. Resonances of mass greater than 1 GeV/c^2 have widths between a few MeV and a few hundreds MeV. The J/ψ

Figure 1.5: The energy dependence of the cross section that shows the SPEAR experiment's ψ signal (from reference [8]): a) multi-hadron, b) e^+e^-, and c) $\mu^+\mu^-$ final states.

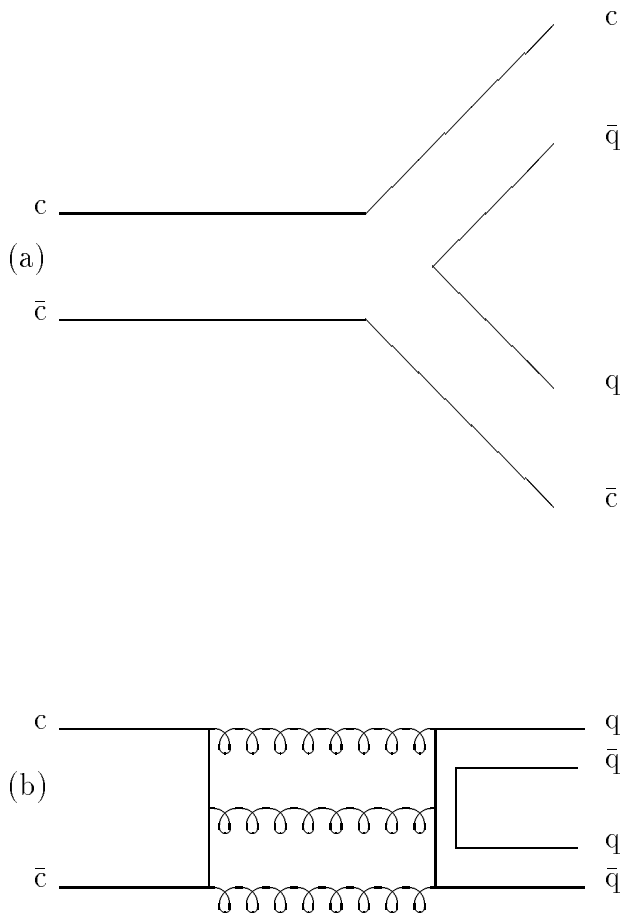

Figure 1.6: Feynman diagrams of strong decays to (a) open charm mesons and (b) light quark mesons. Diagram (a) is OZI-allowed while (b) is OZI-suppressed.

width is 50-1000 times narrower than the other heavy resonances. The best explanation was a new heavy quark forming a new meson, $\bar{c}c$. The narrowness of the J/ψ is attributed to the OZI-rule (Okubo, Zweig and Iizuka) [10, 11, 12]. Strong decays are suppressed since there are no charmed mesons in the final state. To decay into the (eventually identified) lowest mass open charm mesons D^o and $\bar{D}^o$, the charmonium mass must be greater than 3.7 GeV/c^2 ($2M_{D^o}$). A Feynman diagram of a charmonium decay into open charmed mesons is shown in figure 1.6a. In contrast, figure 1.6b

shows the OZI-suppressed charmonium decay to light quark mesons. Essentially, disconnected quark-line diagrams are highly suppressed causing any charmonium resonance below the open charm threshold of 3.7 GeV/c^2 to be narrow. Since a meson is a color singlet, at least two gluons are needed; the charge conjugation quantum number for the J/ψ is -1 which requires an odd number of gluons, i.e. a minimum of three gluons is needed for the J/ψ strong decays. Each gluon exchanged between the disconnected quark lines adds to the suppression of the decay.

1.1.3 The Charmonium Spectrum

The radial excitation of the J/ψ, the ψ', was discovered soon afterward below the open charm threshold. Other narrow resonances of charmonium bound states were expected with different spin and angular momentum quantum numbers below the open charm threshold[2]. Each charmonium state constituent has an intrinsic spin quantum number of $\frac{1}{2}$. The two fermions combine for a total spin quantum number $S = 0, 1$. Each bound state can be labelled by conventional spectroscopic notation $^{2S+1}\mathrm{L}_J$ where L is the orbital angular momentum denoted by S, P, D, F... for $L = 0$, 1, 2, 3... and J is the total spin. The charmonium states can also be characterized by the quantum numbers for total spin J, parity P, and charge conjugation C, and denoted by J^{PC}. For fermion-antifermion systems, the parity and charge conjugation

[2]The $J = 2$ D states are expected to be narrow even though their masses are expected to be above the open charmed threshold. Parity forbids either state to decay into $\bar{D}D$; both states could decay to DD^* if the mass is greater than 3875 MeV/c^2.

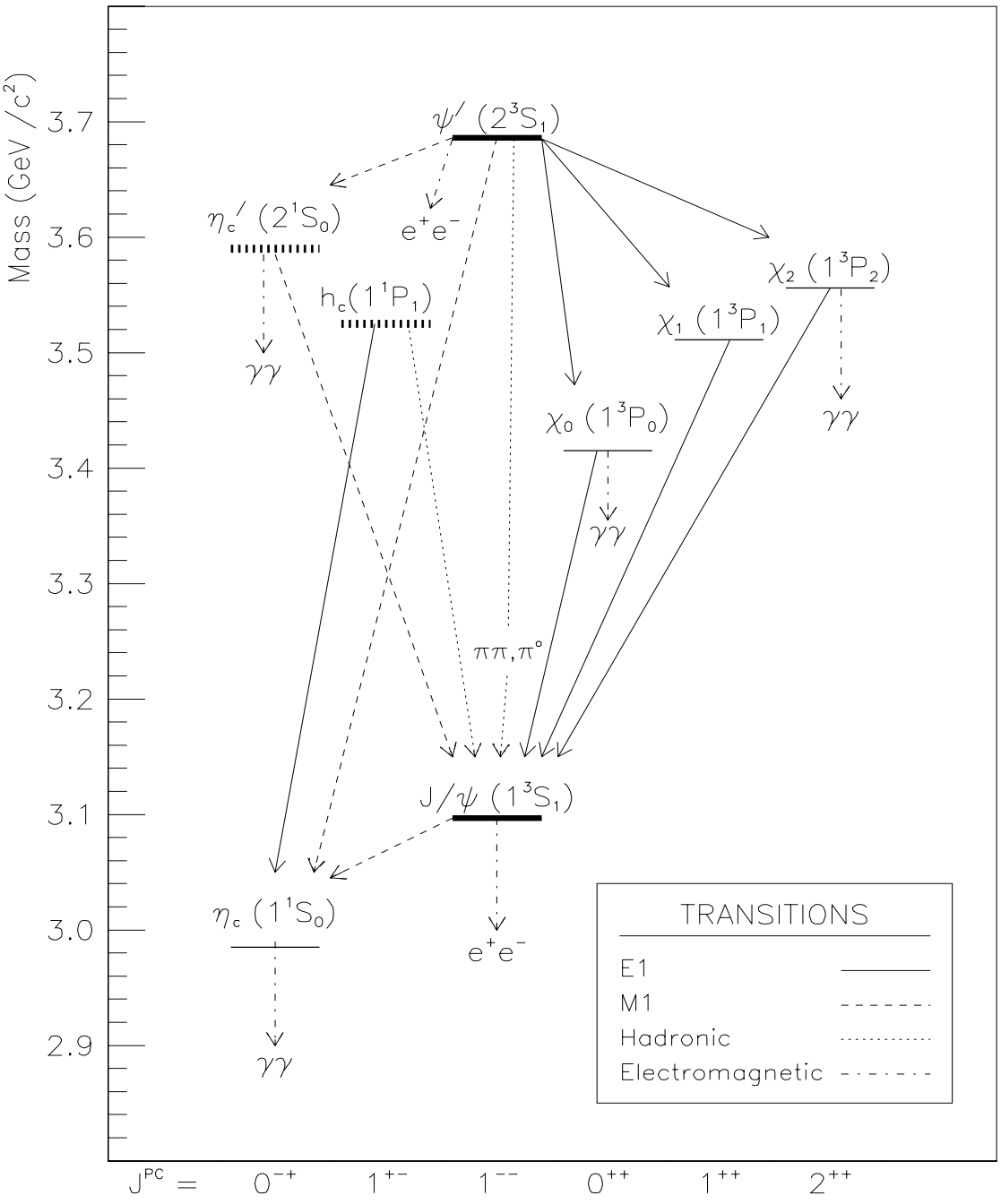

Figure 1.7: The charmonium spectrum below the open charm threshold with the $^1P_1$ located at the spin weighted average of the triplet P wave states. Thick solid lines denote the states which are directly produced by e^+e^- annihilation; states which were unseen or needed to be verified before this experiment are represented by thick broken lines. The known and expected hadronic and electromagnetic transitions and decays that E760 can detect are shown.

are

$$P = (-1)^{L+1} \tag{1.8}$$

$$C = (-1)^{L+S}. \tag{1.9}$$

The J/ψ and ψ' were first formed in e^+e^-annihilation; the intermediate virtual photon of the process dictates that the quantum numbers of the J/ψ and ψ' are $J^{PC} = 1^{--}$. Other charmonium states have been observed through decays of the J/ψ and ψ' (section 1.4) and by direct formation in $\bar{p}p$ collisions (section 1.5). All expected charmonium states below the open charm threshold have been seen through the e^+e^- collisions[3] except the $^1\mathrm{P}_1$. The charmonium spectrum is shown in figure 1.7 with the $^1\mathrm{P}_1$ located at the spin weighted center of gravity of the triplet P states (χ_0, χ_1, and χ_2), see section 1.2.2.

1.2 Theory

QCD is analogous to QED (quantum electrodynamics). In QED, charged particles exchange massless photons; color charged particles exchange massless gluons in QCD. Whereas the photon of QED does not have electrical charge, there are eight different colored gluons in QCD. QCD allows gluons to self-couple and results in confinement (i.e., no unbound quarks or gluons).

[3]The η_c' needs to be verified. See section 1.4, figure 1.10.

The hydrogen atom and positronium have been the testing grounds for QED and for relativistic corrections. QED has been very successful in describing the hydrogen atom. The e^+e^- bound states of positronium are analogous to $\bar{c}c$ bound states of charmonium. Both charmonium and bottomonium, $\bar{b}b$ provide testing grounds for QCD.

Proposed potentials and methods for calculating quantities of the charmonium system vary. Below are descriptions of the general characteristics of potentials and calculational methods. In general, non-relativistic potentials are used with relativistic corrections leading to spin dependent contributions.

1.2.1 Potentials

At short distances, single gluon exchange is approximated by a Coulomb-like interaction

$$V_{short}(r) = -\frac{4}{3}\frac{\alpha_s(r)}{r}; \tag{1.10}$$

this is similar to QED with the exception of a separation distance dependent fine structure constant $\alpha_s(r)$, as compared to $\alpha = \frac{1}{137}$, and a factor of $\frac{4}{3}$ which arises from requiring the quark-antiquark to be in a singlet color state. The strong fine structure constant can be stated in momentum-space as

$$\alpha_s(Q^2) = \frac{12\pi}{(33 - 2n_f)\ln(Q^2/\Lambda^2)}, \tag{1.11}$$

where n_f is the number of fermion flavors with mass below Q and Λ is a characteristic scale (generally taken to be of the order of 200 MeV). The logarithmic dependence of

α_s causes the gluon exchange to be weaker at short distances. The quasi-free behavior of quarks at short distances (large momentum transfer) is called *asymptotic freedom.*

Since there have been no free quarks or gluons observed, it is believed that quarks and gluons are confined. As the distance between quarks increases, the potential increases; an arbitrary form is linear,

$$V_{long}(r) = kr \tag{1.12}$$

where k is a force constant about 1 GeV/fm.

The two extreme distance potentials can be combined simply into

$$V(r) = -\frac{4}{3}\frac{\alpha_s(r)}{r} + kr \tag{1.13}$$

which is called the "Cornell potential" [13]. In momentum space, Richardson [14] proposed the potential

$$V(Q^2) = -\frac{4}{3}\frac{12\pi}{(33-2n_f)}\frac{4\pi}{Q^2}\frac{1}{\ln(1+Q^2/\Lambda^2)}; \tag{1.14}$$

for large Q^2 (small r) the potential behaves as $[\ln(Q^2/\Lambda^2)]^{-1}$ and for small Q^2 (large r) the behavior is Q^{-4}, corresponding to a linear potential. There are other forms of potentials, e.g. purely logarithmic $V(r) = a\ln(r/r_\circ)$, power laws $V(r) = b + cr^\nu$ and combinations of any of the above. For the most part, calculations are done with modified Cornell and Richardson potentials and reproduce the gross $\bar{c}c$ spectra fairly well. As shown in figure 1.8, the potentials behave similarly for distances between 0.1 and 1 fm, the range of $\bar{c}c$ distances for charmonium.

Figure 1.8: The comparison of several potentials shows the same behavior for the relevant separation distance for the charmonium system (from reference [15]).

The modified potentials add parameters to the potential which are usually motivated by QCD concerns. Generally, the Hamiltonian is expanded in $(\frac{v}{c})^2$ as

$$H = H_0 + H_1 + \cdots. \tag{1.15}$$

The nonrelativistic Hamiltonian is

$$H_0 = \frac{p^2}{m} + V_s(r) + V_v(r), \tag{1.16}$$

where p and m are respectively the quark momentum and mass, $V_v(r)$ is a vector-like potential, and $V_s(r)$ is a scalar-like potential. The short range one gluon exchange is in V_v. The long range confining potential cannot be entirely vector-like [16, 17]. The confinement potential is usually taken to be V_s; there can be a vector-like contribution to the confinement potential which would be included in V_v.

The first order term in $(\frac{v}{c})^2$ of the Hamiltonian can be split into a spin independent term H_{SI} and a spin dependent term H_{SD}:

$$H_1 = H_{SI} + H_{SD}. \tag{1.17}$$

The spin independent Hamiltonian is

$$\begin{aligned} H_{SI} = \quad & -\tfrac{p^4}{4m^3} + \tfrac{1}{4m^2}\{\tfrac{2L(L+1)}{r}V_v' + [p^2, V_v - rV_v'] \\ & +2(V_v - rV_v')p^2 + \tfrac{1}{2}(\tfrac{8}{r}V_v' + V_v'' - rV_v''')\}, \end{aligned} \tag{1.18}$$

where the prime ($'$) indicates a derivative with respect to the separation distance r. The spin dependent Hamiltonian is discussed in the next section.

1.2.2 Spin Dependence

The spin dependent Hamiltonian can be split into three terms,

$$H_{SD} = H_{SO} + H_T + H_{SS} \tag{1.19}$$

where the indices SO, T and SS refer to spin-orbit, tensor and spin-spin terms, respectively. These terms were first considered by Pumplin et al. [18] and Schnitzer [19] and are

$$H_{SO} = \tfrac{1}{2m^2 r}(3V_v' - V_s')\langle \vec{L}\cdot\vec{S}\rangle = V_{SO}\langle \vec{L}\cdot\vec{S}\rangle, \tag{1.20}$$

$$H_T = -\tfrac{1}{m^2}(V_v'' - \tfrac{V_v'}{r})\langle T_{12}\rangle = V_T\langle T_{12}\rangle, \tag{1.21}$$

$$H_{SS} = \tfrac{2}{3m^2}(\nabla^2 V_v)\langle \vec{S_1}\cdot\vec{S_2}\rangle = V_{SS}\langle \vec{S_1}\cdot\vec{S_2}\rangle, \tag{1.22}$$

where

$$T_{12} = \frac{1}{3}[3(\vec{S_1}\cdot\hat{r})(\vec{S_2}\cdot\hat{r}) - \vec{S_1}\cdot\vec{S_2}]. \tag{1.23}$$

The expectation values are

$$\langle \vec{L} \cdot \vec{S} \rangle = \frac{1}{2}[J(J+1) - L(L+1) - S(S+1)], \tag{1.24}$$

$$\langle T_{12} \rangle = \frac{-\langle \vec{L} \cdot \vec{S} \rangle^2 - \frac{1}{2}\langle \vec{L} \cdot \vec{S} \rangle + \frac{1}{3}\langle \vec{L}^2 \rangle \langle \vec{S}^2 \rangle}{(2L+3)(2L-1)}, \tag{1.25}$$

$$\langle \vec{S_1} \cdot \vec{S_2} \rangle = \frac{1}{2}[S(S+1) - \tfrac{3}{2}]. \tag{1.26}$$

The P wave states are $L = 1$ and the triplet P wave masses are

$$M_{\chi_0} = M_{SI} - 2V_{SO} - \frac{1}{3}V_T + \frac{1}{4}V_{SS}, \tag{1.27}$$

$$M_{\chi_1} = M_{SI} - V_{SO} + \frac{1}{6}V_T + \frac{1}{4}V_{SS}, \tag{1.28}$$

$$M_{\chi_2} = M_{SI} + V_{SO} - \frac{1}{30}V_T + \frac{1}{4}V_{SS} \tag{1.29}$$

where M_{SI} is from equation 1.18, the spin independent Hamiltonian. The singlet P wave mass is

$$M_{h_c} = M_{SI} - \frac{3}{4}V_{SS}. \tag{1.30}$$

The last four equations can be inverted to find the spin-orbit, tensor, spin-spin and spin independent contributions to the P wave masses:

$$V_T = -\frac{5}{3}M_{\chi_0} + \frac{5}{2}M_{\chi_1} - \frac{5}{6}M_{\chi_2}, \tag{1.31}$$

$$V_{SO} = -\frac{1}{6}M_{\chi_0} - \frac{1}{4}M_{\chi_1} + \frac{5}{12}M_{\chi_2}, \tag{1.32}$$

$$V_{SS} = M_{\chi_{cog}} - M_{h_c}, \tag{1.33}$$

$$M_{SI} = \frac{3}{4}M_{\chi_{cog}} + \frac{1}{4}M_{h_c}, \tag{1.34}$$

where $M_{\chi_{cog}}$ is the spin weighted average of the triplet P wave states:

$$M_{\chi_{cog}} = \frac{\sum(2J+1)M_{\chi_J}}{\sum(2J+1)} = \frac{1M_{\chi_0} + 3M_{\chi_1} + 5M_{\chi_2}}{9}. \tag{1.35}$$

The triplet P wave mass differences are caused by spin-orbit and tensor contributions. Only the spin-spin, or hyperfine, contribution causes the M_{h_c} to be non-degenerate with $M_{\chi_{cog}}$.

The Hamiltonian described above is an expansion to first order in $(\frac{v}{c})^2$; higher order terms may have non-negligible contributions. The virial theorem is used to show the importance of the higher order terms. The expectation value for the kinetic energy $\langle T \rangle$ is

$$\langle T \rangle = \frac{1}{2} \langle \vec{r} \cdot \vec{\nabla} V(\vec{r}) \rangle. \tag{1.36}$$

Assuming a linear distance term dominates at the mean radius of the charmonium system, then $2\langle T \rangle = \langle V \rangle$ or $E_b = 3\langle T \rangle$ (where E_b is the binding energy of the system, $\langle T \rangle + \langle V \rangle$). Using the non-relativistic expression

$$\langle T \rangle = 2 \left(\frac{m_c \langle v^2 \rangle}{2} \right), \tag{1.37}$$

the expectation for the square of the velocity is

$$\langle v^2 \rangle = \frac{E_b}{3m_c}, \tag{1.38}$$

where m_c is the mass of the charm quark. A binding energy of 675 MeV ($= M_{\psi'} - M_{J/\psi}$) and $m_c = 1.5$ GeV/c^2 leads to the estimation that

$$\langle v^2 \rangle \approx 0.15c^2. \tag{1.39}$$

This rough estimate shows that the charmonium system is not completely non-relativistic and that relativistic effects (for example spin dependence) can be important.

1.3 Expectations of the $^1P_1$

Below are summaries of the theoretical expectations for the $^1P_1$ mass, different decay rates and total width. In general, the predictions are based on a potential and calculational method which depend upon a set of parameters. The parameters are determined by fits to existing charmonium (and in some cases bottomonium) experimental data. The summaries are not complete but are presented to give an idea of the many calculations that have been done.

1.3.1 Mass

Using E760's measurement of the χ_1 and χ_2 masses [20] (3510.53 ± 0.13 MeV/c^2 and 3556.15 ± 0.14 MeV/c^2, respectively) and the previously measured average χ_0 mass [21] (3415.1 ± 1.0 Mev/c^2), the spin weighted average mass is

$$M_{\chi_{cog}} = 3525.27 \pm 0.23 \text{ MeV/c}^2. \tag{1.40}$$

The mass difference between the $^1P_1$ and χ_{cog} arises entirely from the hyperfine splitting as shown above. The hyperfine mass splitting is defined here as

$$\Delta_{HF} = -V_{SS} = M_{h_c} - M_{\chi_{cog}}. \tag{1.41}$$

There are a few theoretical papers (for example, references [22, 23, 24]) which predict the singlet state to be degenerate with χ_{cog}, $\Delta_{HF} = 0$.

Early predictions of the $^1P_1$ mass tended to have Δ_{HF} negative. One of the first simple potential model calculations [25] resulted in $\Delta_{HF} = -9$ MeV/c^2; another

Authors	Δ_{HF} (MeV/c^2)	Comment
Gupta et al. [28]	1.4	
Gupta et al. [29]	2.0	Semi-relativistic potential
Gupta et al. [30]	-4.5	
McClary & Byers [31]	5	
Ono & Schöberl [32]	-10	Fit includes light quark mesons
Pantaleone & Tye [33]	1.4	
Badalyan & Yurov [34]	8.0	VCM with $\sigma_1 < 0$
Badalyan & Yurov [34]	1.13	VCM with $\sigma_1 \approx 0$
Badalyan & Yurov [34]	-1.8	VCM with $\sigma_1 > 0$
Halzen et al. [35]	0.7 ± 0.2	
Dixit et al. [36]	-7.3 to 0	Power law
Galkin et al. [37]	-1	
Fulcher [38]	3	
Lichtenberg et al. [39]	-4.1	
Lichtenberg & Potting [40]	-2.9 to 5.4	
Olsson & Suchyta [41]	-4.6	2 spin independent terms
Igi & Ono [42, 43]	1.91 to 3.49	2 loop correction
Chen & Kuang [44]	0.89 to 1.80	2 loop correction

Table 1.1: Theoretical predictions for the hyperfine mass splitting, Δ_{HF}. See the references for more information about the potentials and methods.

calculation [26] resulted in a splitting of -22 MeV/c^2. A modified Coulomb potential [27], which does not satisfy confinement for large r, predicted $\Delta_{HF} = 58$ MeV/c^2.

From the early 1980's until the present, there have been many potentials tried. In table 1.1 is a list of predictions made by theorists; included are comments about the specific potentials used or methods employed, see the individual references for details. As can be seen in table 1.1, Δ_{HF} is predicted to be a few MeV/c^2 and most predictions have Δ_{HF} positive, i.e. mass of the ^{1}P$_1$ is greater than $M_{\chi_{cog}}$.

Author	$\Gamma_{h_c \to \gamma\eta_c}$ (keV)	Comments
Renard [45]	240	
Galkin [37]	559	
Novikov et al. [46]	975	
McClary & Byers [31]	483	Nonrelativistic 660 keV
Chao et al. [47]	385	Nonrelativistic 650 keV
Bodwin et al. [48]	450	Scaling to $\Gamma_{\chi \to \gamma J/\psi}$
Casalbuoni et al. [49]	450	

Table 1.2: Theoretical predictions for the $^1P_1$ (h_c) radiative transition to η_c.

1.3.2 Decay Rates

The expected total width of the $^1P_1$ is expected to be narrow, $\leq 1\ MeV$. The contributions from radiative and hadronic decays are expected to be nearly the same, with the dominant decay expected to be $\eta_c\gamma$. Most calculations relate the partial widths of the $^1P_1$ to the already measured partial widths of other charmonium states.

The radiative transition to the η_c has been calculated several times. In the non-relativistic limit, the transition rate is

$$\Gamma(^1P_1 \to \eta_c\gamma) = \frac{4\alpha e_c^2 E_\gamma^3}{9} \mid \langle f|r|i\rangle \mid^2, \tag{1.42}$$

where e_c is the electric charge of the charm quark, E_γ is the energy of the radiative gamma ray, and the matrix element involves the normalized initial and final state wave functions. The wave functions are model dependent and vary slightly. Table 1.2 shows a few of the theoretical predictions. Bodwin, Braaten and Lepage [48] predict the radiative transition by scaling (using the photon energies) to the $\chi_{0,1,2}$ radiative decays to J/ψ. Coupled channel effects (influence from the open charm threshold) may decrease the radiative width; a 10% decrease has been predicted of the radiative

Authors	$\Gamma_{h_c \to J/\psi\pi\pi}$ (keV)	Comments
Kuang et al. [50]	4.12 (8.24)	Multipole expansion
Chemtob & Navelet [51]	52.6	Semi-perturbative
Chen & Yi [52]	7.1 (14.2)	Multipole, 2 loop
Chen & Yi [52]	4.1 (9.3)	Use Kuang's potential [50]

Table 1.3: Theoretical predictions for the $^1P_1$ (h_c) hadronic transition to $J/\psi\pi\pi$. The multipole expansion widths are for $\alpha_E = \alpha_M$ ($\alpha_E = 2\alpha_M$), see references for details.

widths of the triplet P wave states [13]. Renard also predicts that the M1 transition to the triplet P states is a few keV [45], a small contribution to the total width.

The hadronic transitions from the $^1P_1$ to $J/\psi + X$ are only allowed energetically for X being π^o, $\pi^o\pi^o$, or $\pi^+\pi^-$. A hadronic transition via η is not allowed since $M_\eta > M_{\chi_{cog}} - M_{J/\psi}$. Tables 1.3 and 1.4 show predictions for the $\pi\pi$ and π^o transitions, respectively. All of the authors predict the $J/\psi\pi\pi$ width to be greater than the $J/\psi\pi^o$ width.

The $^1P_1$ inclusive partial widths to hadrons (radiative decay to hadrons) is really the partial width to three gluons (gamma ray and two gluons) where the gluons automatically hadronize. A simple scaling to a known partial width was first done

Authors	$\Gamma_{h_c \to J/\psi\pi^o}$ (keV)	Comments
Kuang et al. [50]	2	Multipole expansion
Chemtob & Navelet [51]	0.0061	Semi-perturbative
Chen & Yi [52]	0.58 (1.16)	Multipole, 2 loop
Chen & Yi [52]	0.29 (0.57)	Use Kuang's potential [50]

Table 1.4: Theoretical predictions for the $^1P_1$ (h_c) isospin violating hadronic transition to $J/\psi\pi^o$. The multipole expansion widths are for $\alpha_E = \alpha_M$ ($\alpha_E = 2\alpha_M$), see references for details.

Authors	$\Gamma_{h_c \to hadrons}$ (keV)	Comments
Renard [45]	120	
Novikov [46]	60 to 350	
Kuang et al. [50]	53.7	Multipole expansion
Chen & Yi [52]	19.3 (35)	Multipole, 2 loop
Chen & Yi [52]	51 (51)	Use Kuang's potential [50]
Bodwin et al. [48]	530	Factorization theorm

Table 1.5: Theoretical predictions for the $^1P_1$ (h_c) hadron decays. The multipole expansion widths are for $\alpha_E = \alpha_M$ ($\alpha_E = 2\alpha_M$), see references for details.

by Barbieri, Gatto and Remiddi [53]:

$$\frac{\Gamma(^1P_1 \to \text{hadrons})}{\Gamma(\chi_1 \to \text{hadrons})} \simeq \frac{5}{2n_f}, \tag{1.43}$$

where $n_f = 3$ is the number of quark flavors in the final state hadrons. The theoretical predictions of the partial width to hadrons is given in table 1.5. Bodwin, Braaten and Lepage [48] also uses the known χ_1 partial width to hadrons to predict the $^1P_1$ radiative partial width to hadrons:

$$\frac{\Gamma(^1P_1 \to \gamma + \text{hadrons})}{\Gamma(\chi_1 \to \text{hadrons})} \simeq \frac{6e_c^2\alpha}{n_f\alpha_s(M_c)}. \tag{1.44}$$

Table 1.6 shows the predicted $^1P_1$ radiative transitions to hadrons. Both the hadronic and radiative transition to hadrons decays are OZI suppressed.

Authors	$\Gamma_{h_c \to \gamma + hadrons}$ (keV)	Comments
Renard [45]	210	
Novikov [46]	7 to 40	
Kuang et al. [50]	5.91	Multipole expansion
Chen & Yi [52]	2.1 (3.7)	Multipole, 2 loop
Chen & Yi [52]	5.7 (5.5)	Use Kuang's potential [50]
Bodwin et al. [48]	15	Factorization theorm

Table 1.6: Theoretical predictions for the $^1P_1$ (h_c) radiative decays to hadrons. The multipole expansion widths are for $\alpha_E = \alpha_M$ ($\alpha_E = 2\alpha_M$), see references for details.

Author	Γ_{h_c} (keV)
Renard [45]	500 to 1000
Kuang et al. [50]	394
Chen & Yi [52]	360
Bodwin et al. [48]	980

Table 1.7: Theoretical predictions for the $^1P_1$ (h_c) total width.

To find the $^1P_1$ partial width to $\bar{p}p$, Kuang et al. uses the η_c partial width:

$$\frac{\Gamma(^1P_1 \to \bar{p}p)}{\Gamma(\eta_c \to \bar{p}p)} \simeq \frac{\Gamma(^1P_1 \to \text{hadrons})}{\Gamma(\eta_c \to \text{hadrons})}; \tag{1.45}$$

they predict a partial width of 0.186 keV. Chen & Yi predict 0.044 keV. If equation 1.43 is used, then the $\bar{p}p$ partial width of the $^1P_1$ is 0.64 keV.

Authors give total widths which are the sum of the partial widths. Some authors add other author's partial widths to their own widths to arrive at a prediction for the $^1P_1$ total width. Table 1.7 shows the theoretical $^1P_1$ total width predictions.

1.4 Spectroscopy by e^+e^- Annihilations

The majority of charmonium spectroscopy has been done using e^+e^- colliders, from the discovery of the charm quark until the middle of the 1980's. Only $\bar{c}c$ states with the same quantum number as the intermediate virtual photon, $J^{PC} = 1^{--}$, can be made directly from e^+e^- annihilations, figure 1.9a. Interactions involving e^+e^- can produce even J $\bar{c}c$ states through two intermediate photons (figure 1.9b), which introduces an additional factor of α^2 in the rate causing the production rate to be 10^{-4} smaller than any one intermediate photon rate. Since $C = -1$ for the $^1P_1$, three

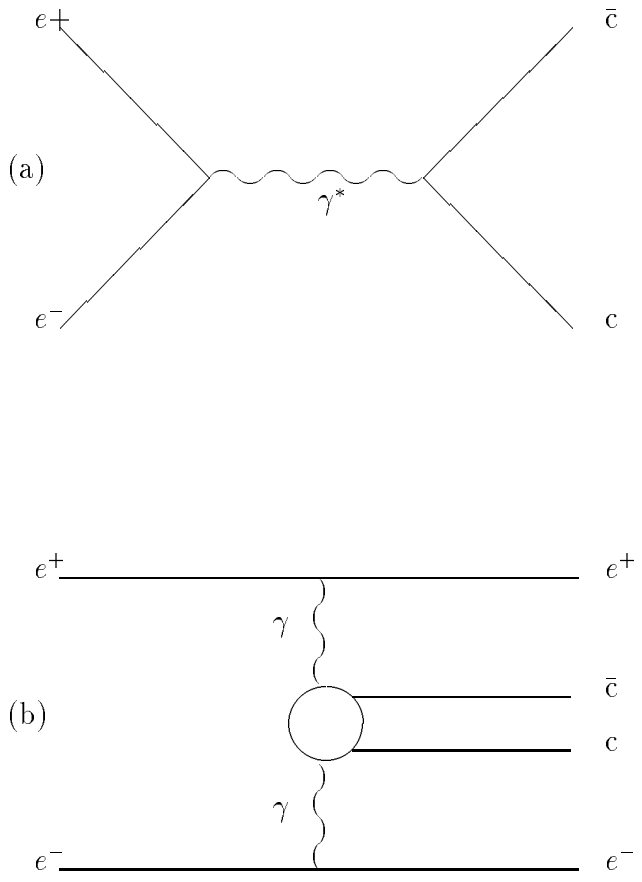

Figure 1.9: Feynman diagrams of direct production of charmonium in e^+e^- annihilation: (a) 1^{--} $\bar{c}c$ states by one virtual photon and (b) even J $\bar{c}c$ states by two intermediate photons.

intermediate photons are needed, which thereby decreases the production rate even more.

Spectroscopy of the $\bar{c}c$ states with quantum numbers other than the photon has been done through the decays of the 1^{--} $\bar{c}c$ states produced by e^+e^- interactions, in particular radiative transitions. The determination of the characteristics of the non-1^{--} $\bar{c}c$ states depends upon an experiment's ability to measure the energy of the decay particle(s). An e^+e^- experiment, Crystal Ball [54], has been able to measure the radiative photons from $\psi' \rightarrow {}^3\mathrm{P}_{0,1,2}$ ($^3\mathrm{P}_{0,1,2}$ are known as $\chi_{0,1,2}$) and the subsequent

Figure 1.10: The inclusive photon spectrum from the ψ' seen by Crystal Ball (from reference [54]).

radiative transition ${}^3\mathrm{P}_{0,1,2} \rightarrow J/\psi$ which are all E1 transitions. Crystal Ball has also seen evidence of M1 transitions $J/\psi \rightarrow \gamma\eta_c$ (the radiative transition from the triplet S state to the singlet S state) and $\psi' \rightarrow \gamma\eta_c'$[4] as well as the hindered M1 transition[5] $\psi' \rightarrow \gamma\eta_c$. The inclusive photon spectrum from the ψ' is shown in figure 1.10, as obtained by the Crystal Ball Experiment. Charge conjugation invariance prohibits the ψ' to radiatively decay to the ${}^1\mathrm{P}_1$.

[4]The η_c' signal is not very strong since the measured energy of the photon is near the threshold of Crystal Ball's detector. The η_c' needs to be verified.

[5]The transition changes principal quantum number; a radially excited state decays into a non-excited state of charmonium.

The $^1P_1$ can only be a decay product of radiative decays of η_c' (E1) and ^3P (M1), depending upon the $^1P_1$ mass. The expected radiative decays of the $^1P_1$ are to η_c (E1) and ^3P (M1), again depending upon the $^1P_1$ mass. Note that the expected small difference of masses between the singlet and triplet P wave states should result in very small radiative rates for such M1 transitions. Crystal Ball searched for the $^1P_1$ through the isospin violating transition $\psi' \to {}^1P_1\pi^o$ [55]; the π^o energy spectrum was studied and no signal was found corresponding to a mass between the J/ψ mass and 3.55 GeV/c^2 ($= M_{\psi'} - M_{\pi^o}$).

1.5 Spectroscopy by $\bar{p}p$ Annihilations

The CERN ISR (Intersecting Storage Ring) R704 experiment was able to directly form and study some of the $J^{PC} \neq 1^{--}$ $\bar{c}c$ states in $\bar{p}p$ collisions before the ISR was shut down in 1984. R704 pioneered $\bar{p}p$ spectroscopy using a cooled $\bar{p}$ beam and a hydrogen gas jet [56]. The two-armed, nonmagnetic detector (geometrical acceptance $\approx 12\%$) used by R704 investigated the electromagnetic decay products of several charmonium states. In particular,

$$\bar{p}p \to \bar{c}c \to \quad e^+e^- + X \tag{1.46}$$

$$\bar{p}p \to \bar{c}c \to \qquad \gamma\gamma \tag{1.47}$$

where the $e^+e^-(\gamma\gamma)$ invariant mass reconstructs to a $\bar{c}c$ state J/ψ or ψ' (η_c or χ_2). For the first time, the 0^{-+}, 1^{++} and 2^{++} charmonium states (η_c, χ_1 and χ_2, respectively) were formed directly. Figure 1.11 show the diagrams for two and three intermediate

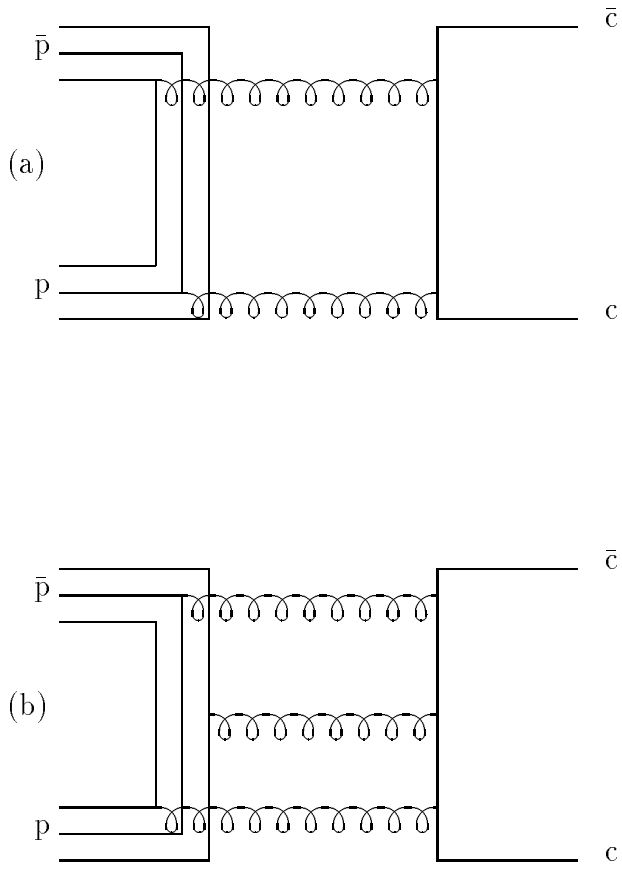

Figure 1.11: The Feynman diagrams of $\bar{c}c$ states produced in $\bar{p}p$ annihilation: (a) two intermediate gluons to form even J $\bar{c}c$ states and (b) three intermediate gluons to form odd J $\bar{c}c$ states.

gluons for forming $\bar{c}c$ states in $\bar{p}p$ annihilations. Near the spin weighted center of gravity of the ^{3}P states, five $J/\psi + X$ candidates were seen [57]. These events can be interpreted as possible evidence for a resonance; a discussion of the five events is presented in section 8.5.

The hard part of doing charmonium spectroscopy with $\bar{p}p$ annihilations is extracting the charmonium signal. Figure 1.12 shows the total $\bar{p}p$ cross section in the charmonium energy range is near 60 mb. The largest expected peak cross section for a charmonium state with an electromagnetic final state ($\bar{p}p \to J/\psi \to e^+e^-$) is 360 nb.

Figure 1.12: The total cross section for $\bar{p}p$ interactions (from reference [58]).

The electromagnetic decay signatures of bound charmonium result in rates that are at least 10^5 smaller than the total $\bar{p}p$ interaction rate. The advantage is that the determination of resonance characteristics, mass and width, are not dependent upon detector resolution but upon knowledge of the $\bar{p}$ momentum and spread of momentum. R704 proved that $\bar{c}c$ states can be separated from the large background and improved the knowledge of the non 1^{--} states.

E760 is modelled after R704. The Fermilab Antiproton Accumulator allows for a factor of 10 increase in the luminosity. Whereas the R704 detector was a two-armed spectrometer, the E760 detector covers the full azimuth and has a larger polar angular acceptance. The overall detector acceptance is 4 to 5 times larger than the

R704 detector. E760's proposed purpose has been to further study the η_c, χ_1 and χ_2 as well as search for the $^1P_1$ and η_c'. E760 uses the electromagnetic decay signatures, equations 1.3 and 1.4, as the main approach to search for $\bar{c}c$ states.

Chapter 2

Experimental Apparatus

The E760 experimental area is located in the low dispersion region of the AP-50 section of the Fermilab Antiproton Accumulator. A schematic representation of the Fermilab accelerator complex is shown in figure 2.1. Figure 2.2 shows a schematic representation of the $\bar{p}$ source and where the E760 detector is located in one of the three straight sections.

A cut-through view of the E760 detector is shown in figure 2.3. Attached to the E760 detector, and shown in figure 2.3, is the proton source, gas jet. In this chapter, the antiproton and proton sources are discussed followed by descriptions of the different components of the E760 detector.

2.1 Antiproton Source

The $\bar{p}$ source is described in detail in the Tevatron's design report [59]; a basic outline describing the $\bar{p}$ source is given in this section along with how the $\bar{p}$ beam characteristics are determined. Protons extracted from Fermilab's Main Ring at F0

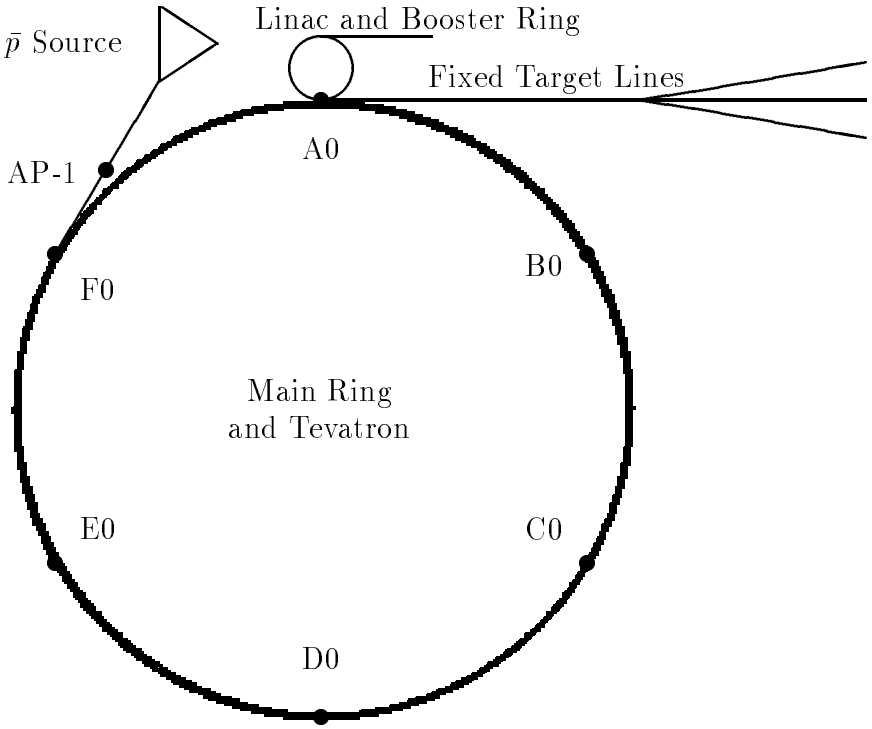

Figure 2.1: A schematic representation of the Fermilab accelerator complex.

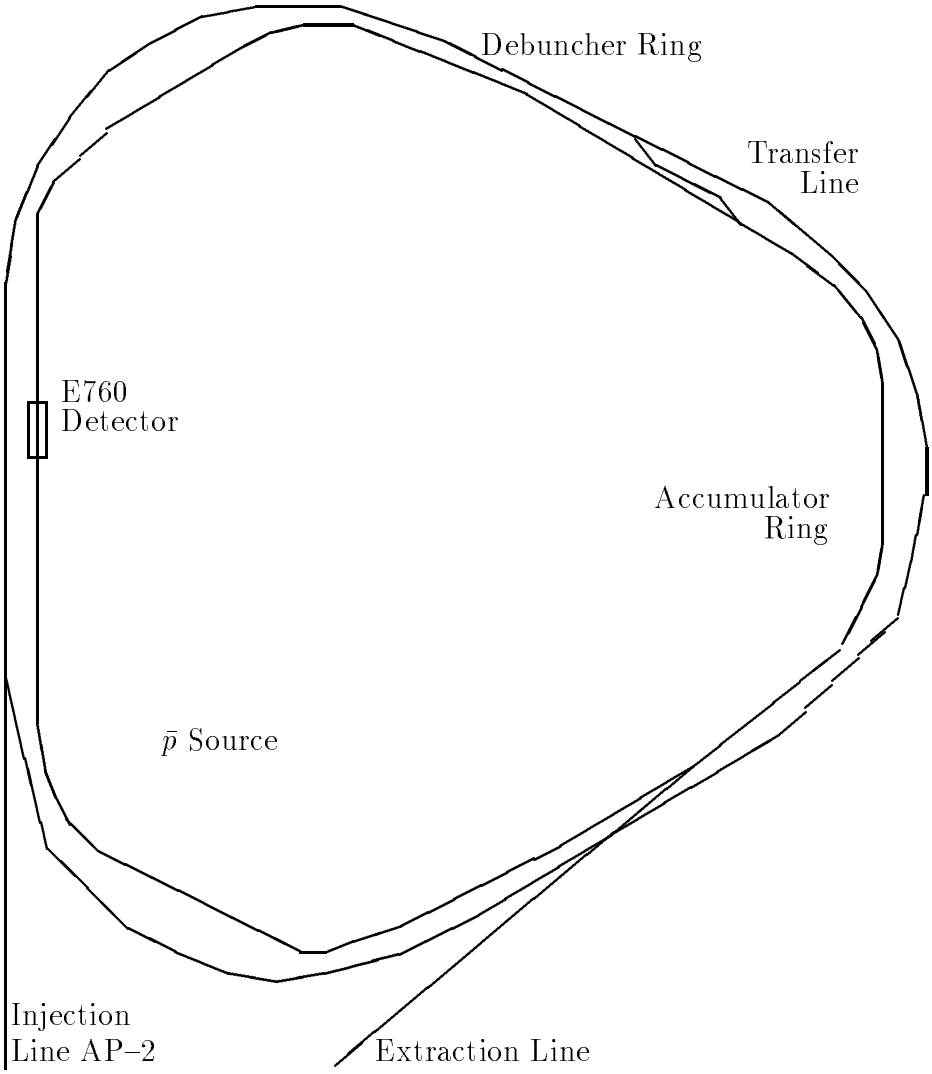

Figure 2.2: A schematic representation of the Fermilab $\bar{p}$ source and the location of E760.

Figure 2.3: A cut-through view of the E760 detector and gas jet.

(see figures 2.1 and 2.2) are transported to the AP-1 target hall. The target, tungsten or tungsten alloy, is 6 cm thick. Each bunch of protons that is sent to the target contains $\approx 10^{12}$ particles. The negatively charged particles produced by the collision of the 120 GeV proton beam and target are collected with a 15 cm long lithium lens with a radius of 1 cm. The lens is pulsed (0.6 msec) with ≈ 500 KA to provide a uniform field gradient (≈ 1000 T/m). The greatest number of antiprotons are produced with energies between 8 and 13 GeV. A bending magnet focuses the negatively charged particles with momentum 8.9 GeV/c into the beam transport line. The rest of the particles are contained by a beam dump.

The $\bar{p}$ bunch is injected into the debuncher ring through the connecting AP-2 beam line. The Debuncher accepts the $\bar{p}$ bunch and then stochastically cools the $\bar{p}$'s which spreads the the $\bar{p}$'s out into a beam, i.e. debunches the antiprotons. The spread

of momentum $(\frac{\Delta p}{p})_{rms}$ of the $\bar{p}$ beam changes in the debuncher ring from 4% to 0.2%. The $\bar{p}$'s are then transferred to the Accumulator. All pions and muons decay before transfer. Electrons lose energy due to synchrotron radiation and are lost.

The Accumulator accepts $\bar{p}$'s and further cools the beam to a nominal momentum spread of $\approx 0.05\%$. The immediate cooling of each transferred set of $\bar{p}$'s removes the $\bar{p}$'s from the phase space needed to accept the next transfer from the Debuncher. The Debuncher and Accumulator cooling operations occur much more quickly than the interval between main ring bunches of 120 GeV protons on the target. The average number of antiprotons that are collected for every 10^6 protons sent to the target is 3.

Accumulation of antiprotons continues until the number of particles in the beam is $\approx 4 \times 10^{11}$. The beam is then decelerated from 8.9 GeV/c to the appropriate momentum. The desired momentum $p_{\bar{p}}$ as a function of center of mass energy E_{cm} is

$$p_{\bar{p}} = \sqrt{\frac{E_{cm}^4}{4m_p^2} - E_{cm}^2}, \tag{2.1}$$

where m_p is the mass of the proton; the relationship between $p_{\bar{p}}$ and E_{cm} is shown in figure 2.4. Once the desired momentum is reached, the beam is further cooled to $(\frac{\Delta p}{p})_{rms} \approx 2 \times 10^{-4}$.

The momentum is calculated from the revolution frequency of the particles f and the orbit length L,

$$c\beta = fL = f(L_0 + \Delta L), \tag{2.2}$$

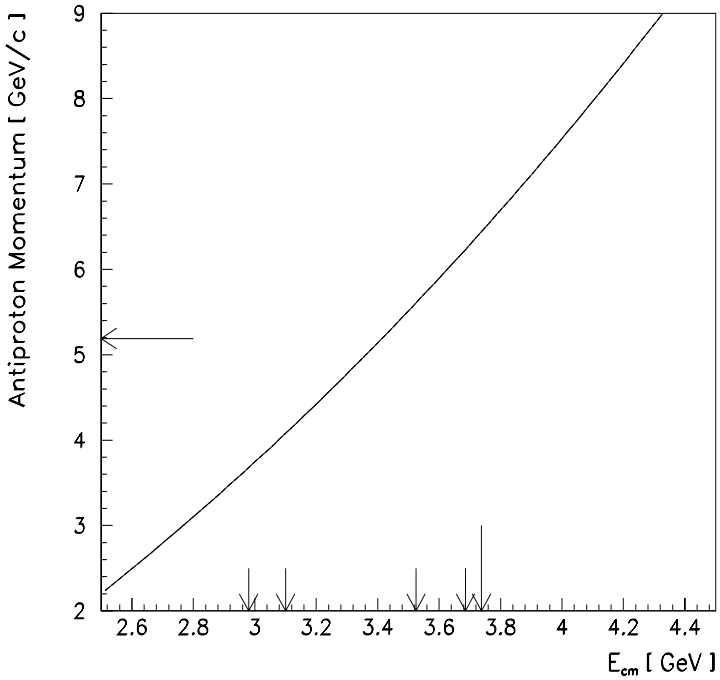

Figure 2.4: The $\bar{p}$ momentum as a function of the energy in the center of momentum frame. The shorter downward arrows point at masses (starting with the smallest energy) η_c, J/ψ, χ_{cog} and ψ', respectively; the larger downward arrow indicates the open charm threshold and the horizontal arrow is the $\bar{p}$ source transition point.

where L_0 is a reference orbit length and ΔL is the difference of the orbit from L_0. The reference orbit [60] is determined from data taken at the ψ'. The orbit length difference ΔL is measured using Beam Position Monitors [61] (BPM); there are 48 BPMs located around the Accumulator Ring.

Keeping the momentum spread of the $\bar{p}$ beam small is important. Stochastic cooling [62] is a technique of using measurements of the beam particles' deviations from the central orbit (longitudinal and transverse) to determine the appropriate kick provided by a kicker magnet, to bring the particles back to the proper orbit. The stochastic cooling keeps the momentum spread small as well as the transverse size

of the beam to be less than 0.5 cm (95% containment) in the low dispersion region. The cooling is also used to restore $\bar{p}$'s to the proper orbit and energy after interacting with the gas jet target.

The momentum spread is calculated by

$$\frac{dp}{p} = \frac{1}{\eta}\frac{df}{f}, \tag{2.3}$$

where η, the momentum slip factor, is defined as

$$\eta \equiv \frac{1}{\gamma^2} - \frac{1}{\gamma_t^2} \tag{2.4}$$

and γ_t^2 depends upon the machine lattice and is associated with the transition point. The spread in frequency is determined from the beam current Schottky noise spectrum [63]. Schottky noise bands appear at integer multiples of the beam revolution frequency (dependent upon beam energy, $f_{rev} \approx 0.62$ MHz); a coaxial quarter wavelength resonant pickup with a principal frequency of 79.323 MHz detects the harmonic of the revolution frequency closest to the principal frequency of the pickup (depending upon the beam energy, the 126^{th} to 129^{th} harmonic). The spectral power density $P(f)$ of the noise is proportional to the particle density $\frac{dN}{df}$:

$$P(f)\Delta f = 2\pi(ef)^2 \frac{dN}{df}\Delta f, \tag{2.5}$$

where e is the charge of the antiproton. A spectrum analyzer[1] is used to analyze the signal; a typical spectrum is shown in figure 2.5. The number of $\bar{p}$'s at a certain frequency, and therefore a specific momentum, is known.

[1] A Hewlett Packard model 8568B analyzer.

Figure 2.5: A typical Schottky power spectrum used to determine beam energy distribution.

The uncertainties of the of the beam energy measurements are discussed in section 7.6. The convolution of the beam energy spread and a Breit-Wigner resonance is presented in section 8.1.

2.2 Proton Source

A molecular hydrogen gas jet provides a proton target nearly at rest. The protons are injected into the Accumulator Ring at 90° to the antiproton beam. The

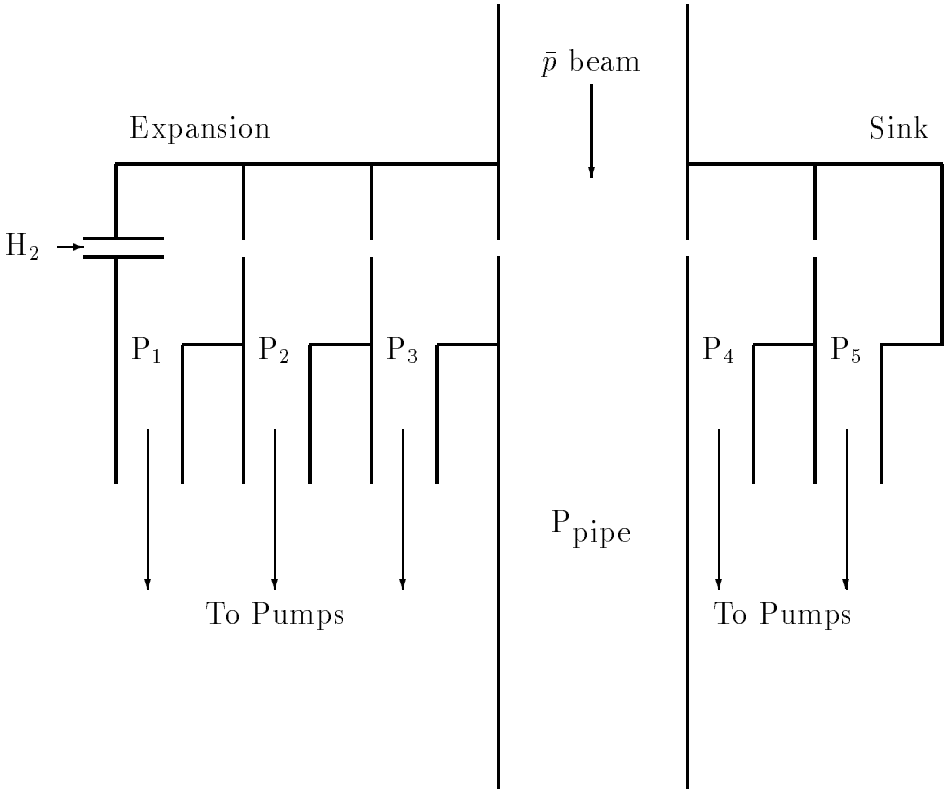

Figure 2.6: A schematic of the molecular hydrogen gas jet. The relationship of the pressures from each chamber and the beam pipe is $P_1 > P_2 > P_3 > P_{pipe} < P_4 < P_5$. The skimmers (not shown) are located around the expansion chambers' exit holes.

accumulator ring is under a vacuum (10^{-8} torr) so as not to scatter $\bar{p}$'s out of the beam pipe. The injection of the hydrogen requires a series of vacuum pumps to be used. A desired point-like interaction region requires that the hydrogen be injected into a small volume and collected quickly with pumps so as not to contaminate the accumulator vacuum. The gas jet apparatus [64],shown schematically in figure 2.6, leads to a dense target of protons and, therefore, a large instantaneous luminosity can be obtained.

The nozzle area of the gas jet and hydrogen are cooled by liquid nitrogen. The low temperature induces hydrogen molecules to cluster. The gas jet has to pass through several chambers. Expansion of the gas in each chamber causes some molecules to be removed from the jet stream by skimmers located around each chamber's exit hole. Vacuum pumps connected to each chamber remove the reflected hydrogen before the gas can exit the chambers and contaminate the accumulator ring vacuum. The resulting gas jet density at the interaction region is typically 3.5×10^{13} atoms/cm^3. The pressure of the hydrogen gas jet, and therefore the gas jet density in the interaction region, can be changed to increase and decrease the instantaneous luminosity.

The transverse dimension of the gas jet[2] when intersecting the $\bar{p}$ beam is < 1 cm^2. With a large beam fill and an orbit frequency ≈ 0.62 MHz, the peak instantaneous luminosity achieved is $\approx 1 \times 10^{31}$ cm^{-2}s^{-1}.

[2]The diameter of the gas jet is 6.3 mm for 95% containment.

Figure 2.7: A typical pulse height spectrum from the luminosity monitor.

2.3 Luminosity Monitor

The luminosity monitor consists of a set of solid state detectors located below the beam pipe. The luminosity monitor's detectors observe and count elastic $\bar{p}p$ scattering near 90° with respect to the $\bar{p}$ beam direction in the lab frame. Several of the detectors are movable to measure the $\bar{p}p$ elastic cross section [65] in the angular region near 90°. A single fixed detector at 86.435° is used to monitor the rate of interactions.

The luminosity is determined from knowledge of the $\bar{p}p$ differential elastic cross section [66] and the acceptance of the fixed detector. The fixed detector is 500 μm

thick and covers a 12 mm $\times$ 48 mm area located 1.47 m below the interaction region. The detector is sufficiently thick to stop protons with recoil energy less than 8 MeV. Each pulse height spectrum, a typical example shown in figure 2.7, is fit to the expected spectrum shape and an exponential background. The resulting number of counts over a known time period is used to determine the luminosity. The uncertainties of the luminosity measurement are discussed in section 7.6.

2.4 Hodoscopes

The E760 detector includes three scintillator hodoscopes. Each of the hodoscopes' elements has its signal split between the hardware trigger logic (section 5.2) and pattern units (latch signals above a certain minimum signal height). Two hodoscopes' signals are also split and connected to FERA ADCs for offline pulse height analysis.

The H1 hodoscope consists of 8 sections, each covering an azimuthal octant. The scintillator is $\approx$ 2 mm thick and slightly curved, resulting in the same scintillator thickness traversed by all particles from the interaction region. The H1 hodoscope is the closest detector element to the interaction point (see figure 2.3) and covers polar angles 9° to 65°. The main purpose of the H1 hodoscope is for the hardware trigger. The H1 hodoscope signals are recorded to perform a pulse height analysis.

H2 hodoscope is located at a radial distance of 16.5 cm. The H2 hodoscope covers the polar angles 12° to 65° with 32 elements distributed about the full azimuth

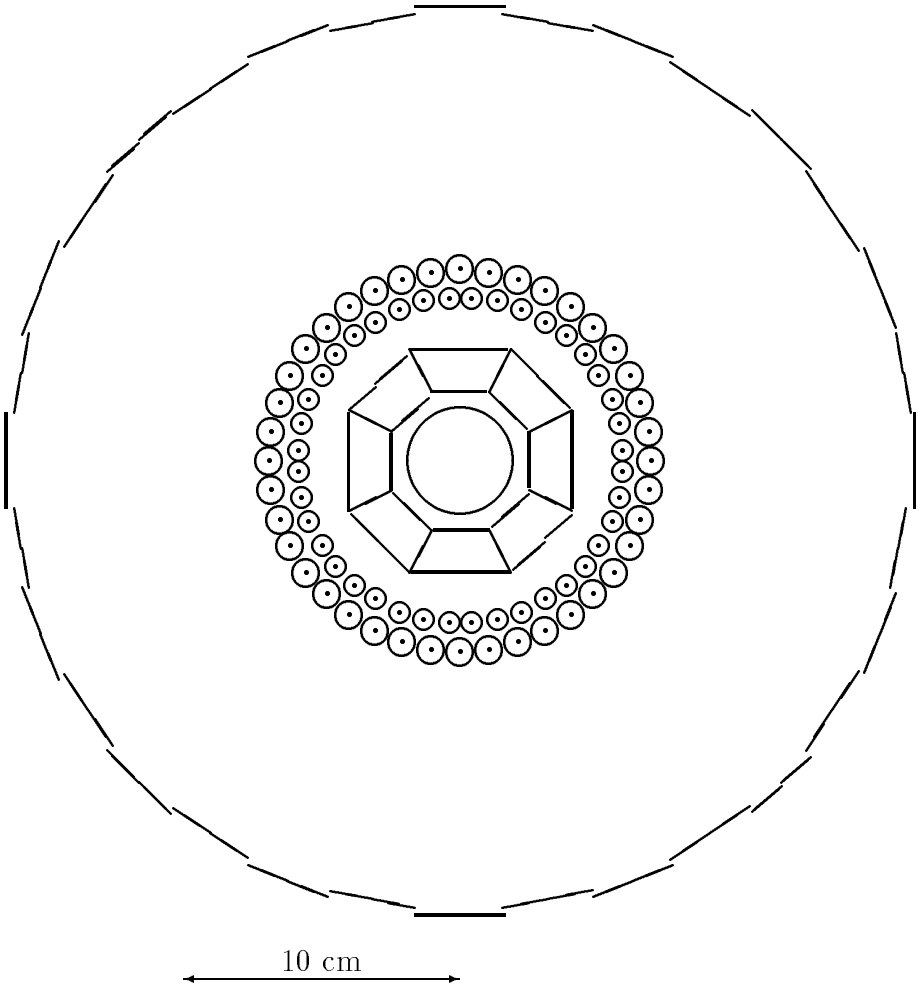

Figure 2.8: A cross sectional ϕ view of the beam pipe surrounded by hodoscopes H1 and H2 separated by the straw tubes. H1 is curved and appears thick when looking along the beam pipe. Not shown between the straw tubes and the H2 hodoscope is the inner tracking detector consisting of the RPC and MWPC.

(see figure 2.8). The thickness of the scintillator is 4 mm. The recorded signals of the H2 hodoscope are used to perform a pulse height analysis to determine the number of charged particles that pass through an H2 element. The H1 and H2 hodoscopes are used to define charged tracks in the hardware trigger logic.

The FCV hodoscope is an eight element full azimuthal detector covering the angles between 2° and 9°. The scintillator is oriented perpendicular to the beam pipe and located $\approx$ 1.8 m downstream of the interaction target (see figure 2.3). The FCV purpose is to detect forward going charged particles. The FCV and H1 hodoscopes combine to provide a veto of charged particles for the hardware trigger logic for neutral events while covering the entire polar angle subtended by both calorimeters.

2.5 Čerenkov Detector

A threshold Čerenkov detector [67] is used to identify e's (electrons and positrons) while rejecting π's (charged pions). The Čerenkov detector is split into azimuthal octants and covers the polar angles between 15° and 70°. Due to the range of π energies, the large polar angular acceptance, and the range of E_{cm} that E760 investigates, each octant of the Čerenkov detector is split into two polar sections by a 0.3 mm thick aluminum foil septum at 38°. Different gases are used in the two polar sections and therefore there are different threshold velocities for Čerenkov light production in the sections. A schematic of an octant of the Čerenkov detector is shown in figure 2.9.

Figure 2.9: One octant of the threshold Čerenkov detector. Each polar section uses a different gas; the sections are separated by an aluminum foil septum.

The backward region ($70° < \theta < 38°$) octants use spherically shaped mirrors to reflect the Čerenkov photons onto a second mirror that is observed by a photomultiplier tube. The backward region is filled with Freon13 gas which has threshold momenta for e's and π's of 13.5 MeV/c and 3.68 GeV/c, respectively, since the index of refraction has $(n-1) = 720 \times 10^{-6}$. The forward region ($38° < \theta < 15°$) is filled with CO_2 gas, $(n-1) = 420 \times 10^{-6}$, which results in thresholds of 17.6 MeV/c and 4.82 GeV/c for e's and π's, respectively. A forward octant mirrors is ellipsoidal with the two foci being the interaction region and an observing photomultiplier tube.

Although e^+e^- from any $\bar{c}c$ state have momenta much greater than the Čerenkov threshold, the number of photoelectrons observed ranges from 1 to 20 depending upon the polar angle. At the forward edge of the Čerenkov detector acceptance (15°), a charged pion from $\bar{p}p \rightarrow \pi^+\pi^-$ will be above the Čerenkov threshold when E_{cm} is greater than 3.41 GeV. However the number of Čerenkov photons produced by a

charged pion is much smaller than from e's and less likely to produce a signal in the photomultiplier tube; therefore discrimination of e's and π's can be accomplished.

2.6 Charged Tracking

The closest charged tracking detector to the interaction point is a two layer set of straw tubes [68] shown in figure 2.8. Each layer consists of forty straw tubes 22 cm long parallel to the beam pipe providing azimuthal angle information. The tubes' centers are located 6 and 7 mm radially from the center of the beam pipe. The inner layer of tubes has a diameter of 8.4 mm and the outer layer a diameter of 9.7 mm. Argon-CO_2-Methane gas is flowed through the straw tubes. Polar angle information is determined from charge division with the distance along the beam pipe measured to $\sigma_z = 1.6$ mm. The drift time is 150 μs and the azimuthal resolution is a few mrad.

Next radially outward is the inner tracking chamber module (see figure 2.3) which consists of two detectors [69] shown schematically in figure 2.10. Closest to the interaction point of the two detectors is a radial projection chamber (RPC); the other detctor is a multi-wire proportional chamber (MWPC). The module is separated into two chambers and employs two gasses: Argon-Ethane and Argon-Isobutane for the RPC and MWPC, respectively. The RPC consists of 80 wires parallel to the beam. Each track is sampled up to sixteen times. Charge division is used for each sampling of the track to help determine the polar angle ($\Delta z = 8$ mm). The MWPC is a set of 320 wires, parallel to the beam. This chamber includes pads etched on the external

Figure 2.10: The inner tracking chamber consisting of a radial projection chamber (RPC) and a multi-wire proportional chamber (MWPC).

cathode to provide polar angle information ($\Delta z = 0.4$ mm). A cross sectional view of the module is in figure 2.11.

The outer most cylindrical tracking detector from the beam pipe is a set of limited streamer tubes (LST) also called Iarocci tubes [70] (labelled as the outer tracking chamber in figure 2.3). The LST consists of two layers of tubes with conductive strips. The conductive strips are oriented longitudinal and transverse providing both azimuthal and polar information. Argon-Isobutane-CO_2 gas is flowed in this chamber. The LST covers polar angles between 22° and 60°.

A forward tracking chamber (FTC) is a flat disc multi-wire proportional chamber with its wires oriented perpendicular to the beam pipe. Located at the downstream end of the Čerenkov detector (see figure 2.3), the FTC covers the polar angles

Figure 2.11: A cross sectional view of the RPC and MWPC. The shaded region is a drift cell in the RPC.

between 10° and 18°. The FTC consists of 3 sets of wires oriented at 60° to one another. Argon-Isobutane is used in the FTC.

The last tracking detector is located 2.7 m downstream of the interaction point and is oriented perpendicular to the beam pipe (the forward straw tubes in figure 2.3). Four sets of straw tubes cover the forward end cap calorimeter. The four sets are at orientations that are 45° to one another. The forward straw tubes are filled with Argon-Ethane gas.

2.7 Forward End Cap Calorimeter

The electromagnetic forward end cap calorimeter [71] consists of 144 rectangular modules arranged in a 13×13 array (see figure 2.12). At each corner of the array there are no modules since these would be behind the central calorimeter. There is

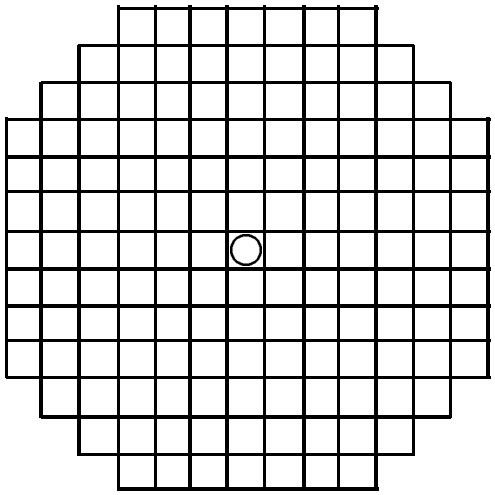

Figure 2.12: A schematic of the forward end cap calorimeter 13×13 array with no corner modules. There is no middle module to allow the beam pipe to pass.

Figure 2.13: A schematic of forward calorimeter module; the layers of the module are described in the text.

no central module for the passage of the beam pipe. The polar angles between 2° and 10° are covered by the forward end cap calorimeter.

Each module consists of 148 layers of alternating lead and scintillator; a schematic of a module is shown in figure 2.13. The transverse dimensions of these layers are 10×10 cm^2. The lead plates are 1 mm thick and the scintillator slabs are 0.64 cm and 0.32 cm thick. The thinner scintillator plates are used alternately with the thicker ones for the back half of each module. Overall the modules are 14.7 radiation lengths. A waveshifter plate $10.0 \times 0.64 \times 51.7$ cm^3 is attached to a side of each module. The waveshifter plate extends past the end of the module and is optically coupled to a photomultiplier tube for detecting light from the scintillators.

2.8 Central Calorimeter

The electromagnetic central calorimeter [72] is the focal point of the E760 detector. Each counter is a lead-glass block and an attached photomultiplier tube. The counters are arranged in a cylindrical 20×64 array ($\theta \times \phi$) totaling 1280 counters and every counter points back to the interaction region. The 64 counters at the same θ in the array are considered a *ring*. The lead-glass blocks are different sizes for the different rings. The central calorimeter covers the angles from 70° to 10° with the rings (and shapes) numbered 1 to 20, respectively (see figure 3.1). The 20 counters from different rings at the same ϕ in the array make up the contents of a *wedge*. The construction of the counters and calorimeter is discussed in the next chapter.

Wedge Numbers from a Ring	Super-wedge Number
1– 9	1
9–17	2
17–25	3
25–33	4
33–41	5
41–49	6
49–57	7
57– 1	8

Table 2.1: The summing pattern for the Level I Summers defining super-wedges for any given ring.

2.9 Central Calorimeter Summers

Although not literally a component of the detector, the central calorimeter summers [73] are used not only for triggering but as a way to determine whether a signal in the central calorimeter is from the interaction of interest (the triggered event) or from another interaction before or after the triggered upon interaction, also known as *pile-up* (discussed in section 6.4). A description of the summed central calorimeter signals follows; figure 2.14 shows how the central calorimeter summer modules are implemented.

The Level I Summer modules split each counter's signal; the majority of the signal (97%) is sent onto the FERA ADCs for recording the signal of each central calorimeter counter. The leftover part of the signal is used in a sum. Each Level I Summer module corresponds to a ring of counters. The counters' signals are summed into octant known as *super-wedges*. Counters at the edge of the octants are used in two Level I sums (see table 2.1). The total number of Level I summed signals for the

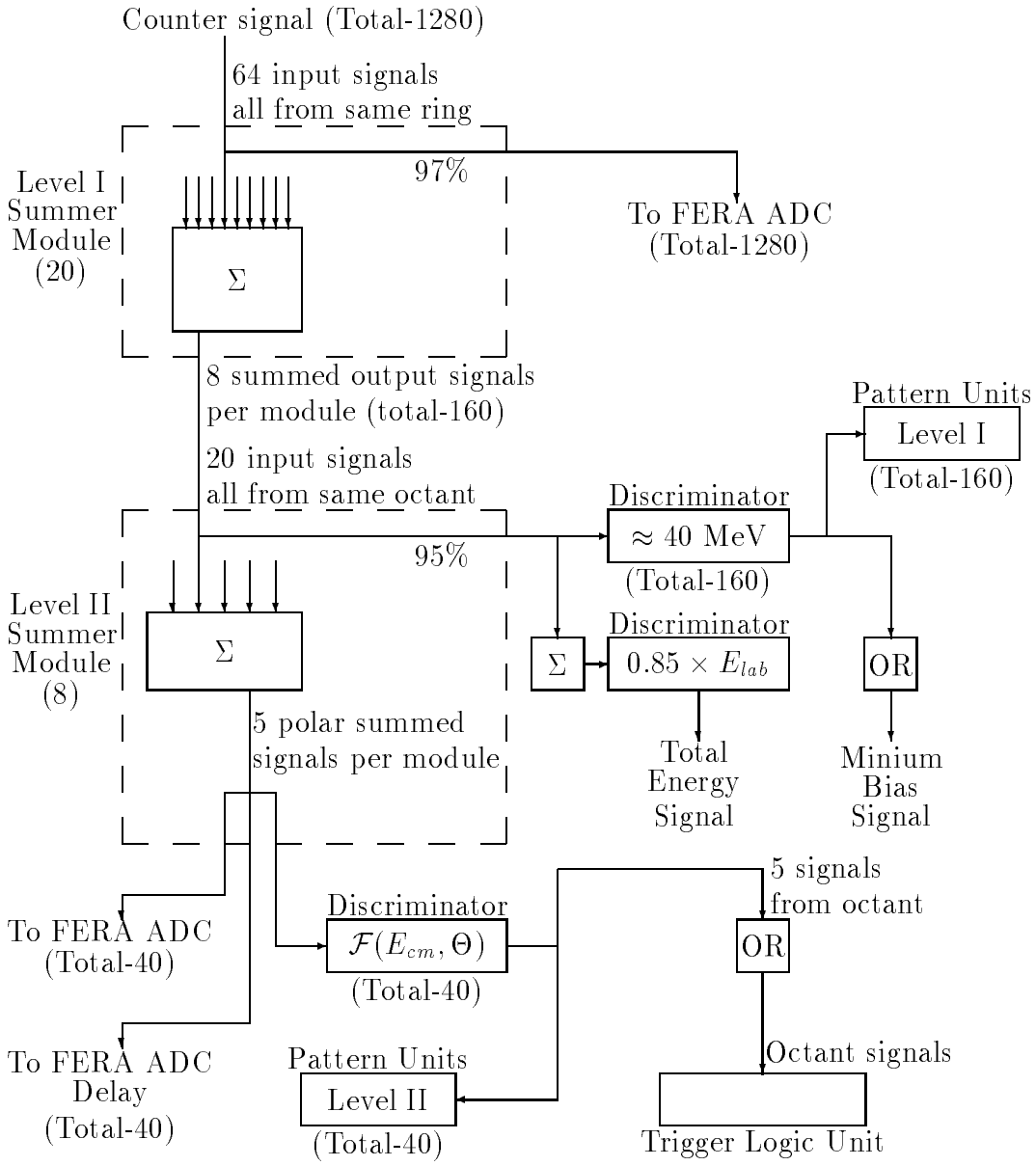

Figure 2.14: A schematic of the hardware logic that includes the central calorimeter summer modules. 1280 central calorimeter counter signals are summed into 160 Level I summed signals (which are also used to from a minimum bias signal), 40 Level II summed signals, and 1 total energy signal.

Ring Numbers from a Super-wedge	Super-ring Number
1– 4	1
4– 8	2
8–12	3
12–16	4
16–20	5

Table 2.2: The summing pattern for the Level II Summers defining super-rings.

twenty modules is $(\theta \times \Phi)$ $20 \times 8 = 160$. The module amplifies the summed signals; these signals are the input signals to the Level II Summer modules.

The Level II Summer modules split the input signals and pass 95% to 160 discriminators which have a common threshold of approximately 40 MeV. This forms the minimum bias and timing of the trigger (see section 5.2). The discriminators are also connected to latches: the Level I pattern units. The 160 Level I signals are also summed to form a total energy trigger which is used in the hardware trigger.

The remaining parts of the split signals in the Level II summer modules, a module for each octant, are weighted, summed and amplified in five polar intervals (*super-rings*) resulting in $(\Theta \times \Phi)$ $5 \times 8 = 40$ Level II signals, also known as *super-blocks*. The super-wedge signals from certain rings which are at the boundary between super-blocks, are used in two Level II sums (see table 2.2). Figure 2.15 shows a beam's view of the calorimeter and marks the areas that are super-blocks.

The weighted summed Level II signals form three sets of signals, 40 Level II super-block signals per set. One set of signals from each super-ring is sent to discriminators with thresholds dependent upon E_{cm} and polar angle of the sum, Θ. The

Figure 2.15: A beam's view of the central calorimeter counters (20×64 for $\theta \times \phi$) showing the boundaries of the 40 overlapping super-blocks (5×8 for $\Theta \times \Phi$); the dashed lines indicate the overlap. The shaded areas are examples of two super-clusters: (Φ, Θ) = (2,1) and (5,3).

thresholds are set at 75% of the expected energy to be deposited by an electron in the super-ring from $\bar{p}p \rightarrow J/\psi + X$ and $J/\psi \rightarrow e^+e^-$. The ring weights in a Level II sum have been determined to normalize the output signals within a super-ring so that electrons that hit anywhere within a super-ring result in the same signal. The discriminator results are used in the hardware trigger.

The other two sets of Level II output signals are sent to FERA ADCs; one set gives the weighted sums for the super-blocks for the trigger interaction and the other

set is delayed resulting in a look at the signals in the super-blocks prior to and/or at the beginning of the trigger. The two sets of Level II FERA ADCs' results and the Level I summer pattern units are used to determine pile-up as described in section 6.4.

Chapter 3

The Central Calorimeter

The central calorimeter consists of 1280 counters, which are F2 lead-glass blocks with an attached photomultiplier tube. The central calorimeter is designed to measure the energy deposited by electromagnetic showers induced by incident electrons, positrons and gamma rays. Below are sections devoted to design criteria, quality control and construction. The calibration of the central calorimeter is discussed in chapter 4.

3.1 Requirements and Design

The physics that is being investigated determines the type of experimental apparatus that is needed. The central calorimeter is designed to search for specific physics signals of interest while being able to identify background signals.

3.1.1 Physics criteria

The basic charmonium signal that E760 is sensitive to is the e^+e^- decay of J/ψ. The calorimeter measurement of the energies and positions of the two decay particles has to be made good enough to reconstruct the correct invariant mass. The measurements depend on calibration (chapter 4) and the inherent properties of the calorimeter. If the counters are too large then the position resolution becomes poor. On the other hand, if the counters are too small then the energy measurement resolution will be degraded; smaller counters imply a larger number of channels which increases the cost.

E760 is also designed to look for final states of two and three gamma rays (χ_2, η_c, $\eta_c' \to \gamma\gamma$ and ${}^1\mathrm{P}_1 \to \gamma\eta_c \to \gamma\gamma\gamma$). The main expected background comes from $n\pi^o$, in particular $\pi^o\pi^o$. A symmetric decay of an energetic π^o will result in both photons inducing electromagnetic showers close to one another. It is important to be able to identify π^o energy deposits. If the counters are too large, then the two showers will appear as one incident particle. The granularity of the calorimeter has to be able to determine when there are two incident particles near each other as in symmetric π^o decays. Asymmetric π^o decays will have a low energy photon. This photon can escape detection by either being below the calorimeter threshold or by missing the apparatus ($\theta_{lab} > 70°$). The acceptance of the detector cannot be increased because of the space taken up by the gas jet apparatus. Hence, the threshold was a crucial consideration in the design of the calorimeter. The counters must have a low energy

Figure 3.1: The design of the central calorimeter with twenty different shaped blocks and their orientation to the interaction region.

detection threshold and accurately measure the large energy deposits of two body final states.

The calorimeter acceptance is determined in the backward direction by the gas jet apparatus. Physics considerations and radiation damage properties of the lead-glass determine the forward acceptance cutoff of the calorimeter. The high background interaction rate is forward peaked; exposure of the lead-glass to this high rate was a consideration. Also a significant fraction of the charmonium decays with high invariant mass e^+e^- pairs can be contained in the region $15^\circ < \theta < 70^\circ$ (as covered by the threshold Čerenkov detector, section 2.5). Therefore, the central calorimeter does not need to cover much of the region forward of 15°. However the detection of other particles in the final state (radiative gamma rays and pions from hadronic decays) is desirable to fully contain the events and to be able to do exclusive fits. The final calorimeter acceptance chosen is polar angles from 10° to 70° and the full azimuth.

Block or Shape Number	Length (cm)	Central θ (degree)	$\Delta\theta$ (degree)	Distance from target (cm)	PMT Size (in)	Fractional PMT Coverage
1	37.80	67.387	5.226	72.44	3.0	0.473
2	38.65	62.259	5.031	75.87	3.0	0.475
3	39.88	57.342	4.803	80.07	3.0	0.476
4	41.50	52.664	4.552	85.08	3.0	0.478
5	43.54	48.246	4.284	90.96	3.0	0.479
6	46.03	44.101	4.007	97.79	3.0	0.481
7	48.98	40.234	3.728	105.62	3.0	0.482
8	50.00	36.644	3.451	114.54	3.0	0.497
9	50.00	33.327	3.183	124.66	3.0	0.520
10	50.00	30.273	2.925	136.07	3.0	0.544
11	50.00	27.472	2.679	148.89	3.0	0.568
12	50.00	24.908	2.449	163.26	3.0	0.593
13	50.00	22.567	2.233	179.34	3.0	0.617
14	50.00	20.434	2.033	197.28	3.0	0.641
15	50.00	18.493	1.848	197.29	2.5	0.546
16	50.00	16.730	1.678	197.29	2.5	0.664
17	50.00	15.130	1.522	197.30	2.0	0.527
18	50.00	13.679	1.380	197.30	2.0	0.644
19	50.00	12.364	1.250	197.30	1.5	0.443
20	50.00	11.174	1.131	197.30	1.5	0.543

Table 3.1: Central calorimeter counters' dimensions and positions; θ is the polar angle. The distance from the target is from the front face of the block to the interaction region. The fractional PMT coverage is the ratio of the areas of the PMT face (the diameter is the PMT size) and the back face of the block.

The forward region (polar angles less than 10°) is covered by the more radiation hard forward calorimeter (section 2.7).

After the material for the central calorimeter was selected (see next section), a Monte Carlo simulation was used to determine the granularity needed to separate symmetrical π^o decays. The final segmentation is 64-fold in the azimuth and 20-fold in the polar angle. Each block points back to the interaction region. The polar segmentation thus requires twenty different sizes of blocks which are the shape known

as an "erect pyramidal frustum with a regular trapezoidal base". The shapes are numbered 1 to 20 going from polar angles 70° to 10° as seen in figure 3.1. The blocks subtend polar angles varying between 1.1° and 5.2° as seen in table 3.1. Each block subtends 5.6° of the azimuthal angle. Counters at the same azimuthal angle constitute a *wedge* while counters of the same shape and located at the same polar angle are considered a *ring*.

3.1.2 Block Criteria

The correct balance between detection threshold, energy range, energy and position resolution, number of channels, radiation hardness, and cost had to be reached. Materials considered were CsI, NaI, BaF_2, BGO, lead-scintillator fibers and lead-glass. Cost, handling and relative ease of manufacture of the counters lead to the choice of lead-glass. The responses of five types of lead-glass were compared using low energy γ's at the University of Illinois Nuclear Physics Laboratory Tagged Photon Facility. F2 lead-glass was found to have twice as much light output as SF5 glass. This is attributed to the longer path length of shower electrons and greater light transmission. The F2 lead-glass radiation length is 3.14 cm versus 2.54 cm for SF5 glass, which means that for the same amount of shower containment, the F2 lead glass has to be 24% longer. The trade off is that the radiation length is greater and F2 lead-glass does not have as good radiation damage properties as the SF5 glass. The radiation damage properties were studied by exposing both types of glass to radiation doses of ^{137}Cs γ's. The transmission of 400 nm light through 40 cm blocks was decreased by a factor

Element Composition	Percentage by Weight
Lead	42.2
Silicon	21.4
Oxygen	29.5
Potassium	4.2
Sodium	2.3
Arsenic	0.15

Table 3.2: F2 lead glass composition.

of 2 at about 300 and 400 rads for the F2 and SF5 blocks, respectively. However, the F2 overall light output, path length, was the deciding factor in its selection for the calorimeter.

The geometrical characteristics of the blocks were discussed in the previous section and are presented in table 3.1. Included in table 3.1 are the block lengths and distances from the interaction point. The blocks vary between 12 and 16 radiation lengths. The first seven block lengths are shorter due to expected smaller energy deposits and the amount of physical space in the experimental area.

The F2 lead-glass chosen is made by Schott Glass Technologies, Inc. The composition of the F2 lead-glass is shown in table 3.2. The radiation length is 3.141 cm and the density is 3.61 g/cm^3. The refractive index is 1.651 at 404.7 nm and the transmission quality of the glass is discussed below in section 3.2.2. The F2 lead-glass was cut and polished by Cosmo Optics, Inc. Each edge of the blocks has a 2 mm chamfer of ground glass finish.

Model Number	Diameter (in)	Length (in)	Number of Dynodes
R3036-02	3.0	5.0	12
R3345-02	2.5	5.0	12
R2154-04	2.0	6.0	10
R580-13	1.5	6.0	10

Table 3.3: The four different photomultiplier tubes' physical characteristics.

3.1.3 Photomultiplier Criteria

The photomultiplier tubes (PMT) need to be able to collect the light efficiently. The PMT's also need a sufficient dynamic linear range from the calorimeter detection threshold to the full energy deposit of a two body final state. The gains of the PMT's also have to be able to drive the electronics involved, i.e. FERA ADC's. Since there are no light guides between the lead-glass blocks and the PMT's, it was not possible to place μ-metal shields beyond the photocathode surfaces. Due to the existence of stray magnetic fields within the accelerator environment, the PMT's have to be insensitive to magnetic fields of up to a few gauss.

PMT's with four different diameters are needed to match the blocks' back face surface areas and to maximize light collection (see table 3.1). Linear focused 3.0 inch PMT's from three manufacturers were tested. The PMT's with good timing precision are generally inferior in light collection, which is important in detecting low energy particles efficiently. Two PMT's, EMI D640 and Hamamatsu R3036, which were specifically manufactured for the experiment, have rise times between 6 and 10 ns and good light collection. E760 chose Hamamatsu tubes on the basis of price.

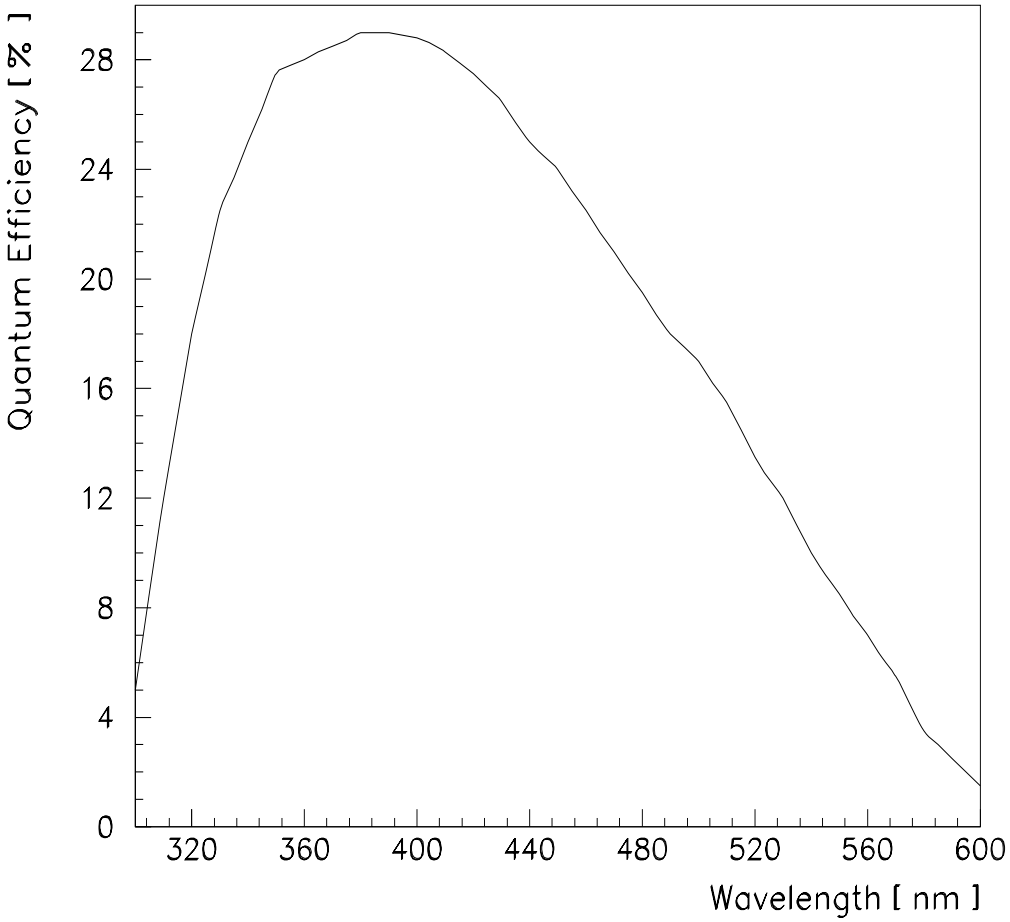

Figure 3.2: The quantum efficiency of the PMT's as a function of wavelength.

The physical characteristics of the four different sized tubes are shown in table 3.3. The PMT's operate with positive high voltage with a bleeder current approximately 200 microamperes. The lengths listed include the base circuit which forms an integral assembly with the PMT. A Bialkali photocathode is coated on a Borosilicate glass window. The sensitive range is between 300 and 650 nm, with the peak sensitivity at 420 nm. Figure 3.2 shows the quantum efficiency of the Hamamatsu PMT's as a function of wavelength.

Figure 3.3: A sketch of a stainless steel wedge unit

3.1.4 Central Calorimeter Support Structure

Each wedge support structure (a *shell*) contains twenty blocks, one of each shape. A wedge unit has to be both mechanically and electrically independent while, ideally, being light tight. Mechanically, a wedge shell has to be able to support the blocks in the correct positions at any angle in azimuth. Electrically, there has to be a way of supplying the operating voltage to the PMT's and a method of transporting the signal to the data acquisition electronics. The units have to be light tight and should ideally contain as little material as possible between the blocks and no gaps.

The entire calorimeter assembly also has to be easily moved and installed onto the beam line.

The wedge assembly unit was chosen to be made of stainless steel. See figure 3.3 for a sketch of one stainless steel wedge unit. The surfaces of the wedge shells (*skins*) are 0.735 mm thick; thin septa (*fins*) of 0.254 mm are located inside the shell creating pockets for the counters. The skins cover 2% of the azimuth; only 0.5% of the polar region covered by the central calorimeter are the fins. The shell surfaces and septa were cut and welded by a laser; this was done by Laser Machining. Stainless steel end plates were also welded at the two ends to complete the pockets containing the end blocks (shapes 1 and 20). Two back panels of black anodized aluminum, which partially absorb escaped Čerenkov light (minimizing crosstalk between counters), allow access to the PMT end of the counters. The downstream back panel has a feed-through plate consisting of a set of block connectors which allow operating voltage and signals to be passed. Included as part of the feed-through plate is a fiber optic feed-through (see sections 3.1.5 and 3.2.4). The front side of the shell is closed off by an opaque PVC panel.

The overall support structure is designed to make each wedge unit serve as a structural element. This means that the blocks serve as structural elements carrying compressive loads. The overall support structure must not add any additional stresses to the lead-glass during movement or transport. Two massive support rings are used to support the wedges. The rings rest on rollers which allows the calorimeter to rotate in ϕ, to bring any wedge to the top for maintenance. The overall support structure is

Figure 3.4: A cut-through view of the central calorimeter attached to the massive support rings and the air caster system assembly (raft).

built with a five air caster system (raft) for movement. The overall raft and support rings are shown in figure 3.4 with a cut away view of the central calorimeter.

3.1.5 Gain Monitoring System

Any electromagnetic calorimeter needs to have its response monitored. Each counter's response to a known signal is needed to monitor the counter's gain. A gain monitoring system has been built into the calorimeter apparatus. The monitoring

Figure 3.5: A sketch of the flashlamp gain monitoring system.

system has to be stable and must not interfere with the calorimeter's ability to detect and measure electromagnetic showers.

The gain monitoring system chosen is a single xenon flashlamp as a light source and plastic polymer fiber optic cables to distribute the light to all counters; the gain monitoring system is sketched in figure 3.5. Each flashlamp pulse is 300 ns and peaks at 400 nm. The light is collected and focused by an elliptical reflector into a rectangular lucite mixing bar (*major mixing bar*). A filter wheel placed between the reflector and mixing bar allows selection of the blue component, green component, or the entire spectrum of the light pulses. The mixing bar uniformly distributes light into sixty-four fiber optic cables (for each wedge) and three cables to monitor

PMT's. The sixty-four fibers are connected to the wedges' fiber optic feed-throughs (section 3.1.4). Inside each wedge, a smaller lucite mixing bar (*minor mixing bar*) distributes the light to twenty fiber optic cables which are connected to the individual counters.

3.2 Quality Control

Before construction of any counter or wedge assembly began, each component was tested. The components tested were the PMT's, lead-glass blocks, the wedge shells and the fiber optic system. This was necessary since most of the construction steps (section 3.3) are not easily reversible. These tests, along with tests during construction, insured a well functioning calorimeter.

3.2.1 Photomultiplier Tubes

Besides making sure that the PMT's worked, a range of operating voltages and a set of gain curves were determined. A test stand was built and used in a darkroom at UCI. The test stand held over forty tubes for testing. The PMT's were exposed to a pulsed green LED and blue flashlamp via reflection from a white diffusing screen. A monitor PMT, which was always in the same position in the test stand, measured the intensity of the light pulses. The relative light output at each position in the test stand was measured by a second monitor PMT. The variation in PMT output pulse height is determined from photoelectron statistics.

Model Number	Photocathode Efficiency (rms/mean)	Voltage-gain Constant (m) (rms/mean)
R3036-02	0.10	0.038
R3345-02	0.14	0.034
R2154-04	0.13	0.027
R580-13	0.13	0.026

Table 3.4: The four different photomultiplier tubes' average variabilities of the photocathode response and voltage-gain constant, m.

After an initial *burn period* at 1800 V, which causes a faulty tube to fail quickly, each tube was subjected to the light pulses. The operating voltage was then adjusted to bring the mean PMT response equal to the stationary monitor PMT pulse height. This was an automated process done iteratively using a thousand pulses before trying a different voltage. Once the *equal response* operating voltages were found, the PMT's were exposed to ten thousand pulses at five operating voltages: the equal response voltage and $\pm$ 50 and $\pm$ 100 volts. For each PMT and light type, the five data points were then fit by the PMT gain equation,

$$gain = b \times V^m, \tag{3.1}$$

where V is the operating voltage, b and m are constants determined by the fit for each PMT (b, which includes the equal response voltage V_o^{-m}, gives the correct gain units and m relates how the gain varies with voltage). The average variabilities (rms/mean) of the photocathode efficiences and voltage-gain constants m are given in table 3.4 for the four different sized tubes. A PMT was rejected if its variability of either the photocathode efficiency or voltage-gain constants was too different from the average.

Figure 3.6: The response of a 3 inch PMT to a range of intensities. The horizontal axis is charge (pC) and the vertical axis is intensity (arbitrary units). During the experiment, full scale corresponds to 2000 pC.

A PMT could also be rejected if the equal response operating voltage was smaller or larger than the expected range of operating voltage (1000 to 1500 volts).

The response of several of the PMT's to a pulsed laser was studied. A 355 nm pulsed laser beam was split and monitored with one PMT. Each PMT was exposed to different intensities of the pulsed laser beam by using a set of linear polarized filters. The response to a range of intensities, shown in figure 3.6, was found to be nearly linear: not deviating by more than 5 to 8% for the larger intensity exposures (corresponding up to a few thousand pC) from the expected response linearly extrapolated from the smaller intensity responses.

A few PMT's were studied for responses to magnetic fields and temperature changes. It was found that the pulse height loss due to a 1 gauss axial field is 5 to 15% for the three largest tubes; the 1.5 inch tube showed no effects from magnetic fields

below 2 gauss. The E760 PMT's showed an order of magnitude less sensitivity to temperature than typical PMT's sensitivity of 1% per degree Celsius.

3.2.2 F2 Lead Glass Blocks

All lead-glass blocks were inspected visually for colloidal particles, bubbles, scratches and chips. The colloidal particles and bubbles could affect light transmission (the overall transmission of the blocks is discussed below). Small cracks could eventually lead to larger cracks and break the block. All scratches and chips were examined to make sure the integrity of each block was good since each block could be put under tremendous pressure (sections 3.1.4 and 3.2.3) and break due to imperfections. If chipping occurred during the manufacturing process, Cosmo Optics would smooth the chipped area and this would decrease the chance of breakage. Any chipped area greater than 1 cm caused a block to be rejected. Shallow scratches that were less than a few centimeters in length were accepted on all surfaces except where the PMT was to be attached.

Due to each block being a structural element of the overall calorimeter, the physical tolerances of the lead-glass blocks were kept stringent The lead-glass blocks were subject to tight tolerances, 0.08 mm. The length of a block was accepted up to 1 cm different than specified (table 3.1) as long as the front face (opposite side of where the PMT is attached) does not extend further than the wedge shell pocket and interfere with the front PVC panel (section 3.1.4).

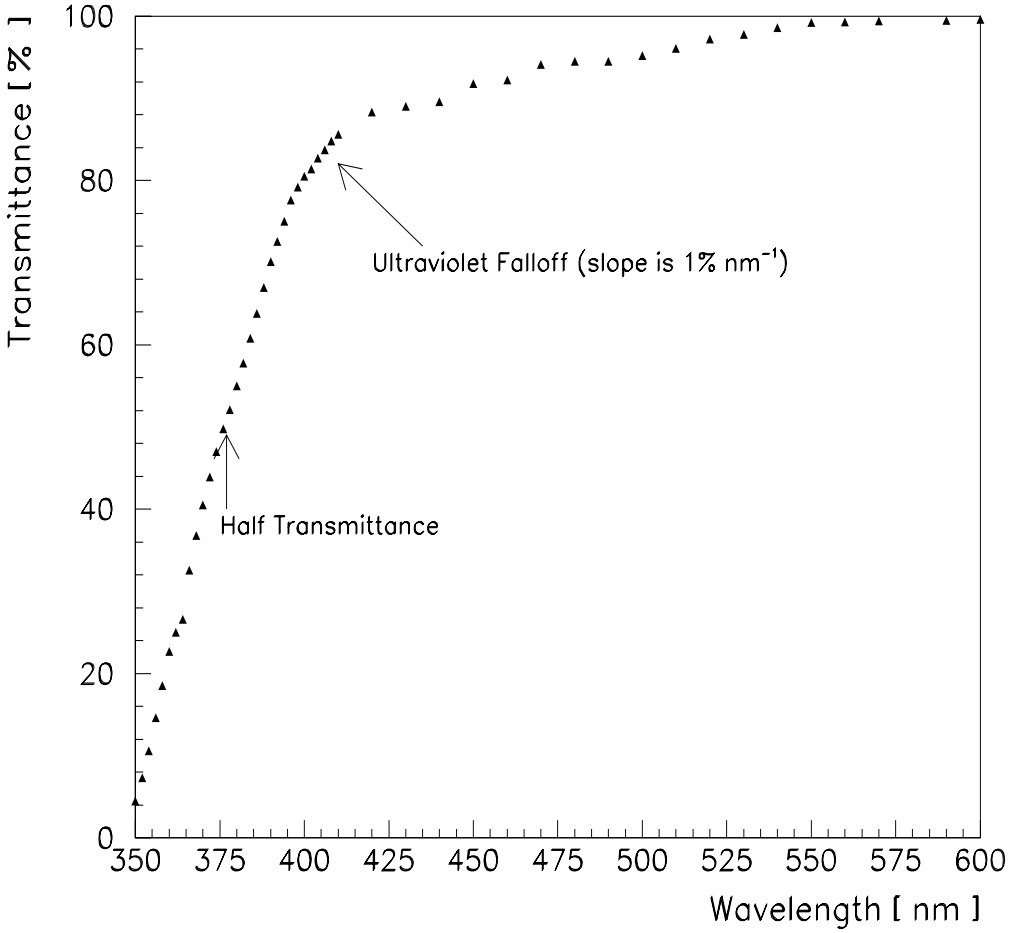

Figure 3.7: A typical lead-glass block transmission spectrum with the half transmittance and ultraviolet falloff (where the transmission spectrum's slope is 0.01 nm^{-1}) are shown.

The transmission of at least ten blocks from each melt (more than half of the blocks) was examined. The transmission measurements were done with a modified spectrophotometer (Appendix A). The spectrophotometer measurements were made at intervals of 2 nm, with an estimated error of ± 0.02 for each transmittance. A typical lead-glass block transmission spectrum is shown in figure 3.7. The lead-glass is nearly transparent for wavelengths greater than 500 nm.

Shape Number	Half Transmittance Wavelength (nm) Meas.	Corr.	Ultraviolet Falloff Wavelength (nm) Meas.	Corr.	Transmittance at Ultraviolet Falloff Meas.	Corr.
1	372.2	378.6	406.7	409.5	0.862	0.834
2	373.4	379.5	408.0	410.6	0.858	0.831
3	372.9	377.9	407.7	410.2	0.859	0.836
4	375.0	379.3	408.9	410.7	0.859	0.840
5	376.1	379.4	409.1	410.4	0.856	0.842
6	375.5	377.5	409.0	409.8	0.864	0.856
7	378.0	377.5	409.6	409.9	0.852	0.850
8	378.5	378.5	409.8	409.8	0.857	0.857
9	379.0	379.0	410.8	410.8	0.845	0.845
10	379.8	379.8	411.2	411.2	0.835	0.835
11	380.6	380.6	411.6	411.6	0.830	0.830
12	380.3	380.3	411.4	411.4	0.832	0.832
13	380.6	380.6	411.4	411.4	0.828	0.828
14	380.6	380.6	411.5	411.5	0.829	0.829
15	380.5	380.5	410.9	410.9	0.831	0.831
16	379.6	379.6	410.8	410.8	0.839	0.839
17	379.2	379.2	410.6	410.6	0.840	0.840
18	379.8	379.8	411.1	411.1	0.831	0.831
19	379.4	379.4	410.8	410.8	0.837	0.837
20	377.3	377.3	410.1	410.1	0.849	0.849

Table 3.5: The lead-glass blocks' transmission characterisitics as described in the text.

The average transmittance between 500 and 560 nm is 0.97. The average wavelength, for each of the twenty shapes, at which the the transmittance is 0.5, half transmittance, is shown in table 3.5. The differences of the half transmittances is caused by the different lengths. Half transmittances, corrected to a 50 cm length, are included in table 3.5. The length correction to the measured transmittance T_{meas} is

$$T_{corr}(\lambda) = [T_{meas}(\lambda)]^{\frac{50}{l}} \tag{3.2}$$

where l is the length of the block in cm. An ultraviolet falloff wavelength was calculated as the point where a fitted polynomial (between 374 and 424 nm) slope was equal

to 0.01/nm (see figure 3.7). The average measured and length corrected ultraviolet falloff wavelength are shown with the measured transmittances at these wavelengths in table 3.5. Table 3.5 shows that the spectrophotometer measurements are consistent for all shapes (lengths). The average characteristics of all blocks measured by the spectrophotometer and corrected to a 50 cm length are 379 nm, 411 nm and 0.84 for half transmittance wavelength, wavelength and transmittance at ultraviolet falloff, respectively. The slope of the ultraviolet falloff was also calculated (straight line fit between 350 and 390 nm); the average corrected slope is 0.0405 nm^{-1}. The transmission spectra characteristics of all of the blocks are the same within the spectrophotometer's error.

3.2.3 Wedges

The wedge shell physical dimension tolerances are as stringent as the lead-glass blocks', 0.08 mm. This was necessary for the structural integrity of the calorimeter. The skins were required to be very flat so that there would be no gaps between wedges which would allow particles to escape detection.

Each wedge shell was measured on a granite table for the correct shape. Several wedge shells were tested to see if the shells would withstand the possible stresses that could occur during the construction process. Milled aluminum dummy blocks filled with lead shot were manufactured to represent a full set (20) of the correct shaped and weighted blocks. The dummy blocks were inserted into the pockets of a wedge

shell and this wedge unit was subject to several tests. While on the granite table, the unit was subject to a 500 kg load (nearly twice the mass of a completed wedge) spread across one skin. The load was removed after several days. After removing the dummy blocks, the wedge shell was remeasured to see if the shape changed; there was no measurable change in shape. The dummy blocks were reinserted into the pockets and further tests involving movement of the wedge unit were conducted. Each wedge shell has two sets of two tapped holes for inserting eye-bolts; the eye-bolts allow for the wedge to be picked up by a crane. Testing both sets of holes, a crane lifted the wedge using the eye-bolts and then the wedge shell was remeasured; no change of shape was seen.

The wedge units could be picked up oriented with the back end of the unit downward. This orientation tested the mechanical supports that are attached to the fins to keep the blocks in the pockets; the tapering of the block keeps it from moving out the smaller end of the pocket. Another test to see if the wedge shells would deform or if the mechanical supports on the fins would fail was to change the vertical crane speed quickly (jerky motion). The mechanical supports worked and the wedge shell shape remained unchanged.

Inside each wedge unit are two harnesses: one electrical, for operating high voltage and signal cables, and one for the fiber optics (discussed in the next section). The high voltage cables are RG-58 and are cut to the appropriate lengths to reach each pocket. The signal cables are all the same length and are RG-174. All cables

are connected by means of three block connectors (two for the high voltage) in the feed-through plate. All cables from every electrical harness were tested.

3.2.4 Fiber Optic System

Two major mixing bars and eighty minor mixing bars were made. The major mixing bars have eighty-one output fiber optic cables (9×9 grid) from which sixty-seven fibers have been chosen for the final gain monitoring system. The minor mixing bars are a smaller version with a 5×5 grid of output fiber optic cables for the twenty blocks inside the wedge and five spares. Twenty of the output fiber optic cables from the minor mixing bars are cut to the length needed to reach each pocket. The five spares are the length needed to reach the farthest pocket from the feed-through.

The major and minor mixing bars are $20 \times 5 \times 5$ cm^3 and $15 \times 4 \times 4$ cm^3, respectively, cut from lucite material. All sides are polished so that the light is internally reflected. The length of each bar is chosen so that the output end face is coherently illuminated.

The input light for the major mixing bar is from the xenon flashlamp by way of the elliptical reflector (see figure 3.5). An optic fiber is the light input for a minor mixing bar. In both cases the light is mixed enough over the length of the mixing bar that the intensities of all the output fibers are within 10% of each other. All of the fibers were tested for each mixing bar to identify defective and low intensity output fiber optic cables.

The fiber optic cables of the minor mixing bars were tested in the following manner. The first major mixing bar was only coupled to 10 output fibers and used with a flashlamp system during the cosmic ray muon test (section 4.1.2). One of these fibers was connected to a fiber optic feed-through similar to the the one used with each wedge unit. Each minor mixing bar was connected to the opposite side of the feed-through. Each fiber optic cable from the minor mixing bar was connected to a fiber optic snap connector (see section 3.3.1) glued to a 40 cm F2 lead-glass block. A PMT attached to the the opposite end of the block was used to measure the light intensity.

Typically, the individual fiber optic output intensity was spread about the average output intensity for the minor mixing bar; the spread of the twenty fiber optics is typically $\pm 10\%$. If the spread of the fiber optic output intensities was greater than 20%, the minor mixing bar was rejected. Also the lower average output intensity mixing bars were rejected. A fiber with an output intensity much less than the average for the mixing bar was replaced by one of the five spare optic fibers. Almost 5% of the designated fiber optic cables of the minor mixing bars were replaced by the spares.

The repeatability of connecting the fiber optic connections was tested. Each possible connection was tested: major mixing bar output fiber to the feed-through, the minor mixing bar input fiber to the feed-through, and the minor mixing bar output fiber to the snap connector attached to the lead-glass. All showed less than a 1% variation of the intensity, showing that the connection was repeatable and

reliable. However, it was shown that the ends of the fiber optic cable had to be cleaned with alcohol and left to dry before connection to insure the small variation of the repeatability stated above. An uncleaned fiber optic could decrease the light intensity up to 12%. The minimum radius of curvature that an optic fiber could be bent before a significant decrease in light output intensity was determined to be ≈ 2 cm.

The major mixing bar was tested inside the flashlamp setup that was used in the final experimental setup. Each fiber optic output cable of the major mixing bar was tested using one minor mixing bar; the intensities were recorded.

3.3 Construction and Testing

The construction of the central calorimeter can be split into four parts: individual counters, flashlamp system, wedge units and the entire calorimeter. Nearly every step in building the calorimeter was subject to testing to assure that the quality of the calorimeter was good.

3.3.1 Individual Counters

After each PMT and lead-glass block had successfully passed the set of quality tests stated above in sections 3.2.1 and 3.2.2, the PMT was attached to the back face of the lead-glass block with Epotek 301 epoxy. A special gluing stand was made that

held twenty lead-glass blocks oriented with the back faces upward. Centered upon the cleaned back face, several drops of epoxy were applied and then a PMT was pushed against the epoxy; pressure was applied until the epoxy covered the entire PMT face without bubbles. The epoxy needed twelve hours to cure after which a fiber optic snap connector was attached in one of the corners of the back face.

The PMT is wrapped in a μ–metal shield two and a half turns. The μ–metal is 0.1 mm thick and 10 cm wide. The lead-glass block is wrapped in one layer of 3 mil white paper. The paper serves two purposes: to cushion the counter inside the wedge units and to reflect Čerenkov light not reflected internally (see section C.4 for Monte Carlo and experimental effects of the paper wrapping). The front face has more than one layer; the flaps from the side faces are folded and taped across the front face. The back face is not covered by the paper.

Each assembled counter was tested with through going cosmic ray muons and a flashlamp, as will be discussed in section 4.1.2. The test was for determining the initial voltages while checking the construction of the counters, optical *goodness* of the PMT–lead-glass glue joint and fiber optic snap connector.

3.3.2 Flashlamp System

The fiber optic output apparatus for optically coupling the output fibers to the lucite block is the same for the major and minor mixing bars. A piece of PVC was milled to the rectangular shape to fit on an end of the major (minor) mixing bar,

$1 \times 5 \times 5$ cm^3 ($1 \times 4 \times 4$ cm^3), and eighty-one (twenty-five) holes were drilled through it in a 9×9 (5×5) grid. The holes are slightly larger than an uncladded optic fiber. The eighty-one (twenty-five) fiber optics were put into the holes and glued into place using epoxy. When the epoxy had dried, the ends of all the fibers, which extended pass the end of the piece of PVC, were polished until even with the PVC face. The PVC–fiber optic apparatus is attached to the lucite mixing bar with epoxy.

The major mixing bar front face sits at a focal point of the flashlamp system's ellipsoidal reflector. Between the reflector and major mixing bar is a filter wheel. The filter wheel is controlled remotely and allows for four settings: no filtration, stop all light, filters to allow the blue or green components of the spectrum. The flashlamp system (flashlamp bulb and electronics, reflector, major mixing bar and filter wheel) is enclosed inside of a box. The minor mixing bars are inside PVC pipe. The ends of the PVC pipes are closed by end caps with holes cut for the fiber optic cables. An opaque epoxy, RTV, was used to fill the end cap holes and hold the fiber optic cables in place while reducing stress to the overall mixing bar apparatus.

3.3.3 Wedges

After a wedge shell had been determined to have the correct shape, the wedge pockets cleaned and twenty counters from different rings successfully tested with cosmic ray muons, the twenty counters were inserted into the wedge shell's pockets. The wedge and counters were entered into a data base program before the actual

insertion; the data base also contains the operating voltage, gain curves for each counter and results of the cosmic ray muon test (section 4.1.2). The insertion of the counters was done carefully to avoid tearing the paper, which could easily be torn upon the wedge shell's stiffing strips or the fins. If the paper wrapping was ripped, the counter was removed, wrapped in a new piece of paper and reinserted; about 10% of the counters had to be rewrapped with paper.

If the counter was successfully inserted into the correct pocket, a mechanical support was attached via a clamp to the fin separating the counter from the next lower counter; the ring 1 mechanical support was connected to the wedge shell end plate. A set screw attached to the mechanical support was tightened against each counter until either the pocket's and counter's tapers did not allow the counter to move further or the front of the counter extended no more that a few millimeters past the end of the pocket's fins.

An operating electrical harness was then attached to the counters. At each position there were three connections of the electrical harness to the PMT; the signal cable, high voltage and ground. The electrical harness was attached to the inner side of one of the skins. The fiber optic harness was attached to the opposite inner skin of the wedge shell. The correct fiber optic, as determined from tests discussed in section 3.2.4, was then connected to each counter at the snap connector. The input fiber optic cable of the minor mixing bar was then connected to the fiber optic feed-through. The ends of the unused fiber optic cables were covered so as not to introduce any extraneous light sources inside the wedge.

The feed-through plate was glued to the downstream outer panel using the opaque epoxy. The outer panels were put on loosely and a front panel was put in place before connecting an outside test harness, electrical cables and fiber optic cable, to the feed-through plate and covering the entire wedge with a dark blanket. Each counter was turned on to its operating voltage and examined with a flashlamp signal to check and see if all connections, electrical and optical, had been made successfully. If all counters were found functioning, the outside test harness was removed and the outer panels' screws were tightened. The opaque epoxy was then used to attach the front PVC panel and fill all possible gaps around the outer panels.

After the epoxy had dried, the wedges were checked for light leaks, i.e. if ambient light could be seen by the counters. The test harness was again attached to the feed-through plate and the counters were turned on at their operating voltages while the fiber optic cable feed-through was covered. The only signals expected were from dark current, cosmic rays and light leaks. By monitoring which counters experienced a continuous signal, the location of a light leak could be found. A flashlight and dark cover would be alternated over an area to see a change in counter response in order to locate the light leak. Light leaks caused by gaps between panels were fixed by using the opaque epoxy. Black paint was used when a light leak was found at one of the laser welds. The paint was allowed to dry in the laser weld divot and then sanded off the wedge skin (no extra material between wedges). The wedge was picked up by a crane to allow for light leak testing on every side of the wedge.

3.3.4 Calorimeter

After a wedge was determined to be light tight and operational, it was placed on the massive support rings. The wedges were at first hung at the bottom of the calorimeter and then built up evenly on each side until the last few wedges were hung into place. Each wedge is held in place by several bolts and positioned with some set crews which also allowed for the wedge to be moved radially.

A crane-supported transport mechanism was used for most wedges. The wedge transport mechanism used a vacuum system, with an air pumping system, to lift the wedges. The wedge was rotated to the correct orientation before being placed upon the previously positioned wedge and connected to the support rings.

After a wedge was positioned on the support rings, the counters in the wedge were tested again at operating voltage looking for light leaks and the response to the flashlamp was compared to earlier tests. When all the wedges were connected to the support rings and positioned, the counters were tested again. The flashlamp system was placed upon the calorimeter raft and sixty-four of the eighty-one fiber optic cables were connected to the wedges' fiber optic feed-throughs after considering the relative output intensity of the fiber optic cables and the relative average light output of the minor mixing bars. The fiber optic cables of the major mixing bar with larger intensities were connected to the minor mixing bars with the smaller average intensities (intensity determination is in section 3.2.4). Again counters from each

wedge were tested at operating voltages to check and see if the counters' responses were acceptable, i.e. on scale.

Some of the inner detectors were inserted and connected to the calorimeter support structure. Before transporting the calorimeter apparatus to the experimental area, the signal cables were connected to the wedges. Sixty-four bundles of twenty signal cables, that were to be connected to the twenty Level I summer modules (section 2.9) in the experimental area, were woven correctly before transport: sixty-four bundles of twenty cables to twenty bundles of sixty-four cables.

A transport frame was attached to the raft. The calorimeter apparatus and support structure were lifted by a crane (by the transport frame) and loaded onto a semi-trailer flat bed truck. The calorimeter was transported two miles and another crane unloaded the raft support apparatus through an access hatch to the experimental area. The transport frame was removed. Every counter was again tested with the flashlamp signal; only one counter was found to be not working.

The five air caster system allowed the raft to be maneuvered in the experimental area. The gas jet and the rest of the inner detectors were inserted and connected to the raft support apparatus. The detectors were connected to the electronics located in the experimental area; the operating high voltage cables were connected to the wedges and the woven signal cable bundles were connected to the Level I summer modules. The entire apparatus and electronic racks were moved into place using the

air caster system. The raft was then aligned with the beam pipe using four motorized screw jacks and eight hydraulic cylinders.

Once in place, the calorimeter counters were all tested, one at a time, with the data acquisition electronics. Tests were done confirming that the counters were operational and that the acquisition electronic channels were labelled correctly. The flashlamp controls, on/off and filter wheel, were also connected to the data acquisition.

Chapter 4

Central Calorimeter Calibration

The completed central calorimeter has never been in a calibration/test beam. An early effort was made to get a relative calibration between counters from the same ring. The initial calibration involved a Monte Carlo and testing with traversing cosmic ray muons. Part of the calorimeter was tested with electron beams. The calibration of the beam tested counters was transferred to the other counters through the initial relative calibration. The calorimeter's calibration is finely tuned in situ as data is taken. This provides a stack by stack calibration. The calibration and quality of the central calorimeter counter signals are monitored with the gain monitoring system (flashlamp) as well as data.

4.1 Initial Calibration

A Monte Carlo has been developed which predicts the number of photoelectrons produced by a single counter. The Monte Carlo results were combined with the number of photoelectrons and gain curves determined from the PMT tests (section 3.2.1)

for initial operating voltages for each counter. The cosmic ray muon tests were then used to initially set the operating voltages for counters from the same ring to have the same response.

4.1.1 Monte Carlo Simulation

A Monte Carlo has been developed to simulate the response of one central calorimeter counter to several different types of incident particles. The Monte Carlo is described in Appendix C. All electromagnetic shower generation is done by the EGS4 code system. Propagation of through-going particles (pions, protons and cosmic ray muons) is done including the effects of dE/dx losses, multiple scattering and δ-ray production. Ray tracing of Čerenkov light is carried out for all charged particles above threshold for producing Čerenkov light. Each photon is propagated to a fate of either being absorbed, escaping the block or hitting the PMT. For the Čerenkov photons which hit the PMT, quantum efficiencies are used to simulate photoelectron production.

The Monte Carlo responses of each lead-glass block shape to 1 and 3 GeV incident electrons has been studied. The number of photoelectrons resulting from the Monte Carlo has been used with the PMT tests to set the initial operating voltages of the counters for the cosmic ray muon tests. The Monte Carlo responses of each shape to through-going cosmic ray muons and test beam pions and protons are discussed in the following sections as well as in Appendix C.

Figure 4.1: The cosmic ray muon test set-up and data acquisition with a counter in position. Distances are not shown to scale.

4.1.2 Cosmic Ray Test

After being assembled, each counter has been tested with through-going cosmic ray muons. The test was conducted with the counters oriented so that the phototube looked upward, as shown in figure 4.1. The average energy of a cosmic ray muon at sea level is approximately 2 GeV; through-going muons that intersect both the front and back faces of the block produce Čerenkov light initially directed towards the PMT. The amount of Čerenkov light collected by the counter's PMT is proportional to the particle's path length and the percentage of the block's back face covered by the PMT.

Twenty-four testing positions located in four dark boxes (each equipped with a patch panel for operating high voltage cables, signal cables and a fiber optic feed-through) allowed for several counters to be tested at the same time. Two scintillator paddles were associated with each testing position: above and below the counter. An upper scintillator paddle (2×3 in^2) was located 68.0 cm from the lead-glass PMT interface: 18.0 cm above the front face of any of the longest blocks. Located 31.1 cm below the lead-glass PMT interface was 4×4 in^2 scintillator paddle. A coincidence of the signals from the PMT's attached to the two scintillator paddles for a testing position formed the trigger for a through-going cosmic ray muon. The coincidence also ensured that the cosmic ray muon path traversed the entire length of the block. However for the smaller blocks, a triggered muon could miss the front face of the block. A small light source was sometimes on the front face of a counter during the test (see next section).

Each position was also equipped with a fiber optic cable (from a minor mixing bar connected to the fiber optic feed-through of the dark box) which was connected to the counter being tested. The spare flashlamp setup with major mixing bar of ten output fiber optic cables, of which four were connected to the dark boxes feed-throughs, provided light pulses to test the stability of the counters during the test run as well as test the gain monitoring system. The initial operating voltage for a counter was determined from the Monte Carlo of the shape and the PMT's gain curve parameters (section 3.2.1).

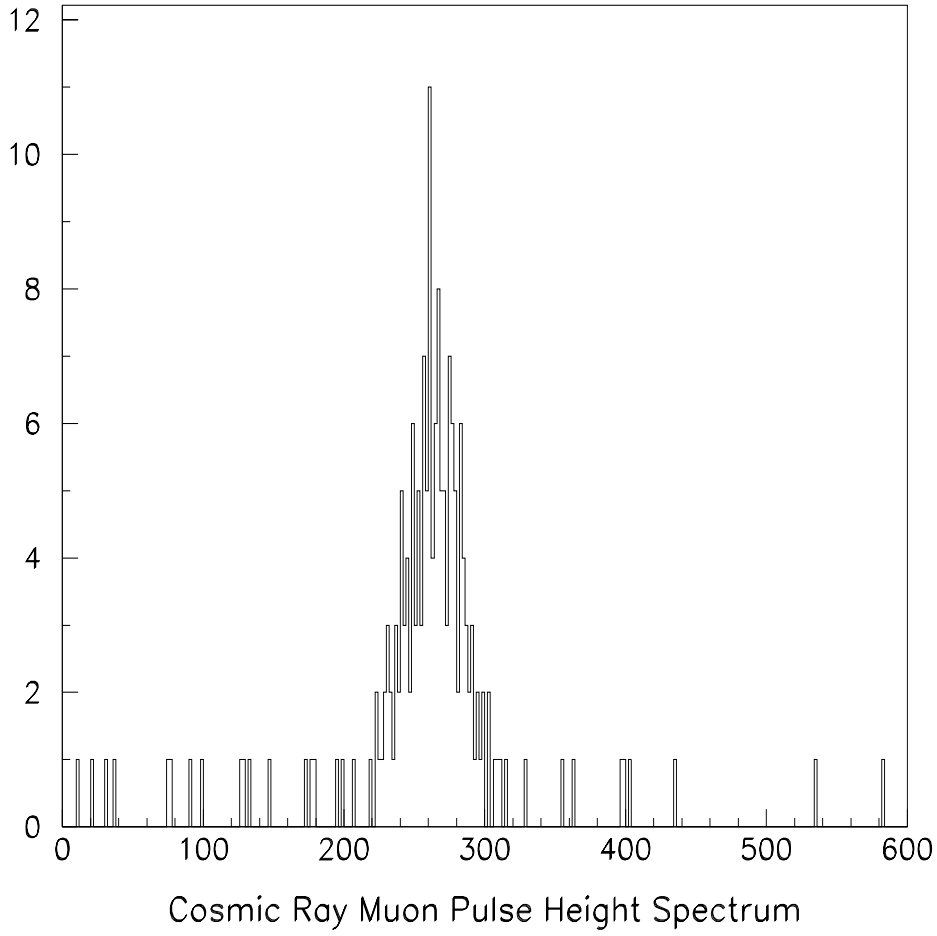

Figure 4.2: A typical spectrum of a counter's response to cosmic ray muons during the initial calibration and testing. Horizontal axis is ADC channel number.

Tests were conducted for twelve to sixteen hours with the flashlamp operating at $\frac{1}{6}$ Hz. The responses to the flashlamp and cosmic ray muons were triggered and recorded by a data acquisition and computer system. Over the course of a cosmic ray test run, each position would trigger upon approximately a thousand cosmic ray events. Figure 4.2 shows a counter's cosmic ray muon response spectrum; the response to the flashlamp system is shown in figure 4.3. The spectra from the flashlamp and cosmic ray muons were fit separately and recorded. The means of the cosmic ray

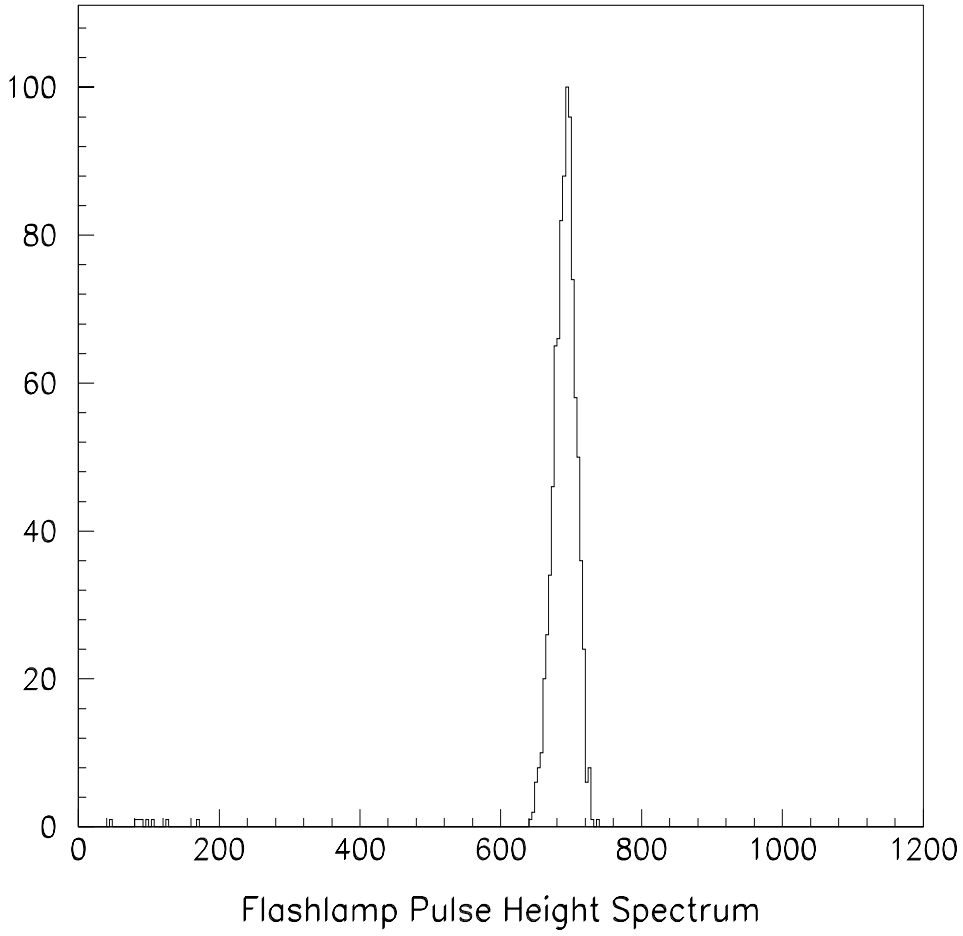

Figure 4.3: A typical spectrum of a counter's response to the flashlamp system during the cosmic ray muon tests. Horizontal axis is ADC channel number.

muon spectra are expected to be the same for all counters from the same ring and used to calibrate the counters with the same shape to have the same gain constant.

A Monte Carlo simulated response to cosmic ray muons was also performed. The Monte Carlo ratio of the expected number of photoelectrons from a 1 GeV incident e^- and a cosmic ray muon was used to further tune operating voltages for counters. The Monte Carlo showed the same distribution characteristics as the cosmic ray muon

tests: a high energy tail due to light from δ-ray production and low energy tails for the smaller blocks due to the incident particles missing the front face.

4.2 Calibration with Particle Beams

Two electron test beams were used to examine a subset of the counters. Sixty counters, comprising three wedges, were examined at beam energies between 1 and 4 GeV. This test beam also included π^-, K^- and $\bar{p}$ particles which allowed study of through-going particles. A low energy test with an e^- beam of energy less than 100 MeV was performed upon five counters that were also tested at the higher energies.

The PMT gains were monitored at each particle beam test as well as during the cosmic ray tests. Attached to the front face of each counter was a ^{207}Bi–plastic scintillator light pulser. A Bi light pulser is cylindrical with a height of 1 cm and a diameter of 1 cm; the Bi is located between two pieces of scintillator. The pulser is a constant light source with the decay electron being contained within the scintillator sandwich. The pulser spectra, as shown in figure 4.4, provide a monitor of the PMT gains. As long as the Bi light pulser is attached to a counter, a known response could be measured independent of the setup.

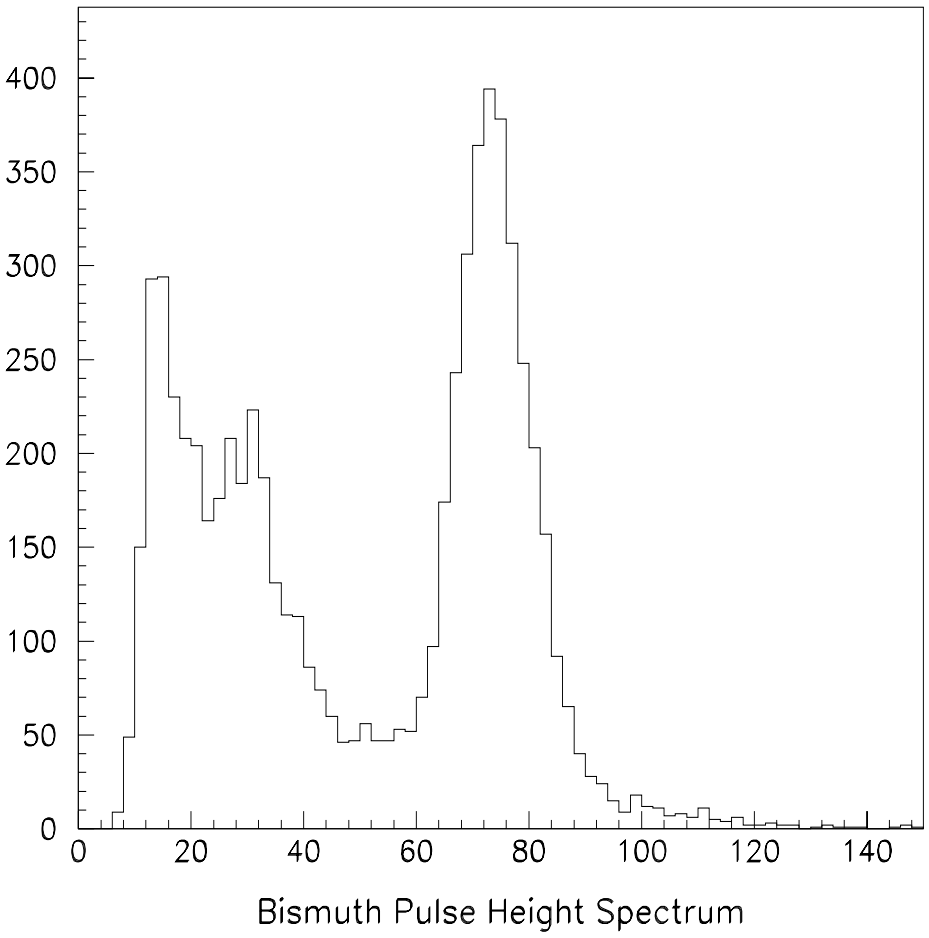

Figure 4.4: A typical spectrum of a counter's response to a Bi light pulser during the cosmic ray muon tests. Horizontal axis is ADC channel number.

4.2.1 High Energy Incident Particles

The equivalent of three wedges of the central calorimeter was studied at the Medium Energy Separated Beam (MESB-B2) of the Alternating Gradient Synchrotron (AGS) at Brookhaven National Laboratory. The MESB-B2 beam line is composed of negatively charged particles; the e^- component of the beam (2%) was tagged using a threshold Čerenkov counter. A trigger for the through-going π^-, K^- and $\bar{p}$ particles was also implemented using a setup of two scintillator paddles (10×10 mm^2 and 100×100 mm^2) similar in concept to the cosmic ray test.

The counters were supported on a horizontal test stand which had three degrees of freedom. The stand allowed for any of the sixty blocks in the three wedge configuration (prototype wedge shells were used) to be aligned with the beam. Two proportional wire chambers with 1 mm pitch and two scintillators (100×150 mm^2) were used to track the particles before the counters. The counters were studied at beam energies of 1, 2, 3 and 4 GeV with a spread of $\pm$ 0.8% ($\sigma(E)/E$). The beam energy was checked by time of flight measurements of e^-'s and $\bar{p}$'s.

The operating voltages were determined from the Monte Carlo simulations, PMT gain curves and the cosmic ray muon results. After studying the response to the e^- beam, the gains were changed so that the FERA ADC full scale corresponded to 6 GeV. With the new gains, the response to both e^-'s and the through-going particles were studied.

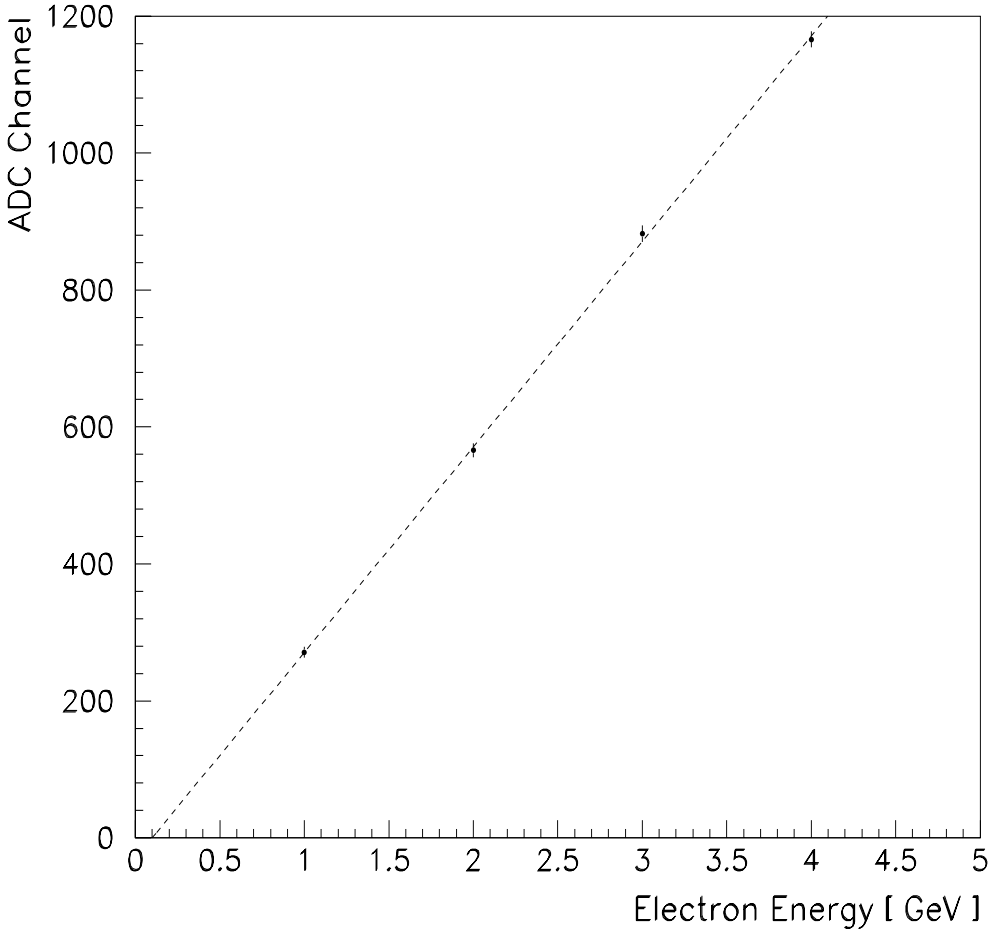

Figure 4.5: The linearity of response to electrons above 1 GeV.

The linearity of response to the four energies is shown in figure 4.5. Above 1 GeV it appears that the response is linear; the non-zero intercept means that the counters' responses at lower energies deviate from the linear response found at higher energies (see the next section and section 7.1). After unfolding the beam energy spread, the measured spread in energy for particles incident upon the center of counters from the middle wedge was found to be

$$\frac{\sigma(E)}{E} = \frac{(3.0 \pm 0.3)\%}{\sqrt{E}} + (1.5 \pm 0.5)\%, \tag{4.1}$$

where E is measured in GeV. The final energy resolution is given in section 7.1.

Since the relative calibration of counters within the same ring was being done with through-going cosmic ray muons, the through-going particles in the MESB-B2 beam line mentioned above were studied. The Monte Carlo showed a few percent difference between the responses of through-going cosmic ray muons with a range of incident angles with respect to the front face and beam particles normal to the front face. The ratio of responses of through-going particles and electrons was studied. Figure 4.6 shows the ratio of responses to incident π^-'s and incident e^- for the counters from the middle wedge for both the AGS and Monte Carlo data for 3 GeV incident particle energy. The electromagnetic shower width is comparable to the width of the larger numbered blocks. Therefore, the incident position is important for the amount of the shower contained within a single counter; the Monte Carlo assumes incident particles to hit the front face near its center. The summing of energy deposits into a 3×3 cluster of counters increases only the electron response. Figure 4.6 shows the ratio of responses for a cluster centered in the middle wedge for both the AGS and Monte Carlo data for 3 GeV incident particle energy. The Monte Carlo response is extrapolated from the response of the shape and a fictitious $30 \times 30 \times 50$ cm^3 lead-glass block (see Appendix C). The differences for the smaller blocks are explained by the material between the counters absorbing energy.

The three wedge configuration allowed for other studies. Electromagnetic shower energy sharing, energy loss due to the material in the cracks between counters and reconstruction of the incident particle track from the energy deposited were studied

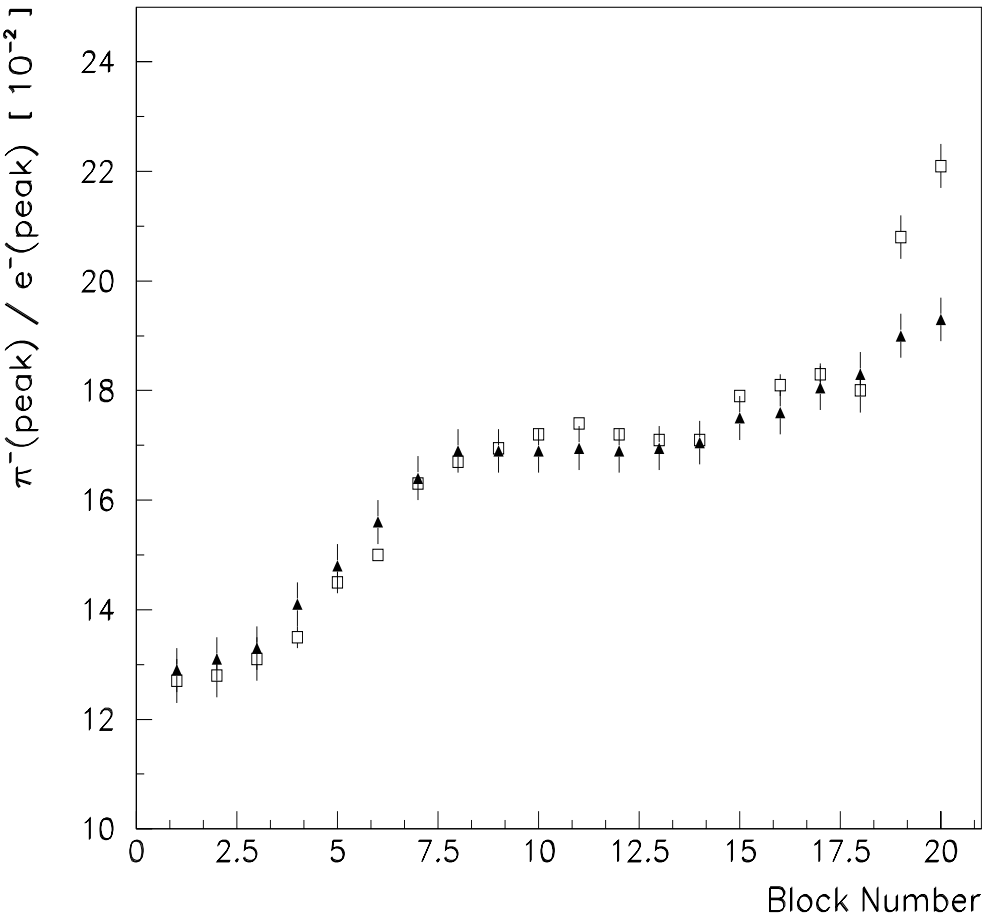

Figure 4.6: The ratio of responses to 3 GeV incident through-going π^- and electrons for individual counters from AGS data (squares) and Monte Carlo generated events (triangles).

as well as the degradation of the energy and position resolution as a function of how close an incident particle hits to a crack. Other tests involving single counters were done and are compared with the Monte Carlo simulations in Appendix C. Also a small target was inserted at approximately where the interaction region would be and the three wedge setup was able to reconstruct π^o's.

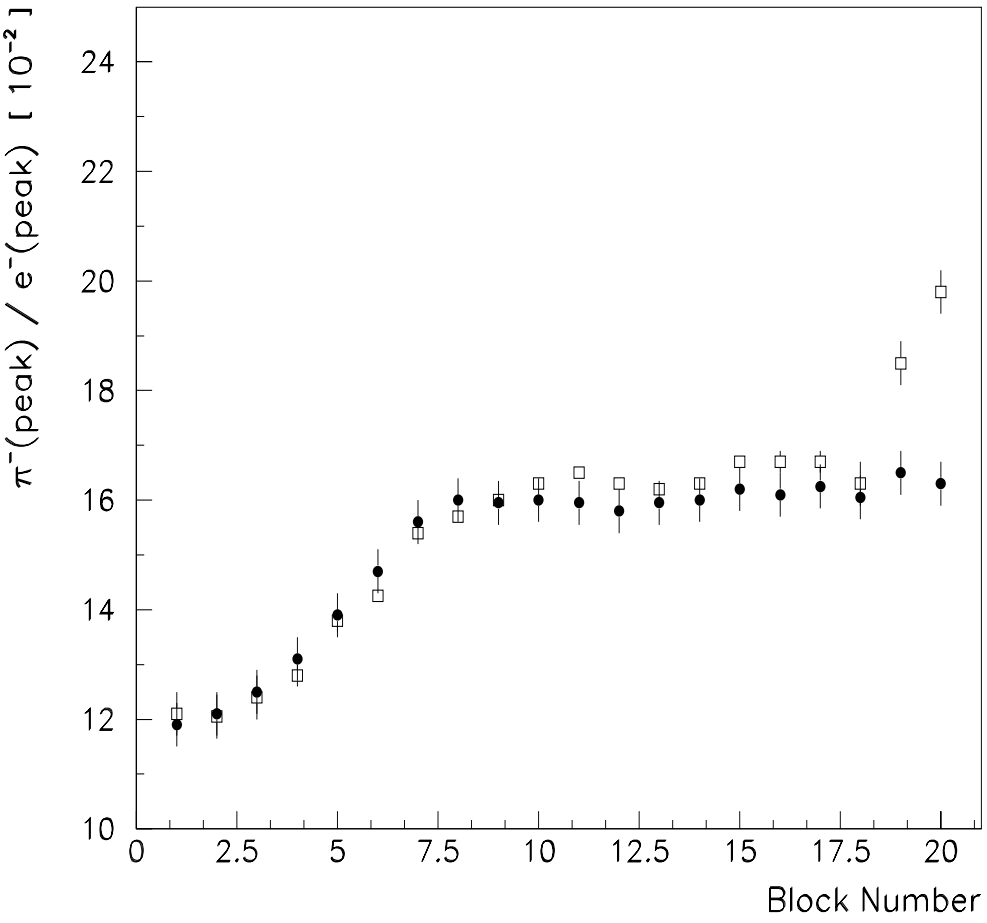

Figure 4.7: The ratio of responses to 3 GeV incident through-going π^- and electrons for a cluster from AGS data (squares) and Monte Carlo extrapolation (circles).

The summed signal was effectively increased by approximately 250 MeV when the incident particle went through the Bi light pulser; an even larger signal occurred when an incident e^- hit near one edge of a counter and then many electromagnetic shower particles escapes the initially hit block and went through the Bi light pulser of the neighboring counter due to the staggering of the blocks. It was determined that the pulsers affected the resolution too much and were removed from the counters after being re-tested in the cosmic ray setup with the new gains and prior to

final installation of the counters into wedges. However, the known Bi light pulser response allowed for the calibration of the beam tested counters to be transferred as a calibration scale for the cosmic ray muon test.

4.2.2 Low Energy Incident Electrons

Five of the counters from the middle wedge tested at the AGS were also studied for low energy e^- response. The University of Illinois at Urbana Nuclear Physics Laboratory (UINPL) microtron provided a beam of 88 MeV e^-'s. Each counter was studied individually.

Each counter was placed at the correct angle inside a small dark box which aligned the counter's symmetry axis with the beam position and direction. A small scintillator paddle (10×10 mm^2) was placed in front of the small dark box opposite from the center of the front face of the block being tested. It was calculated that the beam energy was degraded to 84 MeV by passing through a target (from another experiment), an exit window, the scintillator paddle and one side of the dark box before hitting the counter.

The electron trigger was a coincidence of the signals from the counter and the PMT attached to the scintillator paddle. A qVt multichannel analyzer with a 160 ns external gate was used to collect the charge from the counter being tested. The Bi light pulser signal was close to the pedestal during the test at higher energies and the cosmic ray muon tests (figure 4.4); it was decided to operate the PMT's at a

Counter ID #	e^- Response	e^- FWHM/mean	Pulser Response
01-06	346	0.26	389
09-08	322	0.29	418
15-02	308	0.27	369
17-02	138	0.26	195
19-04	207	0.42	278

Table 4.1: The response to 84 MeV electrons and the light pulser; responses are the peak channel numbers.

higher voltage thus increasing the Bi light pulser signal a hundred channels above pedestal.

Table 4.1 shows responses to both the e^-'s and Bi light pulser at the microtron. The FWHM/mean of the 84 MeV electron response is included in table 4.1. The shape 19 counter tested is one of the smaller shapes which, as in the last section, means that the electromagnetic shower size is a big factor. The incident position affects how much of the shower is contained within the counter. Non-perfect counter alignment and electromagnetic shower particles escaping the shape 19 counter explain the significantly larger FWHM/mean.

The Bi light pulser *equivalent energy* was calculated assuming a linear response in the energy regime between 100 MeV to zero energy by

$$E_{eq} = \frac{R_{pulser}}{R_{e^-}} \times E_{e^-}. \tag{4.2}$$

Another equivalent energy for the Bi light pulser was calculated from the 3 GeV incident e^-'s of the high energy tests of the last section. The two equivalent energies

Counter ID	Equivalent Energy from 84 MeV e^-'s	Equivalent Energy from 3 GeV e^-'s	Calibration Error
01-06	94.4	84.8	–10.2%
09-08	109.0	94.9	–12.9%
15-02	100.6	91.8	– 8.7%
17-02	118.7	132.3	+12.3%
19-04	112.8	99.9	–11.4%

Table 4.2: The light pulsers equivalent energies calculated from responses to 84 MeV and 3 GeV electrons. The calibration error is from assuming a linear response to a counter calibrated at 3 GeV for a low energy incident electron.

are shown in table 4.2 along with the percentage error that would be made if linearity is assumed for the response using a calibration at 3 GeV for energies below 100 MeV.

Other tests were performed using the 84 MeV incident e^-'s. The responses of a counter operating with the voltage increased by 100 volts showed the expected mean increases from the previously determined PMT gain curves while not changing the FWHM/peak. Counter wrapping tests are compared with the Monte Carlo simulation in Appendix C.

4.3 Calibration with Data

The completed calorimeter's operating voltages were determined from the beam tests at high energies. The cosmic ray muon test allowed for the calibrations of the beam tested counter's to be transferred to the non-beam tested counters. The final calibration gain constants have been done in situ. Several methods have been tried to calibrate the calorimeter. The first methods discussed below are marginal due

to statistics. The majority of the 1990 data was calibrated in this manner using data collected at the J/ψ energy. In 1991, a better method using $\bar{p}p \rightarrow \pi^o\pi^o$ was used to calibrate the calorimeter for every $\bar{p}$ stack. The calibration of the counters determined by the above methods of sections 4.1 and 4.2 was good to better than 20% and provided a good starting point for the methods described below.

4.3.1 $J/\psi \rightarrow e^+e^-$ Data

During 1990, the calibration was done for the counters in the rings numbered 1 to 15 with e^- and e^+ from J/ψ events. This calibration required that the experiment spend time acquiring e^- and e^+ at the J/ψ peak.

The e^- and e^+ energies can be determined kinematically by the polar angles measured by the tracking. The gains of the nine counters forming the 3×3 cluster defining an electron or a positron energy deposit were equally adjusted so that the measured summed signal was equal to the energy as determined kinematically by the polar angle. A counter's new gain would be the average of the adjustments from the entire J/ψ sample. The process was iterative; using new gains, the entire J/ψ sample was run again making new adjustments. The process was repeated until the difference in iterative gains was less than a few percent.

The number of times that each counter in the fifteen rings was hit directly varied between a few and a dozen. The statistics for any one counter was quite poor. A method of equalizing the gains from each counter was tried and is described in the

next section. Kinematically, for both the e^- and e^+ to be within the acceptance of the central calorimeter, both had to be between rings 1 and 15; $\psi' \rightarrow e^+e^-$ extended the acceptance to ring 17 with much less statistics due to the smaller cross section. An attempt to *bootstrap* the calibration to the forward rings was tried and is discussed in section 4.3.3.

4.3.2 Punch Through Data

Signals from punch through particles from $\bar{p}p \rightarrow \pi^+\pi^-$ and elastic $\bar{p}p$ interactions have been used to try to calibrate the counters within a ring to have the same responses. A signal is defined to be a punch through particle when only one counter has a response; the Čerenkov light from a through-going particle should only be contained in one block. Assuming that the cosmic ray tests actually determined operating voltages, such that all the counters within the same ring had the same gain, the differences in the gains in the final experimental setup were caused by the full electronic readout. Using the punch through interactions, each counter's electronic channel could be adjusted to yield the same gain constant for counters in the same ring.

The interaction length, the hadronic equivalent of the radiation length, for the F2 lead-glass is 49 cm, approximately the length of most of the blocks. Therefore, it was expected that the probability of a punch through is e^{-1} per particle. However, due to the high rate of the hardware trigger for these events, the hardware trigger

was prescaled (the trigger is discussed in Chapter 5). The number of punch through signals per counter is nearly the same number as of e^- or e^+ from the J/ψ events directly hitting a counter.

Each counter of a ring was normalized with the punch through signals and then the ring was considered as one object to be calibrated. The rings were then calibrated using the e^- or e^+ from the J/ψ events, thereby increasing the statistics. This combination process was not significantly better than using the $J/\psi \rightarrow e^+e^-$ events alone. If more punch through signals could have been recorded, this method might have proven to be better.

4.3.3 π^o Data

A bootstrap method of calibrating the counters of the forward rings used some of the many π^o's found in the data. Decays of π^o's were used when one gamma ray hit a forward counter and the other gamma ray hit a counter that was already calibrated by the methods described in the two previous sections. The invariant mass of the two clusters was used to adjust the gains of the uncalibrated counters in the forward rings; the gamma ray hitting a calibrated counter was considered perfectly measured.

As in the J/ψ data, the average adjustments were used to determine new gains and an iterative process was used. It was found best to do the iterative process one ring at a time. For instance, ring 16 counters would be calibrated with gamma rays hitting counters in this ring when the partner gamma rays were located in the

previously calibrated counters of rings 1 to 15. When counters from ring 16 were considered calibrated, ring 17 counters were then calibrated. The process was iterated until the counters' calibration gain constants changed by no more than a few percent.

With the requirements of the partner gamma ray having a larger polar angle than the gamma ray being used to make the gain adjustment, and the opening angle of the π^o gamma rays large enough for the clusters to be separated, this method did a little better statistically. However, the errors of the gain constants for the forward counters were slightly larger than the errors of the gain constants determined for the other counters.

4.3.4 $\bar{p}p \rightarrow \pi^o\pi^o$ Data

The methods described in the previous three sections were used in 1990 to calibrate the calorimeter; calibration could only be performed whenever data was taken at the J/ψ energy (the π^o method of the last section required the J/ψ data for a starting point). The method used for the 1991 data allowed calibration to be performed on data taken every stack using $\bar{p}p \rightarrow \pi^o\pi^o$ events. These events are not prescaled and the gamma rays populated the entire calorimeter. Although the gamma rays nearly follow the $\pi^o\pi^o$ angular distribution, which is the same as the $\pi^+\pi^-$ distribution, the forward rings do get hit, not as often as the other rings.

When there are two sets of two clusters, with each set having an invariant mass roughly equal to the π^o mass, the direction of the π^o's are roughly determined. From

the polar angle of a π^o, the energy of the π^o, and therefore the two gamma rays' total energy, is determined. This predicted energy is used to adjust the gain constants of counters involved forming both clusters. This method ignores the opening angle and treats overlapping clusters as one energy to be adjusted. The process is iterative. Three cluster events which satisfied the $\pi^o\pi^o$ hypothesis are also used. Other neutral two body reactions, $\pi^o\eta$ and $\eta\eta$, are used to check the calibration.

The $\bar{p}p \rightarrow \pi^o\pi^o$ method has been found to be superior to the previously used methods. The statistics of $\pi^o\pi^o$ events collected over an entire stack is sufficient to calculate gain constants for all of the calorimeter's counters.

4.4 Monitoring of the Calibration

In a sense, the best monitor of the calibration is the comparison of calibration gains as a function of time, i.e. for each stack. Two other methods, flashlamp gain monitoring and punch through particles, are used to monitor the gain constants and are discussed below. These methods also allowed monitoring of the radiation damage to the calorimeter.

4.4.1 Flashlamp Response

As described in the previous chapter, the response of each counter to the flashlamp was studied and recorded at each step during the construction and initial testing.

The flashlamp only provides a monitor and not a calibration since the flashlamp individual flashes vary in intensity and decrease slowly over time. The average flashlamp intensity seen by a counter is equivalent to a 1 to 2 GeV signal.

The flashlamp system was designed to study the calorimeter response over time to different parts of the Čerenkov light spectrum. The flashlamp system's filters allow monitoring different parts of the spectrum. Any counter's decrease in response to the flashlamp system can be caused by a decrease in flashlamp intensity, a malfunctioning photomultiplier tube or a yellowing of the lead glass due to radiation damage.

The flashlamp intensity is monitored by three phototubes. Three of the output fiber optic cables of the major mixing bar (section 3.1.5) are used to transport the flashlamp pulses to the phototubes. The responses of the three monitor phototubes are used to monitor the flashlamp intensity and normalize each flashlamp pulse. The monitor phototubes' stabilities are monitored by response to a Bi light pulser (section 4.2). The flashlamp intensity has slowly decreased over the course of data taking.

Malfunctioning photomultiplier tubes are identified by both flashlamp response and comparison of calculated gain constants every stack. Only two PMTs have failed and have been turned off. The flashlamp responses of these two PMTs did not differ from other counters before failure.

Radiation damage would be seen as a decrease of the response to the flashlamp by a large number of the calorimeter counters. No area of the calorimeter has been

identified as having radiation damage. A discussion of radiation damage and curing of lead-glass blocks can be found in Appendix B.

4.4.2 Punch Through Particles

The punch through events are collected each stack and also provide a monitor. As with the attempt to calibrate with the punch through particles for the 1990 data, statistics for any counter for a stack is small due to the hardware prescale. However, over the course of several stacks the response of a counter to punch through particles can be used as a monitor.

Figure 4.8 shows the ADC channel spectra for two counters encompassing the entire 1991 data run. The mean channel numbers of the peaks are different since the counters are different lengths and have different percentages of the block's back face covered by the PMT. The low channel tail is from particles which interact in the counter and do not result in a large hadronic interaction (the signal is contained in the one counter). Figure 4.9 shows the same counters with the spectra corrected by each counter's gain constant (ADC channel $\times$ gain constant) resulting in *energy* spectra; note that the punch through signal is proportional to the charge particle path length and not the incident energy.

Figure 4.10 shows the ADC channel as a function of run number for punch through particles for one counter. Not all of the run numbers are represented; the density of data points is a function of the integrated luminosity per run, E_{cm} and

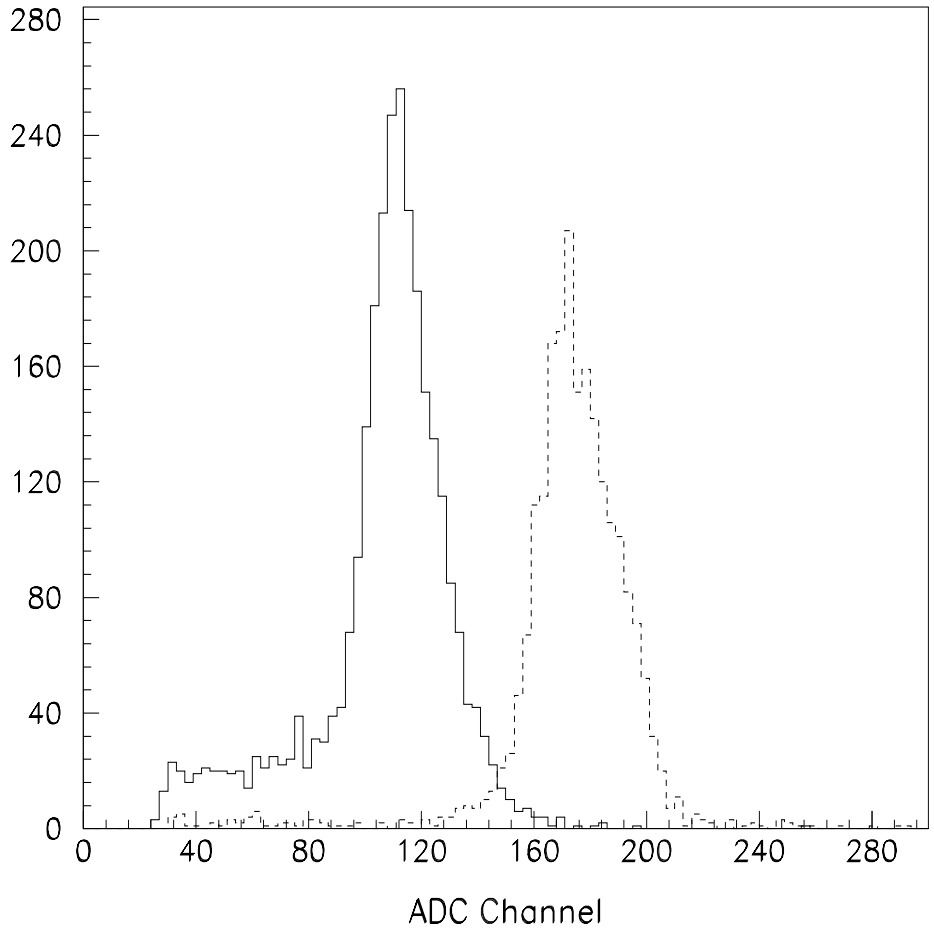

Figure 4.8: The ADC channel spectra for two counters' responses to punch through particles. The difference in mean channel is due to the different counter lengths and the percentage of the block's back face covered by the PMT.

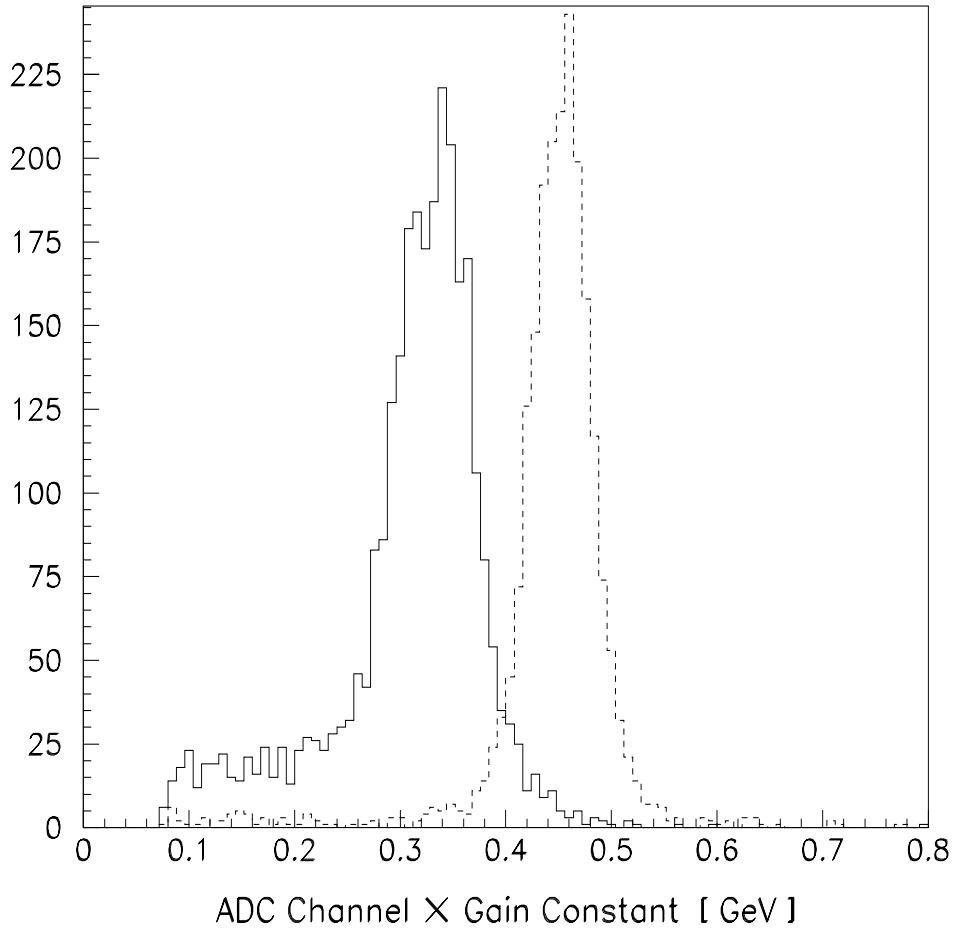

Figure 4.9: Two counters' spectra of the ADC channel multiplied by the counter's gain constant for punch through particles. The difference in mean value is due to the different counter lengths and the percentage of the block's back face covered by the PMT.

hardware prescale factor. The apparent discontinuity, drop in ADC level, at Run 1441 is from a change of the operating voltage. The nominal full scale FERA ADC energy equivalent is 5 GeV: a nominal gain constant of 2.6415 MeV/(ADC channel). The calibration gain constants prior to Run 1441 and the PMT gain curves were used to adjust the operating voltages so that all counters would have the nominal gain constant. Figure 4.11 shows the punch through particles *energies* as a function of run for the same counter. The resultant punch through signals show that the gain constants have been consistent for the entire 1991 data taking period.

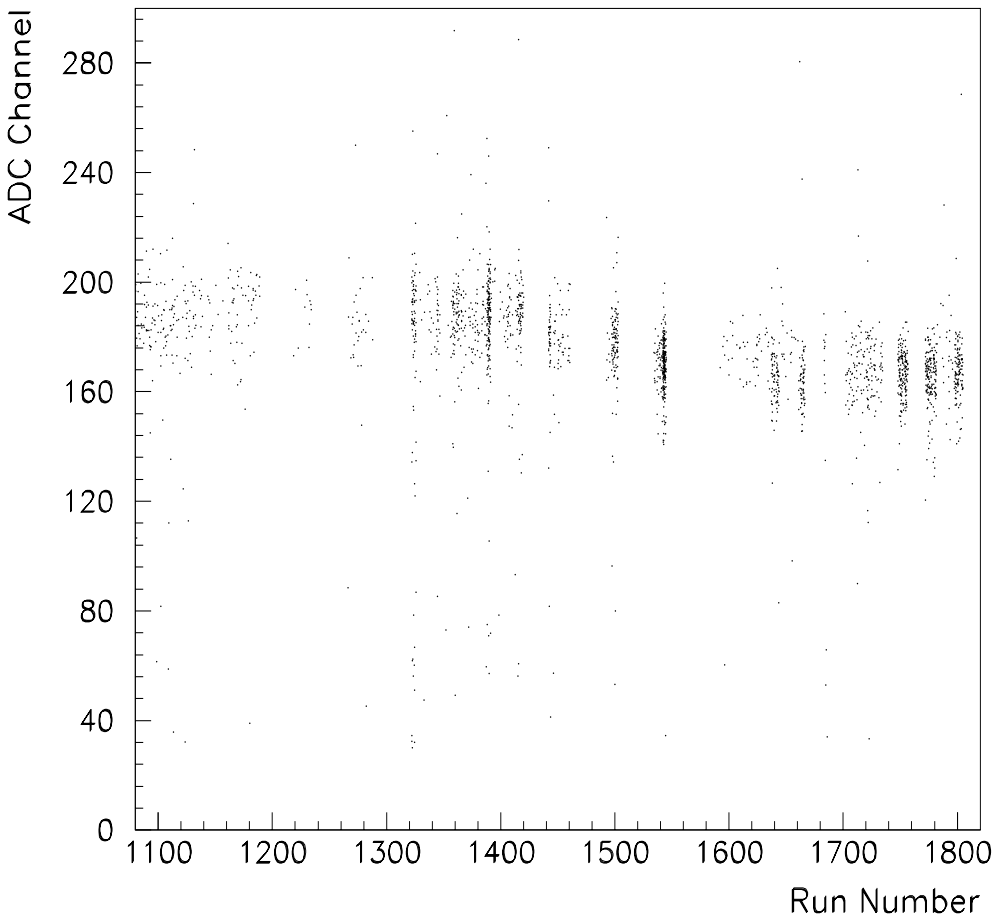

Figure 4.10: The ADC channel punch through response for one of the counters as a function of run number.

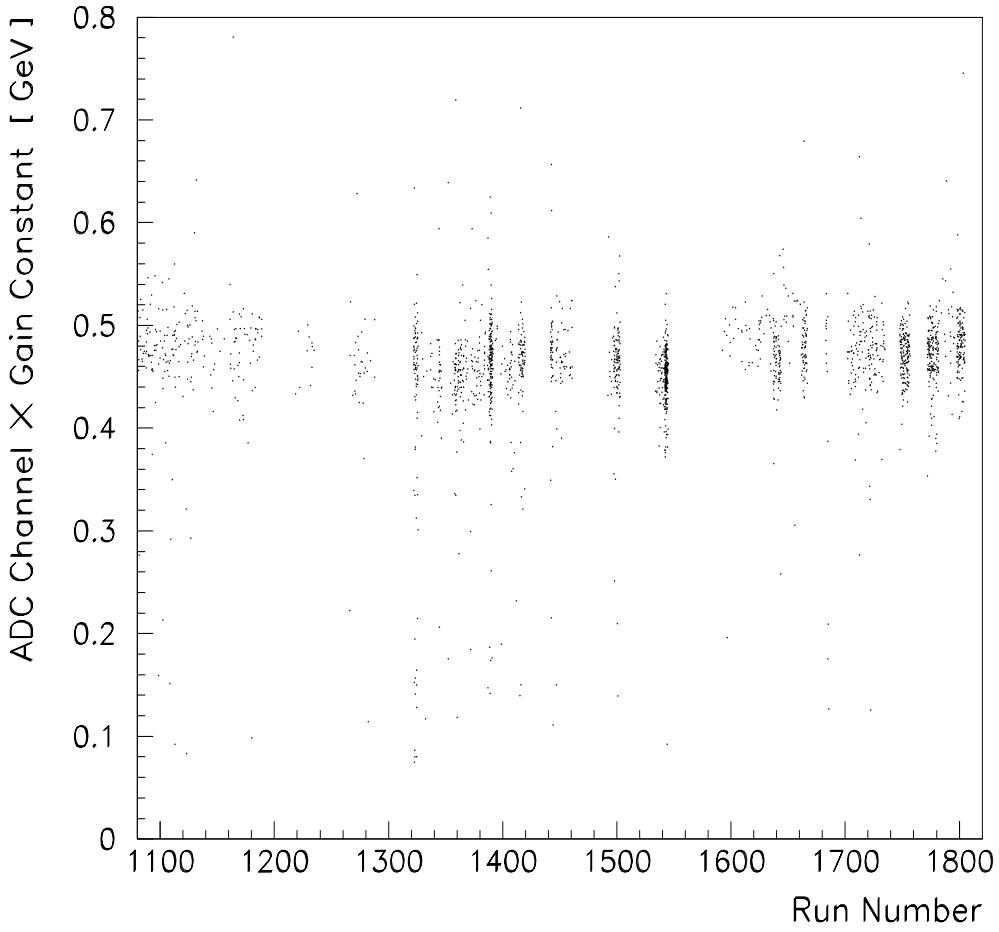

Figure 4.11: The ADC channel punch through response multiplied by the gain constant for one of the counters as a function of run number.

Chapter 5

Data Collection

The overall physics trigger is composed of a set of hardware triggers and a set of software triggers. The triggers are for different types of physics events. Presented in this chapter are the data readout, a description of the signals which form the electronics logic used for the hardware trigger, and the online processor program that includes the software trigger. Figure 5.1 is a schematic of the electronics, ACP system (CPUs) and data pathways which comprise the data acquisition system. Also included in this chapter is a step by step procedure of the data taking process for one beam fill or stack. The last section of this chapter describes the data taken during the 1991 FNAL fixed target run.

5.1 Data Readout

The data acquisition system includes two memory look-up units, MLUs, and a gatemaster. A MLU is a programmable logic module which forms four different

Figure 5.1: A schematic of the data acquisition system.

output logic signals from sixteen input logic signals. The two MLUs are called[1] the master MLU and charged MLU, and the outputs of these modules are labelled MMLU# and CMLU#, respectively. The next section describes the input signals to the MLUs; a description of the logic performed in the MLUs is in section 5.3. The gatemaster is a custom built module that initiates gates, initiates read out, and resets the electronics for different types of triggers. The different trigger types are prioritized by the gatemaster: in order of priority – luminosity, ACNET, scaler, MMLU1, MMLU2, MMLU3, MMLU4, minimum bias, pedestal, forward calorimeter cosmic ray, flashlamp, and other monitor or calibration triggers. The physics triggers are labelled MMLU#.

The timing signal[2], or strobe, for the electronics is the minimum bias signal, the OR of the 160 Level I central calorimeter sums (see section 2.9). The central calorimeter FERAs have a 150 ns gate width for physics triggers; the gate width is 300 ns for flashlamp triggers.

All CAMAC crates, the left column of figure 5.1, are read out for charged triggered interactions; whereas only the calorimeter and trigger CAMAC crates are read out for neutral triggers. Each CAMAC crate is read out by a Smart Crate Controller [74] (SCC). The data is sent directly to a set of VME based data buffers (RBUF).

---

[1] In 1990, the setup of the MLUs was different with a neutral MLU instead of a charged MLU.

[2] The OR of the H1 hodoscope elements is used as the timing strobe for the charged MLU.

For the non-physics triggers, the information from specific modules is recorded. The luminosity monitor data are recorded every five minutes from a qVt interface located in a trigger CAMAC crate. The $\bar{p}$ beam information provided by the accelerator network (ACNET data) is read out every three minutes by an interface module in one of the trigger CAMAC crates. Many of the signals that are connected to pattern units are also connected to scaler modules in a trigger CAMAC crate, which are read out every five minutes, and to visual scalers, which count for ten second intervals and then reset. The flashlamp system operates at a $\frac{1}{6}$ Hz and the counters' responses to each flash are recorded; the rate of recording the flashlamp monitor tubes' responses to the bismuth light pulsers (sections 4.2 and 4.4.1) is also $\frac{1}{6}$ Hz.

5.2 Logic Signals

The definitions of the charged MLU inputs are shown in table 5.1. A charged track is defined when both an H1 element and an H2 element are hit and are consistent with a particle coming from the interaction region. For every H1 element there are six H2 elements for the definition of a charged track for the 1991 data run[3]. The H2 cluster bit is a trial bit which can be used to search for $\bar{p}p \rightarrow \phi\phi X$ if both ϕ's decay into K^+K^- which hit neighboring H2 elements (defining an H2 cluster). The H2 coplanarity requirement is one H2 element hit with one of the three opposite H2

[3]In 1990, there were only four H2 elements assigned to each H1 element.

Bit	Symbol	Meaning
1	h	≥ 1 charged track
2	hh	≥ 2 charged tracks
3	H2=2	#H2 element hits = 2
4	H2>2	#H2 element hits > 2
5	H2=2 clus	#H2 cluster hits = 2
6	H2>4	#H2 element hits > 4
7	H1>2	#H1 element hits > 2
8	H1>4	#H1 element hits > 4
9	e	#(Čerenkov cell with a charge track) ≥ 1
10	ee	#(Čerenkov cell with a charge track) ≥ 2
11	COPL	2 H2 elements coplanar
12	FCH OR	≥ 1 forward hodoscope element hit
13	FCAL OR	≥ 1 forward calorimeter hit
14	unused	
15	unused	
16	unused	

Table 5.1: The definition of the charged MLU input bits; some of the meanings are further explained in the text.

Bit	Symbol	Meaning
1	1 opposite 1	Level II octants coplanarity
2	1 opposite 3 PBG	Level II octants coplanarity
3	Any two adjacent	Level II octants
4	CCAL or	minimum bias
5	1 e- psi trigger	One Level II super-block
6	CCAL veto	No Level II super-block
7	unused	
8	unused	
9	ETOT	Total energy
10	FCAL OR	Forward calorimeter hit > 100 MeV
11	CMLU1	Charged MLU output CMLU1
12	CMLU2	Charged MLU output CMLU2
13	CMLU3	Charged MLU output CMLU3
14	CMLU4	Charged MLU output CMLU4
15	FCH OR	≥ 1 Forward hodoscope element
16	H1 OR	≥ 1 H1 element

Table 5.2: The definition of the master MLU input bits; some of the bits are further explained in the text.

elements being hit, roughly requiring two charged particles to be separated in the azimuth by $\pi \pm 0.5$ radians.

Table 5.2 shows the definitions of the master MLU input bits. The Level II octants are the OR of the five super-blocks' discriminators which come from the same octant. As discussed in section 2.9, the super-blocks' discriminator thresholds are based upon the expected energies of a J/ψ decay; the total energy signal is also discussed in that section. The main central calorimeter requirement (master MLU bit 2) is that two large energy deposits are in different Level II octants separated by at least 90° in the azimuth. This is accomplished by a coplanarity requirement of the Level II octants: one octant and one of the three opposite octants having super-blocks above threshold[4] and will be referred to as the PBG bit. The threshold for the total energy bit is 85% of available lab energy deposited in the central calorimeter. The H1 and forward hodoscope bits are included to veto charged particles for the neutral event trigger. The forward calorimeter bit is also used as a veto requirement with the total energy trigger for neutral events. Master MLU trigger bits 3 to 6 are test bits and have not been used as requirements in the hardware trigger during data taking.

[4]A tighter coplanarity requirement of opposing octants having a super-block above threshold (master MLU bit 1) has been used for data taking at and below the J/ψ formation energy.

5.3 Hardware Trigger

The previously described MLU input logic signals are the level 1 trigger; the master MLU's four outputs are the level 2 trigger and correspond to the four physics trigger inputs of the gatemaster. The primary charged physics trigger, MMLU1, is essentially an inclusive J/ψ trigger,

$$\bar{p}p \rightarrow J/\psi X, \tag{5.1}$$

and the subsequent J/ψ decay to e^+e^-. MMLU2 is the secondary charged physics trigger which looks for two-body events:

$$\bar{p}p \rightarrow \bar{p}p, \tag{5.2}$$

$$\bar{p}p \rightarrow \pi^+\pi^-, \tag{5.3}$$

$$\bar{p}p \rightarrow K^+K^-. \tag{5.4}$$

These events are also used as a monitor (the punch through signals as discussed in sections 4.3.2 and 4.4.2). Test triggers are investigated using MMLU3. The neutral trigger, MMLU4, is for two types of neutral events, which are defined by no signals in the H1 and forward charged hodoscopes. The first type is neutral events with two large coplanar energy deposits in the central calorimeter (PBG) which triggers upon

$$\bar{p}p \rightarrow \gamma\gamma, \tag{5.5}$$

$$\bar{p}p \rightarrow \eta_c X \rightarrow \gamma\gamma X. \tag{5.6}$$

Multi-gamma final states are the second neutral event type which are triggered upon by using the total energy bit.

Bit #	Symbol Name	Logic Vector (1A)	(1B)
1	1 opposite 1		
2	1 opposite 3 PBG	1	
3	Any two adjacent		
4	CCAL or		
5	1 e- psi		
6	CCAL veto		
7	unused		
8	unused		
9	ETOT 1		
10	ETOT 2		
11	CMLU1	1	
12	CMLU2		1
13	CMLU3		
14	CMLU4		
15	FCH OR		
16	H1 OR		

Table 5.3: MMLU1 bit requirements (1 representing that a bit must be ON) for the inclusive J/ψ trigger. Logic vector (1A) requires PBG and some charged element requirements defined by a charged MLU output (CMLU1); a different charged MLU output (CMLU2) forms logic vector (1B) with no calorimeter requirement. The primary charged physics trigger (MMLU1) is the OR of logic vectors (1A) with (1B).

Before starting the data acquisition, the MLUs have to be programmed. A program allows for different bit requirements to be set for logic vectors and which logic vectors are to be ORed to form one of the four outputs. A logic vector in an MLU is the AND of all the input bits with requirements; requirement for a bit is either a bit is ON (1) or OFF (0). Below are the hardware trigger requirements that have been used during the 1991 data taking during the search for the $^1P_1$; the primary charged physics trigger is used to demonstrate how the logic vectors from both of the charged and master MLUs form the trigger.

Bit #	Symbol Name	Logic Vector (1a)	(1b)
1	h		
2	hh		1
3	NH2=2		1
4	NH2>2		
5	NH2=2 clus		
6	NH2>4	0	
7	NH1>2		0
8	NH1>4	0	
9	e		1
10	ee	1	
11	COPL		1
12	FCH OR		
13	FCAL OR		
14	unused		
15	unused		
16	unused		

Table 5.4: CMLU1 bit requirements (1 and 0 representing that a bit must be ON or OFF, respectively) of the inclusive J/ψ trigger with central calorimeter requirement. Logic vector (1a) is the two electron sub-trigger; the one electron sub-trigger is logic vector (1b). The CMLU1 output is the OR of the logic vectors (1a) with (1b); the output is used in the master MLU logic vector (1A).

MMLU1, the primary charged physics trigger (inclusive J/ψ trigger), relies upon the Čerenkov detector and large energy deposits in the central calorimeter. The hardware trigger consists of two master MLU logic vectors shown in table 5.3. Logic vector (1A) requires that there be two coplanar large energy deposits in the central calorimeter (PBG) and some charged element requirements (CMLU1), which are shown in table 5.4. The two charged MLU logic vectors, (1a) and (1b), are respectively the two and one electron sub-triggers, and the OR of these logic vectors is CMLU1. The one electron sub-trigger is more stringent about the number of

Bit #	Symbol Name	Logic Vector (2a)
1	h	
2	hh	
3	NH2=2	1
4	NH2>2	
5	NH2=2 clus	
6	NH2>4	
7	NH1>2	0
8	NH1>4	
9	e	
10	ee	1
11	COPL	1
12	FCH OR	
13	FCAL OR	
14	unused	
15	unused	
16	unused	

Table 5.5: CMLU2 bit requirements (1 and 0 representing that a bit must be ON or OFF, respectively) of the inclusive J/ψ trigger with no central calorimeter requirement. Logic vector (2a) is a stringent two electron sub-trigger. The CMLU2 output is used in the master MLU logic vector (1B).

H1 and H2 elements than the two electron sub-trigger[5]. The second logic vector of MMLU1, (1B), does not require information about the calorimeter and uses a very stringent two electron sub-trigger of the CMLU2 logic vector (2a), shown in table 5.5. Combining the logic vectors, the requirements can be written as three triggers:

$$(\mathrm{PBG}) \otimes (\mathrm{ee}) \otimes (\overline{\mathrm{H1}> 4}) \otimes (\overline{\mathrm{H2}> 4}), \tag{5.7}$$

$$(\mathrm{PBG}) \otimes (\mathrm{e}) \otimes (\mathrm{hh}) \otimes (\mathrm{COPL}) \otimes (\mathrm{H2}= 2) \otimes (\overline{\mathrm{H1}> 2}), \tag{5.8}$$

$$(\mathrm{ee}) \otimes (\mathrm{COPL}) \otimes (\mathrm{H2}= 2) \otimes (\overline{\mathrm{H1}> 2}), \tag{5.9}$$

[5]For some of the other resonance data taking, a third logic vector was included which was a zero electron sub-trigger.

where the bar over a bit's symbol represents the bit must be OFF – vetoing on the bit. The first is referred to as the two electron trigger while the second is called the one electron trigger. The last trigger is the strict two electron trigger with no central calorimeter requirements. The primary charged physics trigger MMLU1 is the OR of these three triggers.

The charged two body trigger, MMLU2, is nearly the same as the no central calorimeter–two electron trigger. The amount of light collected resulting from each hadron of reactions 5.2, 5.3 and 5.4 is a function of the type of interaction in the central calorimeter and distance from the phototube, or a punch through particle (just the Čerenkov light from traversing a counter). The hadron signals can be a wide range of possible *energy depositions* in the central calorimeter. Therefore, there is no central calorimeter signal requirement; a Čerenkov requirement is not applied since charged pions can produce Čerenkov light in the forward cells (section 2.5). All fully contained two body events correspond to signals only in the central calorimeter; the detectors in the forward direction are used as vetoes. The secondary charged trigger (MMLU2) is

$$(\mathrm{hh}) \otimes (\mathrm{H2}= 2) \otimes (\mathrm{COPL}) \otimes (\overline{\mathrm{H1}> 2}) \otimes (\overline{\mathrm{FCH\ OR}}) \otimes (\overline{\mathrm{FCAL\ OR}}). \qquad (5.10)$$

The neutral physics trigger MMLU4 consists of two triggers. Both of the triggers require that there are no H1 or FCH elements hit. The first trigger requires two large energy deposits separated by 90° in the azimuth. The other trigger occurs when the central calorimeter total energy is greater than 85% of the expected total energy and

there is no energy deposit in the forward calorimeter. The forward calorimeter has to be in veto for the total energy trigger in order to cut the rate of triggers from interactions that satisfy the total energy requirement in the central calorimeter. The two triggers are

$$(\mathrm{PBG}) \otimes (\overline{\mathrm{H1\ OR}}) \otimes (\overline{\mathrm{FCH\ OR}}), \tag{5.11}$$

$$(\mathrm{ETOT}) \otimes (\overline{\mathrm{H1\ OR}}) \otimes (\overline{\mathrm{FCH\ OR}}) \otimes (\overline{\mathrm{FCAL\ OR}}); \tag{5.12}$$

the OR of these two triggers forms the neutral trigger, MMLU4.

The rate of interactions which satisfies the charged two body trigger is large and is therefore prescaled. The prescaling occurs between the master MLU outputs and the inputs to the gatemaster. The MMLU2 prescaling has varied between 5 and 200 depending upon the instantaneous luminosity and center of mass energy. The test trigger (MMLU3) can be prescaled when it is used. The gatemaster includes a hardware minimum bias trigger that only requires a minimum bias signal (section 2.9), which is prescaled 10^5 into the gatemaster.

5.4 ACP System

When the RBUFs are filled with the event's signals, the event information is read out by a node of the ACP system. The ACP system[75, 76] is a set of computing processors, CPUs, consisting of 25 slave nodes and one boss node located in two VME crates (see figure 5.1). The slave nodes run a three part program which is described

below. The boss node polls each slave node to see whether or not the node can accept the RBUFs' event information. After the slave node's input event buffer is full, it informs the boss node to look for another slave node to accept events. The slave node with a full input event buffer then processes each event in the input event buffer.

The first part of the slave nodes' program organizes the event information. The signal information of an event is placed into two identical event buffer arrays. One of the event buffer arrays is passed to the other two parts of the program if the hardware trigger is a physics trigger or minimum bias trigger; the second event buffer array remains available to be copied to the output event buffer when the decision is made to keep the event. The non-physics types of data (luminosity, ACNET, scaler and so forth) are passed directly to the output event buffer.

The second part of the slave node's program (ACP2) analyzes some of the information of the charged detectors and fills a small summary array. Basically, ACP2 builds simple tracks from more elements than are used to build hardware tracks and puts this information into a summary array.

More information is supplied by the third part of the program (ACP3) in another summary array. The decision of whether to record a physics event occurs in ACP3 by use of the software trigger. ACP3 analyzes the calorimeters' signals treating both the central and forward calorimeters as one detector. A minor analysis of each event is done and software trigger bits are set. The software trigger bits are then compared with a list of software triggers bit requirements, which form the software trigger that

allow filtration of the interesting interactions. Although many parameters used in the analysis can be changed on a run to run basis, the parameters have been constant throughout data taking; the parameters that can be changed are noted below.

ACP3 starts by converting all central calorimeter counter and forward calorimeter module signals to energies from gain constants, which are updated every few stacks. The counters and modules are then ordered in a list by energy (largest to smallest energy deposits). The list's top element is checked to see if the energy is above half the minimum energy threshold (a parameter for each calorimeter); 75 MeV and 150 MeV are the minimum energy thresholds for the central and forward calorimeters, respectively. The counters (modules) that form a 3×3 grid[6] about the list's top element form a cluster. If the resulting total energy from a cluster is above the minimum energy threshold, the counters and modules are assigned to that cluster and removed from the list. Clusters are identified until there are no more counters or modules greater than half the minimum threshold or no cluster total energy above threshold. Counters and modules from the two calorimeters are not combined together to form any clusters.

The clusters' centers of gravity are found in terms of ring and wedge numbers for the central calorimeter clusters (vertical and horizontal module numbers for the forward calorimeter) in tenths of block units. A lookup table is used to adjust the energy and position of the central calorimeter clusters due to energy lost between

[6]The size of the grid can be a function of ring number or forward calorimeter.

counters. The cluster energies are then summed with the counters and modules not used to make any clusters to calculate the total energy deposited in the calorimeters.

All pairs of clusters are combined to calculate all possible invariant masses. Since numerical operations involving real numbers are much slower than integer operations in the ACP system, all event calculations are done with integers; the square of each invariant mass is used. The resulting values are compared with a list of squares of neutral particle masses. If a pair's result is close enough to a particle's mass squared, a software trigger bit can be set.

Another software trigger bit can be set if a cluster's energy in a particular ring number is close enough to the energy of a photon from an electromagnetic decay: $\bar{p}p \rightarrow \gamma X$, where X is a particle in a particle mass table down loaded to the slave node's program. The *recoil* gamma ray energy is a function of the expected total energy, the mass of X and polar angle (ring number). The cluster energy is compared to a lookup table made when the slave node's program is initialized.

Two body kinematics are checked when both of the two greatest energy clusters are in the central calorimeter. The coplanarity of the cluster position has to be good to one block; the absolute difference in position of the two clusters in wedge block units has to be 32 ± 1 blocks. At initialization, a lookup table for the two body kinematics using ring numbers and $\bar{p}$ momentum is created. The look up table is created for the following two body systems: $\gamma\gamma$, e^+e^-, $\pi^+\pi^-$, K^+K^-, $\bar{n}n$ and $\bar{p}p$; note that the first four (last two) reactions have nearly the same kinematics.

Bit	Name/Symbol	Description and Comment
1	≥ 2.5	At least 1 invariant mass pair greater than 2.5 GeV
2	1 cluster	Total # of clusters = 1
3	2 clusters	Total # of clusters = 2
4	3 clusters	Total # of clusters = 3
5	4 clusters	Total # of clusters = 4
6	5 clusters	Total # of clusters = 5
7	6 clusters	Total # of clusters = 6
8	≥ 7 clusters	Total # of clusters ≥ 7
9	1 π^o	1 exclusive π^o
10	2 π^o's	2 exclusive π^o's
11	≥ 3 π^o's	at least 3 exclusive π^o's
12	≥ 1 π^o	at least 1 exclusive π^o
13	1 η	at least 1 η formed
14	≥ 2 ηs	at least 2 exclusive η's
15	J/ψ, η_c Inv Mass	formed by a pair of clusters
16	ψ', η_c', χ_2 Inv Mass	formed by a pair of clusters
17	Any Punch Thru	Any 1 counter cluster
18	Recoil Mask	Cluster fits recoil γ
19	2 Body e^+e^-	and $\gamma\gamma$; cluster energy requirement
20	2 Body $\bar{p}p$	and $\bar{n}n$; no cluster energy requirement
21	2 Body $\pi^+\pi^-$	and K^+K^-; no cluster energy requirement
22	> 0.85 E_total	Total Energy greater than 85% of lab energy
23	> 0.90 E_total	Total Energy greater than 90% of lab energy
24	$> 80\%$ E_perp	Total Momentum perpendicular to $\bar{p}$ direction
25	≥ 2.0	At least 1 invariant mass pair greater than 2.0 GeV
26	MMLU1	MMLU1 gatemaster trigger
27	MMLU2	MMLU2 gatemaster trigger
28	MMLU3	MMLU3 gatemaster trigger
29	MMLU4	MMLU4 gatemaster trigger–neutral trigger
30	Minimum Bias	from gatemaster trigger
31	At least $1e^-$	1 cluster fits energy and 2 body kinematics
32	Error Mask	problem with event buffer

Table 5.6: The bits that make up the software trigger bits in ACP3. Further explainations of the bits can be found in the text.

Particle	Mass Window (MeV)	
	Lower Limit	Upper Limit
π^o	105	165
η	460	640
η_c	2535	3430
J/ψ	2630	3560
χ_2	3020	4090
η_c'	3050	4130
ψ'	3130	4240

Table 5.7: The invariant mass windows for a pair of clusters used by the ACP slave node's program.

The software trigger bits[7] are shown in table 5.6; most of the names and comments are self explanatory. The difference between the *exclusive* (bits 9, 10, 11, 12, and 14) and the other *formed* invariant masses is that each of the clusters forming the exclusive invariant mass pair must not combine with other clusters to form one of the acceptable invariant masses. The formed invariant mass bits (13, 15, and 16) mean that at least one pair of clusters forms an invariant mass which is inside the mass window. The invariant mass windows are also parameters which have been constant throughout the data taking period and are shown in table 5.7. The mass windows for the π^o and η are the expected resolution of the detector while the charmonium mass windows are $\pm 15\%$ of the resonance mass. Notice that the η_c and J/ψ (χ_2, η_c' and ψ') mass windows overlap and therefore the acceptable mass window for bit 15 (16) is 2535 to 3560 MeV (3020 to 4240 MeV). The recoil mask bit is $\pm 15\%$ of the expected energy of a gamma ray as a function of polar angle from the reaction $\bar{p}p \rightarrow \gamma X$ where X can be γ, π^o, η, or any of the $\bar{c}c$ states as long as the center

[7] Note that some of the software trigger bits' definitions have changed between the 1990 and 1991 data runs.

of mass energy is 150 MeV greater than the mass of X. The 'any punch through', 'perpendicular energy' and 'at least 1 e^-' bits (17, 24 and 31) are not used for any triggers and are trial software trigger bits.

The resulting ACP3 software trigger bits are compared to a list of bit requirements for software triggers. The software trigger, or level 3 trigger, that has been used during the data taking is discussed in the next section. If there is a match, the second event buffer array with the two summary arrays, from ACP2 and ACP3, are written to the output event buffer. The ACP3 summary array consists of the total energy deposited, cluster information (energy and positions in counter/module unit numbers), and found particles and recoil gamma ray information.

When a slave output event buffer is full, the node notifies the boss node. When the boss node is not busy, the slave node's output event buffer is transferred to the input buffer of the controlling data acquisition program running on a μVAX II. This program writes the buffer events to 8 mm tape and distributes events to two computers for monitoring purposes.

5.5 Software Trigger

The software triggers have been consistent throughout the 1991 data run. The triggers are very general to ensure that good events are not thrown away by the ACP slave nodes' program. Table 5.8 shows the output of the program that prepares the

Trigger Number	Mask Trigger	Mask Don't Care	Prescale Factor	Comment Description
1	04100000	04100000	1	MMLU2: $\pi^+\pi^-$ 2 body kin.
2	04080000	04080000	1	MMLU2: $\bar{p}p$ 2 body kin.
3	11000000	11000000	1	MMLU4: ≥ 2.0 GeV inv. mass
4	10100000	10100000	1	MMLU4: $\gamma\gamma$ 2 body kin.
5	10080000	10080000	1	MMLU4: $\bar{n}n$ 2 body kin.
6	10400000	10400000	1	MMLU4: Total Energy $\geq 90\%$
7	02000000	02000000	1	MMLU1: Everything
8	10000000	10000000	1000	MMLU4: Neutral min. bias
9	20000000	20000000	1	Hardware minimum bias

Table 5.8: The ACP software triggers used during the 1991 data taking period. The masks are in hexadecimal. The "Don't Care Mask" is a misnomer; the bits that are required to be OFF are the "Trigger Mask" subtracted from the "Don't Care Mask". In another words, the "Don't Care Mask" defines which software trigger bits have requirements and the "Trigger Mask" defines which of these are required to be ON. In 1991, no software trigger bits were required to be OFF; triggers which did veto upon software trigger bits were used during the 1990 data taking.

software triggers. The trigger masks are in hexadecimal. The table's caption explains how to understand which software trigger bits have requirements.

All primary charged trigger and hardware minimum bias trigger events are selected and therefore recorded: software triggers 7 (MMLU1) and 9 (Minimum Bias). The secondary charged trigger events are cut to only pass events where the highest energy deposits conform with the two body kinematics: software triggers 1 and 2 which are respectively

$$(\text{MMLU2}) \otimes (\text{2 Body } \pi^+\pi^-), \tag{5.13}$$

$$(\text{MMLU2}) \otimes (\text{2 Body } \bar{p}p). \tag{5.14}$$

Several neutral triggers have been used ranging from the two highest energy deposits fitting two body kinematics to 90% of the total available energy having been deposited.

The neutral two body kinematic software triggers are 4 and 5, which are respectively

$$(\text{MMLU4}) \otimes (\text{2 Body } \pi^+\pi^-), \tag{5.15}$$

$$(\text{MMLU4}) \otimes (\text{2 Body } \bar{p}p) \tag{5.16}$$

(using the appropriate softwarer trigger bit names from table 5.6); the former is for $\bar{p}p \to \gamma\gamma$ and the latter for $\bar{p}p \to \bar{n}n$ events. Software trigger 6,

$$(\text{MMLU4}) \otimes (> 90 \text{ E\_total}), \tag{5.17}$$

is the neutral total energy software trigger. The 2.0 GeV invariant mass trigger for neutral events is a general trigger to look for high mass objects which decay to $\gamma\gamma$; software trigger 4 can be considered a subset of software trigger 3,

$$(\text{MMLU4}) \otimes (\geq 2.0). \tag{5.18}$$

A neutral minimum bias, software trigger 8 (MMLU4), which accepts every thousandth neutral trigger which does not satisfy the other neutral software triggers is recorded to check the efficiency of the other neutral software triggers.

5.6 Procedure and Monitoring

The procedures for data taking and monitoring have been spread out among several sections of a *How To* binder which is located in the E760 counting room. The procedures have evolved with the data taking. Below is a summary of the procedures during data taking and monitoring.

The largest unit of E760 data taking is a beam fill or $\bar{p}$ stack. The accumulation of $\bar{p}$'s (stacking) takes between 1.5 and 3.0 days; stacking rates vary between 0.2 and 1.0 mA/hr. After stacking and initial beam cooling, the beam is decelerated to the correct momentum and further cooled to reduce the momentum spread. The time between the end of stacking and the beam being ready for data taking can be several hours.

While the beam is being cooled, several steps are necessary to prepare the read-out electronics and data acquisition system. All of the electronics are essentially reinitialized. The detector components are turned on to operating voltages to allow for some initial warmup period: 15 minutes has been sufficient. The programmable logic units other than the MLUs are set up; the outputs of these units define most of the hardware bits which are the inputs to the MLUs. The MLUs are programmed when the hardware triggers are downloaded to the units. The ACP system is initialized by loading the node programs on to the CPUs. The VAX data acquisition program is then used to take pedestals for all of the FERA ADCs with the gas jet off. A program analyzes and determines pedestal values; the shift crew then compares the pedestal values and widths to a previous set of pedestals. If the new set of pedestals is acceptable, the pedestal values and widths are recorded into a data base. The ACP software triggers can then be prepared; the calorimeter gain constants can also be prepared. The software triggers have been consistent; the gain constants are updated every few stacks.

When the beam has been determined stable and the spread of momentum is considered appropriate, the gas jet is turned on. The VAX data acquisition program is started, which requires the $\bar{p}$ momentum to be entered to within a few MeV/c. The $\bar{p}$ momentum, the software triggers, gain constants, pedestals and ACP3 parameters are downloaded to each slave node by the VAX data acquisition program. Each slave node program is then initialized and calculates the lookup tables discussed in section 5.4. The visual scalers are checked against previous rates while an initial instantaneous luminosity is determined. If both the rates and luminosity are acceptable, then the VAX data acquisition program initiates data acquisition.

The VAX data acquisition program passes events to two separate monitor programs. The non-physics events (e.g. ACNET and scaler data) are passed to the front end monitor program which allows monitoring the data acquisition for changes over a long period of time. A separate VAX workstation is dedicated to receiving the physics events and processing the events with an online detector program. The online detector program produces histograms of quantities, such as hit maps and energy spectra, to monitor all aspects of the components of the detector for a run.

After the data acquisition is started, the detector monitor program is used to monitor the detector components continually. The front end monitor does the same for the scaler and ACNET data. The scalar rates are checked visually every few hours. Once a shift, a gas check is done to monitor the amount of gas in reserve and the pressures for the gas jet and the detector components which use gases.

An E760 run constitutes a data set which is written to one 8 mm tape. The length of a run has varied in time (half an hour to several hours) and integrated luminosity (between 20 and 100 pb^{-1}). The change of runs is done without exiting the data acquisition program and takes less than a minute.

5.7 1991 Data Taking Summary

During the 1991 FNAL fixed target run, E760 collected ≈ 30 pb^{-1} of data ranging in center of mass energies from 2950 MeV (below the η_c resonance) to 4200 MeV (the injection $\bar{p}$ momentum of 8.9 GeV/c). Nearly half of this was dedicated to the search for the $^1P_1$. The data was taken over the course of four months interspersed with data taking involving the resonances η_c, J/ψ, χ_2, and ψ', as well as searching for the η_c'.

Parts of sixteen stacks were dedicated for the $^1P_1$ search. The luminosity weighted center of mass energy and integrated luminosity involved for the charged and neutral analyses of this thesis is presented in table 5.9. The stacks are labelled in chronological order; the data and running conditions are sometimes referred to by stack number. The difference between the integrated luminosities of the charged and neutral analyses is due to trouble using the neutral DSTs (these DSTs are discussed in the next chapter) and the trigger conditions. The neutral DSTs start with the 3^{rd} stack due to the FCAL OR bit not being available to the trigger before this stack.

Stack Number	Center of Mass Energy (MeV)	Integrated Luminosity (nb^{-1}) Charged An.	Neutral An.
1	3524.197	822.71	
2	3523.902	783.71	
3	3522.498	979.91	924.04†
4	3523.119	489.53	445.75†
5	3524.867	1040.81	1040.81
6	3526.178	1336.72	1134.58
7	3525.468	1310.38	1251.92
8	3525.999	1364.09	1298.20
9	3526.460	1139.62	932.63
10	3525.133	1017.41	781.40
11	3527.011	1016.39	804.91
12	3525.713	885.00	818.73
13	3526.104	940.39	877.47
14	3525.914	980.30	527.69
15	3526.336	910.96	910.96
16	3526.074	875.59	667.55

Table 5.9: The energies and integrated luminosities for the charged and neutral analyses for the sixteen stacks dedicated to the $^1P_1$ search. Trouble with the neutral DSTs account for the different integrated luminosities; the neutral DSTs were not started until the 3^{rd} stack.
†The forward calorimeter was in veto for the neutral total energy trigger for part of stacks 3 and 4; the integrated luminosities used for events collected by this trigger for the 3^{rd} and 4^{th} stacks are 558.64 nb^{-1} and 436.60 nb^{-1}, respectively.

Chapter 6

Data Reduction and Analysis

The sections of this chapter can be split into three categories. The first category is the filtering of data and the creation of neutral DSTs. Two sections describing the offline code that pertains to the central calorimeter are the second category. The last category is the cuts involved in candidate event selection.

6.1 Filtering

After a data run has ended, the data tape is transferred to a tape drive on one of the E760 workstations; a program[1] is run using the data tape as input. This program serves several purposes; the data is filtered and split into several data sets, statistics for all detectors are generated and a preliminary analysis of charged events is done.

Events from both of the two charged physics triggers (MLU1 and MLU2) are selected and written to separate data files[2]. The MLU1 events are also subject to

[1]The program is entitled DO_DST. Although DST is part of the program's name, only filtering is done; no data summary is done at this level.

[2]The files are labelled RUN#_MLU1.DST and RUN#_MLU2.DST, respectively.

analysis producing a very preliminary charmonium data sample based upon the easily identified inclusive J/ψ decays (equation 1.3). This has been very useful for a quick count of candidate events when a resonance is being scanned with one stack; this has not been applicable during the $^1P_1$ search.

A similar file[3] is made for neutral events except an event selection based upon the ACP3 software trigger bits is done; the ACP3 software trigger bits were described in table 5.6. For an event to be written to this file, one of the following sets of requirements is met:

- there exists an invariant mass ≥ 2.0 GeV/c^2 in the event,
- the two largest energy deposits satisfy two body kinematics for $\gamma\gamma$ events,
- there are more than two clusters and one pair of clusters results in an invariant mass[4] that is associated with a π^o, or
- the number of clusters is ≥ 6 and two η invariant masses are formed by four clusters[5]

A calibration file is made with further cuts involving the filtered neutral events to select all $\bar{p}p \rightarrow \pi^o\pi^o$. Within a stack, the calibration files are combined into one

[3]The file name is RUN#_MLU4.DST.

[4]Neither of the two clusters can be used with a different cluster to form a separate acceptable invariant mass (section 5.4).

[5]Same as previous footnote.

file and used to calibrate the entire stack of data (section 4.3.4). The calibration is usually finished within a few days of the end of a stack.

Further filtering of MLU1 and MLU4 events occurs[6]. During the quick analysis of MLU1 events by the filtering program, if there is an invariant mass pair greater than 2.2 GeV/c^2 then the event is written to the file. The events with at least one invariant mass $\geq$ 2.5 GeV/c^2 software bit ON for MLU4 events are written to the other file.

A further filtering of the MLU1 data is performed by doing the following basic analysis. For each energy in a stack, a file[7] is written containing events with two charged particles that satisfy a very loose electron identification with a large invariant mass. The loose electron identification allows for missing Čerenkov detector signals in the septa region.

6.2 Neutral DSTs

The neutral DSTs consist of short summaries for all neutral events. The central calorimeter clustering algorithm and pile-up analysis, which are described in the following sections, are used in making the summaries for the neutral DSTs. The central

[6]The resulting events are written to files labelled RUN#_COM1.DST and RUN#_COM4.DST, respectively.

[7]These files are called MINI DSTs.

calorimeter cluster energy threshold is 25 MeV while 50 MeV is the threshold for a cluster in the forward calorimeter.

A neutral event summary contains information about the formed clusters in both the forward and central calorimeter. For all formed clusters, the position and energy are in the summary as well as a hit map of the counters or modules in a 3×3 grid that are assigned to the cluster (see the next section). The pile-up determinations for the central calorimeter clusters (section 6.4) are included. Also included in each summary is information which uniquely identifies the event, the extra energy in the counters and modules not associated with clusters, and hit maps for the H1, H2 and Čerenkov detectors.

6.3 Clustering

Determining which blocks constitute a particle's energy deposit has been under investigation since the AGS test (section 4.2.1). The basic cluster configuration is a 3×3 grid centered upon the largest energy deposit in an area. The clustering algorithm has evolved to distinguish single electromagnetic shower inducing particles from coalesced gamma rays from symmetric π^o decay.

The original version (and a basic outline of the current version) uses the 3×3 grid and the energy deposit's center of gravity to determine the position of the incident particle. The 3×3 grid of all counters with signals above pedestals is formed around the counter with the highest energy deposit in the hit counter list (or a small section of

the calorimeter in the current version of the clustering algorithm). After the counters included in the formed cluster are removed from the hit counter list, another energy deposit is located for clusterization. Clusters are formed until there are no more counters above threshold for the central energy deposit and no 3×3 grid energy above the total cluster energy threshold; this is similar to the ACP program's clustering algorithm (section 5.4).

The current, and better, offline version looks for local energy deposit maxima and forms clusters about the maxima. A single 3×3 cluster is formed about an energy deposit maximum when the nearest maximum is more than 4.25 block units away in any direction; in this case, the energy deposit is considered an isolated cluster.

Each isolated cluster energy deposit position is corrected by using the sum of two exponentials, shower core and tail profiles [77]. The parameterization of the two profiles is determined from studying the e^+e^- energy deposits from data taken at the J/ψ resonance. These energy deposits are also used to study energy loss of the electromagnetic shower due to the stainless steel septa. The cluster energy is corrected for energy loss.

The distances in both ring and wedge units (x_r and x_w, respectively, in units of blocks) between an energy deposit's center of gravity and the center of the central block of a 3×3 grid are used to correct the position of the incident particle. The new position is dependent upon these measured distances and parameterization of the electromagnetic shower. The corrected ring distance from the center of the central

	Value	
Parameter	Ring	Wedge
A	0.2601	0.3138
a	0.0321	0.0397
B	0.2574	0.1969
b	0.1860	0.1715

Table 6.1: The empirically determined parameters for correcting the position of an energy deposit in the central calorimeter, equation 6.1. All paramters are in units of blocks.

block (similarly for the corrected wedge distance) is

$$d_r = A_r(1 - e^{-\frac{x_r}{a_r}}) + B_r(1 - e^{-\frac{x_r}{b_r}}), \tag{6.1}$$

where A, B, a, and b are constants determined empirically from $J/\psi \rightarrow e^+e^-$ and d is the same direction from the center of the central block as x. Table 6.1 contains the empirically determined parameters. The corrected position is then translated from the block coordinate system (ring and wedge) to the laboratory system (θ and ϕ).

The electromagnetic shower energy lost in the septa is corrected for by using a parameterization of the shower profile and the position of the incident particle. The distance from the closest ring and wedge edges of the block: y_r and y_w, respectively, where $d_r + y_r = d_w + y_w = \frac{1}{2}$ of a block. The total energy deposited in a 3×3 grid, E_{seen}, is corrected to

$$E_{corr} = \frac{E_{seen}}{(1 - F_{half}e^{-\frac{y_r}{f_{half}}})(1 - G_1e^{-\frac{y_w}{g_1}} - G_2e^{-\frac{y_w}{g_2}})}, \tag{6.2}$$

where F_{half} and f_{half} depend upon which half of the block the particle is incident upon, due to the staggering of blocks in the ring direction, and the two sets of parameters in the wedge direction (G_i and g_i) are due to the two wedge shells separating blocks

Paramter	Value	Paramter	Value
F_{low}	0.0614	G_1	0.1474
f_{low}	0.1357	g_1	0.0204
F_{high}	0.0857	G_2	0.1594
f_{high}	0.0508	g_2	0.0784

Table 6.2: The empirically determined parameters for correcting the energy of an energy deposit in the central calorimeter, equation 6.2. Paramters f and g are in units of blocks while parameters F and G are dimensionless.

in the azimuth. The parameters F_{low} and f_{low} (F_{high} and f_{high}) are used when the determined polar angle θ of the incident particle is less than (greater than) than the θ that corresponds to the center of the central block. The parameters are empirically determined from $J/\psi \rightarrow e^+e^-$ data and are presented in table 6.2.

A cluster mass M_{cl} is formed by taking the counters in a 5×5 grid and forming an invariant mass for the cluster,

$$M_{cl} = \sqrt{\left(\sum_i E_i\right)^2 - \left(\sum_i \vec{p}_i\right)^2} \tag{6.3}$$

where E_i is the energy of the i^{th} counter and $\vec{p}_i = E_i\hat{x}_i$ where $\hat{x}_i$ is the unit vector from the interaction point to the center of the i^{th} counter. A single cluster energy deposit is split into two clusters when the cluster mass is > 100 MeV. A group of counters is also split into two clusters when two energy deposit maxima are separated by less than 4.25 block units.

The two profiles are used when separating two nearby energy deposit maxima or when an isolated energy deposit's cluster mass is > 100 MeV. The energies of the blocks common to both clusters are shared (the assumption being that each deposit is caused by separate electromagnetic showers). The fractions of the energy deposited

in a shared counter (a counter that is assigned to the two clusters) is a function of the distance between the shared counter and the two main counters (where the energy deposit maxima are located) and the shower profiles. The determination of the fractions of any shared counter is an iterative process and is complete when the profiles for each shower deposit are satisfied.

The method of splitting energy deposits has succeeded in identifying energy deposits from coalesced π^o decays (see figure 7.5). The clustering algorithm described above assumes all incident particles are electromagnetic shower inducing particles: electrons, positrons or gammas. Hadronic interactions can be punch through particles (see sections 4.3.2 and 4.4.2), have symmetric energy deposits, or asymmetric energy deposits. Since a punch through particle signal is only one counter, the exact position of a punch through cannot be determined and it is nominally positioned at the center of the counter hit. Large signals resulting from hadronic interactions may or may not mimic electromagnetic shower signals. Both symmetric and asymmetric hadronic signals can be split due to the resulting cluster mass or by virtue of having two energy maxima.

6.4 Pile-up

Pile-up is defined to be extraneous signals from interactions, other than the event being triggered upon, nearby in time. The central calorimeter counters' FERA ADCs are gated for 150 ns. Triggered signals are supposed to start 20 ns after the

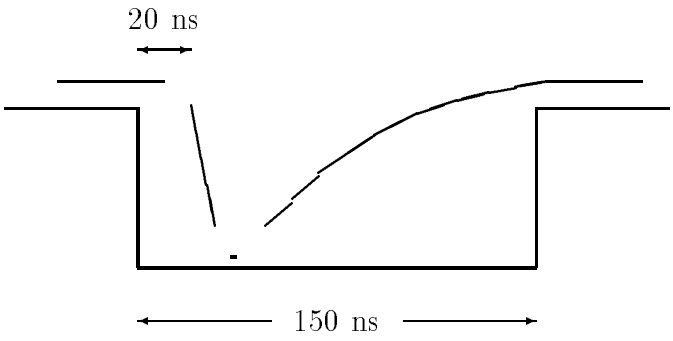

Figure 6.1: A single calorimeter counter signal shown in relationship to the FERA ADC gate.

start of the gate as shown in figure 6.1. Interactions occurring nearby in time cause signals, such as the one shown in figure 6.1, to be shifted in time with respect to the FERA gate. The tail of the signal shown in figure 6.1 is not a good representation; the central calorimeter counter signals are long, with 90% of the charge being collected in 240 ns (an additional 7% of the charge is collected in the following 150 ns). Hence, most pile-up signals come from previous interactions, when tails of earlier large energy deposits are collected within the triggered gate for the central calorimeter.

The data acquisition electronics do not have any timing information for the individual counter signals. However, signals from both the Level I and II summers can be used to identify pile-up signals. Below is a description of the signals available and how they are used to determine whether or not a central calorimeter signal/cluster is caused by the interaction triggered upon. Analysis code determines the extraneous signals as *out-time* clusters as well as identifying the trigger interaction signals as

in-time clusters. However, there are some signals which can neither be identified as being in-time nor out-time clusters and are classified as *non-determined* clusters.

The Level I signals that are used come from the 160 latches, or pattern units. The 160 discriminated signals, discussed in section 2.9, that form the minimum bias are connected to latch units. The pattern units essentially give a 30 ns *snapshot* about the minimum bias signal for the event (the peak of an in-time signal). During the 1990 data taking run, the discriminator energy threshold was $\approx$ 80 MeV; amplifiers were installed prior to the 1991 data taking run, reducing the effective threshold of the pattern units to $\approx$ 40 MeV. However, the pattern unit thresholds do not necessarily correspond to the cluster energy threshold since a cluster's energy deposit can involve more than one 1×9 set of counters which make up a Level I sum.

The 40 Level II summer discriminators are used for the hardware trigger and set with thresholds which correspond to expected e^+e^- pairs from $\bar{c}c$ decays and are not used for pile-up determination. As discussed in section 2.9, each of the 40 Level II sums is also split into two signals which go to FERA ADC's. The difference between the two recorded signals is that one signal is timed the same as the individual counters signals, ADC_{trigg}, and the other is delayed to look at the energy prior to and/or at the beginning of the trigger, ADC_{delay}. Figure 6.2 shows the three configurations of the ADC_{delay} gate width and delay amount used during the 1990 and 1991 data taking periods. In 1990, the ADC_{delay} gate width was 150 ns; during the first (second) part of data taking in 1990 the delay was 100 ns (150 ns) and the overlap was 50 ns (none), see figure 6.2a (figure 6.2b). After studying both 1990 configurations, it was decided

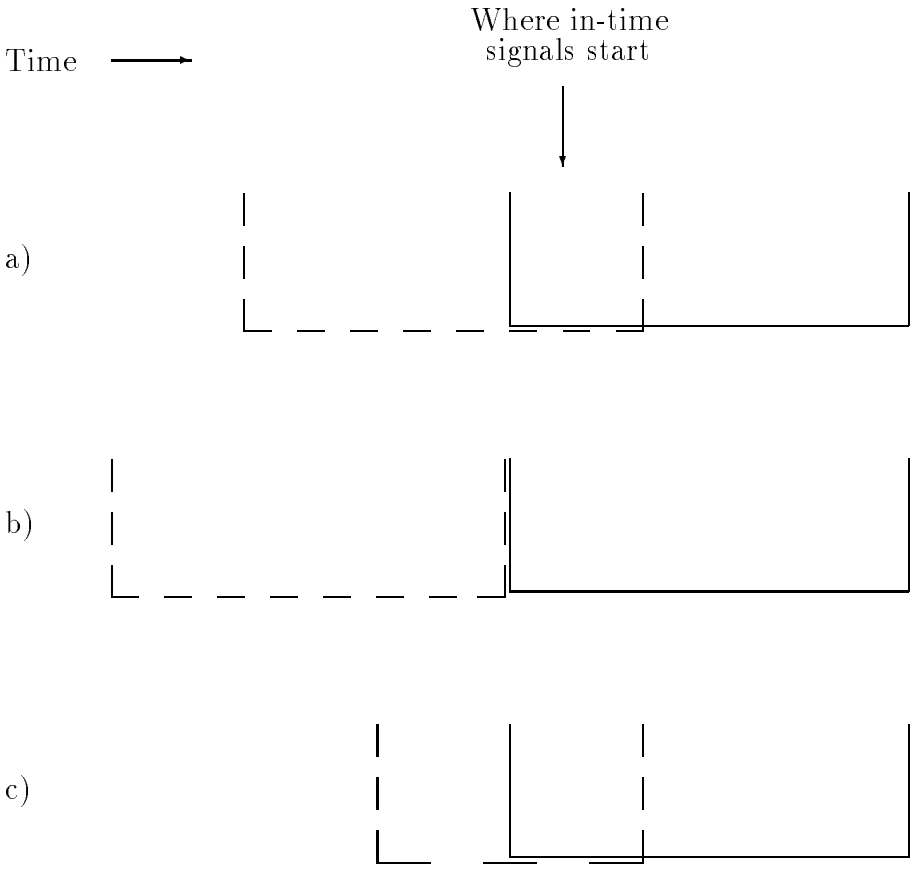

Figure 6.2: The three configurations of overlap of the two Level II summer signals: (a) 1990 overlapped gates, (b) 1990 separated gates, (c) 1991 overlapped gates.

to use an overlap of the two ADC gates of 50 ns and shorten the gate width to 100 ns for the delayed gate thus making the delay amount 50 ns, shown in figure 6.2c.

For all three configurations shown in figure 6.2, a ratio for each super-block is defined as

$$R_{II} = \frac{ADC_{delay}}{ADC_{trigg}}. \tag{6.4}$$

A range of acceptable ratios R_{II} has been determined for each configuration which defines the in-time signals. If the ratio of a super-block is less than the acceptable range, then there is at least one energy deposit in the super block which came after the trigger interaction; the 1990 time separated gates (figure 6.2b) could not distinguish these types of signals. On the other hand, when a super-block's ratio is greater than the range, there is at least one energy deposit which came from an earlier interaction. Note that a super-block can contain more than one cluster; a super-block's ratio is strongly influenced by large energy deposits.

All clusters are initially assumed to be non-determined clusters in the offline pile-up analysis code. There are several possible criteria for determining whether a cluster is an in-time or out-time cluster. If a cluster does not fit any of the in-time or out-time cluster criteria for all the steps, the cluster remains as a non-determined cluster. If during the pile-up analysis a cluster is determined to satisfy criteria of an in-time cluster, it is declared as such and the analysis moves onto the next cluster. When a cluster is determined to be an out-time cluster, it is declared as such and the analysis continues with that cluster. A determined out-time cluster can satisfy the in-time cluster criteria at a later step in the pile-up analysis and be declared an

in-time cluster, which would then cause the analysis to move onto the next cluster. Clusters are given every chance to satisfy the in-time cluster criteria.

The pile-up analysis uses the position determined by the clustering algorithm to determine which counter the cluster is centered about. Certain counters are in overlap regions for the Level I and Level II summers; therefore counters can be in 1 or 2 pattern units and 1, 2, or 4 super-blocks. The following are the pile-up analysis steps taken using the 1991 configuration which is the relevant set-up for the $^1P_1$ search.

- The first step checks to see if the cluster is isolated in one of the super-blocks and that the FERA ADCs are above a threshold. The threshold is nearly equivalent to ≈ 30 MeV collected by ADC_{trigg} which corresponds to ADC_{delay} being a few counts above pedestal for in-time signals. If a cluster is isolated within a super-block (no other clusters are located in the super-block) and above threshold, either an in-time or out-time determination is made using R_{II}.

- The second step uses the Level I pattern units by comparing the amount of energy deposited by a cluster in a pattern unit, $E_{PU}^{cluster}$, with the summed energy deposited in the 1×9 set of counters of the Level I sum, E_{PU}^{summer}. For each pattern unit that the cluster has deposited energy (three pattern unit 1×9 sets can be affected by a 3×3 grid energy deposit), an in-time cluster determination results when the $E_{PU}^{summer} - E_{PU}^{cluster} < 10$ MeV and the pattern unit is ON; an

out-time cluster determination occurs when $E_{PU}^{cluster} > 50$ MeV and the pattern unit is OFF.

- The third step requires the cluster's energy deposit to be greater than 75% of the total energy deposited in a super-block. When more than one cluster is in a super-block, the larger energy deposit is the main contribution to the super-block's ratio, R_{II}, and therefore the ratio is used to determine the larger energy deposit cluster to be an in-time or out-time cluster.

- The last step uses the super-block's R_{II} when there are two nearly equal energy deposits within a super-block. If both of the two clusters make up between 45% and 55% of the super-block's deposited energy and R_{II} satisfys the in-time range criteria, then both clusters are declared to be in-time clusters. However, when R_{II} does not satisfy the in-time range criteria, it is unknown which cluster causes the ratio to be in the out-time ratio range and no declaration is made for either cluster at this step.

Isolated clusters are easily determined as well as nearby clusters which are in different super-blocks. Nearby clusters can also be in the same super-block. In the case of one of the clusters being in another super-block, a determination can be made for that cluster. When the other cluster (or even both clusters) is only in one super-block, the determination relies upon the pattern units or relative size of the energy deposits. The pattern units are only helpful when the cluster deposits enough energy into a pattern unit and when the clusters do not share pattern units. The determination of small energy deposits (< 100 MeV) is difficult when there are nearby

clusters. Some of the small energy clusters are declared in-time clusters due to small fluctuations during the ADC digitization process.

6.5 Charged Event Selection

The detector's response to e^+e^- from data taken at the J/ψ resonance has been studied to develop a basic set of cuts for identifying inclusive J/ψ events. A Quantity, called *electron quality weight*, combines information from the many components that make the E760 detector have been used to identify electron tracks. The electron quality weight, EQW, is a likelihood ratio of an electron hypothesis to a background hypothesis for a charged track.

The EQW of each track is the product of ratios, probabilities of each hypothesis, for several detector component measured quantities. The EQW product is

$$EQW \equiv \prod_i \frac{f_i^{elec}(x_i)}{f_i^{bkgd}(x_i)}, \tag{6.5}$$

where x_i is the i^{th} detector component quantity and f_i^{elec} and f_i^{bkgd} are the probability distributions of this quantity for electrons and background, respectively. The detector component quantities used to define EQW are:

- pulse height in the H2 hodoscope as a function of polar track angle;
- pulse height in the Čerenkov counter, correcting for polar angle dependence and the different mirrors' photoelectron yields;

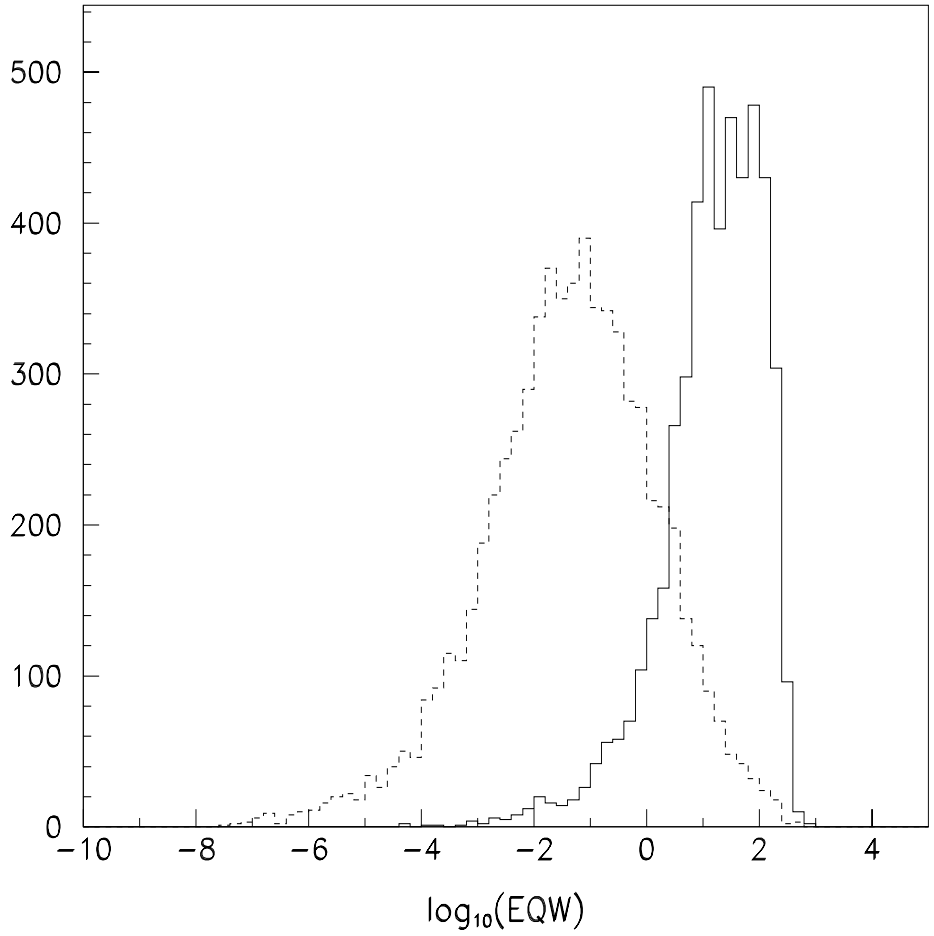

Figure 6.3: The $\log_{10} EQW$ for electrons (solid line) and background charged tracks (dashed line).

- the second moment of the central calorimeter energy deposit in the polar direction (rings);

- the second moment of the central calorimeter energy deposit in the azimuth (wedges);

- energy deposit containment in a 3×3 grid versus a 5×5 grid centered about the cluster position; and

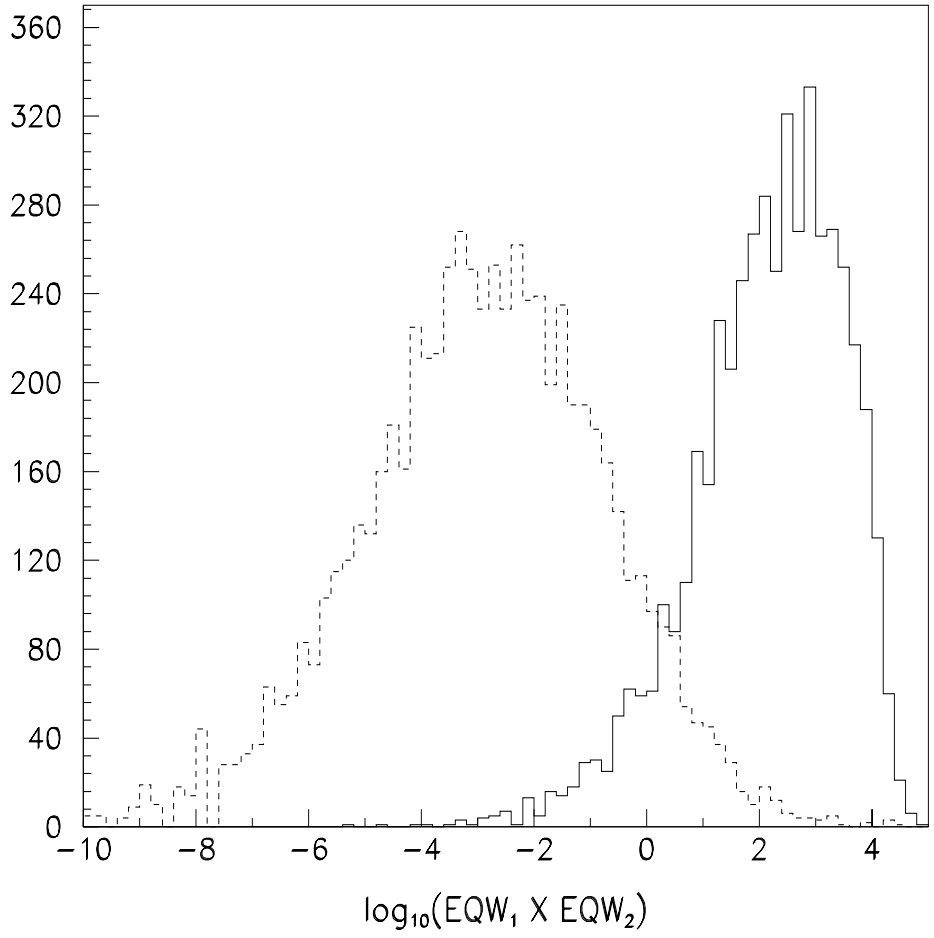

Figure 6.4: The $\log_{10}$ (product of two EQW) for e^+e^- (solid line) and background charged tracks (dashed line).

- a dE/dx measurement in the RPC, when the RPC is considered working.

The electron probability distribution for each detector component quantity is determined from studying kinematically fitted data taken at the J/ψ. Charged data taken at the $^1\mathrm{P}_1$ are used to determine the background probability distributions. The EQW for electrons from J/ψ decays and from background charged tracks is shown

in figure 6.3. The product, $EQW_1 \times EQW_2$ (the EQW's of each track), separates events with e^+e^- from the background events and is shown in figure 6.4.

6.5.1 Inclusive J/ψ Events

The inclusive selection requires the product of EQW's of the two charged tracks associated with the largest energy deposits to be consistent with e^+e^- events. A further cut on the characteristics of the energy deposit is a cluster mass cut (see equation 6.3). Events with either of the two largest energy deposits having a cluster mass $M_{cl} > 100$ MeV are eliminated to reject symmetric π^o energy deposits where one of the gamma rays has converted. This forces the e^- and e^+ to be isolated energy deposits. Both of the largest energy deposits are required to be in-time clusters.

A nominal fiducial volume cut eliminating electrons and positrons in ring 1 (backwards direction) is necessary so that all of the electromagnetic shower is contained. A fiducial cut in the forward direction is not necessary since when an electron (positron) is that far forward, the accompanying positron (electron) goes out the back of the calorimeter and also because the Čerenkov detector stops at 15° which is sufficiently far from the edge of the calorimeter. A further fiducial cut from the boundary of ring 1 and 2 (64.8°) to 62.0° is necessary due to shadowing by the backward Čerenkov cell's phototubes. Depending upon the azimuthal angle, a particle could pass through the phototube. Any charged particle that passes through a phototube's photocathode generates a signal which is generally of magnitude larger than electron

tracks from the rest of the cell. Also electrons (identified kinematically at the J/ψ) in this polar region which do not pass through a Čerenkov detector phototube generally do not result in Čerenkov photoelectrons. The placement of the backward Čerenkov cells' phototubes does not make it possible to discriminate electrons at polar angles $> 62°$.

The invariant mass of the the two largest energy deposits is calculated:

$$M_{inv} = \sqrt{(E_1 + E_2)^2 - (\vec{p}_1 + \vec{p}_2)^2}, \tag{6.6}$$

where E and $\vec{p}$ are the energies and momenta of the two largest energy clusters. Since $E_i \gg m_e$, the electrons and positrons are considered massless and the invariant mass can be calculated as

$$M_{inv} = \sqrt{2E_1E_2(1 - cos\zeta)}, \tag{6.7}$$

where ζ is the opening angle between the two clusters. The events where

$$2.9 \text{ GeV/c}^2 > M_{inv} > 3.3 \text{ GeV/c}^2 \tag{6.8}$$

are considered inclusive J/ψ events.

6.5.2 Exclusive Charged Events

The exclusive event selection starts from the inclusive event selection. The exclusive J/ψ reactions are

$$\bar{p}p \rightarrow \quad J/\psi\pi^o \quad \rightarrow e^+e^-\gamma\gamma, \tag{6.9}$$

$$\bar{p}p \rightarrow \quad J/\psi\pi^o\pi^o \quad \rightarrow e^+e^-\gamma\gamma\gamma\gamma, \tag{6.10}$$

$$\bar{p}p \rightarrow \quad J/\psi\pi^+\pi^- \quad \rightarrow e^+e^-\pi^+\pi^-. \tag{6.11}$$

All final state particles are subject to the backward fiducial volume cut: $\theta_i < 62°$. The exclusive selection for each reaction (described below) includes a modified cut on the number of clusters, where the central calorimeter's cluster threshold for the central counters is 5 MeV and the threshold for the total energy deposited is 20 MeV. There are further requirements for the non-electron particles including different geometrical cuts. Events are fit by SQUAW routines to the appropriate reaction hypothesis.

The pile-up analysis is used to reject events with unassociated clusters; an unassociated cluster is defined as an in-time or a non-determined cluster with > 100 MeV energy deposited which is not associated with any of the final particles of the reaction being investigated. In addition, the forward calorimeter clusters, using the timing of its summed signals to define whether a cluster signal is from the trigger interaction or not, are treated the same as the central calorimeter clusters. No unassociated clusters are allowed for final states which do not have charged pions. In-time or non-determined clusters with energies < 100 MeV can be final state particles; otherwise these small energy clusters are ignored.

The γ's from events for reaction 6.9 and 6.10, are allowed to populate the forward calorimeter and therefore there is no forward fiducial cut. The γ's located in the central calorimeter are subject to the same invariant cluster mass cut as the e^+ and e^- clusters. The invariant mass of a $\gamma\gamma$ pair, $M_{\gamma\gamma} = M_{inv}$ (equation 6.7) must

be near the π^o mass,

$$50 \text{ MeV/c}^2 < M_{\pi^o} < 200 \text{ MeV/c}^2. \tag{6.12}$$

The $J/\psi\pi^o$ candidate events are subject to a 6C fit. A 7C fit is done to the $J/\psi\pi^o\pi^o$ candidate events.

For reaction 6.11, both the π^+ and π^- are required to have good charged tracks and are therefore subject to a geometrical cut of $\theta > 15°$. The modified cluster cut is relaxed since a charged pion signal in the central calorimeter may be large and/or asymmetric (and therefore can be split into two clusters) and also the low energy charged pions do not necessarily generate a central calorimeter signal . The unassociated cluster cut is only applied when an extra energy deposit (> 100 MeV) is not associated with one of the four charged tracks. The pions are required to be well separated in the azimuth from the e^+e^- tracks by requiring that the four charged particles hit different H2 elements. Since a charged track can cause signals in two neighboring H2 elements, the requirement is that tracks can not be from contiguous H2 elements. A 3C fit is performed on possible $J/\psi\pi^+\pi^-$candidate events.

6.6 Neutral Event Selection

The search for radiative decays of the $^1\text{P}_1$ to η_c (reaction 1.2) begins with the neutral DSTs. The η_c is identified by either decaying to $\gamma\gamma$ (reaction 1.4) or to three neutral mesons (π^o, η and/or η') which all subsequently decay into pairs of gamma rays. The search for the all neutral channels involves either a 3γ or 7γ final state.

The energy of the transition gamma ray is $\approx$ 545 MeV which is approximately the average energy of the gamma rays in the center of mass for the 7γ final state.

Since no pile-up information for the forward calorimeter is included in the neutral DSTs, a forward as well as backward fiducial cut is made; no clusters are allowed in the forward calorimeter. All gamma rays are required to be away from the edges of the central calorimeter, $13^\circ < \theta_\gamma < 62^\circ$. Any cluster that is associated with a γ is expected to have a cluster mass $<$ 100 MeV. The cluster mass is used to reject symmetric π^o energy deposits.

The number of clusters, on-time or non-determined, must equal exactly the number of final state particles, i.e., no extra in-time or non-determined clusters of any energy ($>$ 25 MeV) are allowed. The 3γ and 7γ final states are permitted to have different minimum energies for the gamma rays: 100 MeV and 50 MeV, respectively. Other cuts which are different, depending upon the final state, are described below.

Background for the 3γ final state comes from π^o's and η's. Events are rejected whenever one of the three two-cluster invariant masses is near one of these masses: equation 6.12 and

$$400 \text{ MeV/c}^2 < M_\eta < 700 \text{ MeV/c}^2. \tag{6.13}$$

An event is kept when one of the invariant mass combinations is near the η_c mass:

$$2.7 \text{ GeV/c}^2 < M_{\eta_c} < 3.2 \text{ GeV/c}^2. \tag{6.14}$$

The events which pass the invariant mass requirements are then fit ($5C$) by the SQUAW routines.

The large number of 7 cluster neutral events and the many possible orderings of the gamma rays has led to applying several criteria before attempting a fit of an event. The total longitudinal and transverse lab momenta of the gamma rays have the requirements:

$$5.0 \text{ GeV/c} < \sum_{i=1}^{7} P_{\|_i} < 6.2 \text{ GeV/c} \tag{6.15}$$

and

$$\sum_{i=1}^{7} P_{\perp_i} < 200 \text{ MeV/c}. \tag{6.16}$$

All combinations of pairs of gamma rays are tried. An acceptable order occurs when one gamma ray's measured energy is within 50% of the expected transition energy and the other six gamma rays are paired to make three neutral mesons. The invariant mass of a pair is accepted when it is near the π^o mass (equation 6.12), η mass (equation 6.13), or η' mass:

$$750 \text{ MeV/c}^2 < M_{\eta'} < 1150 \text{ MeV/c}^2. \tag{6.17}$$

A combination is fit ($8C$) by SQUAW routines to one of the following reactions:

$$\bar{p}p \rightarrow {}^1\mathrm{P}_1 \rightarrow \gamma\eta_c \rightarrow \quad \gamma\pi^o\pi^o\pi^o \tag{6.18}$$

$$\gamma\pi^o\pi^o\eta \tag{6.19}$$

$$\gamma\pi^o\pi^o\eta' \tag{6.20}$$

$$\gamma\pi^o\eta\eta \tag{6.21}$$

$$\gamma\pi^o\eta\eta' \tag{6.22}$$

$$\gamma\pi^o\eta'\eta' \tag{6.23}$$

$$\gamma\eta\eta\eta \tag{6.24}$$

$$\gamma\eta\eta\eta' \tag{6.25}$$

$$\gamma\eta\eta'\eta' \tag{6.26}$$

$$\gamma\eta'\eta'\eta' \quad \rightarrow 7\gamma. \tag{6.27}$$

The η_c has been observed to decay [21] into $\pi^o\pi^o\eta$ and $\pi^o\pi^o\eta'$ (reactions 6.19 and 6.20); decays involving 1 or 3 π^o's are isospin violating (reactions 6.18 and 6.21 to 6.23). Furthermore, the hypotheses

$$\bar{p}p \rightarrow {}^1\mathrm{P}_1 \rightarrow \quad \gamma\eta' \rightarrow \gamma\pi^o\pi^o\pi^o \tag{6.28}$$

$$\gamma\eta' \rightarrow \gamma\pi^o\pi^o\eta \tag{6.29}$$

$$\gamma\eta \rightarrow \gamma\pi^o\pi^o\pi^o \quad \rightarrow 7\gamma, \tag{6.30}$$

are also tried when the transition gamma ray energy matches the appropriate hypothesis. All combinations are tried and the largest χ^2 fit probabilities for reactions 6.18 to 6.30 are kept for each event.

If any of the χ^2 fit probabilities is $> 1\%$ for an event, then two different sets of possible background reactions are tried using the same meson mass windows (equations 6.12, 6.13 and 6.17) for all possible combinations. The first set assumes 4 neutral mesons decaying to 8γ where one gamma ray is not detected. The possible $(5C)$ fits to the following hypotheses are performed:

$$\bar{p}p \rightarrow \quad \pi^o\pi^o\pi^o\pi^o \tag{6.31}$$

$$\pi^o\pi^o\pi^o\eta \tag{6.32}$$

$$\pi^o\pi^o\pi^o\eta' \tag{6.33}$$

$$\pi^o\pi^o\eta\eta \tag{6.34}$$

$$\pi^o\pi^o\eta\eta' \tag{6.35}$$

$$\pi^o\pi^o\eta'\eta' \tag{6.36}$$

$$\pi^o\eta\eta\eta \tag{6.37}$$

$$\pi^o\eta\eta\eta' \tag{6.38}$$

$$\pi^o\eta\eta'\eta' \tag{6.39}$$

$$\pi^o\eta'\eta'\eta' \tag{6.40}$$

$$\eta\eta\eta\eta \tag{6.41}$$

$$\eta\eta\eta\eta' \tag{6.42}$$

$$\eta\eta\eta'\eta'. \tag{6.43}$$

The second set of hypotheses is two neutral mesons plus ω, with ω decaying to $\pi^o\gamma$, resulting in 7γ. Combinations are fit $(8C)$ to the following possible background reactions:

$$\bar{p}p \rightarrow \quad \pi^o\pi^o\omega \tag{6.44}$$

$$\pi^o\eta\omega \tag{6.45}$$

$$\pi^o\eta'\omega \tag{6.46}$$

$$\eta\eta\omega \tag{6.47}$$

$$\eta\eta'\omega \tag{6.48}$$

$$\eta'\eta'\omega. \tag{6.49}$$

The largest χ^2 fit probabilities for all 7γ possible final states (reactions 6.18 to 6.30) and background reactions (reactions 6.31 to 6.49) are kept and compared. An event is assigned to the hypothesis with the largest χ^2 fit probability.

Chapter 7

Acceptances and Efficiencies

The central calorimeter performance is presented before the acceptances and efficiencies are discussed. The position and energy resolutions are necessary for a Monte Carlo simulation of the different reactions which is used to determine the acceptances. The Monte Carlo is also dependent upon the angular distributions of the reactions. The trigger and analysis efficiencies are measured by reactions and presented below. The final efficiencies are tabulated for the reactions. A discussion of uncertainties of the luminosity and beam energy measurements is given at the end of this chapter.

7.1 Central Calorimeter Performance

The central calorimeter performance can be described in terms of the two algorithms outlined in the last chapter: clusterization and the pile-up determination. The resolutions for the position (θ and ϕ) and energy of a cluster are important for identification of events by kinematical fitting. Resolving the photons from symmetric

π^o decays is another important goal of the clustering algorithm. The pile-up algorithm allows for central calorimeter signals from interactions other than the trigger interaction to be identified and discarded.

7.1.1 Clustering Algorithm

The position and energy resolution of isolated clusters is determined from analysis of $J/\psi \rightarrow e^+e^-$. The positions determined from the central calorimeter (θ_{CCAL} and ϕ_{CCAL}) are compared to angles determined by the charged tracking ($\theta_{Tracking}$ and $\phi_{Tracking}$). The difference between the two position determinations is shown in figure 7.1 for *good* charged tracks, i.e. those for which all of the charged tracking components of the detector contribute to the angle determinations. The charged tracking resolutions for both angles[1] are 2.5 mrad; when unfolded from the measured differences, result in average central calorimeter angular resolutions of $\overline{\sigma_\theta} = 5.7$ mrad and $\overline{\sigma_\phi} = 12.3$ mrad. These angular resolutions result in nearly the same position distance resolutions at the counters:

$$\sigma_\theta = \frac{\sigma_{X_R}}{r}, \tag{7.1}$$

$$\sigma_\phi = \frac{\sigma_{X_W}}{r \sin\theta}, \tag{7.2}$$

$$\tag{7.3}$$

where σ_{X_R} and σ_{X_W} are the ring and wedge position resolutions, respectively, at the lead glass blocks. Both σ_{X_R} and σ_{X_W} are < 1 cm.

[1]The average angular charged tracking resolutions are 7 and 4 mrad for $\overline{\sigma_\theta}$ and $\overline{\sigma_\phi}$, respectively.

a)

b)

Figure 7.1: The central calorimeter angular resolutions (a) θ and (b) ϕ. Unfolding the charged tracking resolutions (2.5 mrad for good charged tracks), the average central calorimeter angular resolutions are $\overline{\sigma_\theta} = 5.7$ mrad and $\overline{\sigma_\phi} = 12.3$ mrad.

a)

b)

Figure 7.2: The central calorimeter energy resolution for (a) the energy range 1.5 to 4.5 GeV (e^+e^- energy deposits from J/ψ decays) and (b) the crack correction, C_c, $\times E_{seen}$.

The e^+e^- energy deposits from J/ψ decays are between 1.5 and 4.5 GeV. Figure 7.2a shows the difference between the energy measured E_{CCAL}, including corrections for the loss due to the septa, and the predicted energy. The predicted energy is calculated from kinematics and the angles determined from the charge tracking. The contribution of the crack correction (equation 6.2),

$$C_c = \frac{E_{corr} - E_{seen}}{E_{seen}}, \tag{7.4}$$

to the energy resolution is shown in figure 7.2b where the average energy of the electrons is 2.5 GeV. A fit to figure 7.2b leads to the parameterization of the energy resolution:

$$\frac{\sigma_E}{E} = \frac{5.5\%}{\sqrt{E}} + 0.14C_c + \frac{0.005}{E}, \tag{7.5}$$

where both σ_E and E are in GeV; the last term is for pedestal fluctuations.

The response of the central calorimeter to electromagnetic showers induced by low energy gamma rays can be different from the higher energy deposits that have been used to tune the clustering algorithm. A possible non-linearity of energy scale of the counters has been a concern since the early beam energy tests, section 4.2.2. It appeared that for a 100 MeV particle, counters calibrated by particles of energy greater than 1 GeV would underestimate the energy by $\approx 10\%$. The Monte Carlo simulation of a single counter (section 4.1.1 and Appendix C) also shows this response. Figure 7.3 shows the ratio of the expected number of photoelectrons, based upon the assumption of a linear response between zero and a high energy calibration point, and the number of photoelectrons from the Monte Carlo simulation, see equation C.1 and discussion. The energy is underestimated by 10% for incident energies of 30, 50

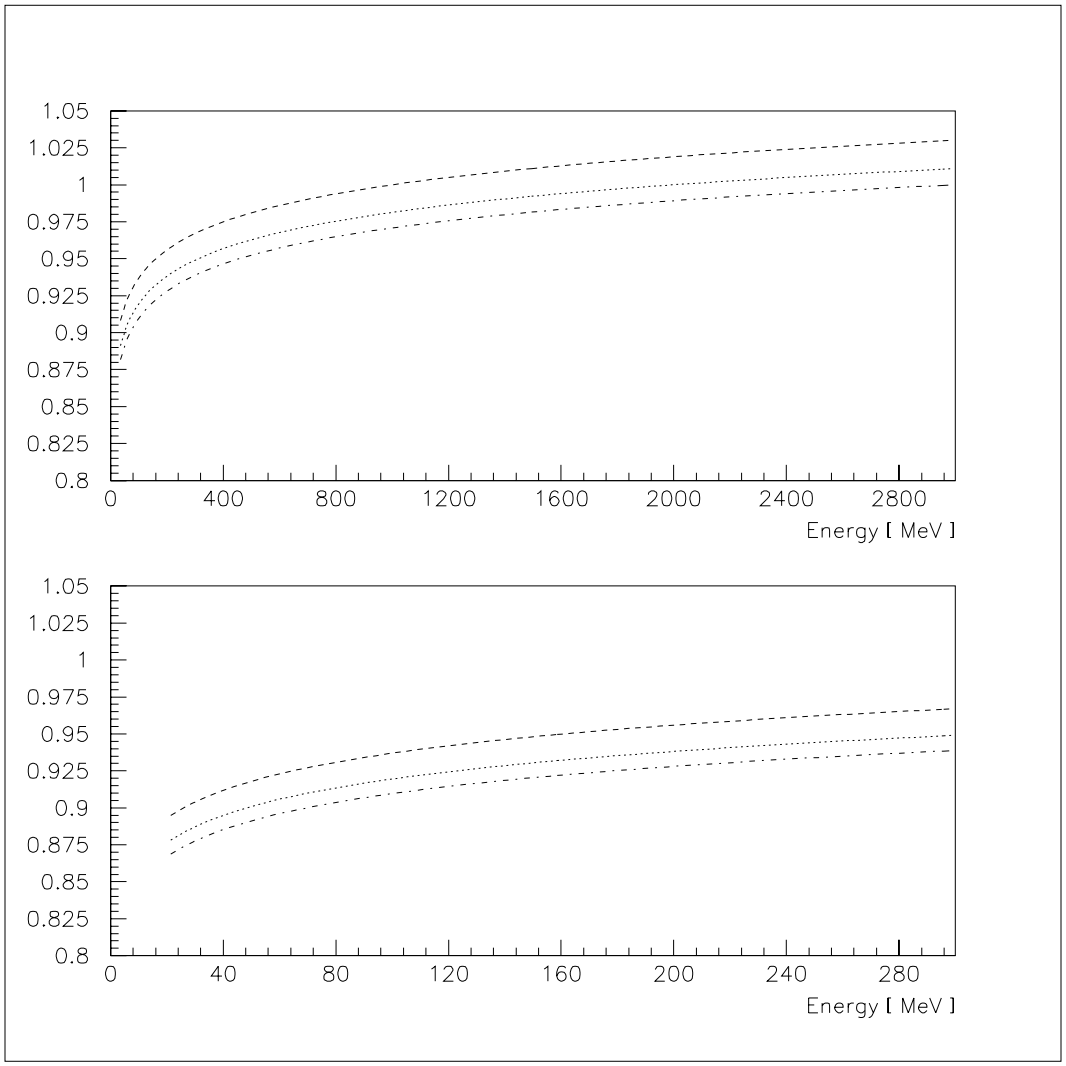

Figure 7.3: The Monte Carlo ratios of photoelectrons: linear relationship using a calibration at 1, 2, and 3 GeV (dashed, dotted, and dash-dotted, respectively) versus Monte Carlo output.

and 70 MeV when using a calibration point of 1, 2 and 3 GeV, respectively, according to this Monte Carlo prediction.

The response to low energy photons by the entire central calorimeter is better than initial indications cited above. The radiative decays of the χ_1 and χ_2 provide not only high energy e^+e^- deposits but also gamma rays of known energy as a function of polar angle, 300 MeV to 1.3 GeV. The measured energies of the photons show less

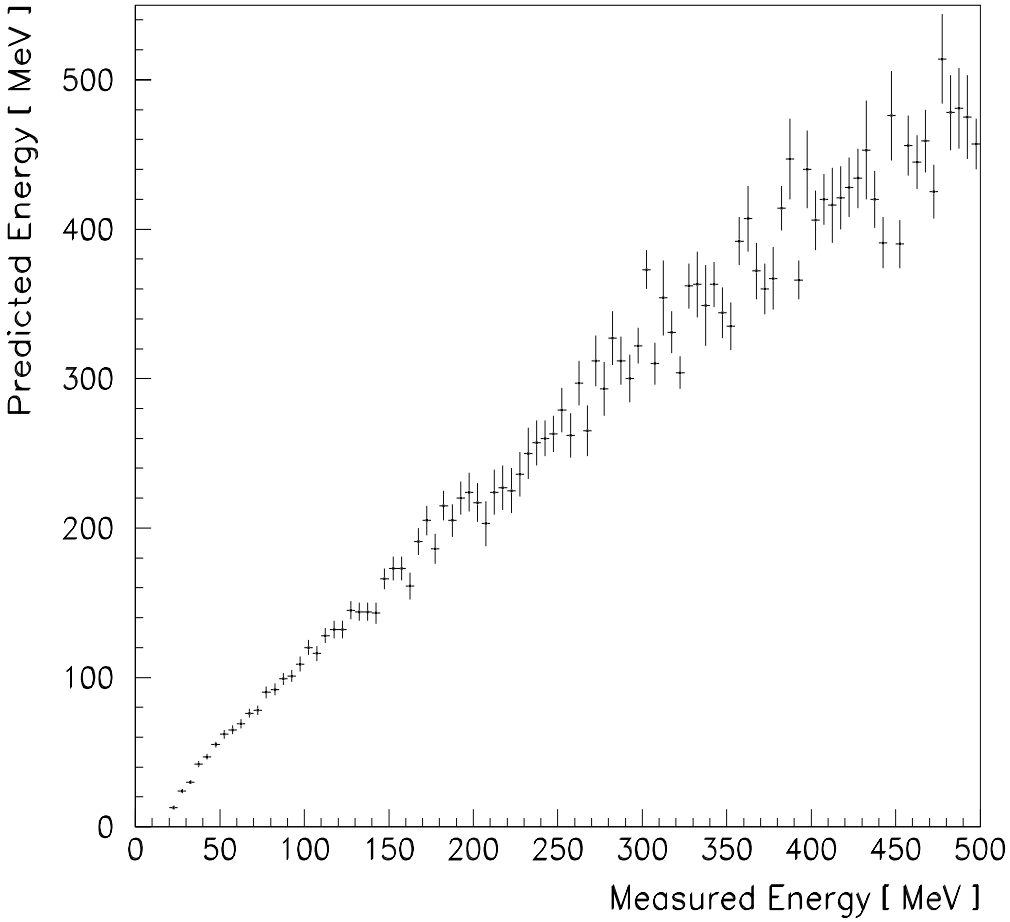

Figure 7.4: Predicted versus measured energy for the smallest energy photon from $\bar{p}p \rightarrow \pi^o\pi^o$.

than a 1% systematic shift from the predicted energies. For energy deposits less than 300 MeV, predicted energies from a $2C$ fit of $\bar{p}p \rightarrow \pi^o\pi^o$ events, where the energy of the lowest energy photon is not provided, are compared to the measured energies of the low energy photon. Figure 7.4 shows the predicted and measured energies for photon energies less than 500 MeV (perfect energy determination would result in a slope of 1.0); the average underestimation is 6%, which is comparable to the energy resolution in this energy range.

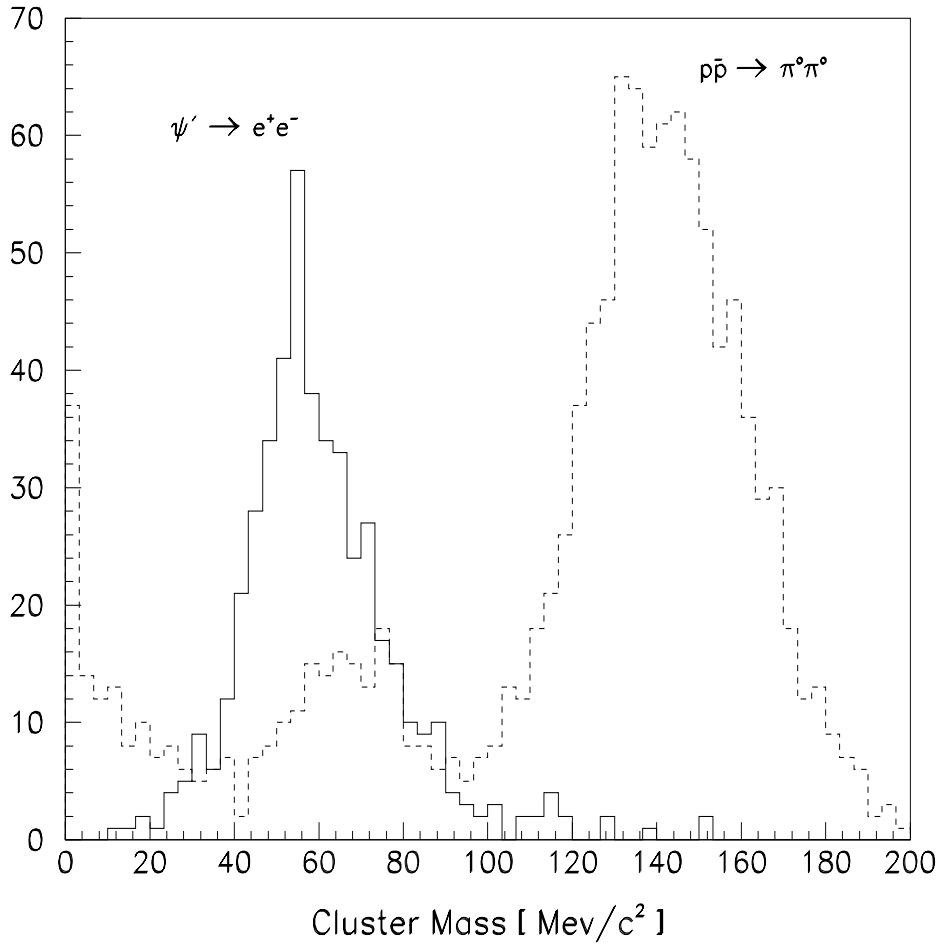

Figure 7.5: The cluster masses from exclusive e^+e^- and $\pi^o\pi^o$ events at the ψ' resonance.

The ability to separate symmetric π^o decays from isolated showers is dependent upon the cluster mass, equation 6.3. Plotted in figure 7.5 is the cluster masses for energy deposits from exclusive e^+e^- and $\pi^o\pi^o$ events from data at the ψ' resonance. The isolated showers from e^+e^- events show a peak centered near 50 MeV/c^2 with very few cluster masses $>$ 100 MeV/c^2. The $\pi^o\pi^o$ events show three peaks: the largest peak is centered at the π^o mass and corresponds to symmetric decays where the two gamma rays are close together and are contained within a 5×5 grid; the other

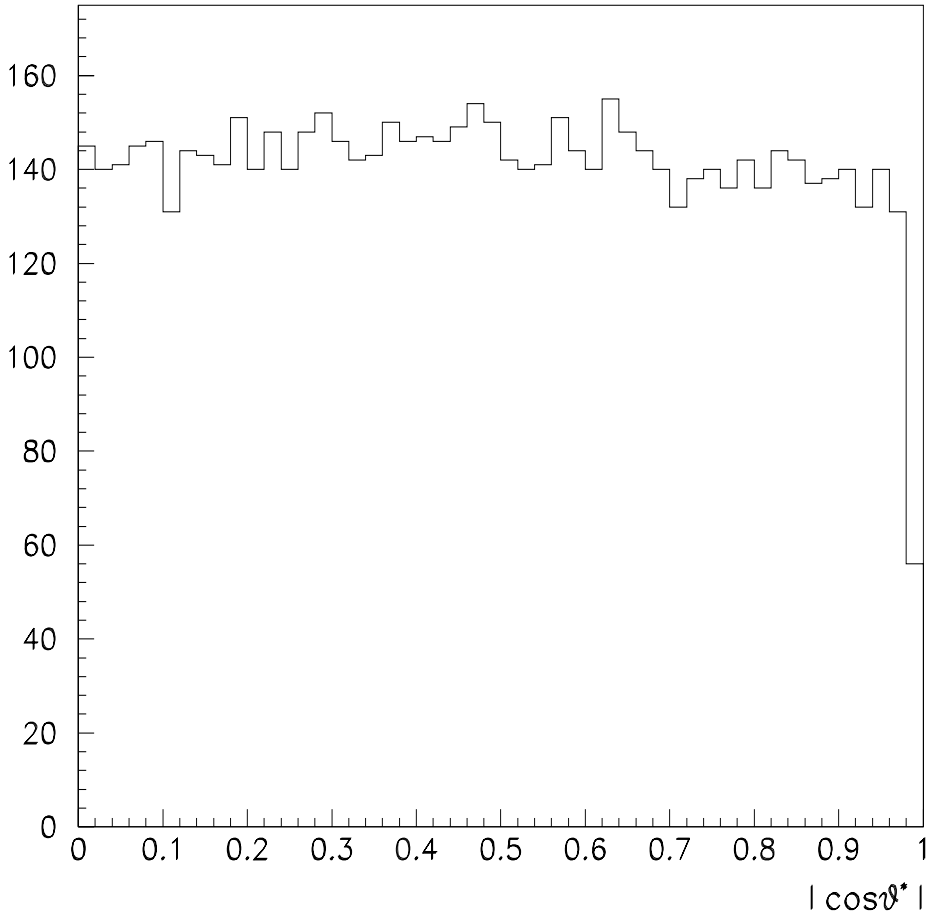

Figure 7.6: The angular distribution of photons in the π^o rest frame from $\bar{p}p \rightarrow \pi^o\pi^o$ events; θ^* is the angle between a photon's direction and the π^o boost direction. Data is for π^o's away from the central calorimeter edges.

peaks are isolated photon clusters from asymmetric decays with the lower cluster mass values coming from low energy gamma ray showers which produce signals in a small number of blocks (a single counter response results in 0 cluster mass). The ability to separate symmetric π^o decay photons and reconstruct π^o's, is shown in figure 7.6 for $15° < \theta_{\pi^o} < 50°$ in the lab, away from the central calorimeter edges. Plotted is the cosine of the angle, in the π^o rest frame, of the photon direction with respect to the

π^o boost direction, $\cos\theta^*$. The only loss in the angular distribution of photons from energetic π^o decays is from highly asymmetric π^o decays, $|\cos\theta^*| \approx 1$, where the low energy photon escapes detection.

7.1.2 Pile-up

The general philosophy of the pile-up determination was to try to avoid mis-labelling signals from the triggered interaction as out-time. In trying to guarantee the correct determination of signals from the trigger interaction, signals from other interactions (which should be declared as out-time) are occasionally declared as in-time or non-determined. A set of good $\bar{p}p \to \pi^o\pi^o$ events is used to investigate the performance of the pile-up determination. This sample is selected with the following criteria: three of the four photons must have energies greater than 200 MeV; there can be no more than four clusters with energy greater than 200 MeV in the recorded event; and a four cluster $6C$ fit must have a χ^2 fit probability greater than 10%.

For large energy clusters, the pile-up routines are essentially 100% efficient for determining a signal as in-time (seen for e^+e^- decays of the J/ψ and the radiative photon from the χ states). The $\pi^o\pi^o$ events allow study down to the energy threshold of the central calorimeter. Figure 7.7 shows the efficiency of determining an interaction signal as not being out-time (i.e., either in-time or non-determined). The pile-up algorithm appears to be nearly perfect for clusters above 120 MeV. Below this cluster

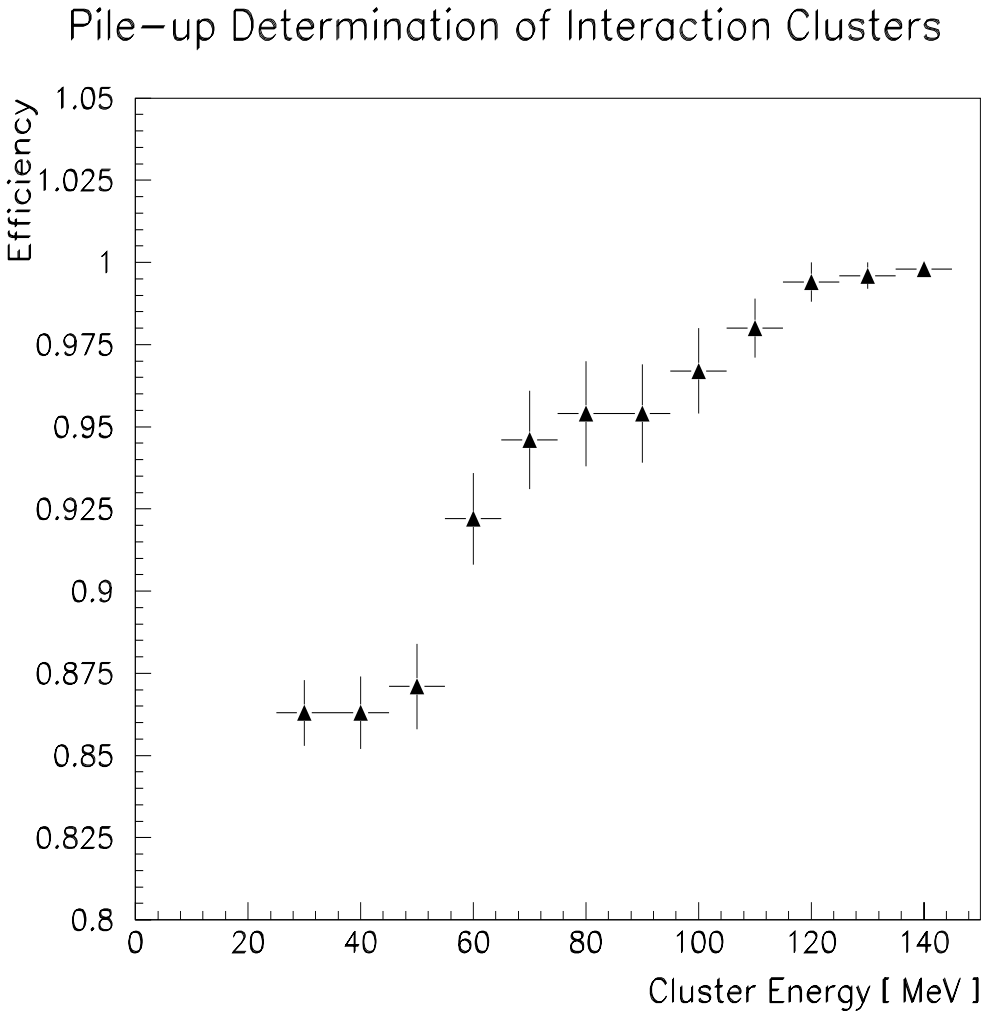

Figure 7.7: The efficiency of the determination of triggered interaction cluster from good $\bar{p}p \to \pi^o\pi^o$ events as a function of photon cluster energy.

energy, the efficiency of determining an interaction cluster as not being out-time decreases as the energy decreases; at the neutral data analysis threshold, 25 MeV, the efficiency is ≈ 0.85. The loss of events due to the inefficiency of out-time determination of interaction clusters is a function of the frequency that a final state particle will have a low energy cluster; for the $\pi^o\pi^o$ data sample studied, the loss is $\approx 1.5\%$.

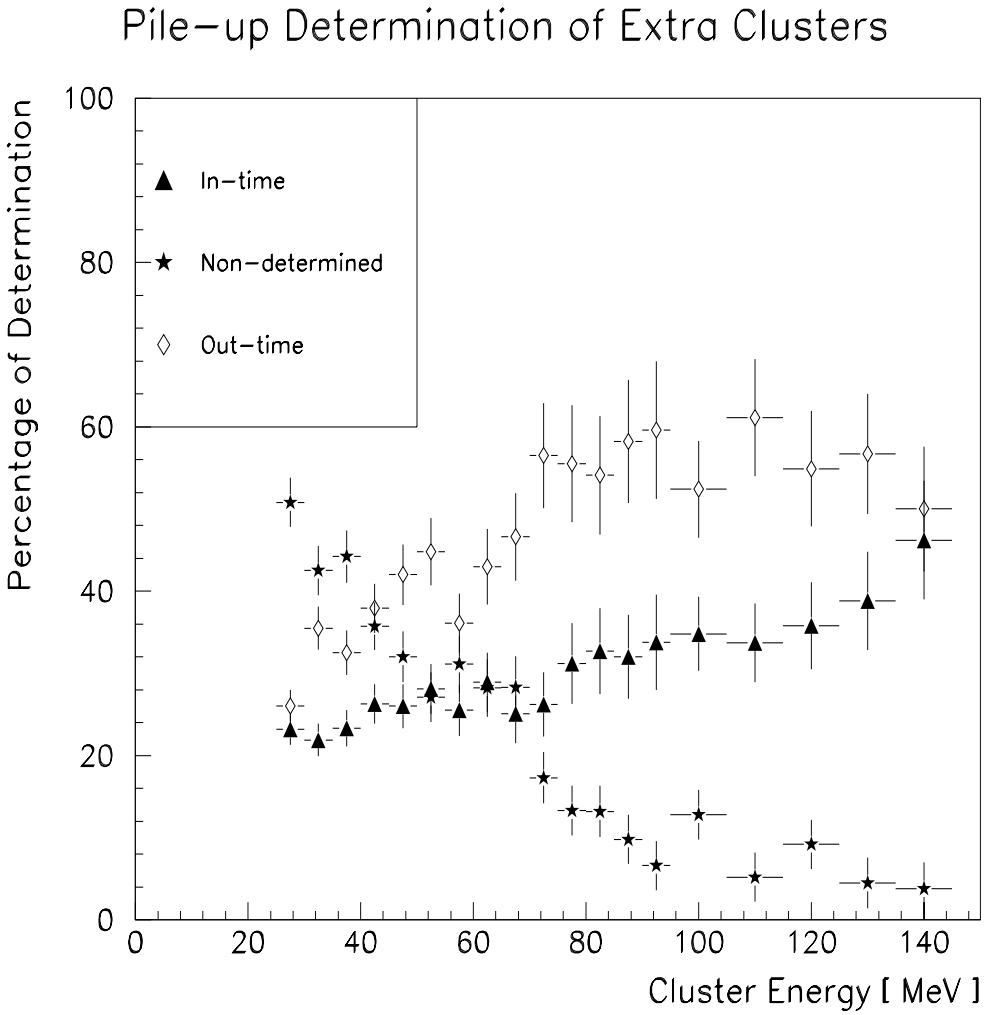

Figure 7.8: The determination percentages of non-triggered interaction signals from good $\bar{p}p \rightarrow \pi^o\pi^o$ events as a function of cluster energy: in-time, non-determined, and out-time are the triangles, stars and diamonds, respectively.

The determination of the extra clusters from the good $\pi^o\pi^o$ events is shown in figure 7.8. A fairly large percentage of the extra clusters are declared in-time or non-determined. Table 7.1 shows the number of extra clusters which are declared in-time or non-determined for events which have at least one extra cluster declared as such; table 7.2 shows the largest energy deposit for these extra clusters. The percentage of time that there are extra in-time or non-determined clusters with energies greater

Number of in-time or non-determined extra clusters	Percentage (%)
1	69.1
2	21.6
3	6.3
4	1.7
5	0.9
≥ 6	0.3

Table 7.1: The number of extra clusters which are declared as in-time or non-determined shown as a percentage for events which have at least one extra cluster declared as such.

Energy Range	%	Energy Range	%
25 to 30	12.9	70 to 80	5.2
30 35	10.6	80 90	4.0
35 40	10.5	90 100	3.8
40 45	9.0	100 125	6.1
45 50	7.2	125 150	5.1
50 60	10.3	150 175	3.7
60 70	8.2	175 200	3.6

Table 7.2: The largest energy for the extra clusters which are declared as in-time or non-determined shown as a percentage for events which have at least one extra cluster declared as such.

than 100 MeV in an event is a few percent (1 to 3% for the good $\pi^o\pi^o$ data). These events are probably when two $\bar{p}p$ interactions occur within the timing resolution of the trigger; there is a $\approx 1.7\%$ probability that there is a second interaction which results in a central calorimeter signal (rate of 350 kHz) in a 50 ns window.

7.2 Geometrical Acceptances

The acceptances are dependent upon the angular distribution of the final state. The angular distribution for each channel has been determined using the helicity formalism. A Monte Carlo employing the angular distributions of the reactions gives the geometrical acceptances.

7.2.1 Helicity Formalism

The angular distributions for the reactions have been determined using the helicity formalism [78]. The helicity formalism yields the transition amplitude in terms of the production and decay amplitudes for different helicities. In figure 7.9, diagrams of the $^1\mathrm{P}_1$ reactions, $J/\psi + X$ (with J/ψ decaying to e^+e^-) and $\eta_c + \gamma$, are shown with the helicity formalism parameters; this designation and the method used are described by Richman [79]. The angular distribution is proportional to the amplitude squared when the initial states are averaged over and the final states are

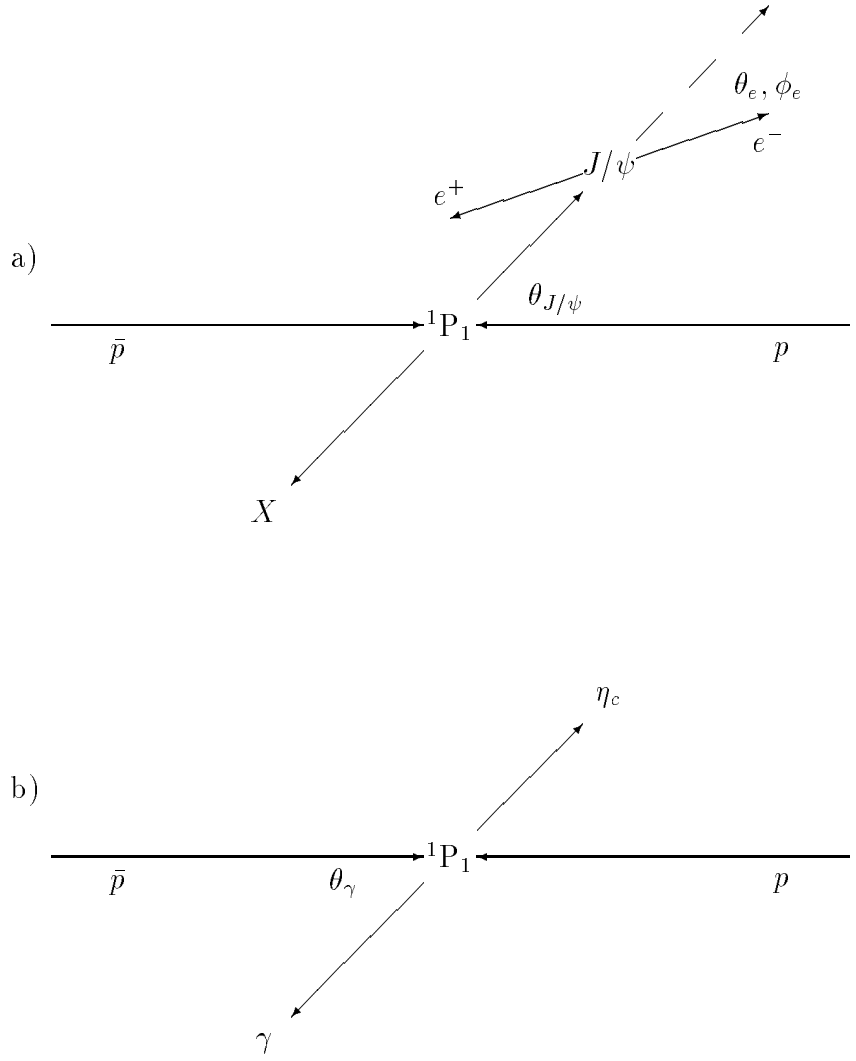

Figure 7.9: Diagrams displaying the $^1\mathrm{P}_1$ reactions and the helicity formalism angles in the center of mass ($\theta_{J/\psi}$ and θ_γ) and the J/ψ rest frame angles (θ_e and ϕ_e): (a) $^1\mathrm{P}_1 \rightarrow J/\psi X$ and J/ψ decays to e^+e^- and (b) $^1\mathrm{P}_1 \rightarrow \eta_c\gamma$. $\phi_{J/\psi}$ (ϕ_γ) is arbitrary; ϕ_e is 0 when the electron momentum vector is in the same plane as the momentum vectors of the J/ψ and $\bar{p}$.

summed over:

$$\frac{d\sigma}{d\Omega} \propto \sum_{initial} \sum_{final} \mid \mathcal{M} \mid^2 . \tag{7.6}$$

The production amplitude is B_{λ_1,λ_2} where λ_1 and λ_2 are the helicities of the proton and antiproton, respectively. For the charged (neutral) reactions, the decay amplitude is $A_{\mu,\sigma}$ where μ and σ are respectively the helicities of the J/ψ (η_c) and X (γ), where X can be $\pi\pi$ with[2] $J^P = 0^+$ or a π^o. The charged reactions have a further J/ψ decay amplitude of C_{λ_a,λ_b} where λ_a and λ_b are the electron and positron helicities, respectively. The corresponding amplitude for the η_c decay exists but does not affect the final angular distribution since the η_c (as well as π^o, η, and η') decays isotropically.

Each amplitude is normalized such that the sum of the squares of the individual amplitudes is 1 (e.g. $\sum_{\lambda_1,\lambda_2} B^2_{\lambda_1,\lambda_2}$ =1). Due to parity and charge conjugation conservation, there are some relations that the amplitudes must obey. The general parity result for an amplitude M for process $\alpha \rightarrow i + j$ is

$$M_{\lambda_i,\lambda_j} = \eta_i \eta_j \eta_\alpha (-1)^{s_i + s_j - s_\alpha} M_{-\lambda_i,-\lambda_j} \tag{7.7}$$

where η and s are the parity and spin of the particle. Parity conservation in the production causes

$$B_{\lambda_1,\lambda_2} = -B_{-\lambda_1,-\lambda_2}, \tag{7.8}$$

resulting in

$$B_{+,-} = -B_{-,+}, \tag{7.9}$$

[2] $J = 0$ is expected to be favored since the phase space is small.

$$B_{+,+} = -B_{-,-}, \tag{7.10}$$

where + and − represent helicities $+\frac{1}{2}$ and $-\frac{1}{2}$, respectively. Meanwhile, charge conjugation in the production only allows

$$B_{\lambda_1,\lambda_2} = B_{\lambda_2,\lambda_1} \tag{7.11}$$

resulting in

$$B_{+,-} = B_{-,+}, \tag{7.12}$$

$$B_{+,+} = B_{+,+}. \tag{7.13}$$

Conditions 7.9 and 7.12 are contradictory for non-zero values of B_1 and B_{-1} ($B_\nu = B_{\lambda_1,\lambda_2}$ and $\nu = \lambda_1 - \lambda_2$); therefore, $B_1 = B_{-1} = 0$ and $B_{+,+} = -B_{-,-}$. Parity conservation of the J/ψ decay and the small mass of the electron and positron result in $C_0 \to 0$ and $C_{+,-} = C_{-,+}$. A constraint due to parity on the decay amplitude occurs for the $J/\psi\pi\pi$ decay of the $^1\mathrm{P}_1$; it results in the condition $A_{0,0} = -A_{0,0} = 0$ and $A_{1,0} = -A_{-1,0}$. Since the photon helicity is ± 1, $A_{0,0} = 0$ for $\eta_c\gamma$ and $A_{1,0} = A_{-1,0}$. The parity constraint on the $^1\mathrm{P}_1$ decay amplitude to $J/\psi\pi^o$ results in two amplitudes A_0 and A_1 since $A_{\mu,\sigma} = A_{-\mu,-\sigma}$.

In terms of these amplitudes, the transition amplitude of an overall process is given by

$$\mathcal{M} \propto \sum_\mu B_{\lambda_1,\lambda_2} A_{\mu,\sigma} D^{J_{h_c}*}_{\lambda_1-\lambda_2,\mu}(\phi_{J/\psi}, \theta_{J/\psi}, -\phi_{J/\psi}) C_{\lambda_a,\lambda_b} D^{J_{J/\psi}*}_{\mu,\lambda_a-\lambda_b}(\phi_e, \theta_e, -\phi_e), \tag{7.14}$$

where the J/ψ subscript refers to the J/ψ direction with respect to the $\bar{p}$ direction in the center of mass frame and the e subscript refers to the electron direction in the

J/ψ rest frame with respect to the J/ψ boost direction. The $\eta_c\gamma$ overall amplitude does not have the last two factors and the gamma ray direction is substituted for the J/ψ direction. Applying the constraints mentioned above, working through the algebra and keeping track of all the terms, the angular distribution, or the form of the differential cross section, is determined. The simplest is the $\eta_c\gamma$ decay of the $^1\mathrm{P}_1$:

$$\frac{d\sigma}{d\Omega} \propto \sin^2\theta_\gamma. \tag{7.15}$$

The $^1\mathrm{P}_1$ decay to $J/\psi\pi\pi$ with $J/\psi \to e^+e^-$ angular distribution is

$$\frac{d\sigma}{d\Omega} \propto \sin^2\theta_{J/\psi}(1+\cos^2\theta_e) + \sin^2\theta_{J/\psi}\sin^2\theta_e\cos(2\phi_{J/\psi}-2\phi_e). \tag{7.16}$$

The $J/\psi\pi^o$ with $J/\psi \to e^+e^-$ angular distribution involves unknown $^1\mathrm{P}_1$ decay amplitudes:

$$\begin{aligned}\frac{d\sigma}{d\Omega} \propto \;& A_1^2 sin^2\theta_{J/\psi}(1+\cos^2\theta_e) - A_1^2\sin^2\theta_{J/\psi}\sin^2\theta_e\cos(2\phi_{J/\psi}-2\phi_e) \\ & +2A_0^2\cos^2\theta_{J/\psi}\sin^2\theta_e + A_1A_0\sin 2\theta_{J/\psi}\sin 2\theta_e\cos(\phi_{J/\psi}-\phi_e).\end{aligned} \tag{7.17}$$

7.2.2 Monte Carlo

An event Monte Carlo has been developed which generates events with the appropriate angular distribution for a reaction. The energies and positions of the final particles are also generated to simulate the detector's resolutions. The appropriate geometrical and energy threshold cuts that are applied during the analysis are made and an acceptance is determined. The inclusive J/ψ and 3γ final state acceptance α_{geom} are presented in table 7.3. The range of acceptances for the $J/\psi\pi^o$ final state

Final State	Acceptance
$J/\psi\pi^+\pi^-$	0.239
$J/\psi\pi^o\pi^o$	0.192
$J/\psi\pi^o$	0.32 to 0.54
$\eta_c\gamma \rightarrow 3\gamma$	0.368

Table 7.3: The geometrical acceptances of the inclusive J/ψ and 3γ final states. The range of values for the $J/\psi\pi^o$ final state is for a range of the $^1P_1$ decay helicity amplitudes.

is for a range of $^1P_1$ decay helicity amplitudes. The 7γ final state acceptances are in table 7.10.

7.3 Trigger Efficiencies

Both the hardware and software trigger requirements contribute to the trigger efficiencies. Each of the trigger bits that have a requirement for a trigger contributes to the total trigger efficiency. Efficiencies resulting from requiring a bit to be ON or OFF are discussed below. Common to both the charged and neutral hardware triggers is the coplanarity of large energy deposits in the central calorimeter bit, PBG. From the J/ψ and ψ' data sets, ϵ_{PBG} is essentially 1.0.

7.3.1 Charged Trigger

The main contribution to the inefficiency of the charged trigger is due to space between elements of the H1 and H2 hodoscopes. Charged particles which do not hit an element of the H1 or H2 hodoscopes do not form a charge track in the trigger.

Charged tracks (with signals in both H1 and H2) which are not the charged particles which formed the trigger, have been plotted as a function of ϕ in figure 7.10 (all H2 elements are superimposed onto one element). The efficiency of requiring the hadron hardware trigger bit to be ON is given by the deficit of hits at the edges of the H2 element,

$$\epsilon_h = 0.961 \pm 0.005. \tag{7.18}$$

The efficiency of requiring the two hadron hardware trigger bit to be ON for charged non-two body final states is

$$\epsilon_{hh} = \epsilon_h^2 = 0.924 \pm 0.01. \tag{7.19}$$

Extra hit elements of the H1 and H2 hodoscopes also contribute to inefficiencies of the charged trigger. Clean samples of J/ψ and inclusive J/ψ from the χ_2 resonance data are used to see how often the trigger bits (H1$>$ 2, H2$>$ 2) are ON indicating an extra hodoscope element has been hit. Events are selected based upon satisfying the two electron trigger (see logic statement 5.7); the pattern units associated with the MLUs are checked for the status of each of the bits. The $\approx$ 3600 J/ψ ($\approx$ 1400 χ_2) events are split into data sets of $\approx$ 900 (350) events to study rate effects. Figures 7.11 and 7.12 show the efficiency of vetoing on the H1$>$ 2 and H2$>$ 2 bits, respectively, as a function of each hodoscope's rate. A fit gives the efficiency resulting from vetoing on the H1$>$ 2 bit status in the pattern unit as

$$\epsilon_{H1} = (1.020 \pm 0.009) - (0.097 \pm 0.009) \times (\text{H1 OR rate in MHz}); \tag{7.20}$$

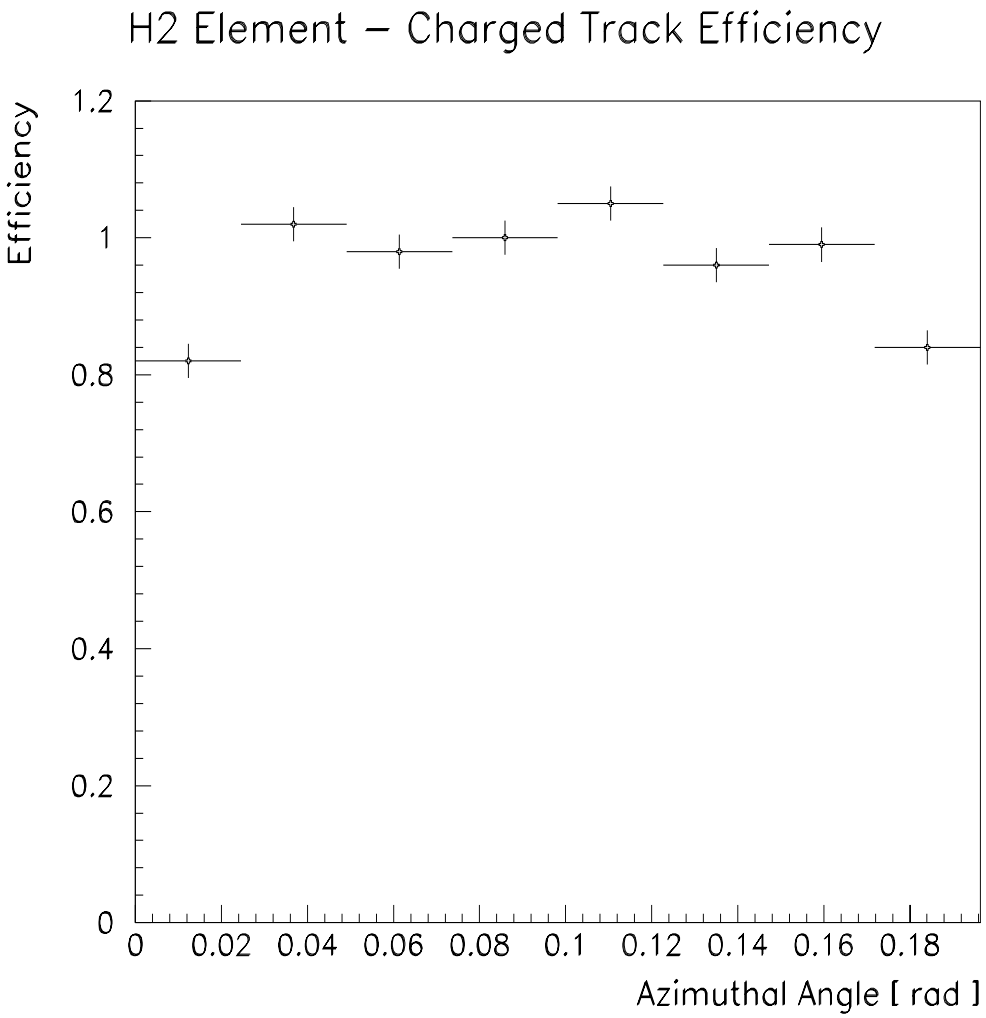

Figure 7.10: The efficiency of the hadron hardware trigger bit is seen by the decrease of the number of tracks at the edges of an H2 element (all H2 elements are superimposed onto one H2 element) as compared to the number that cross the center of an H2 element.

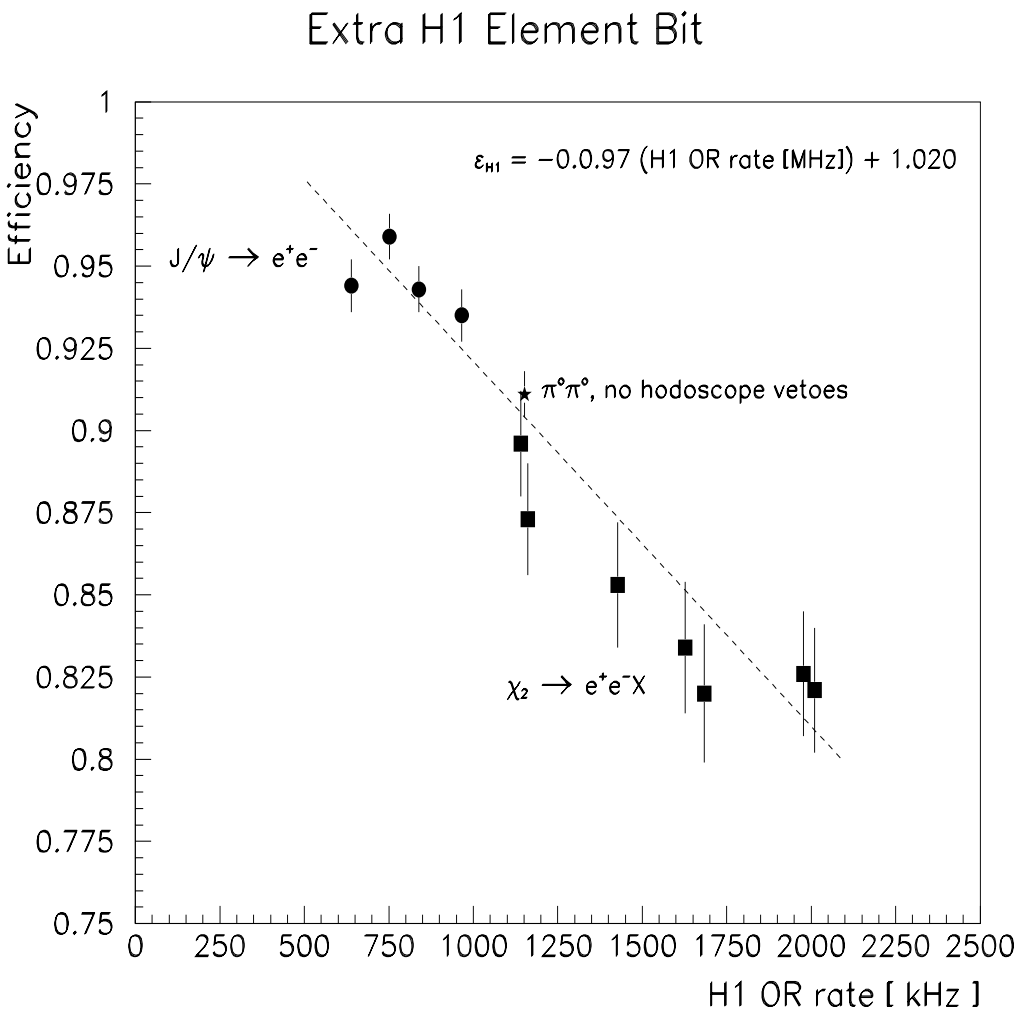

Figure 7.11: The efficiency resulting from vetoing on the pattern unit information as a function of the H1 OR rate for extra H1 element bits: charged events – vetoing on the H1$>$ 2 information for events collected with the two electron trigger at the J/ψ (circles) and χ_2 (squares) resonances; neutral events – H1 OR information for $\pi^o\pi^o$ events (star) collected when no hodoscopes are used as vetoes.

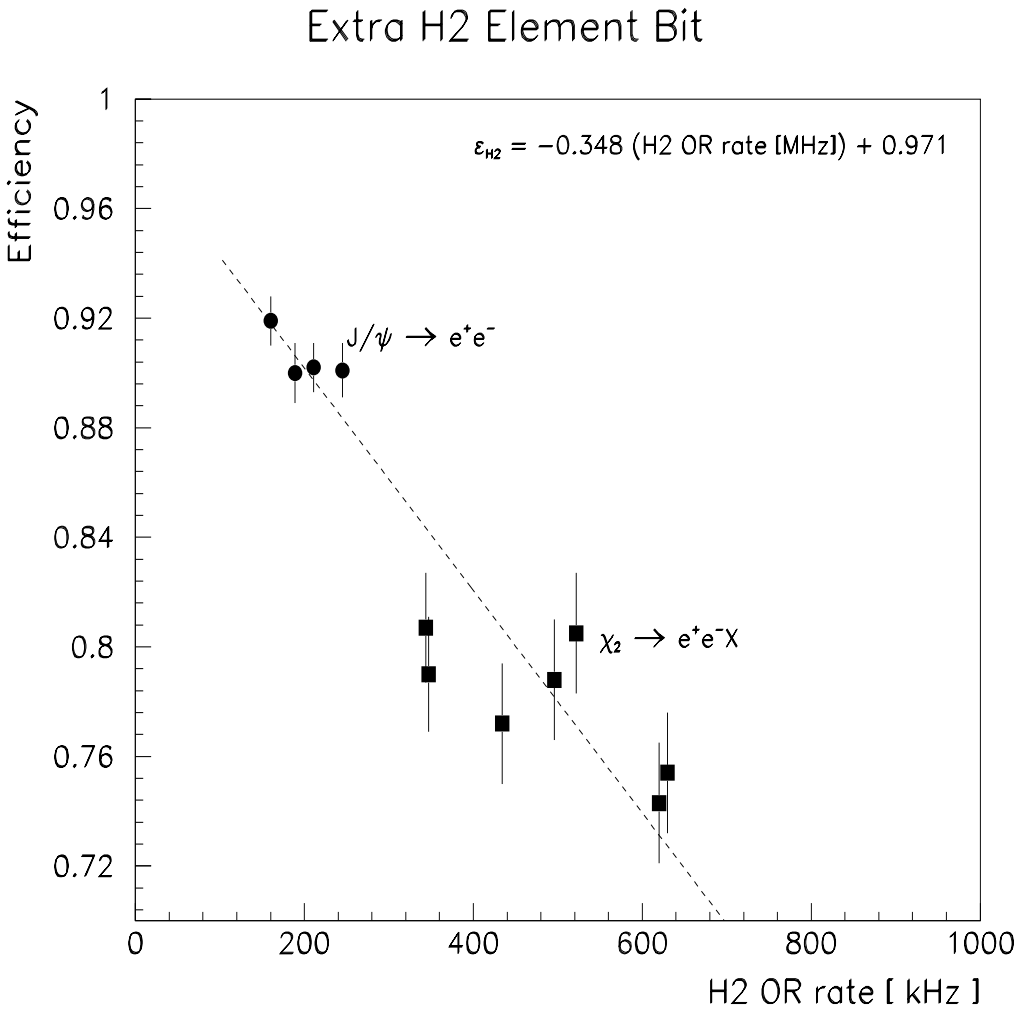

Figure 7.12: The efficiency resulting from vetoing on the pattern unit information as a function of the H2 OR rate for extra H1 element bits: vetoing on the H2$>$ 2 information for events collected with the two electron trigger at the J/ψ (circles) and χ_2 (squares) resonances.

Stack	H1 OR rate			H2 OR rate		
Number	min	max	ave	min	max	ave
1	787	2188	1439	229	656	436
2	901	1926	1421	265	595	429
3	582	1726	1182	168	528	353
4	848	1631	1264	249	500	380
5	1145	2257	1747	336	707	529
6	999	2296	1617	289	708	486
7	1078	2324	1644	315	685	494
8	1048	2381	1712	302	742	516
9	1167	2300	1765	397	691	532
10	1412	2292	1782	413	714	536
11	1388	2004	1693	414	609	507
12	976	1799	1477	292	540	440
13	1350	2212	1776	396	685	535
14	1260	2022	1647	366	616	491
15	1448	2211	1847	424	683	557
16	1833	2364	2031	555	702	616

Table 7.4: The H1 and H2 rates for each stack. All rates are in kHz.

for H2$>$ 2 the fit is

$$\epsilon_{H2} = (0.971 \pm 0.009) - (0.348 \pm 0.030) \times (\text{H2 OR rate in MHz}). \qquad (7.21)$$

One datum point of figure 7.11 is from the efficiency resulting from vetoing on the H1 OR bit's status in the pattern unit for a special neutral trigger (see next section); the results are in agreement. Table 7.4 shows the minimum, maximum and average rates for each $^1P_1$ stack for the H1 OR and H2 OR.

The efficiency resulting from vetoing on the extra H1 bit due to information from the pattern unit needs to be corrected. The pattern unit's gate width is 30 ns while the strobe to the trigger deciding MLUs is 5 ns wide. Therefore, it is possible that a bit is OFF when the MLU makes a decision, but the pattern unit has the bit ON; this means that ϵ_{H1} underestimates the efficiency resulting from vetoing on the

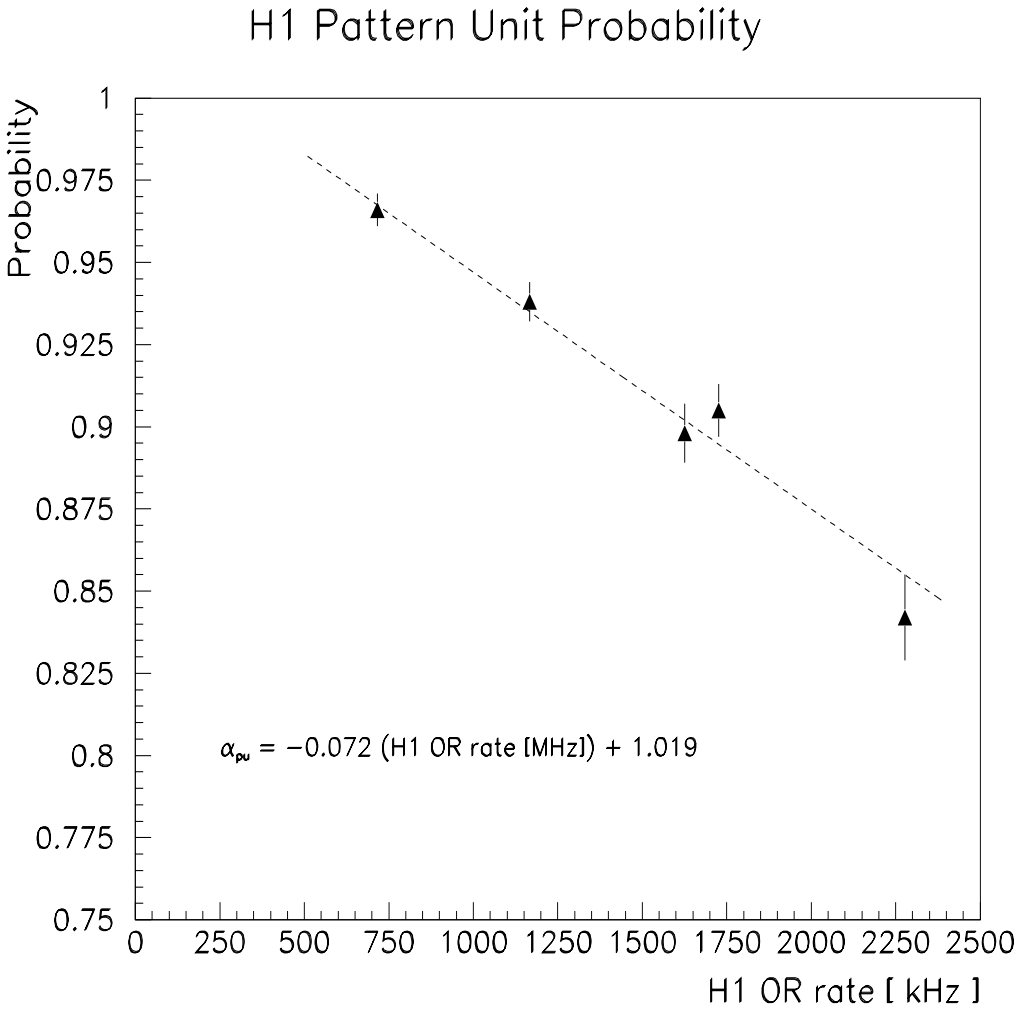

Figure 7.13: The probability that a pattern unit correctly shows the H1 OR bit OFF for $\bar{p}p \to \pi^o\pi^o$ as a function of the H1 OR rate.

extra H1 element bits in the trigger. A correction is made using the probability that the pattern unit correctly shows the bit being OFF when the trigger vetoes on the bit. The probability of the correct designation of the H1 OR bit in the pattern unit for $\bar{p}p \to \pi^o\pi^o$ is shown as a function of rate in figure 7.13. A fit gives the probability as

$$\alpha_{pu} = (1.019 \pm 0.009) - (0.072 \pm 0.009) \times (\text{H1 OR rate in MHz}). \qquad (7.22)$$

Final State	ϵ_{COPL}
$J/\psi\pi^+\pi^-$	0.999
$J/\psi\pi^o\pi^o$	0.999
$J/\psi\pi^o$	0.929

Table 7.5: The coplanarity bit efficiencies for different reactions as determined by an event generating Monte Carlo.

The corrected trigger efficiency resulting from vetoing on an extra H1 element bit is $\frac{\epsilon_{H1}}{\alpha_{pu}}$. All other trigger bits investigated in this chapter (H2> 2, FCH OR, and FCAL OR) have negligible corrections; less than 0.2% of the events have the pattern unit ON for a bit when the trigger required the bit OFF.

The efficiency of the H2=2 bit being ON is the same as the efficiency resulting from vetoing on the H2> 2 bit. The efficiencies resulting from vetoing on the hodoscope bits in the two electron trigger, H1> 4 and H2> 4 bits, are related to the cubes of the inefficiencies[3] of the H1> 2 and H2> 2 bits:

$$\epsilon'_{H1} = 1 - (1 - \tfrac{\epsilon_{H1}}{\alpha_{pu}})^3, \tag{7.23}$$

$$\epsilon'_{H2} = 1 - (1 - \epsilon_{H2})^3. \tag{7.24}$$

The efficiency of the coplanarity requirement is determined from the event generating Monte Carlo discussed in the last section and the values are shown in table 7.5.

The hardware trigger identification of electrons and positrons is dependent upon the polar angle of the particle. The J/ψ data set is used to study the effect of the Čerenkov septum at $\theta_{lab} = 38°$. At the J/ψ, when the electron enters the septum

[3]H1> 4 and H2> 4 require three *separate* extra hodoscope elements to be hit; therefore, ϵ'_{H1} and ϵ'_{H2} are underestimated, however, any corrections would be small since $\epsilon'_{H2} = 0.98$ when $\epsilon_{H2} = 0.75$.

region the positron does also, since the septum for J/ψ data corresponds to $\cos\theta_{cm} = 0$; however for a $^1P_1$ event, the Monte Carlo never has both the electron and positron in the septum region. Data taking at the J/ψ included a provision for both particles near the septum with a zero electron trigger along with the one and two electron triggers described in section 5.3. A comparison of the e^+e^- events acquired by the zero and two electron triggers with all other inefficiencies removed results in a determination of the two electron bit efficiency to be

$$\epsilon_{ee} = 0.88 \pm 0.01. \tag{7.25}$$

The one electron bit efficiency, ϵ_e, is found to be ≈ 1.0.

Since the charged trigger events are passed by the ACP slave node program, there is no software trigger inefficiency. The total trigger efficiency for the charged events can be written as

$$\begin{aligned}\epsilon_{trig} = \quad & \epsilon_{PBG} \times \epsilon_{hh} \times [\epsilon_{ee} \times \epsilon'_{H1} \times \epsilon'_{H2} + \\ & (1 - \epsilon_{ee} \times \epsilon'_{H1} \times \epsilon'_{H2}) \times \epsilon_e \times \tfrac{\epsilon_{H1}}{\alpha_{pu}} \times \epsilon_{H2} \times \epsilon_{COPL}]\end{aligned} \tag{7.26}$$

when there are only two charged particles in the final state. When there are four charged particles in the final state, the second term in the square brackets is dropped and the H1 and H2 efficiencies of the first term change from ϵ'_{H1} and ϵ'_{H2} to $\frac{\epsilon_{H1}}{\alpha_{pu}}$ and ϵ_{H2}, respectively. The total trigger efficiences are

$$\epsilon_{trig}(J/\psi\pi^o) = \epsilon_{trig}(J/\psi\pi^o\pi^o) = 0.89, \tag{7.27}$$

$$\epsilon_{trig}(J/\psi\pi^+\pi^-) = 0.37, \tag{7.28}$$

when average values for the H1 OR and H2 OR rates from the $^1P_1$ data taking are used (see table 7.4). The $\epsilon_{trig}(J/\psi\pi^+\pi^-)$ takes into account the requirement that the pions and e^+e^- are not in contiguous H2 hodoscope elements. During a stack, the trigger efficiency changes by less than 1% for the $J/\psi\pi^o$ and $J/\psi\pi^o\pi^o$ final states; the range for the $J/\psi\pi^+\pi^-$ trigger efficiency is 0.32 to 0.44 and the luminosity averaged values for the stacks range from 0.35 to 0.40.

7.3.2 Neutral Trigger

The inefficiencies of the neutral hardware trigger result from the vetoes on the detector component bits. The H1 efficiency found for the charged trigger (the extra hodoscope element hit) is the same for the neutral trigger. To confirm this, one data run has been taken with no vetoes of the H1 OR bit or the FCH OR bit required for the neutral trigger. The frequency of the H1 OR bit being ON in the pattern unit for reconstructed $\bar{p}p \to \pi^o\pi^o$ events is 14.5%. Each π^o has the probability of Dalitz decay of 1.2% and each photon has an $\approx 1.0\%$ probability of converting in the beam pipe before the H1 hodoscope, $\alpha_{convert}$; the accidental H1 rate is corrected to be 8.8%. This datum point is included in figure 7.11.

The forward hodoscope bit (FCH OR) is ON for 3.5% of the $\pi^o\pi^o$ events collected without the hodoscope vetoes[4]. The rate dependence of the FCH OR bit has also been studied using the same charged event data sets as have been used above for

[4]These events are independent of the events for which the H1 OR bit is ON.

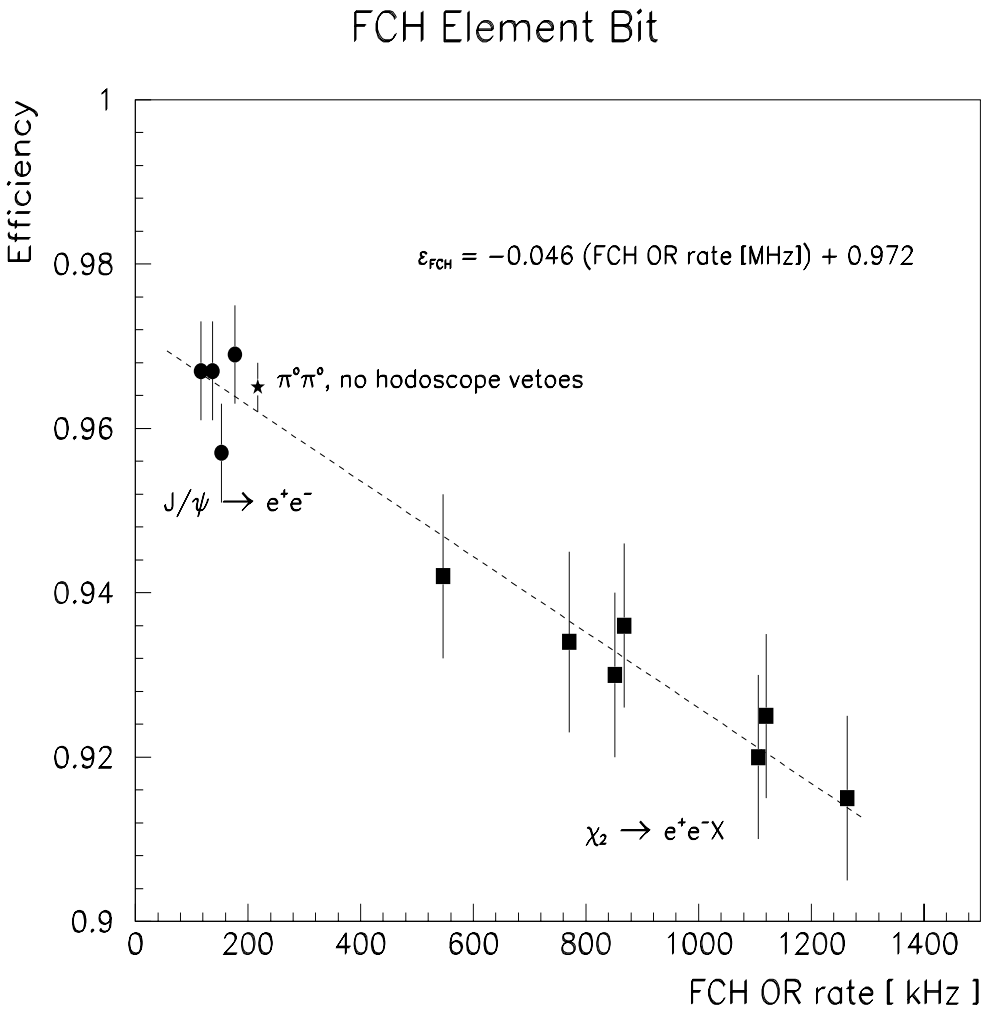

Figure 7.14: The efficiency resulting from vetoing on the FCH OR bit as a function of the FCH OR rate: charged events – events collected with the two electron trigger at the J/ψ (circles) and χ_2 (squares) resonances; neutral events – $\pi^o\pi^o$ events (star) collected when no hodoscopes are used as vetoes.

Stack	FCH OR rate			FCAL OR rate		
Number	min	max	ave	min	max	ave
1	455	1026	754			
2	612	1136	880			
3	467	1221	885	510	1190	900
4	561	964	764	710	1120	960
5	239	498	380	890	1420	1180
6	198	489	333	621	1141	903
7	223	472	343	734	1200	1003
8	209	510	355	806	1327	1089
9	259	489	382	532	873	739
10	288	491	372	577	915	723
11	301	421	356	605	796	693
12	217	376	315	431	723	612
13	275	473	372	539	877	710
14	254	425	340	485	774	636
15	293	472	386	563	854	724
16	397	486	432	749	874	801

Table 7.6: The forward hodoscope and calorimeter rates for each stack. All rates are in kHz. Vetoing on the FCAL OR bit was not done until the 3^{rd} stack and the FCAL OR rate is estimated before the 6^{th} stack. The forward hodoscope (calorimeter) was improved after the 4^{th} (8^{th}) stack reducing the rate.

studying the other hodoscopes, excluding χ_2 events where the gamma ray goes into the forward calorimeter. Figure 7.14 shows the rate dependence and the resulting fit for the efficiency resulting from vetoing on the FCH OR bit is

$$\epsilon_{FCH} = (0.973 \pm 0.003) - (0.046 \pm 0.005) \times (\text{FCH OR rate in MHz}). \qquad (7.29)$$

The minimum, maximum and average FCH OR rates for each $^1P_1$ stack is shown in table 7.6.

The forward calorimeter veto of 7γ final state events has a rate dependence. The efficiency resulting from vetoing on the FCAL OR bit for events collected with the two electron trigger at the J/ψ resonance and good $\pi^o\pi^o$ events (section 7.1.2)

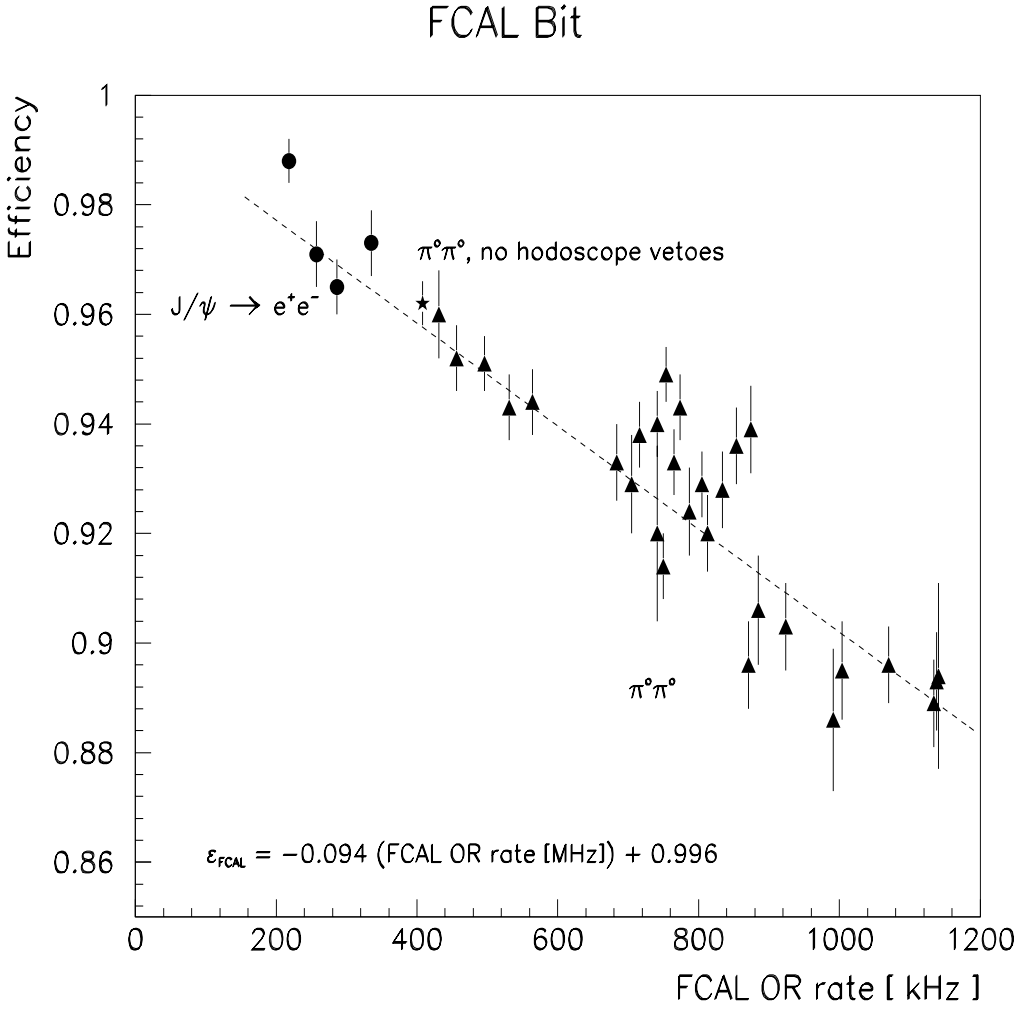

Figure 7.15: The efficiency resulting from vetoing on the FCAL OR bit as a function of the FCAL OR rate: charged events – events collected with the two electron trigger at the J/ψ (circles) resonance; neutral events – good $\pi^o\pi^o$ events (triangles).

Stack	$\epsilon_{ETOT-hard}$	$\epsilon_{ETOT-soft}$	Stack	$\epsilon_{ETOT-hard}$	$\epsilon_{ETOT-soft}$
1	1.00	1.00	9	0.98	0.98
2	1.00	1.00	10	0.97	0.99
3	1.00	1.00	11	0.97	0.98
4	1.00	1.00	12	0.96	0.98
5	1.00	0.98	13	0.96	0.98
6	0.99	0.98	14	0.96	0.97
7	0.99	0.99	15	0.95	0.97
8	0.98	0.99	16	0.96	0.96

Table 7.7: The efficiency of the hardware and software ETOT trigger bits for each stack.

is shown in figure 7.15. The rate dependent efficiency resulting from vetoing on the FCAL OR bit is

$$\epsilon_{FCAL} = (0.996 \pm 0.006) - (0.094 \pm 0.007) \times (\text{FCAL OR rate in MHz}). \qquad (7.30)$$

The minimum, maximum and average FCAL OR rates[5] for each $^1P_1$ stack is shown in table 7.6.

The collection of 7γ final states relies upon triggering the hardware ETOT bit while the FCAL OR bit is OFF. The efficiency of the ETOT bit has been studied with the selection of good $\pi^o\pi^o$ events. A stack dependence has been found and the efficiency of the hardware ETOT and the efficiencies are presented in table 7.7. The decrease of efficiency of the hardware ETOT trigger bit over time is due to the slow decrease of the central calorimeter counters' gains.

The ACP slave node program affects the 3γ and 7γ events differently. The 3γ final state should satisfy the software trigger's > 2 GeV invariant mass bit. The

[5]The FCAL OR bit was not available in the trigger until the 3^{rd} stack and the FCAL OR rate is estimated before the 6^{th} stack.

software efficiency for the 3γ state is estimated to be

$$\epsilon_{INV} = 0.995 \pm 0.002; \tag{7.31}$$

the inefficiency is due to the simplistic clustering and energy corrections performed in the ACP slave node program as well as the gain constants that are loaded. The 90% total energy software trigger is influenced more by the gain constants that are loaded into the ACP slave node program. The gain constants have been updated every few stacks; however near the end of the 1991 data run, the gain constants remained unchanged. The efficiency of the software ETOT trigger bit has also been studied for each stack and the values are presented in table 7.7 after removal of the hardware ETOT bit inefficiency.

The trigger efficiency for the 3γ final state is

$$\epsilon_{trig}(3\gamma) = \epsilon_{PBG} \times \frac{\epsilon_{H1}}{\alpha_{pu}} \times \epsilon_{FCH} \times \epsilon_{INV} \times (1 - \alpha_{convert})^3 \tag{7.32}$$

where a factor $\alpha_{convert}$ is included for each photon. When average rates are used, $\epsilon_{trig}(3\gamma) = 0.88$. The range of efficiencies goes from 0.85 to 0.91 and the luminosity weighted averages for a stack range from 0.87 to 0.89.

The 7γ final state trigger efficiency is given by

$$\epsilon_{trig}(7\gamma) = \frac{\epsilon_{H1}}{\alpha_{pu}} \times \epsilon_{FCAL} \times \epsilon_{ETOT-hard} \times \epsilon_{ETOT-soft} \times (1 - \alpha_{convert})^7, \tag{7.33}$$

where the individual run efficiencies are rate and stack dependent. The trigger efficiency for the 7γ final states using the average rates is 0.78. The range of efficiencies goes from 0.72 to 0.87 and the luminosity weighted averages for a stack range from 0.74 to 0.82.

7.4 Analysis Efficiencies

A common cut to both the charged and neutral analyses is the cluster mass cut. Figure 7.5 shows that the efficiency of requiring $M_{cl} < 100$ MeV/c^2 for a large energy deposit is

$$\epsilon_{cl} = 0.961 \pm 0.009 \tag{7.34}$$

for $\psi' \to e^+e^-$ events. The cluster mass cut on 7γ final states mainly removes events where two of the gamma rays are close to one another; the energies of the neutral mesons are small enough that most of the two photon decays result in isolated clusters.

7.4.1 Charged Analysis

The major charged analysis cut involves the product of $EQW_1 \times EQW_2$ (see section 6.5). The cut has an efficiency of

$$\epsilon_{EQW} = 0.906 \pm 0.011 \tag{7.35}$$

from study of J/ψ and ψ' data. The electron quality weight cut is redundant with the cluster mass cut; the latter is not used for the electron clusters. The unassociated cluster cut efficiency is estimated to be

$$\epsilon_{ucc} = 0.97 \pm 0.01; \tag{7.36}$$

unassociated in-time and non-determined clusters above 100 MeV are from two nearly simultaneous $\bar{p}p$ interactions. This results in the inclusive J/ψ selection efficiency of

$$\epsilon_{inc} = \epsilon_{EQW} \times \epsilon_{ucc} = 0.88 \pm 0.014. \tag{7.37}$$

Final State	ϵ_{an}
$J/\psi\pi^o$	0.83 ± 0.02
$J/\psi\pi^o\pi^o$	0.73 ± 0.02
$J/\psi\pi^+\pi^-$	0.75 ± 0.03

Table 7.8: The final charged analysis efficiencies. The contiguous H2 cut for the charged pions is not included; it is accounted for in the trigger efficiency.

The efficiency of the pile-up determination for the gamma ray final states has been simulated by the event Monte Carlo; the efficiency is $\epsilon_{pile} = 0.987 \pm 0.005$ (0.941) for the $J/\psi\pi^o$ ($J/\psi\pi^o\pi^o$) final state. The charged pions are only subjected to the pile-up cut if the pion results in any kind of signal in the central calorimeter[6]; the efficiency is estimated as $\epsilon_{pile} = 0.95 \pm 0.02$ for the $J/\psi\pi^+\pi^-$ final state. Each gamma ray is subjected to the cluster mass cut and contributes to the analysis efficiency. The efficiency of requiring two good charged tracks for the charged pions is estimated to be $\epsilon_{tracks} = 0.90 \pm 0.02$. The efficiency of the H2 contiguous cut for the charged pions is included in the determination of the trigger efficiency.

The final charged analysis efficiency is given by

$$\epsilon_{an} = \epsilon_{inc} \times \epsilon_{pile} \times \epsilon_{tracks} \times (\epsilon_{cl})^{\#\gamma}. \tag{7.38}$$

Efficiencies of the charged analyses are presented in table 7.8.

[6] Approximately 73% of the $\psi' \to J/\psi\pi^+\pi^-$ events have central calorimeter clusters associated with the charged pion tracks.

Stack Number	CCAL OR rate min	max	ave	Stack Number	CCAL OR rate min	max	ave
1	157	461	302	9	258	478	377
2	187	434	304	10	285	485	368
3	118	373	246	11	299	415	352
4	180	363	275	12	216	372	313
5	237	493	372	13	272	468	368
6	196	480	329	14	250	420	335
7	219	475	339	15	288	464	379
8	205	500	349	16	385	476	421

Table 7.9: The central calorimeter rates for each stack. All rates are in kHz.

7.4.2 Neutral Analysis

The neutral analysis efficiencies are not as straight forward as the charged analysis efficiencies. The extra cluster cut is rate dependent; the efficiency of the cut as a function of the central calorimeter rate for the good $\pi^o\pi^o$ events is shown in figure 7.16. The rate dependence of the extra cluster cut efficiency is

$$\epsilon_{ecc} = (0.911 \pm 0.006) - (0.278 \pm 0.020) \times (\text{CCAL OR rate in MHz}). \qquad (7.39)$$

Table 7.9 shows the minimum, maximum and average CCAL OR rate for the $^1P_1$ stacks[7].

The cut of no forward calorimeter clusters affects the 3γ and 7γ analyses differently due to the presence of the veto on the FCAL OR bit in the trigger for 7γ events. Figure 7.17 shows the forward calorimeter cluster cut efficiency as a function

[7]There was a problem in the production of the stack 16 neutral DSTs resulting in a rate independent central calorimeter extra cluster cut efficiency of $\epsilon_{ecc} = 0.52 \pm 0.02$.

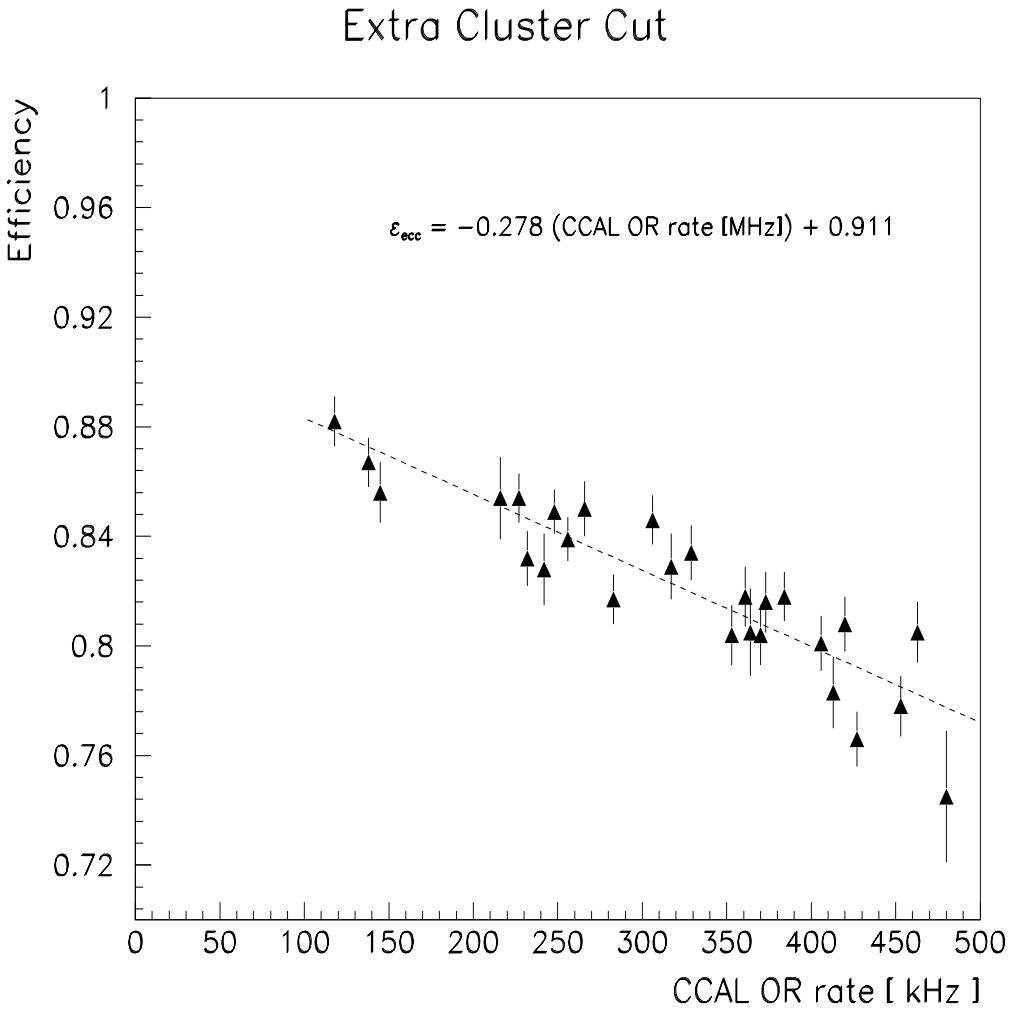

Figure 7.16: The efficiency of the extra cluster cut as a function of central calorimeter rate for $\pi^o\pi^o$ events.

of rate for good $\pi^o\pi^o$ events; a fit gives

$$\epsilon_{ecf} = (0.979 \pm 0.004) - (0.881 \pm 0.035) \times (\text{H1H2 OR rate in MHz}), \qquad (7.40)$$

where the H1H2 OR[8] rate is used since the FCAL OR threshold changed in the middle of the 1991 data taking. For the 7γ analysis, the $\pi^o\pi^o$ events that have the FCAL OR bit ON are removed from the data sample and the forward calorimeter

[8]The H1H2 OR is the coincidence between the H1 OR and H2 OR.

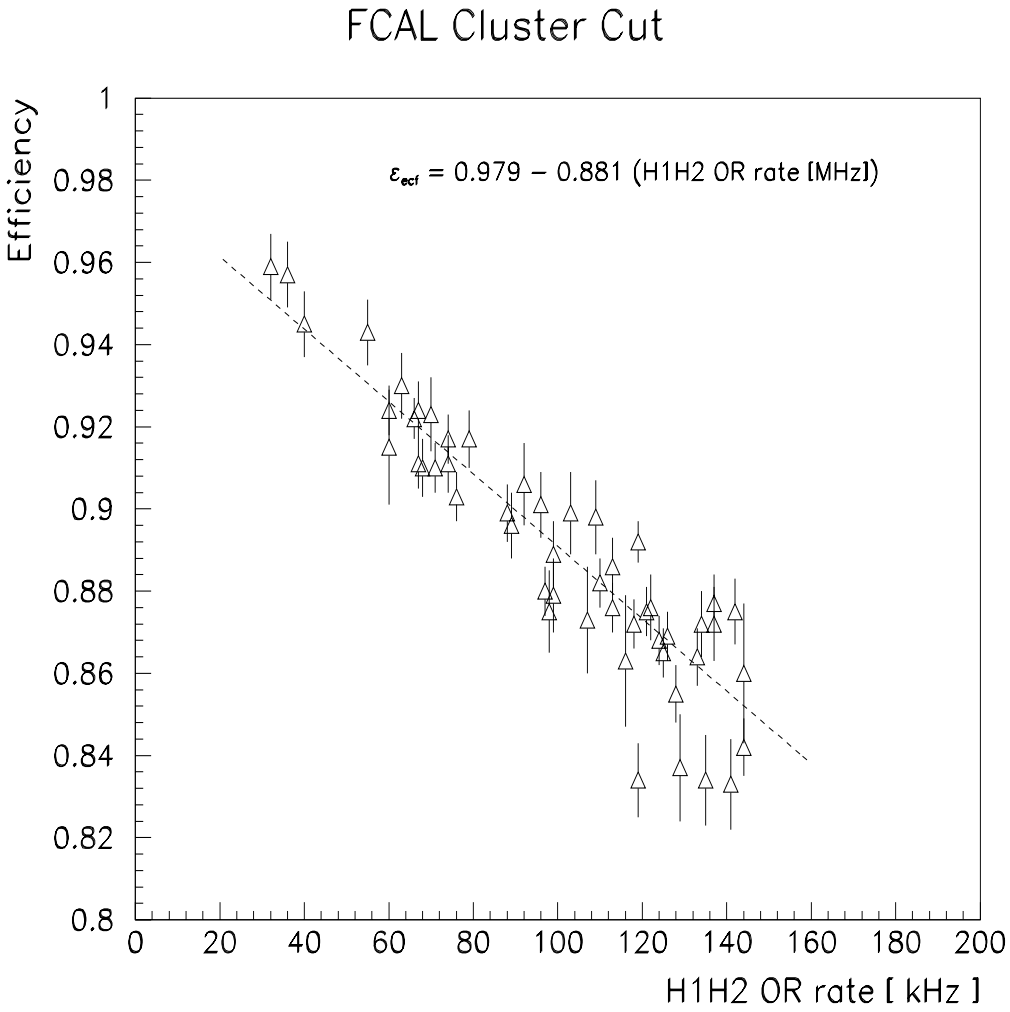

Figure 7.17: The efficiency of the forward calorimeter cluster cut as a function of H1H2 OR rate for $\pi^o\pi^o$ events.

cluster cut is found to be rate dependent,

$$\epsilon'_{ecf} = (0.993 \pm 0.004) - (0.694 \pm 0.035) \times (\text{H1H2 OR rate in MHz}), \qquad (7.41)$$

as shown in figure 7.18.

The 3γ analysis includes cuts of π^o and η particles. The efficiency of this cut is determined from the event Monte Carlo and using the cut upon the sample of the χ_2

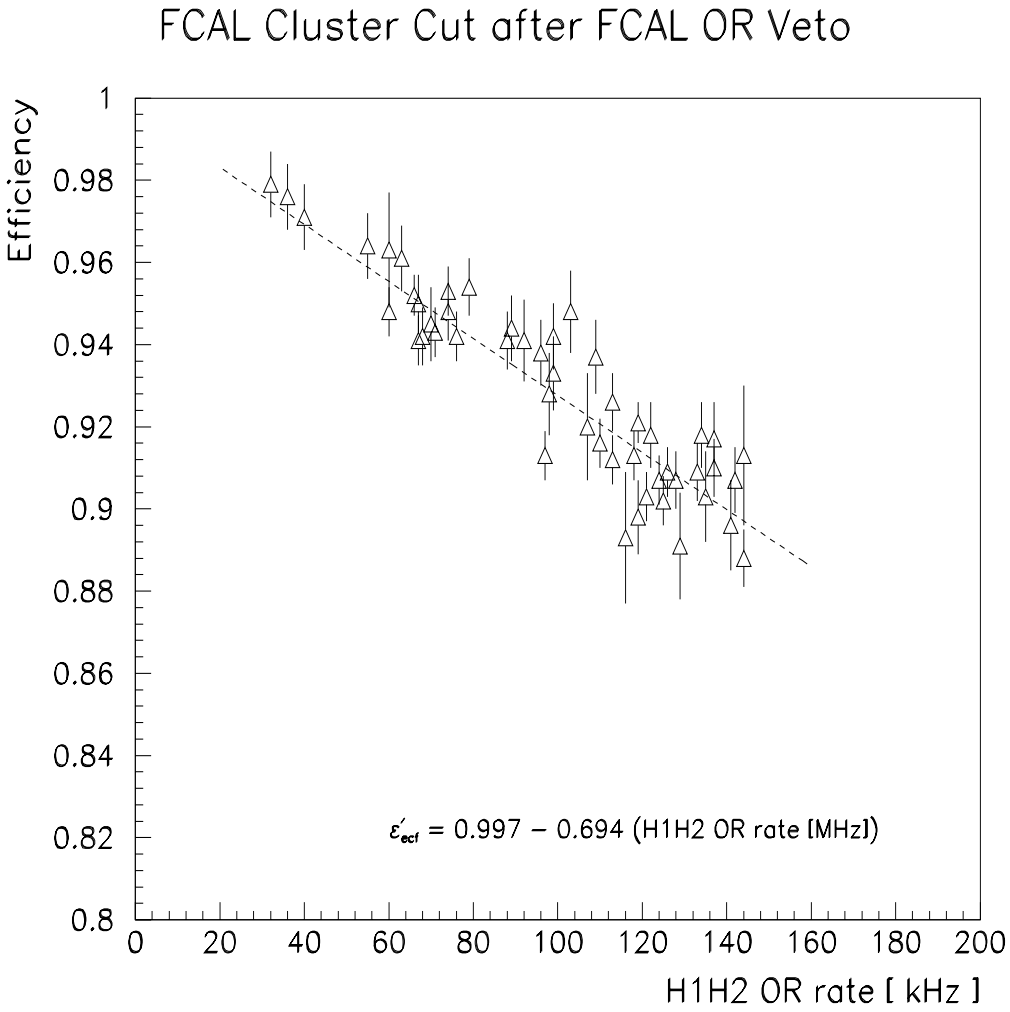

Figure 7.18: The efficiency of the forward calorimeter cluster cut as a function of H1H2 OR rate for $\pi^o\pi^o$ events; events with the FCAL OR bit ON in the trigger are removed from the sample.

events. Both results determine the π^o and η cut to be

$$\epsilon_{\pi^o\eta} = 0.81 \pm 0.01. \tag{7.42}$$

The χ^2 fit probability is required to be greater than 10%. The 3γ analysis efficiency is

$$\epsilon_{an}(3\gamma) = \epsilon_{cl}^3 \times \epsilon_{ecc} \times \epsilon_{ecf} \times \epsilon_{\pi^o\eta} \times \epsilon_{fit}; \tag{7.43}$$

Reaction $\bar{p}p \rightarrow {}^1\mathrm{P}_1 \rightarrow$	Geometrical Acceptance α_{geom}	Pile-up Cut Efficiency ϵ_{pile}	Cluster Mass Efficiency ϵ'_{cl}	Fit Analysis Efficiency ϵ_{fit}
$\gamma\eta_c \rightarrow \pi^o\pi^o\pi^o\gamma$	0.1805	0.976	0.892	0.315
$\gamma\eta_c \rightarrow \pi^o\pi^o\eta\gamma$	0.1361	0.977	0.908	0.386
$\gamma\eta_c \rightarrow \pi^o\pi^o\eta'\gamma$	0.1173	0.978	0.922	0.421
$\gamma\eta_c \rightarrow \pi^o\eta\eta\gamma$	0.0995	0.994	0.937	0.388
$\gamma\eta_c \rightarrow \pi^o\eta\eta'\gamma$	0.0862	0.987	0.932	0.415
$\gamma\eta_c \rightarrow \pi^o\eta'\eta'\gamma$	0.0820	0.987	0.916	0.450
$\gamma\eta_c \rightarrow \eta\eta\eta\gamma$	0.0738	0.998	0.944	0.425
$\gamma\eta_c \rightarrow \eta\eta\eta'\gamma$	0.0684	0.998	0.934	0.656
$\gamma\eta_c \rightarrow \eta\eta'\eta'\gamma$	0.0758	1.000	0.925	0.482
$\gamma\eta_c \rightarrow \eta'\eta'\eta'\gamma$	0.1344	1.000	0.899	0.455
$\gamma\eta' \rightarrow \pi^o\pi^o\pi^o\gamma$	0.1789	0.934	0.851	0.347
$\gamma\eta' \rightarrow \pi^o\pi^o\eta\gamma$	0.1856	0.934	0.805	0.375
$\gamma\eta \rightarrow \pi^o\pi^o\pi^o\gamma$	0.3408	0.946	0.540	0.355

Table 7.10: The Monte Carlo geometrical acceptances and the analysis efficiencies for the 7γ final states as determined from 10,000 Monte Carlo events. The cluster mass cut efficiencies for the 7γ final states are determined by whenever two gamma rays are less than 100 mrad apart.

using the average cluster cut efficiencies, $\epsilon_{an}(3\gamma) = 0.47$. The efficiency ranges from 0.42 to 0.54 and the luminosity weighted stack efficiencies range from 0.45 to 0.50.

The 7γ event Monte Carlo has been used to study the pile-up cut and the cluster mass cut efficiencies (how often two of the gamma rays are less than 150 mrad apart); these are shown for each 7γ final state in table 7.10. The 7γ analyses involve comparison to several background hypotheses; included in table 7.10, are the efficiencies for the correct hypothesis being the best fit for 10,000 Monte Carlo events. The 7γ analysis efficiency is

$$\epsilon_{an}(7\gamma) = \epsilon_{ecc} \times \epsilon'_{ecf} \times \epsilon_{pile} \times \epsilon'_{cl} \times \epsilon_{fit} \tag{7.44}$$

and is dependent upon the final state.

Reaction $\bar{p}p \rightarrow {}^1\mathrm{P}_1 \rightarrow$	Final Efficinecy
$J/\psi\pi^o$	0.32 ± 0.02
$J/\psi\pi^o\pi^o$	0.12 ± 0.01
$J/\psi\pi^+\pi^-$	0.067 ± 0.005
$\gamma\eta_c \rightarrow \gamma\gamma\gamma$	0.15 ± 0.02
$\gamma\eta_c \rightarrow \pi^o\pi^o\pi^o\gamma$	0.029 ± 0.002
$\gamma\eta_c \rightarrow \pi^o\pi^o\eta\gamma$	0.027 ± 0.002
$\gamma\eta_c \rightarrow \pi^o\pi^o\eta'\gamma$	0.026 ± 0.002
$\gamma\eta_c \rightarrow \pi^o\eta\eta\gamma$	0.021 ± 0.002
$\gamma\eta_c \rightarrow \pi^o\eta\eta'\gamma$	0.019 ± 0.001
$\gamma\eta_c \rightarrow \pi^o\eta'\eta'\gamma$	0.019 ± 0.001
$\gamma\eta_c \rightarrow \eta\eta\eta\gamma$	0.017 ± 0.001
$\gamma\eta_c \rightarrow \eta\eta\eta'\gamma$	0.024 ± 0.002
$\gamma\eta_c \rightarrow \eta\eta'\eta'\gamma$	0.020 ± 0.002
$\gamma\eta_c \rightarrow \eta'\eta'\eta'\gamma$	0.032 ± 0.002
$\gamma\eta' \rightarrow \pi^o\pi^o\pi^o\gamma$	0.029 ± 0.002
$\gamma\eta' \rightarrow \pi^o\pi^o\eta\gamma$	0.031 ± 0.002
$\gamma\eta \rightarrow \pi^o\pi^o\pi^o\gamma$	0.036 ± 0.002

Table 7.11: The final efficiencies for the different reactions.

7.5 Final Efficiencies

The final efficiency for a particular reaction is the product of the geometrical acceptance, trigger efficiency and analysis efficiency:

$$\epsilon_{tot} = \alpha_{geom} \times \epsilon_{trig} \times \epsilon_{an}. \tag{7.45}$$

The $J/\psi\pi^o$ and $J/\psi\pi^o\pi^o$ channel efficiencies are essentially not rate dependent and the total efficiency[9] is given in table 7.11. The average rates are used to calculate the final efficiency for $J/\psi\pi^+\pi^-$ (3γ) that is presented in table 7.11; the range of efficiencies is 0.057 to 0.079 (0.13 to 0.18). The 7γ final efficiencies are also presented

[9]For $J/\psi\ \pi^o$, the median value for the range of α_{geom} in table 7.3 is used.

in table 7.11 using the average rates; the efficiencies range around the values in the table by $\pm 15\%$.

Data from the ψ' resonance confirms the efficiency determination for the $J/\psi\pi\pi$ channels. The expected number of events ($\psi' \to J/\psi\pi^o\pi^o, J/\psi\pi^+\pi^-$) is determined from the observed number of $\psi' \to e^+e^-$ and corrected for acceptances, efficiencies and branching fractions [21]. The expected number of events for $J/\psi\pi^o\pi^o$ ($J/\psi\pi^+\pi^-$) is 122 ± 6 (109 ± 10); the observed number is 113 (104).

7.6 Energy and Luminosity Uncertainties

The beam center of mass energy is

$$E_{cm}^2 = 2(1+\gamma)(m_p c^2)^2; \tag{7.46}$$

the uncertainty of the center of mass energy for any data run is

$$\delta E_{cm} = \frac{\gamma^3 m_p^2 c^4 \beta^2}{E_{cm}} \frac{\delta\beta}{\beta}. \tag{7.47}$$

The velocity uncertainty is from equation 2.2 and is

$$\frac{\delta\beta}{\beta} = \sqrt{\left(\frac{\delta f}{f}\right)^2 + \left(\frac{\delta L}{L}\right)^2}, \tag{7.48}$$

where the length uncertainty is $\delta L = \delta L_0 + \delta(\Delta L)$. The frequency measurement is made accurately, $\frac{\delta f}{f} = 1.5 \times 10^{-7}$. The reference orbit length uncertainty is due to the mass uncertainty of the ψ'; the reference orbit length is 474.048 m with an uncertainty of 0.67 mm which corresponds to the ψ' mass uncertainty of 0.1 MeV/c^2 [21]. The

deviation of the orbit length measured by the BPMs has an estimated uncertainty of 1 mm due to the least significant bit of the BPMs. The overall uncertainty of the beam energy is 190 keV.

The uncertainty in the luminosity monitor's determination of the luminosity is dependent upon the uncertainties of the $\bar{p}p$ elastic cross section in this region (2.0%) and the geometrical acceptance of the silicon detector (2.0%). These combine for a systematic error of 4.0%. A statistical error of 3% for the luminosity determination comes from the necessity to subtract an exponential background from the pulse height spectrum, see figure 2.7.

Chapter 8

Results and Conclusions

First, a brief discussion of the convolution of a Breit-Wigner resonance with the beam energy distribution is presented. The method of determining resonance parameters is presented before the results of the analyses are presented. In conclusion, the significance of the signals is discussed and upper limits of the products of branching ratios are presented.

8.1 Expected Cross Sections

The Breit-Wigner cross section, as a function of center of mass energy E_{cm}, for the formation by $\bar{p}p$ annihilation and decay of a resonance R of spin J, mass M_R and total width , $_R$ is

$$\sigma_{BW}(E_{cm}) = \frac{(2J+1)}{(2S_p+1)(2S_{\bar{p}}+1)} \frac{4\pi(\hbar c)^2}{(E_{cm}^2 - 4(m_p c^2)^2)} \frac{, \,^2_R B_{in} B_{out}}{(E_{cm} - M_R c^2)^2 + , \,^2_R/4}, \quad (8.1)$$

where S_i is spin for the proton and antiproton, B_{in} and B_{out} are the branching ratios for the resonance's formation channel ($\bar{p}p \rightarrow R$) and decay channel, respectively. The decay branching ratio contains all subsequent decays to the final state particles.

When $E_{cm} = M_R c^2$, the cross section for a particular final state becomes

$$\sigma_{peak} = \frac{(2J+1)4\pi\hbar^2 B_{in} B_{out}}{(M_R^2 - 4m_p^2)c^2}. \tag{8.2}$$

When the resonance is the $^1\mathrm{P}_1$ and the mass is taken to be near $M_{\chi_{cog}}$, the peak cross section becomes

$$\sigma_{peak} = 1.64 \text{ mb} \times B(^1\mathrm{P}_1 \to \bar{p}p) \times B(^1\mathrm{P}_1 \; decay) \times B(subsequent \; decays); \tag{8.3}$$

of course, the measured peak cross section is further reduced by the total efficiency.

The beam energy width is finite, which results in the cross section for any point being the convolution of a Breit-Wigner resonance with the center of mass energy distribution:

$$\sigma(E_{cm}) = \int_0^\infty \sigma_{BW}(E') F_{beam}(E' - E_{cm}) dE', \tag{8.4}$$

where F_{beam} is the center of mass energy distribution due to the beam spread. The beam spread is determined from the spread in revolution frequencies, equation 2.3. In the center of mass frame, the energy is related to the frequency by (equation 7.46)

$$E_{cm}^2 = 2m_p^2 c^4 \left(1 + \frac{1}{\sqrt{1 - (fL/c)^2}}\right). \tag{8.5}$$

The frequency spread, figure 2.5, is used to determine F_{beam}; the Schottky noise spectrum is approximated by a gaussian. For determining a run's beam energy distribution, the Schottky noise spectra associated with the run are averaged to get the beam frequency distribution.

8.2 Method of Fitting Data

A datum point for fitting consists of events grouped according to runs, energy bins, or stacks. When grouped by runs, the datum point's energy and integrated luminosity are the run's energy and integrated luminosity. If energy bins or stacks are used to group the events, the datum point's energy is calculated by the integrated luminosity weighted average of the energies of the runs.

Data points are then fitted by using a maximum likelihood method. The expected number of events for a datum point ν_i is a function of the cross section (equation 8.4), the total integrated luminosity $\mathcal{L}_i$, the total efficiency ϵ_{tot} associated with the point, and a background cross section σ_{bkg}:

$$\nu_i = \mathcal{L}_i \times [\sigma(E_{cm,i}) \times \epsilon_{tot} + \sigma_{bkg}]. \tag{8.6}$$

The likelihood function Λ for N data points is the product of N Poisson functions,

$$\Lambda = \prod_{i=1}^{N} \frac{\nu_i^{n_i} e^{-\nu_i}}{n_i!}, \tag{8.7}$$

where n_i is the number of events observed for the i^{th} datum point. The log-likelihood function, $\ln(\Lambda)$, is maximized resulting in fitted values for the mass, width, product of branching ratios ($B_{in}B_{out}$), and the background cross section.

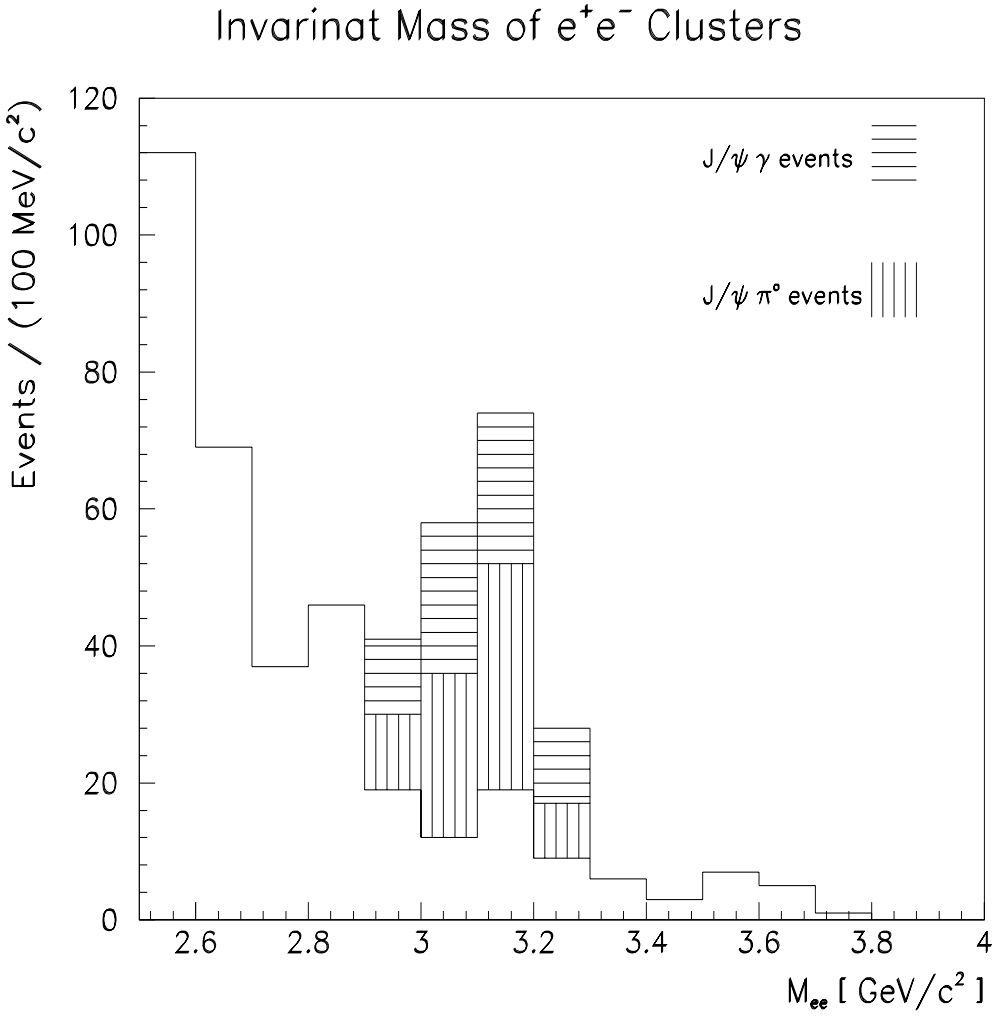

Figure 8.1: The reconstructed invariant mass of the e^+e^- pair for all 16 stacks.

8.3 Charged Channels

The reconstructed invariant masses of the two tracks associated with the e^+e^- pair, are shown in figure 8.1; events from all 16 stacks are shown. The excess of events at 3.1 GeV/c^2 are inclusive J/ψ events. These events are identified as either $J/\psi\pi^o$ or $J/\psi\gamma$; the number of events of each type is shown in table 8.1. The possible reasons for the $J/\psi\gamma$ events is presented after the results of fitting the $J/\psi\pi^o$ data set.

Stack	$J/\psi\pi^o$	$J/\psi\gamma$	Stack	$J/\psi\pi^o$	$J/\psi\gamma$
1	1	4	9	4	7
2	2	4	10	8	6
3	3	4	11	3	3
4	1	4	12	9	4
5	2	8	13	6	4
6	10	3	14	7	3
7	3	4	15	4	2
8	8	8	16	3	1

Table 8.1: The number of $J/\psi\pi^o$ and $J/\psi\gamma$ events for each stack.

8.3.1 $J/\psi\pi^o$ Events

The number of events divided by the integrated luminosity for each stack is shown in figure 8.2. In figure 8.3, the events from runs with center of mass energies near 3526 MeV are grouped into 200 keV bins. In both figures, there appears to be a larger observed cross section around 3526 MeV with a 2 pb background.

The events grouped by stack or by bins of 100, 200 and 300 keV, have been subjected to the maximum likelihood analysis described in the previous section. In each case, the resonance width has had to be fixed; if left to vary, the result is zero width due to the small statistics and large beam width. The resonance width is fixed at values from 250 keV up to 1250 keV in increments of 250 keV. The mass is found to be 3526.15 ± 0.15 MeV/c^2 (statistical error from the fit); the other parameters are dependent upon the fixed resonance width and are presented in table 8.2. An upper limit (90% CL) of 1.1 MeV for the resonance width is set. If the data for all sixteen stacks are fit to a flat background, the cross section is 4.7 events per pb^{-1}.

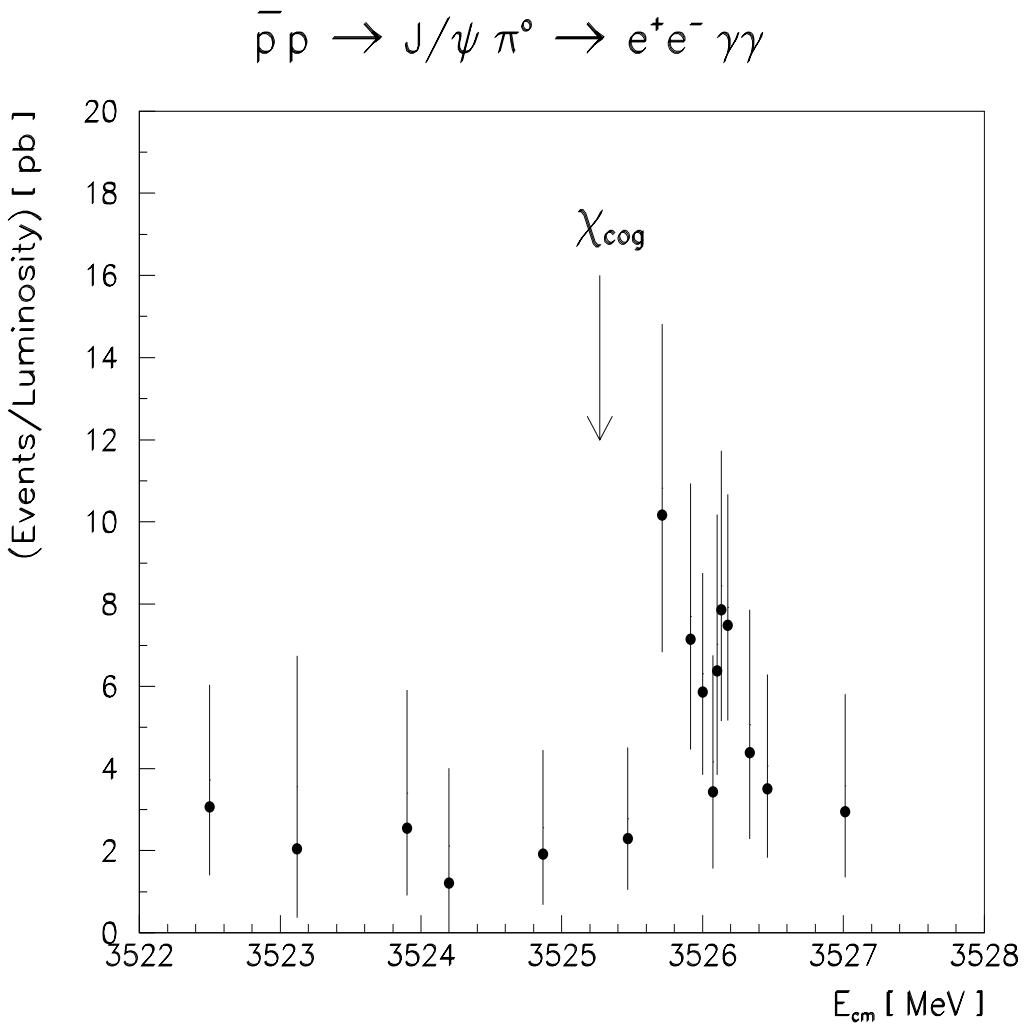

Figure 8.2: The number of events divided by integrated luminosity for each stack. The error bars are statistical.

The ratio of the maximum values of the likelihood functions for the hypothesis of a resonance and a background, $\Lambda(H_1)$, to the flat background hypothesis, $\Lambda(H_0)$, is used to form a test statistic $\xi = -2\ln\lambda$ where $\lambda = \Lambda(H_0)/\Lambda(H_1)$ [80]. The probability that a fictitious resonance results from fluctuations of a flat background has been investigated with Monte Carlo simulations of the data points; E760 data points' energies and integrated luminosities are used along with Possion distributed numbers of events based upon the fit to a flat cross section, 4.7 events per pb^{-1}. The

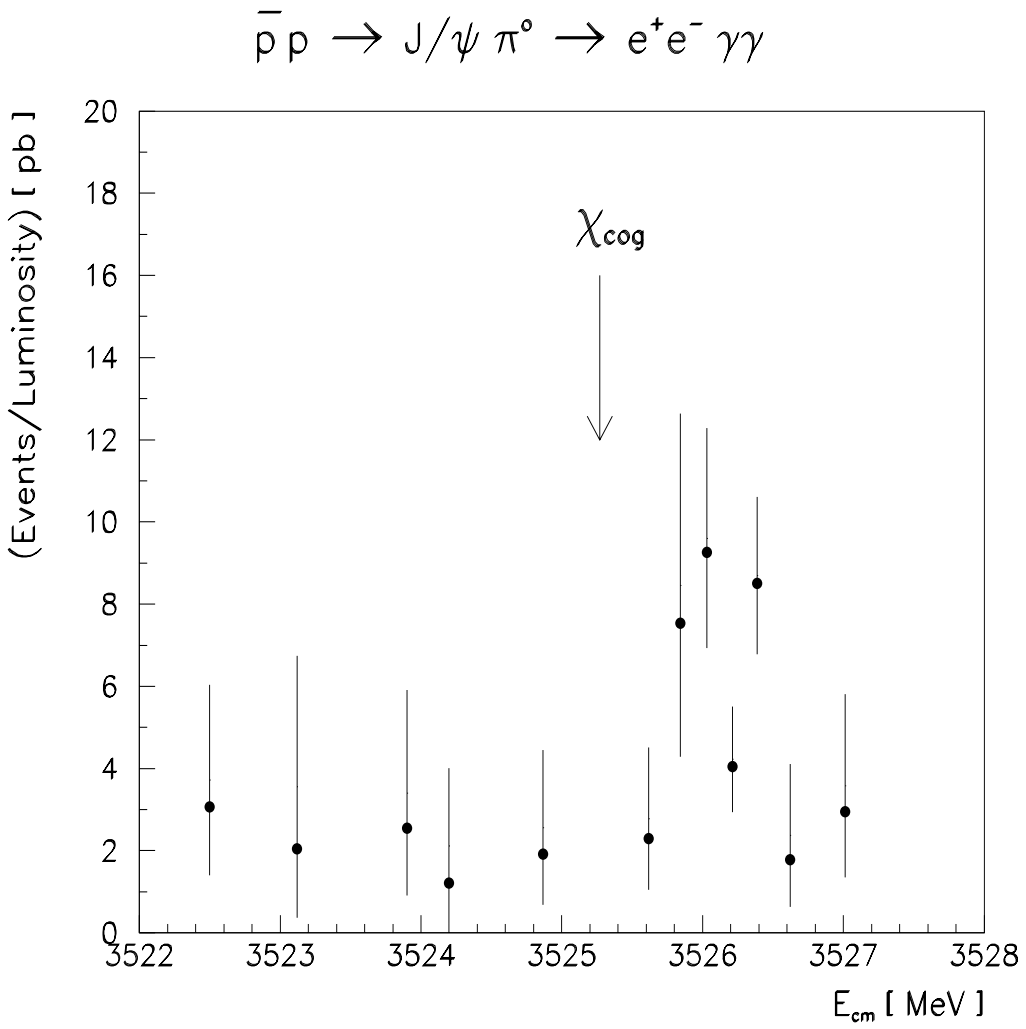

Figure 8.3: Same as figure 8.2 except for runs near 3526 MeV/c^2 are grouped in 200 keV bins. The error bars are statistical.

Monte Carlo experiments are fitted in the same manner as above and the test statistic is calculated; the percentage of the Monte Carlo test statistics ξ_{MC} which are greater than the real experiment's test statistic ξ_{exp} gives the statistical significance of the resonance. Table 8.3 shows ξ_{exp} and the statistical significance based upon 10,000 Monte Carlo experiments for different energy bin widths and resonance widths.

Width (keV)	$B(^1\mathrm{P}_1 \to \bar{p}p) \times B(^1\mathrm{P}_1 \to J/\psi\pi^o)$ ($\times 10^{-7}$)	σ_{bkg} (pb)
250	1.0 ± 0.3	2.1 ± 0.3
500	1.2 ± 0.4	1.9 ± 0.2
750	1.5 ± 0.4	1.8 ± 0.2
1000	1.7 ± 0.5	1.7 ± 0.2
1250	2.0 ± 0.5	1.6 ± 0.2

Table 8.2: The resulting values of the fit parameters for fixed resonance widths. The resonance mass is independent of the resonance width and is found to be 3526.15 ± 0.15 MeV/c^2 (this error and the table's entry errors are statistical and from the fit).

Bin Width (keV)	Γ_R (keV)	ξ_{exp}	Statistical Significance
100	250	14.0	0.6×10^{-3}
100	500	13.3	1.5×10^{-3}
100	750	12.6	1.7×10^{-3}
100	1000	11.9	2.5×10^{-3}
100	1250	11.2	3.1×10^{-3}
200	250	13.9	0.6×10^{-3}
200	500	13.3	0.7×10^{-3}
200	750	12.6	1.2×10^{-3}
200	1000	12.0	1.9×10^{-3}
200	1250	11.3	2.6×10^{-3}
300	250	13.2	1.3×10^{-3}
300	500	12.7	1.9×10^{-3}
300	750	12.1	2.4×10^{-3}
300	1000	11.5	3.6×10^{-3}
300	1250	10.9	4.6×10^{-3}

Table 8.3: The experiment's test statistic ξ_{exp} and the fraction of Monte Carlo experiments with $\xi_{MC} \geq \xi_{exp}$ out of 10,000 simulations, which results in the statistical significance (for different binning of the data and resonance widths).

The 2 events per pb^{-1} background observed near the resonance corresponds to a continuum cross section $\sigma(\bar{p}p \to J/\psi\pi^o) \approx 100$ pb, which is in agreement with what is predicted for the continuum [81]. The continuum $J/\psi\pi^o$ cross section is predicted to increase with energy; agreement with this prediction is seen in data taken near $\sqrt{s} \approx 3.6$ GeV, where the continuum cross section is measured to be ≈ 155 pb.

8.3.2 $J/\psi\gamma$ Events

The $^1P_1$ is forbidden to decay radiatively to J/ψ by charge conjugation invariance. The number of $J/\psi\gamma$ events found divided by the integrated luminosity is constant, ≈ 4 pb, within the region investigated as shown in figure 8.4. No resonance is evident. The test statistic from fitting the $J/\psi\gamma$ data to a resonance[1] with a flat background is compared to Monte Carlo experiments' test statistics (Poisson distributed number of events based upon a flat cross section); 30% of the Monte Carlo test statistics are larger than the $J/\psi\gamma$ data test statistic, i.e. there is no statistical significance for a $J/\psi\gamma$ resonance.

There are several possible explanations for the $J/\psi\gamma$ events. One possible explanation is that some of these events are actually $J/\psi\pi^o$ events where one of the gamma rays escapes detection, *feed down*; only a few of the events fit this hypothesis. However, at $\sqrt{s} \approx 3.6$ GeV there are a few $J/\psi\gamma$ events which is consistent with feed down from the $J/\psi\pi^o$ continuum.

[1] Fixed widths have been used: between 250 and 1250 keV.

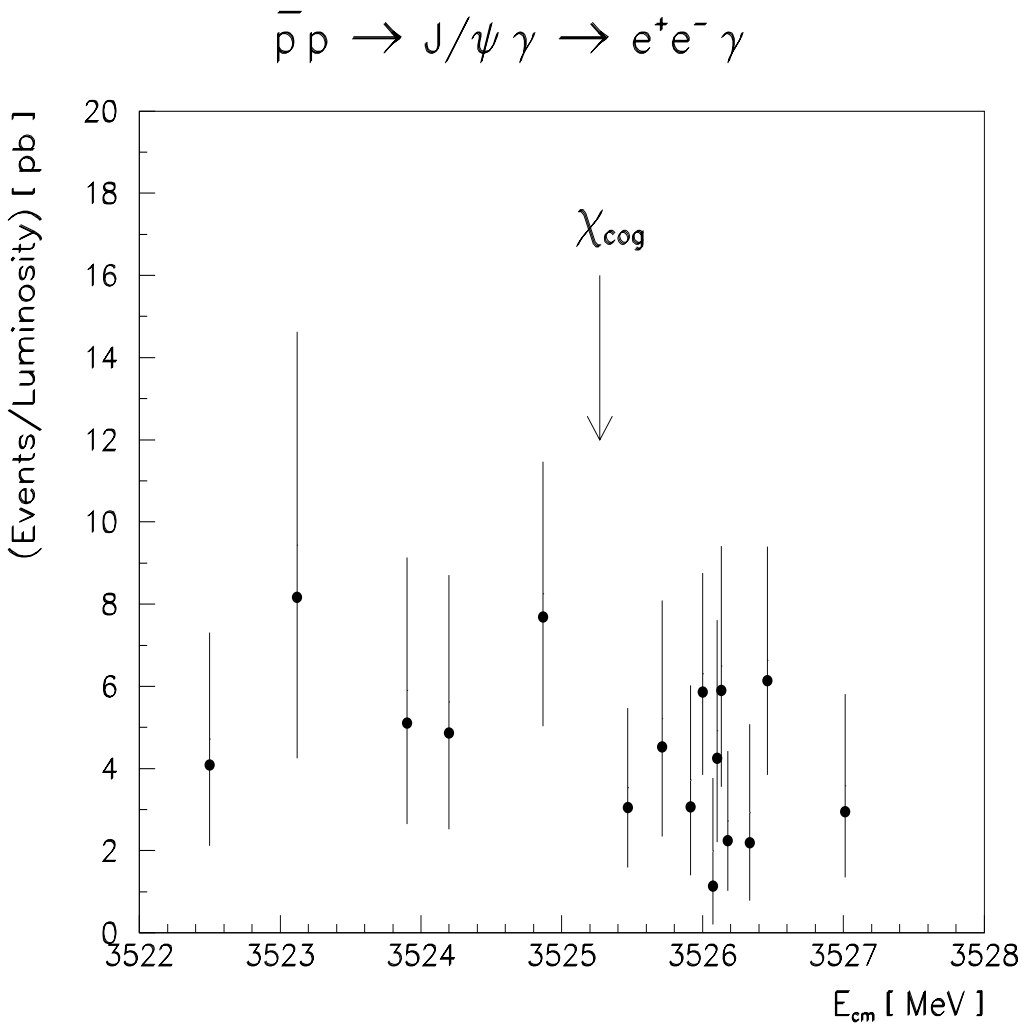

Figure 8.4: The number of events divided by integrated luminosity for each stack. The error bars are statistical.

Using the Breit-Wigner resonance cross section[2] (equation 8.1) for the χ_1 and χ_2 states, cross sections of 2.3 pb and 2.6 pb result, respectively, from the tails of the two triplet P wave resonances. A total efficiency [20] of ≈ 0.4 for $J/\psi\gamma$ events reduces this to an expected observed cross section of ≈ 2 pb (the beam energy convolution has not been considered).

[2]The Breit-Wigner resonance shape may not be appropriate for the tails of a resonance.

Another possible explanation involves $\bar{p}$'s that have been straggled by the gas jet. The $\bar{p}$'s lose enough energy so that they are no longer caught in the main frequency harmonic being used for stochastic cooling; however, the new revolution frequencies are stochastically cooled at a different harmonic, and therefore the lower energy $\bar{p}$'s stay in the machine. Unfortunately, there is no measurement of this phenomenon; the momentum pickup's Schottky noise spectrum shows a long lowside tail (as in figure 2.5) and eventually a second peak (not pictured) which has only been observed and not recorded. It is possible that such a second peak at lower energy, convoluted with the χ_1 resonance, results in a $J/\psi\gamma$ cross section consistent with that observed.

8.3.3 $J/\psi\pi\pi$ Results

No events fit exclusively either of the $J/\psi\pi\pi$ channels. The 90% CL upper limits for the product of branching ratios are

$$B(^1\mathrm{P}_1 \to \bar{p}p) \times B(^1\mathrm{P}_1 \to J/\psi\pi^o\pi^o) \leq 2.1 \times 10^{-8}, \tag{8.8}$$

$$B(^1\mathrm{P}_1 \to \bar{p}p) \times B(^1\mathrm{P}_1 \to J/\psi\pi^+\pi^-) \leq 4.3 \times 10^{-8}. \tag{8.9}$$

8.4 Neutral Channels

The 3γ channel shows no evidence for a resonance as seen in figure 8.5. The data can be used to set an upper limit on the product of branching ratios. The same

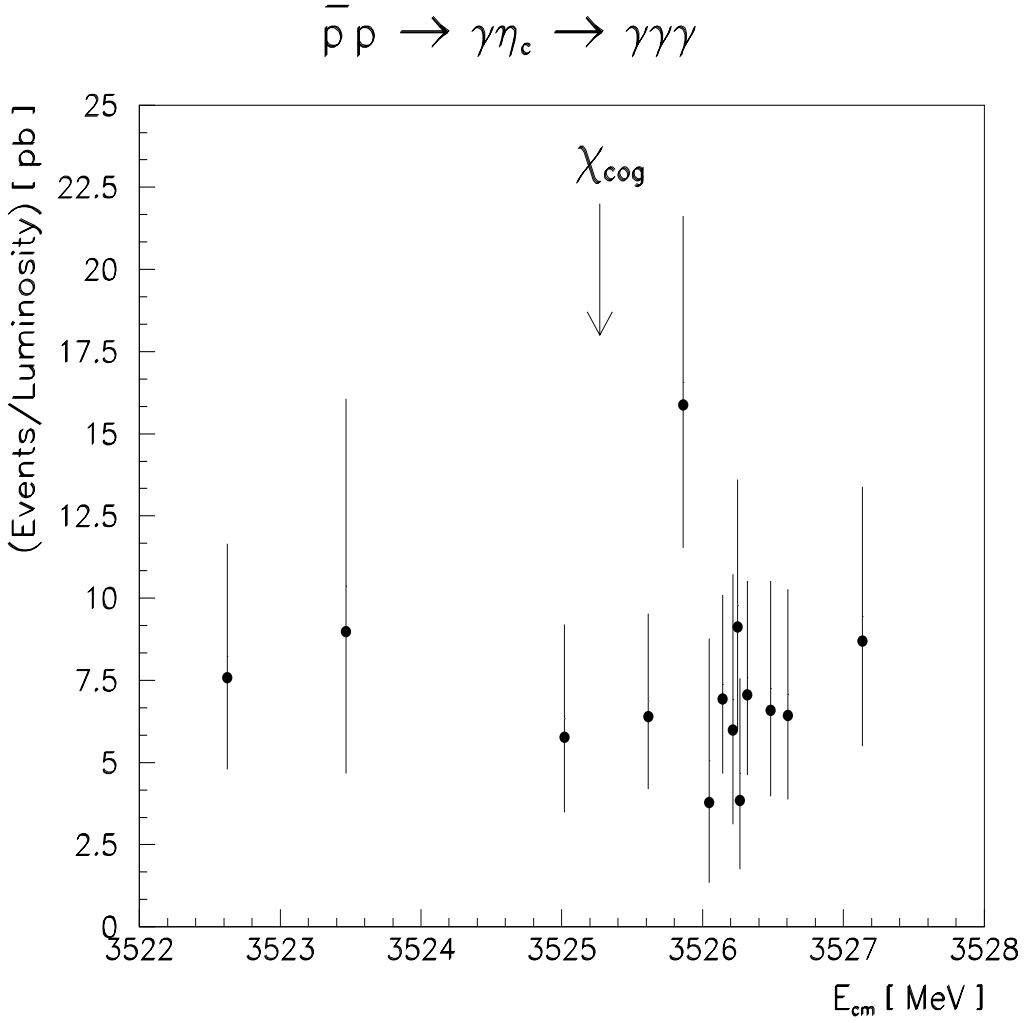

Figure 8.5: The results of the search for $\eta_c\gamma \rightarrow 3\gamma$ final state.

method will be used to set upper limits for the product of branching ratios for the 7γ final states.

An upper limit is placed by comparing the data from stacks which are in the resonance region with the data from outside of the peak region; the resonance region is defined to be ± 400 keV/c^2 of the $^1\mathrm{P}_1$ mass as found by the $J/\psi\pi^o$ analysis. The number of events in the resonance region, n_R, is assumed to have two contributions, the resonance (N_R) and the background (N_B); the number of events attributed to the

background is determined from the non-resonance region number of events n_B:

$$N_B = n_B \times \frac{\mathcal{L}_{peak}}{\mathcal{L}_{off}}, \tag{8.10}$$

where $\mathcal{L}_{peak}$ and $\mathcal{L}_{off}$ are the sums of the integrated luminosities of the stacks in the resonance and non-resonance regions, respectively. The number of events attributed to the resonance is

$$N_R = n_R - N_B; \tag{8.11}$$

assuming Poisson statistics, the uncertainty is

$$\Delta N_R = \sqrt{n_R + n_B \times \left(\frac{\mathcal{L}_{peak}}{\mathcal{L}_{off}}\right)^2}. \tag{8.12}$$

The 90% CL upper limit for the number of resonance events N_L is determined when the integral of a gaussian (mean N_R, $\sigma = \Delta N_R$, and integration limits of 0 and N_L) is equal to 0.9 of the integral from 0 to ∞. The corresponding product of branching ratios upper limit for the resonance region is found using the equation for the peak cross section (equation 8.3) and the total efficiency.

For the 3γ final state, the number of extra events in the resonance region[3] is 3.6 with an uncertainty of 10.8; the 90% CL upper limit to the number of events is 20.6 events (which corresponds to an efficiency corrected cross section of 19.6 pb, the final efficiency can be found in table 7.11). Using $B(\eta_c \to \gamma\gamma) = 3.47 \times 10^{-4}$ [82], the 90% CL upper limit is

$$B(^1\mathrm{P}_1 \to \bar{p}p) \times B(^1\mathrm{P}_1 \to \gamma\eta_c) \leq 3.44 \times 10^{-5}. \tag{8.13}$$

[3]When this is done for the $J/\psi\pi^o$ data, the number of events attributed to the resonace is 34.2 and the uncertainty is 8.8; in contrast, for the $J/\psi\gamma$ data the excess number of events is -6.3 with an uncertainty of 8.5.

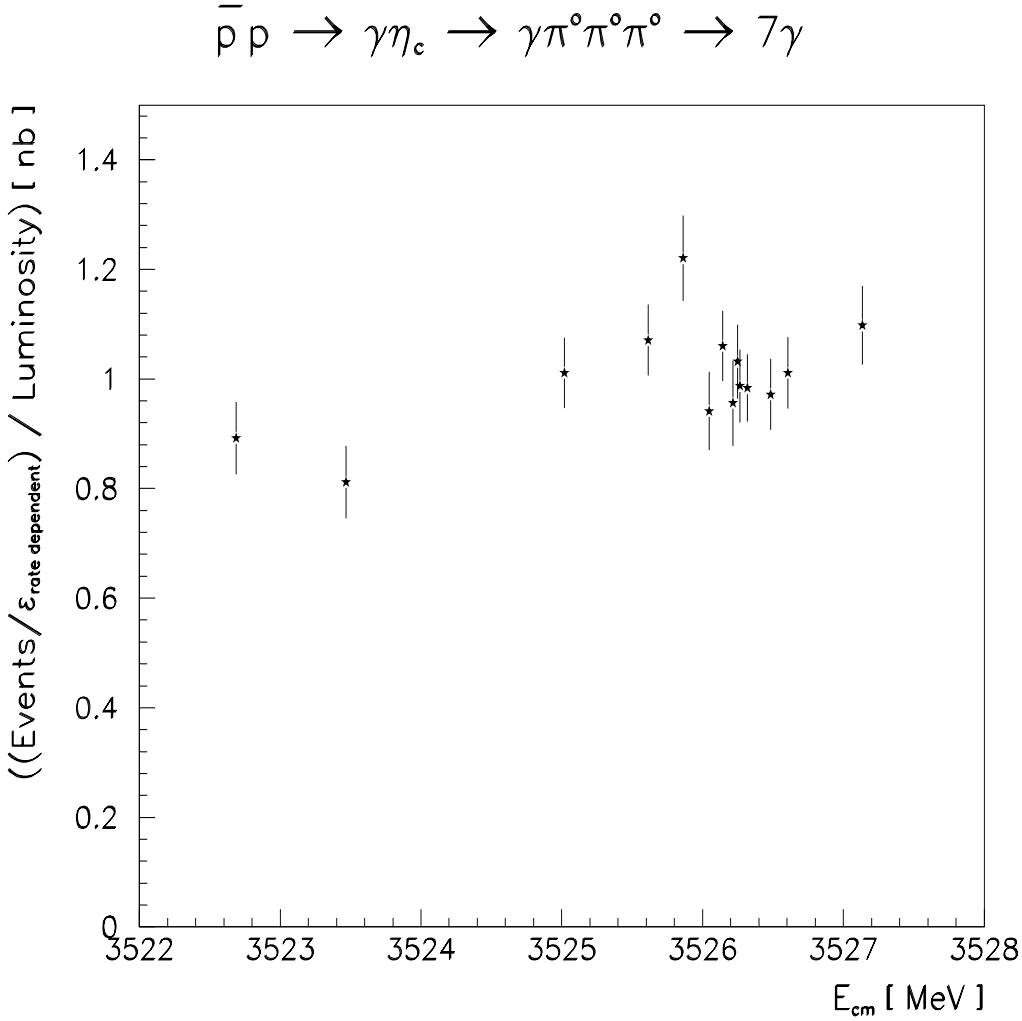

Figure 8.6: The results of the search for a resonance from $\bar{p}p \rightarrow \eta_c\gamma \rightarrow \pi^o\pi^o\pi^o\gamma$, a 7γ final state. The number of events is corrected on a run by run basis for the rate dependent efficiencies (binned by stack).

The number of events for a stack, corrected on a run by run basis for the rate dependent efficiencies, divided by the integrated luminosity for the stack is shown for the 7γ final states in figures 8.6 to 8.18. Each datum point of the plots is the sum for a stack of the rate dependent corrected values of the numbers of events for the runs (N_{run}),

$$\sum_{run} \frac{N_{run}}{\frac{\epsilon_{H1}}{\alpha_{pu}} \times \epsilon_{FCAL} \times \epsilon_{ETOT-hard} \times \epsilon_{ETOT-soft} \times \epsilon_{ecc} \times \epsilon'_{ecf}}, \tag{8.14}$$

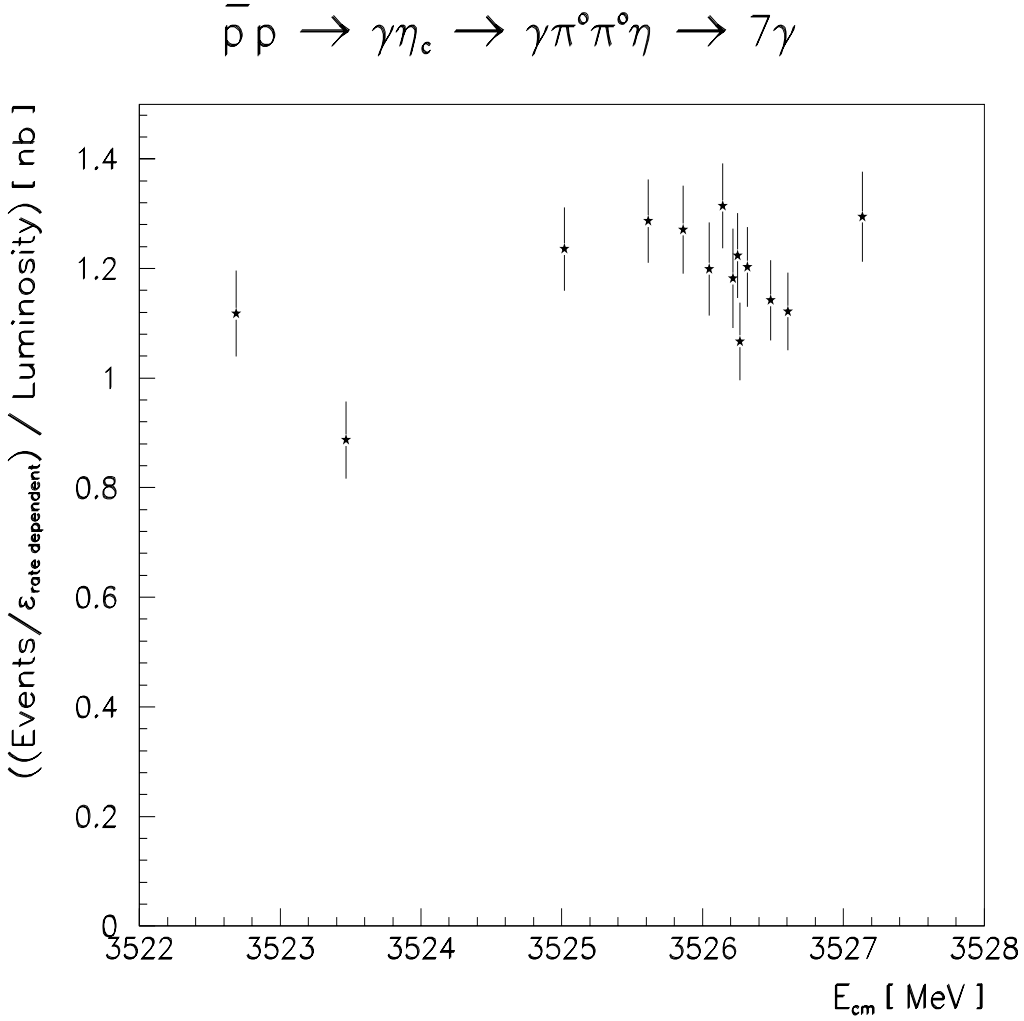

Figure 8.7: The results of the search for a resonance from $\bar{p}p \rightarrow \eta_c\gamma \rightarrow \pi^o\pi^o\eta\gamma$, a 7γ final state. The number of events is corrected on a run by run basis for the rate dependent efficiencies (binned by stack).

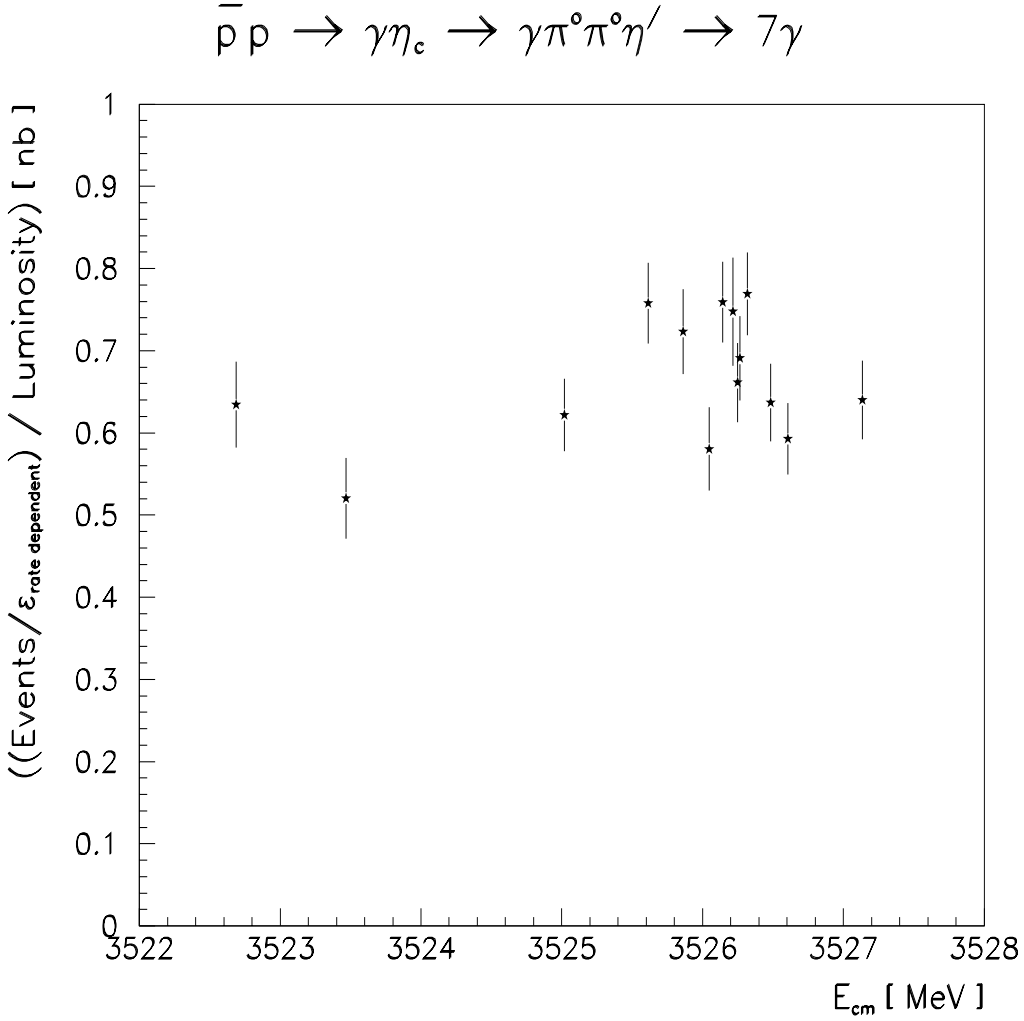

Figure 8.8: The results of the search for a resonance from $\bar{p}p \rightarrow \eta_c\gamma \rightarrow \pi^o\pi^o\eta'\gamma$, a 7γ final state. The number of events is corrected on a run by run basis for the rate dependent efficiencies (binned by stack).

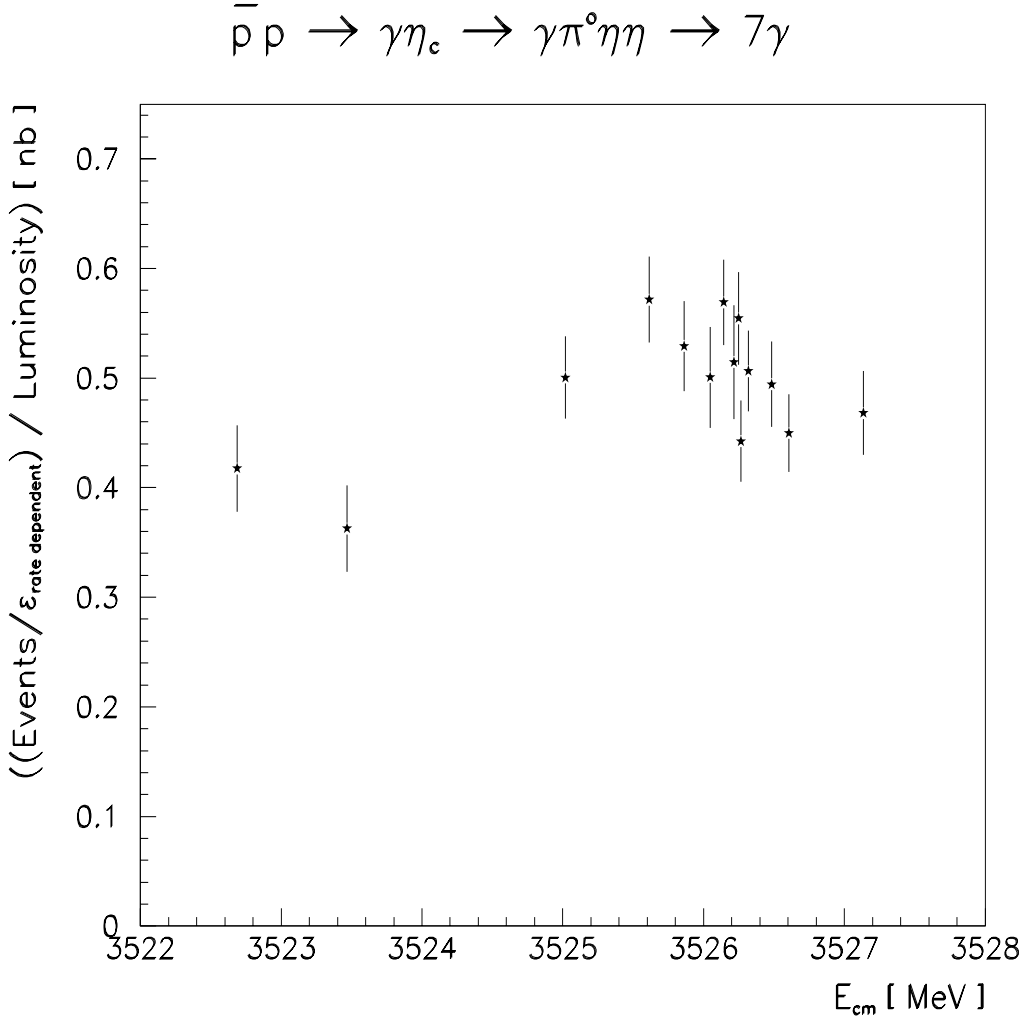

Figure 8.9: The results of the search for a resonance from $\bar{p}p \rightarrow \eta_c\gamma \rightarrow \pi^o\eta\eta\gamma$, a 7γ final state. The number of events is corrected on a run by run basis for the rate dependent efficiencies (binned by stack).

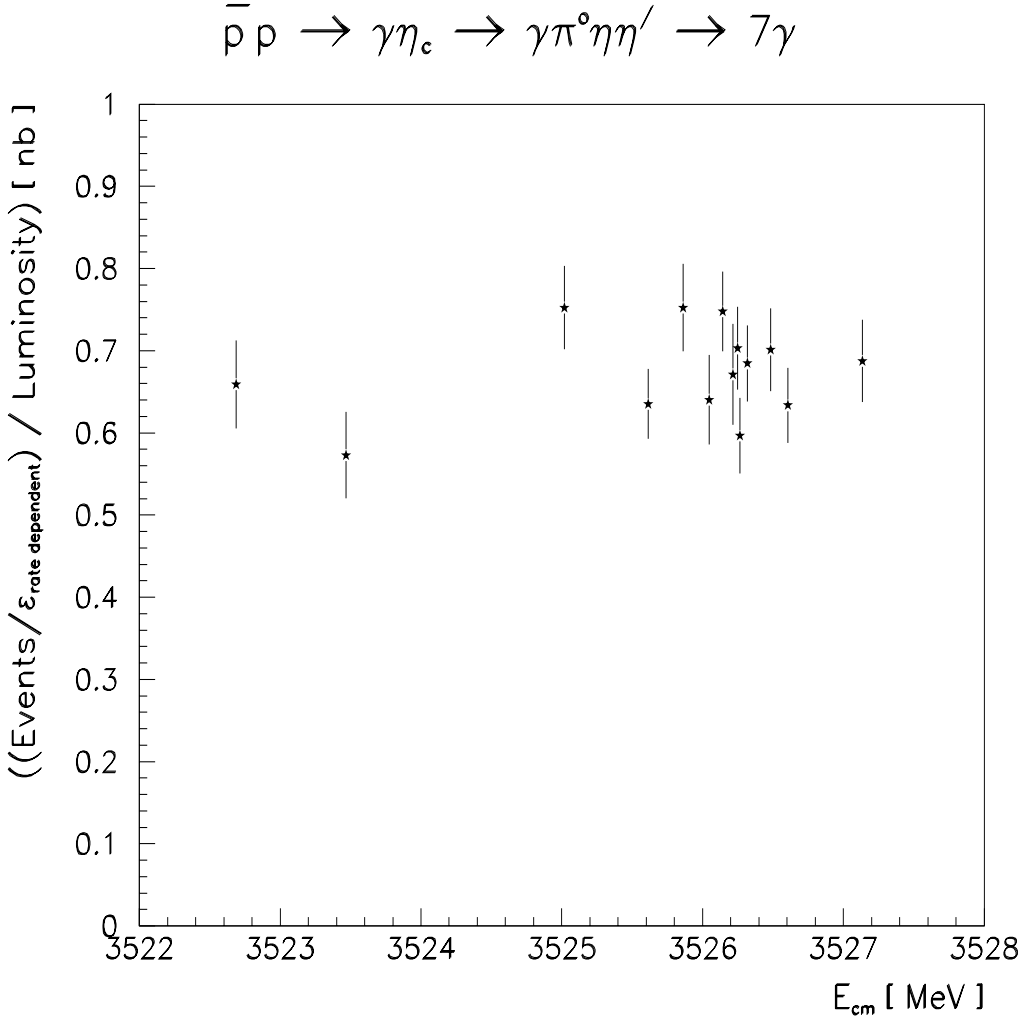

Figure 8.10: The results of the search for a resonance from $\bar{p}p \rightarrow \eta_c\gamma \rightarrow \pi^o\eta\eta'\gamma$, a 7γ final state. The number of events is corrected on a run by run basis for the rate dependent efficiencies (binned by stack).

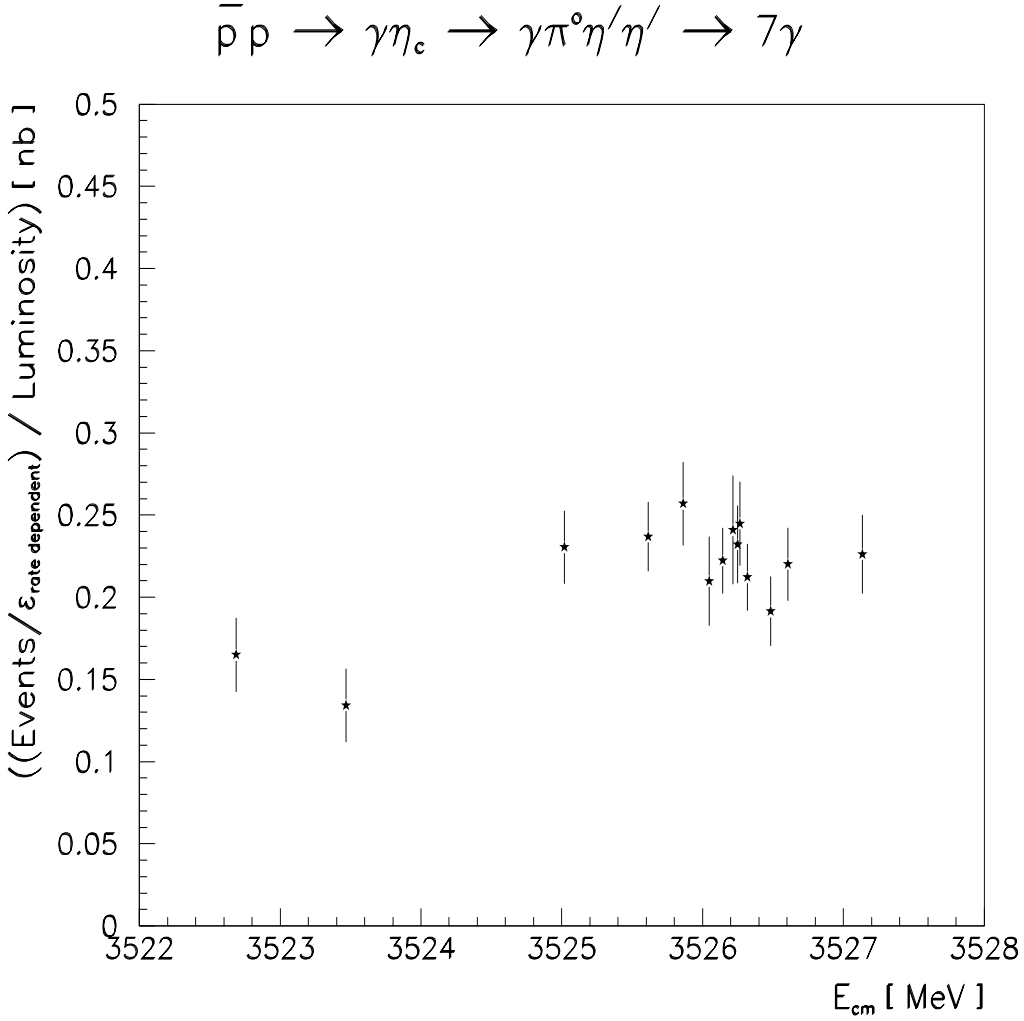

Figure 8.11: The results of the search for a resonance from $\bar{p}p \rightarrow \eta_c\gamma \rightarrow \pi^o\eta'\eta'\gamma$, a 7γ final state. The number of events is corrected on a run by run basis for the rate dependent efficiencies (binned by stack).

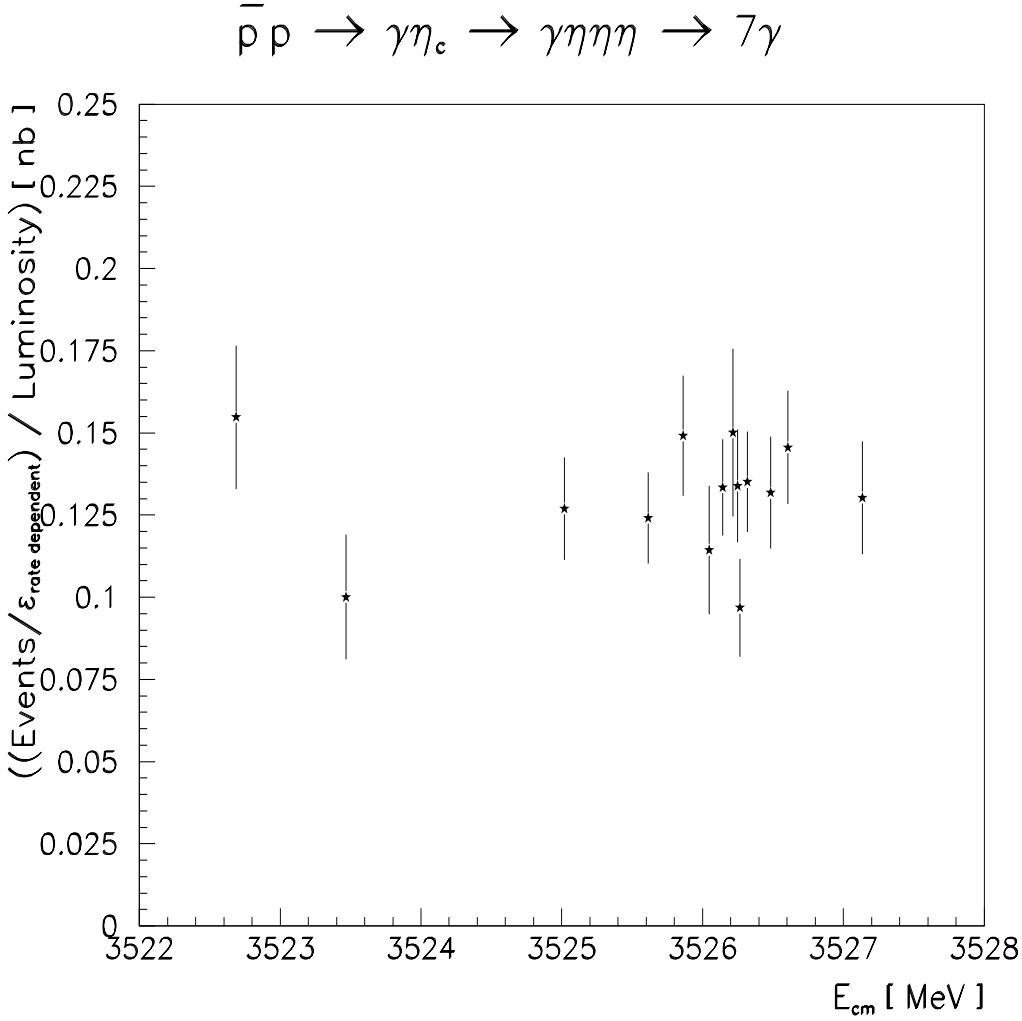

Figure 8.12: The results of the search for a resonance from $\bar{p}p \rightarrow \eta_c\gamma \rightarrow \eta\eta\eta\gamma$, a 7γ final state. The number of events is corrected on a run by run basis for the rate dependent efficiencies (binned by stack).

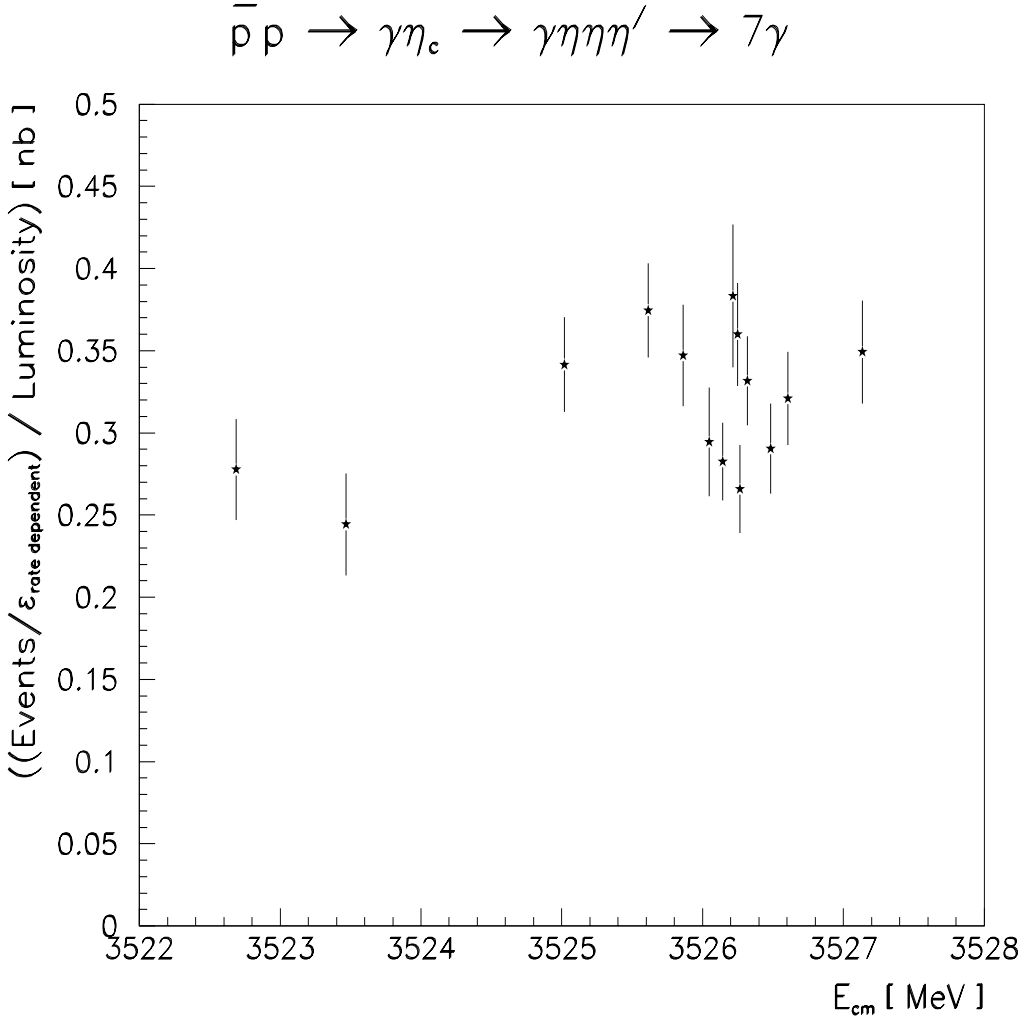

Figure 8.13: The results of the search for a resonance from $\bar{p}p \rightarrow \eta_c\gamma \rightarrow \eta\eta\eta'\gamma$, a 7γ final state. The number of events is corrected on a run by run basis for the rate dependent efficiencies (binned by stack).

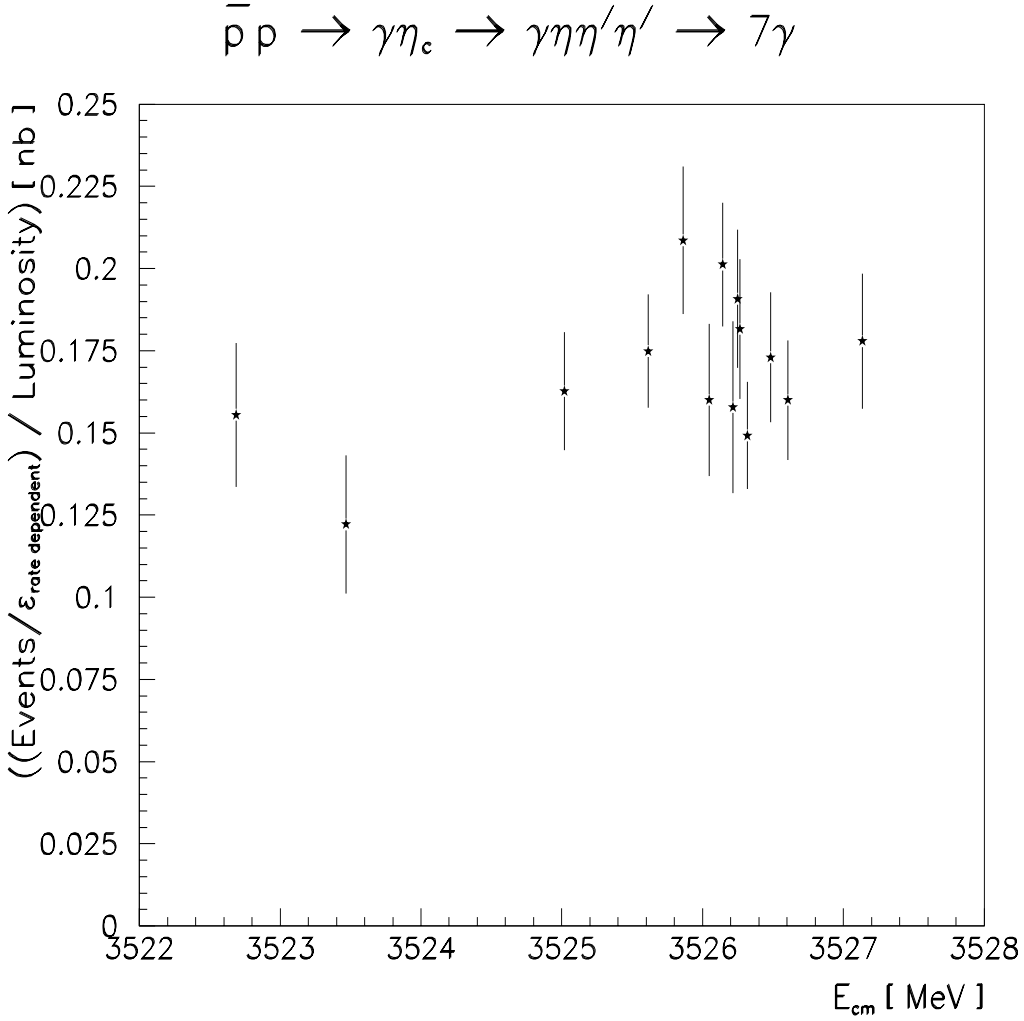

Figure 8.14: The results of the search for a resonance from $\bar{p}p \rightarrow \eta_c\gamma \rightarrow \eta\eta'\eta'\gamma$, a 7γ final state. The number of events is corrected on a run by run basis for the rate dependent efficiencies (binned by stack).

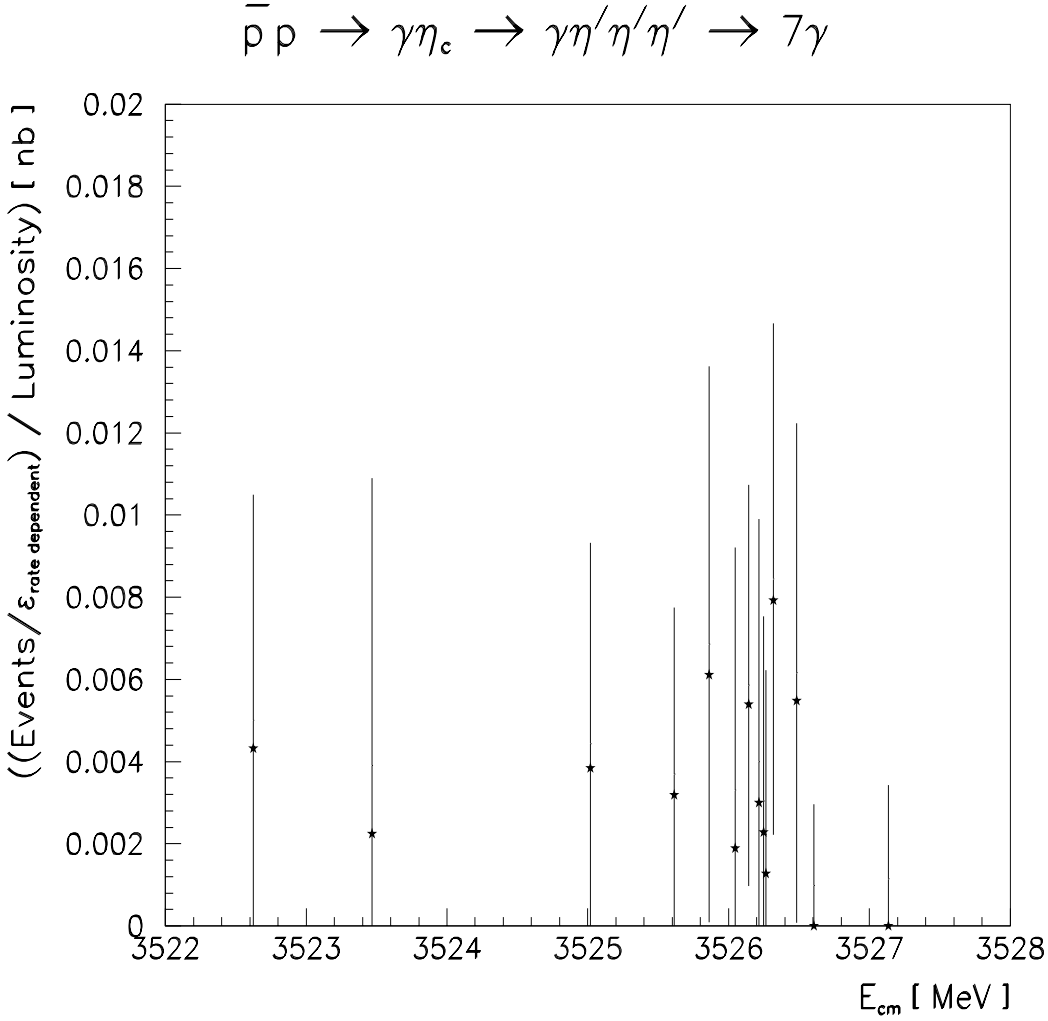

Figure 8.15: The results of the search for a resonance from $\bar{p}p \rightarrow \eta_c\gamma \rightarrow \eta'\eta'\eta'\gamma$, a 7γ final state. The number of events is corrected on a run by run basis for the rate dependent efficiencies (binned by stack).

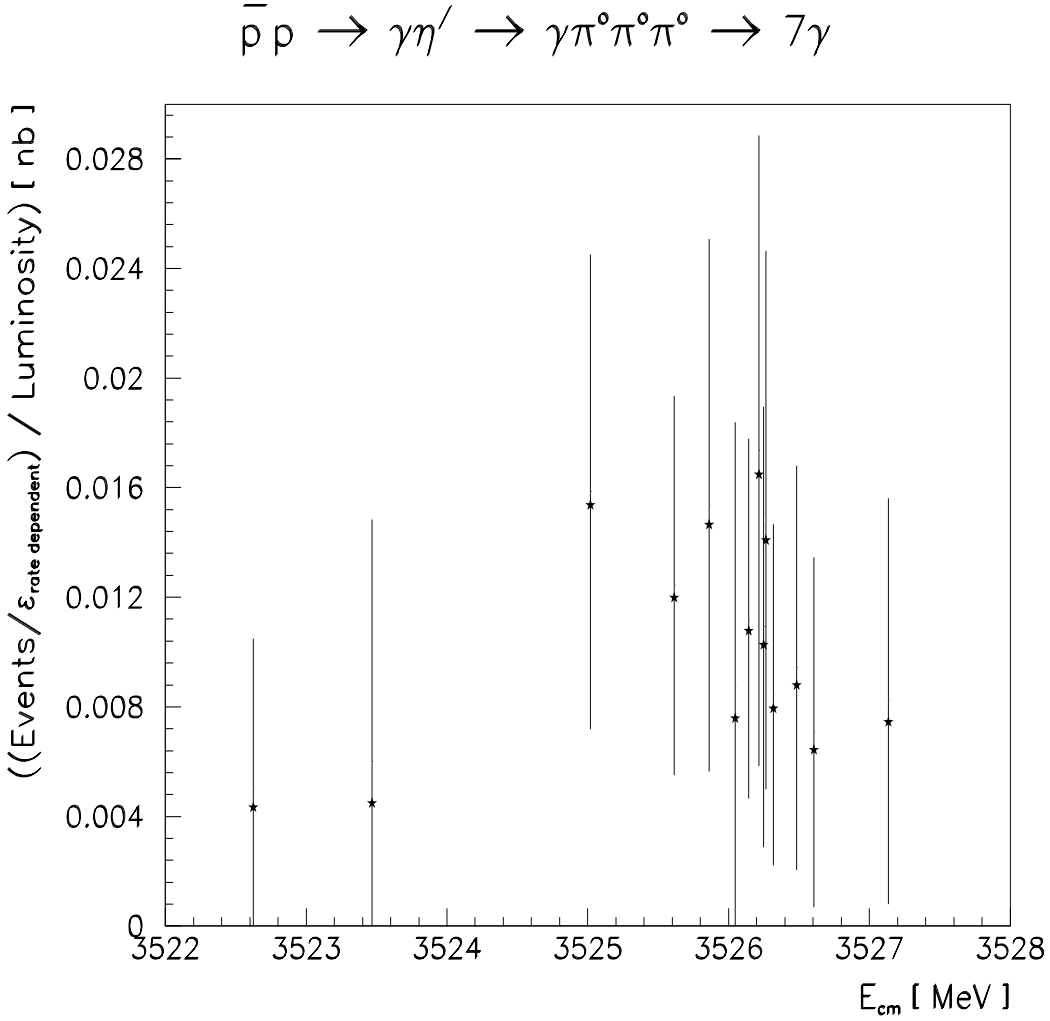

Figure 8.16: The results of the search for a resonance from $\bar{p}p \rightarrow \eta'\gamma \rightarrow \pi^o\pi^o\pi^o\gamma$, a 7γ final state. The number of events is corrected on a run by run basis for the rate dependent efficiencies (binned by stack).

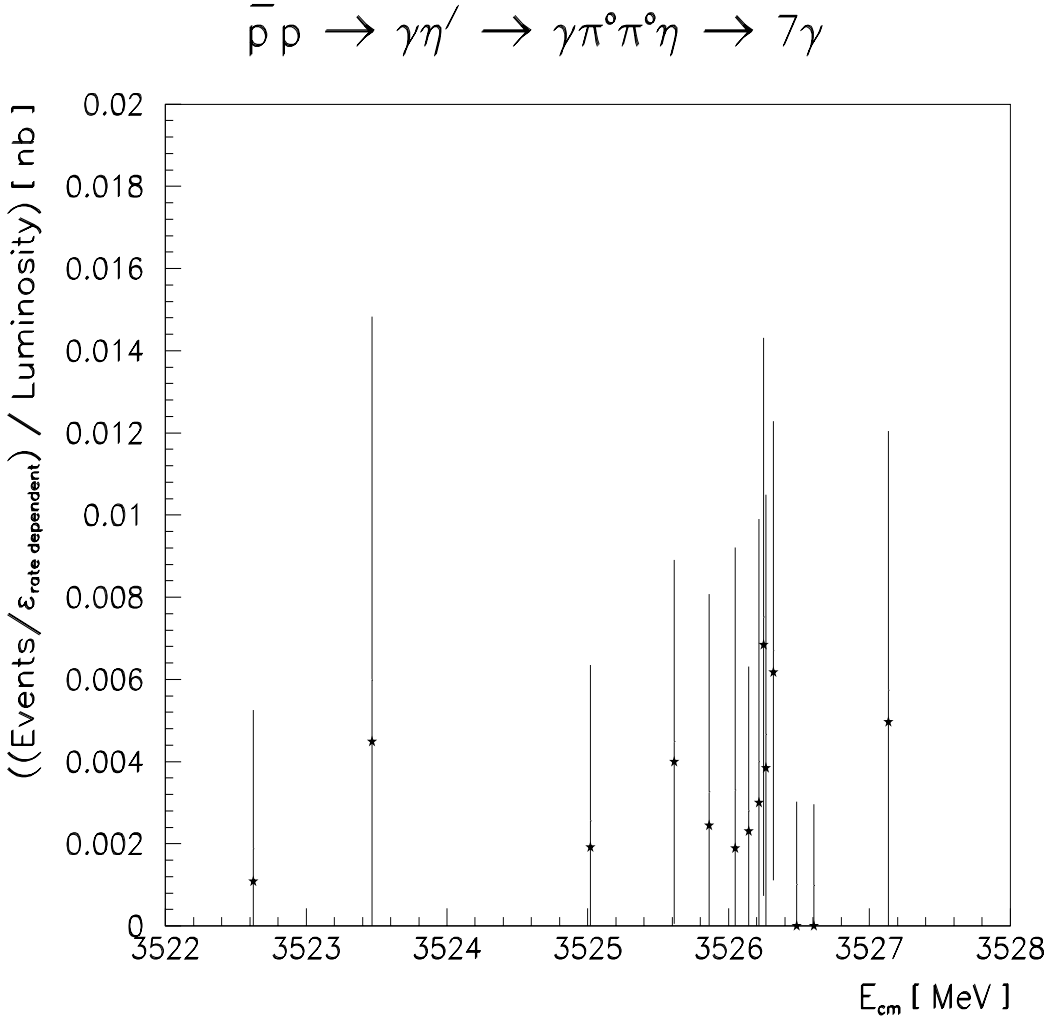

Figure 8.17: The results of the search for a resonance from $\bar{p}p \rightarrow \eta'\gamma \rightarrow \pi^o\pi^o\eta\gamma$, a 7γ final state. The number of events is corrected on a run by run basis for the rate dependent efficiencies (binned by stack).

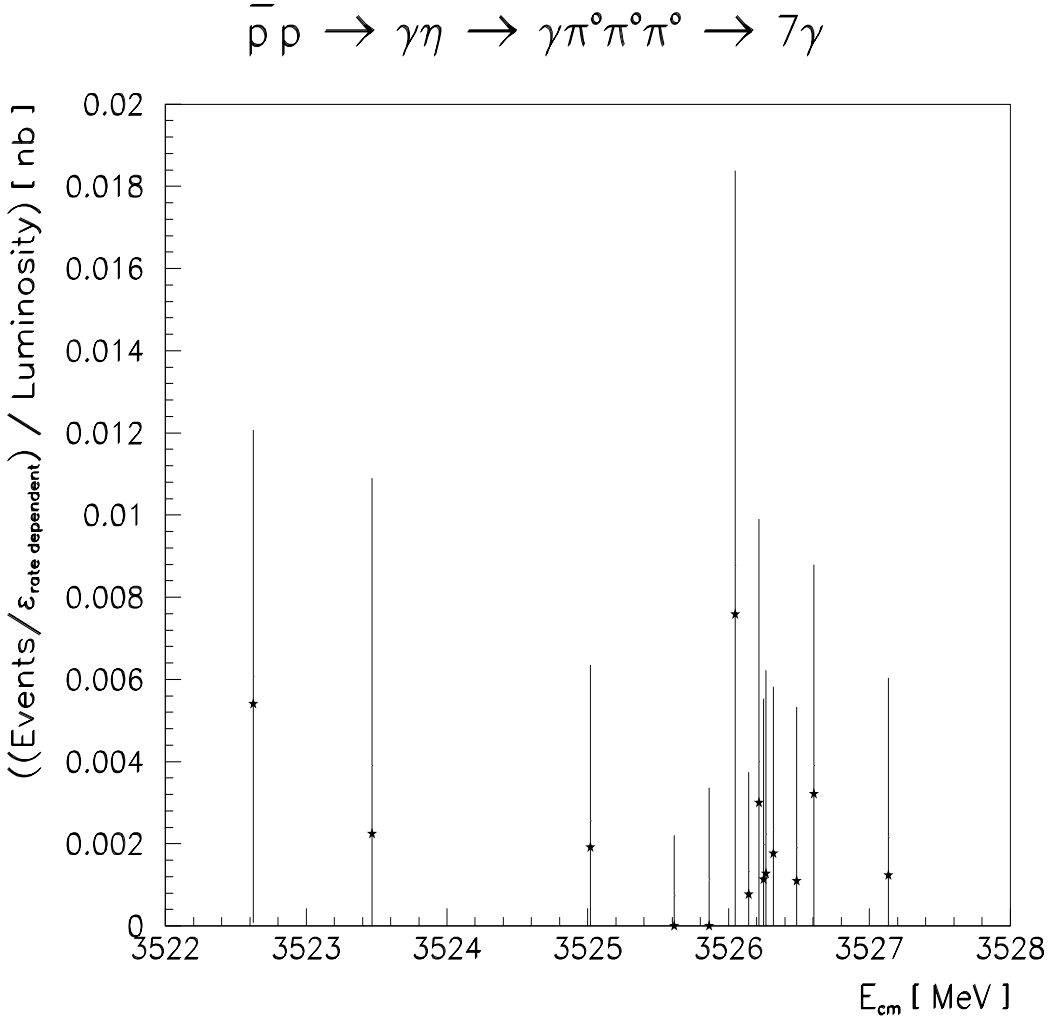

Figure 8.18: The results of the search for a resonance from $\bar{p}p \rightarrow \eta\gamma \rightarrow \pi^o\pi^o\pi^o\gamma$, a 7γ final state. The number of events is corrected on a run by run basis for the rate dependent efficiencies (binned by stack).

7γ State	Branching Ratio Product Upper Limit (90% CL)		
$\gamma\eta_c \to \gamma\pi^o\pi^o\eta$	$B(^1\mathrm{P}_1 \to \bar{p}p)B(^1\mathrm{P}_1 \to \gamma\eta_c)$	$\leq$	1.1×10^{-4}
$\gamma\eta_c \to \gamma\pi^o\pi^o\eta'$	$B(^1\mathrm{P}_1 \to \bar{p}p)B(^1\mathrm{P}_1 \to \gamma\eta_c)$	$\leq$	2.2×10^{-3}
$\gamma\eta_c \to \gamma\pi^o\pi^o\pi^o$	$B(^1\mathrm{P}_1 \to \bar{p}p)B(^1\mathrm{P}_1 \to \gamma\eta_c)B(\eta_c \to \pi^o\pi^o\pi^o)$	$\leq$	1.6×10^{-6}
$\gamma\eta_c \to \gamma\pi^o\eta\eta$	$B(^1\mathrm{P}_1 \to \bar{p}p)B(^1\mathrm{P}_1 \to \gamma\eta_c)B(\eta_c \to \pi^o\eta\eta)$	$\leq$	1.1×10^{-5}
$\gamma\eta_c \to \gamma\pi^o\eta\eta'$	$B(^1\mathrm{P}_1 \to \bar{p}p)B(^1\mathrm{P}_1 \to \gamma\eta_c)B(\eta_c \to \pi^o\eta\eta')$	$\leq$	2.5×10^{-4}
$\gamma\eta_c \to \gamma\pi^o\eta'\eta'$	$B(^1\mathrm{P}_1 \to \bar{p}p)B(^1\mathrm{P}_1 \to \gamma\eta_c)B(\eta_c \to \pi^o\eta'\eta')$	$\leq$	1.7×10^{-3}
$\gamma\eta_c \to \gamma\eta\eta\eta$	$B(^1\mathrm{P}_1 \to \bar{p}p)B(^1\mathrm{P}_1 \to \gamma\eta_c)B(\eta_c \to \eta\eta\eta)$	$\leq$	7.8×10^{-6}
$\gamma\eta_c \to \gamma\eta\eta\eta'$	$B(^1\mathrm{P}_1 \to \bar{p}p)B(^1\mathrm{P}_1 \to \gamma\eta_c)B(\eta_c \to \eta\eta\eta')$	$\leq$	1.7×10^{-4}
$\gamma\eta_c \to \gamma\eta\eta'\eta'$	$B(^1\mathrm{P}_1 \to \bar{p}p)B(^1\mathrm{P}_1 \to \gamma\eta_c)B(\eta_c \to \eta\eta'\eta')$	$\leq$	3.9×10^{-3}
$\gamma\eta_c \to \gamma\eta'\eta'\eta'$	$B(^1\mathrm{P}_1 \to \bar{p}p)B(^1\mathrm{P}_1 \to \gamma\eta_c)B(\eta_c \to \eta'\eta'\eta')$	$\leq$	5.5×10^{-3}
$\gamma\eta' \to \gamma\pi^o\pi^o\pi^o$	$B(^1\mathrm{P}_1 \to \bar{p}p)B(^1\mathrm{P}_1 \to \gamma\eta')$	$\leq$	5.8×10^{-5}
$\gamma\eta' \to \gamma\pi^o\pi^o\eta$	$B(^1\mathrm{P}_1 \to \bar{p}p)B(^1\mathrm{P}_1 \to \gamma\eta')$	$\leq$	5.6×10^{-7}
$\gamma\eta \to \gamma\pi^o\pi^o\pi^o$	$B(^1\mathrm{P}_1 \to \bar{p}p)B(^1\mathrm{P}_1 \to \gamma\eta)$	$\leq$	7.7×10^{-8}

Table 8.4: The upper limits (90% CL) for the product of branching fractions from the 7γ channel analyses. The method is outlined in the text using the known branching fractions from reference [21].

divided by the integrated luminosity for the stack. Upper limits from the 7γ analysis can be placed upon the product of branching fractions in the same manner as has been done with the 3γ final state; the results are shown in table 8.4. Known branching fractions from reference [21] have been used.

8.5 Discussion

The $^1\mathrm{P}_1$ resonance has been detected through the decay to $J/\psi\pi^o$. The mass of the $^1\mathrm{P}_1$ is found to be

$$M_{h_c} = 3526.15 \pm 0.15 \pm 0.19 \text{ MeV/c}^2, \tag{8.15}$$

where the first error is the statistical error as determined from the fit and the second error is the systematic error from the uncertainty of the beam energy calibration.

This implies the hyperfine mass splitting (equation 1.41) is

$$\Delta_{HF} = 0.88 \pm 0.47 \text{ MeV}; \tag{8.16}$$

therefore, $M_{h_c} > M_{\chi cog}$. An upper limit (90% CL) of the resonance width is set at

$$, _{h_c} \leq 1.1 \text{ MeV}. \tag{8.17}$$

A determination of the width is not possible in these data due to the low statistics and large width of the beam energy distribution. Assuming 1.0 MeV $\geq , _{h_c} \geq 0.5$ MeV, the product of the production and decay branching ratios of the $^1\mathrm{P}_1$ is

$$(1.2 \pm 0.4) \times 10^{-7} \leq B(^1\mathrm{P}_1 \rightarrow \bar{p}p)B(^1\mathrm{P}_1 \rightarrow J/\psi\pi^o) \leq (1.7 \pm 0.5) \times 10^{-7}. \tag{8.18}$$

If the largest predicted partial width for the $J/\psi\pi^o$ decay from table 1.4, 2 keV, and a 750 keV total width is assumed, then the production branching fraction is 5.5×10^{-5} which is close to the corresponding value for the χ_1.

E760's measurement of the $^1\mathrm{P}_1$ conflicts with the R704 interpretation of its five $J/\psi + X$ events as a resonance. When R704's energy scale is adjusted by using both experiments' measurements of the χ_1 and χ_2 masses, the five events are centered at 3524.60 ± 0.85 MeV/c^2, less than $M_{\chi cog}$, or Δ_{HF} is -0.67 ± 1.08. This is different from (1.55 MeV lower), but not incompatible with, the E760 result (equation 8.16). The five events also imply an order of magnitude larger product of branching ratios than found above; if R704's resonance interpretation is true, E760 should have seen an excess of several hundred events. E760 has not seen such a large signal. One of the five events can be attributed to the same background as seen by E760, the $J/\psi\pi^o$

continuum and $J/\psi\gamma$, and the remaining four events may be misidentified $\bar{p}p \to \pi^o\pi^o$ (where the π^o's undergo Dalitz decay and/or gamma rays convert in the beam pipe). When the E760 charged data set is subject to the analysis cuts applied by R704 and corrections are made for the different acceptances and integrated luminosities, four such events result. Hence, the five $J/\psi + X$ events that R704 observed near the expected $^1\mathrm{P}_1$ mass are most likely background events.

An upper limit for the $^1\mathrm{P}_1$ to decay to $J/\psi\pi\pi$ can be determined from the two upper limits for $J/\psi\pi^o\pi^o$ and $J/\psi\pi^+\pi^-$ (equations 8.8 and 8.9). The combined limit[4] assumes one third of the $J/\psi\pi\pi$ decays will be $J/\psi\pi^o\pi^o$ decays. The upper limit (90% CL) for product of branching ratios is

$$B(^1\mathrm{P}_1 \to \bar{p}p) \times B(^1\mathrm{P}_1 \to J/\psi\pi\pi) \leq 3.2 \times 10^{-8}. \tag{8.19}$$

Using this result and the product of branching ratios for a 750 keV resonance width from the $J/\psi\pi^o$ analysis (see table 8.2), an upper limit (90% CL) can be set

$$\frac{B(^1\mathrm{P}_1 \to J/\psi\pi\pi)}{B(^1\mathrm{P}_1 \to J/\psi\pi^o)} \leq 0.21. \tag{8.20}$$

Predicted values for this ratio (see tables 1.3 and 1.4) are greater than 2; the experimental limit is not compatible with any of these predictions. However, Voloshin [83] predicts that hadronic transitions from an excited triplet S state to the singlet P state in the bottomonium system will favor π^o over $\pi\pi$ (by an order of magnitude). If the same prediction applies to the hadronic transitions in charmonium from the $^1\mathrm{P}_1$ to the J/ψ, then this prediction is in agreement with E760's experimental result.

[4]Independent upper limit measurements , $_i$ for the same mode result in the combined upper limit $\frac{1}{\Gamma} \geq \sum \frac{1}{\Gamma_i}$.

The upper limit (90% CL) for the product of branching ratios of the expected dominant decay channel and the production channel is

$$B(^1\mathrm{P}_1 \to \bar{p}p) \times B(^1\mathrm{P}_1 \to \gamma\eta_c) \leq 2.6 \times 10^{-5}; \tag{8.21}$$

this limit is the combined upper limits for the 3γ final state (equation 8.13) and two 7γ final states (the first two entries in table 8.4). If the branching fraction for production found above, using the assumptions of 750 keV total width and 2 keV $J/\psi\pi^o$ partial width of the $^1\mathrm{P}_1$, then $B(^1\mathrm{P}_1 \to \gamma\eta_c) \leq 0.47$; however, this uses a partial width from a method that predicts a ratio for the hadronic transitions which contradicts E760's result, equation 8.20. Of course, if $B(^1\mathrm{P}_1 \to \bar{p}p)$ is smaller then $B(^1\mathrm{P}_1 \to \gamma\eta_c)$ is larger and $\gamma\eta_c$ can be the dominating partial width.

Other upper limits for the product of branching ratios for 7γ final states involving unobserved η_c decay modes are in table 8.4. Also included in the table are product of branching fractions for radiative decays to η' and η; the upper limits (90% CL) are

$$B(^1\mathrm{P}_1 \to \bar{p}p) \times B(^1\mathrm{P}_1 \to \gamma\eta') \leq 5.5 \times 10^{-7}, \tag{8.22}$$

where two limits are combined, and

$$B(^1\mathrm{P}_1 \to \bar{p}p) \times B(^1\mathrm{P}_1 \to \gamma\eta) \leq 7.7 \times 10^{-8}. \tag{8.23}$$

8.6 Conclusion

A resonance has been found in $\bar{p}p$ annihilations near the spin weighted center of gravity of the triplet P wave charmonium states; the resonance is identified as the

singlet P wave state, $^1P_1$ or h_c. E760 is the first experiment to observe the singlet P state in charmonium. The $^1P_1$ has only been observed in one decay channel ($J/\psi\pi^o$) with small statistics; however, the probability that the data is a fluctuation from a flat background is small ($\approx 10^{-3}$). Searches for a less than 1 MeV wide resonance in other decay channels ($J/\psi\pi\pi$, $\gamma\eta_c$, $\gamma\eta'$, and $\gamma\eta$) give null results and upper limits to the product of branching ratios have been set. Future work by the E760 collaboration will attempt to confirm this result and, hopefully, will observe the $^1P_1$ in more than the one decay channel.

Bibliography

[1] B.J. Bjorken and S.L. Glashow. *Phys. Rev. Lett.*, 10:531, 1963.

[2] O.W.. Greenberg. *Phys. Rev. Lett.*, 13:598, 1964.

[3] Schwitters and Strauch. *Ann. Rev. Nucl. Sci.*, 26:89, 1976.

[4] Litke et al. *Phys. Rev. Lett.*, 30:1189, 1973.

[5] Iliopoulos Glashow and Maiani. *Phys. Rev.*, D2:1285, 1970.

[6] N. Cabbibo. *Phys. Rev. Lett.*, 10:531, 1963.

[7] J.J. Aubert et al. *Phys. Rev. Lett.*, 33:1404, 1974.

[8] J.E. Augustin et al. *Phys. Rev. Lett.*, 33:1406, 1974.

[9] C. Bacci et al. *Phys. Rev. Lett.*, 33:1408, 1974.

[10] S. Okubo. *Phys. Lett.*, 5:1975, 1963.

[11] G. Zweig. In *Symmetries in Elementary Particle Physics*, page 192, 1965.

[12] J. Iizuka. *Prog. Theor. Phys. Suppl.*, 37-38, 1966.

[13] E. Eichten et al. *Phys. Rev.*, D21:203, 1980.

[14] J.L. Richardson. *Phys. Lett.*, 82B:272, 1979.

[15] P. Franzini and J. Lee-Franzini. *Phys. Rep.*, 81:239, 1982.

[16] A.B. Henriques et al. *Phys. Lett.*, 64B:85, 1976.

[17] D. Gromes. *Phys. Lett.*, 202B:262, 1988.

[18] J. Pumplin et al. *Phys. Rev. Lett.*, 35:1538, 1975.

[19] H.J. Schnitzer. *Phys. Rev. Lett.*, 35:1540, 1975.

[20] T.A. Armstrong et al. *Nucl. Phys.*, B373:35, 1992.

[21] Particle Data Group. Review of Particle Properties. *Phys. Rev.*, D45:1, 1992.

[22] W. Buchmüller. *Phys. Lett.*, 112B:479, 1982.

[23] P. Moxhay and J.L. Rosner. *Phys. Rev.*, D28:1132, 1983.

[24] L.P. Fulcher. *Phys. Rev.*, D42:2337, 1990.

[25] J.S. Kang. *Phys. Rev.*, D20:2978, 1979.

[26] D. Beavis et.al. *Phys. Rev.*, D20:2345, 1979.

[27] K.J. Miller and M.G. Olsson. *Phys. Lett.*, 116B:450, 1982.

[28] S.N. Gupta et al. *Phys. Rev.*, D26:3305, 1983.

[29] S.N. Gupta et al. *Phys. Rev.*, D34:201, 1986.

[30] S.N. Gupta et al. *Phys. Rev.*, D39:974, 1989.

[31] R. McClary and N. Byers. *Phys. Rev.*, D28:1692, 1983.

[32] S. Ono and F. Schöberl. *Phys. Lett.*, 118B:419, 1982.

[33] J. Pantaleone and S.H.H. Tye. *Phys. Rev.*, D37:3337, 1988.

[34] A.M. Badalyan and V.P. Yurov. *Phys. Rev.*, D42:3138, 1990.

[35] F. Halzen et al. *Phys. Lett.*, 283B:379, 1992.

[36] V.V. Dixit et al. *Phys. Rev.*, D42:166, 1990.

[37] V.O. Galkin et al. *Sov. J. Nucl. Phys.*, 51:705, 1990.

[38] L.P. Fulcher. *Phys. Rev.*, D44:2079, 1991.

[39] D.B. Lichtenberg et al. *Phys. Rev.*, D45:3268, 1992.

[40] D.B. Lichtenberg and R. Potting. *Phys. Rev.*, D46:2150, 1992.

[41] M.G. Olsson and C.J. Suchyta III. *Phys. Rev.*, D36:1459, 1987.

[42] K. Igi and S. Ono. *Phys. Rev.*, D36:1550, 1987.

[43] K. Igi and S. Ono. *Phys. Rev.*, D37:1338, 1988.

[44] Y.Q. Chen and Y.P. Kuang. *Phys. Rev.*, D46:1165, 1992.

[45] F.M. Renard. *Phys. Lett.*, 65B:157, 1976.

[46] Novikov et al. *Phys. Rep.*, 41:1, 1978.

[47] K.T. Chao et al. *Phys. Lett.*, 301 B:282, 1993.

[48] G.T. Bodwin et al. *Phys. Rev.*, D46:1914, 1992.

[49] R. Casalbuoni et al. *Phys. Lett.*, 302B:95, 1993.

[50] Y.P. Kuang et al. *Phys. Rev.*, D37:1210, 1988.

[51] M. Chemtob and H. Navelet. *Phys. Rev.*, D41:2187, 1990.

[52] G.P. Chen and Y.P. Yi. *Phys. Rev.*, D46:2918, 1992.

[53] R. Barbieri et.al. *Phys. Lett.*, 61B:465, 1976.

[54] E.D. Bloom and C.W. Peck. *Ann. Rev. Nucl. Part. Sci.*, 33:143, 1983.

[55] A. Khare. *Phys. Lett.*, 137B:422, 1984.

[56] C. Baglin et al. *Nuc. Phys.*, B286:592, 1987.

[57] C. Baglin et al. *Phys. Lett.*, B171:135, 1986.

[58] V. Flamino et al. *Compilation of Cross-sections III: p and $\bar{p}$ Induced Reactions*, CERN-HERA 84-01:290, 1984.

[59] Design Report: Tevatron 1 Project, Fermi Natioanl Accelerator Laboratory. Batavia, IL, (unpublished), September 1984.

[60] T.A. Armstrong et al. *Phys. Rev.*, D47:772, 1993.

[61] T. Bagwell et al. Fermilab Technical Memo 1254, Fermi National Accelerator Laboratory, 1984.

[62] Cern Accelerator School. *Antiprotons for Colliding Beam Facilites, October 1983*, Cern report CERN84-15, 1984.

[63] D. Broussard. Cern Accelerator School 1985. *Advance Accelerator Physics*, CERN 87-03 vol. II:416, 1987.

[64] M. Macri. Gas Jet Targets. *CERN Accelerator Summer School 1983*, CERN 85-15, 1985.

[65] E760 Collaboration. Proton-antiproton Elastic Scattering. To be published.

[66] M.M. Block and R.N. Cahn. *Rev. Mod. Phys.*, 57(2):563, 1985.

[67] C. Biino et al. *Nucl. Inst. & Meth.*, A317:135, 1992.

[68] C. Biino et al. *Nucl. Inst. & Meth.*, A271:417, 1988.

[69] R. Calabrese et al. *Nucl. Inst. & Meth.*, A277:116, 1989.

[70] G. Barisone et al. Report A.E./89-6, I.N.F.N., 1989.

[71] M.A. Hasan et al. *Nucl. Inst. & Meth.*, A295:73, 1990.

[72] L. Bartosek et al. *Nucl. Inst. & Meth.*, A301:47, 1991.

[73] R. Ray et al. *Nucl. Inst. & Meth.*, A307:254, 1991.

[74] S. Hansen et al. *IEEE Trans. on Nucl. Sci.*, 34:1003, 1987.

[75] I. Gaines et al. *Computer Physics Communications*, 45:323, 1987.

[76] C. Gay et al. *IEEE Trans. on Nucl. Sci.*, 34:870, 1987.

[77] G.A. Akopdjanov et al. *Nucl. Instr. and Meth.*, 140:441, 1977.

[78] M. Jacob and G.C. Wick. *Annals of Physics*, 7:404, 1959.

[79] J.D. Richman. An Experimenter's Guide to the Helicity Formalism. *DOE Research and Development Report*, 1984.

[80] A.G. Frodesen et al. *Probability and Statisics in Particle Physics*. 1979.

[81] M.K.. Gaillard et.al. *Phys. Lett.*, 110B:489, 1982.

[82] E760 Collaboration. Measurement of the $\gamma\gamma$ Partial Widths of Charmonium Resonances. To be published.

[83] M.B. Voloshin. *Sov. J. Nucl. Phys.*, 43:1011, 1986.

[84] Kirsebom and Sollie. *Nucl. Instr. and Meth.*, A245:351, 1986.

[85] A.V. Inyakin et al. *Nucl. Instr. and Meth.*, 215:103, 1983.

[86] B. Rossi. *High Energy Physics*. Prentice–Hall, Inc., Englewood Cliffs, NJ, 1970.

Appendix A

Spectrophotometer Modifications

A spectrophotometer was modified to measure the transmittance of the E760 central calorimeter lead-glass blocks. Due to the length of the lead-glass blocks (see table 3.1), physical modifications to a spectrophotometer setup were necessary. Due to some inherent problems with the modified spectrophotometer setup, software modifications were also necessary. This appendix explains the necessary modifications.

There are two types of variable wavelength spectrophotometers: photo-diode array and conventional scanning. Photo-diode array spectrophotometers are advantageous since a whole spectrum can be measured within seconds instead of the longer time a conventional scanning spectrophotometer takes to turn a grating. A Hewlett-Packard 8451A Diode Array Spectrophotometer was employed in this work. The 8451A is capable of 2 nm resolution between 190 and 820 nm and the sample time is one second. Hewlett-Packard has also developed computer software which allows a personal computer (an IBM AT was used) to control the 8451A spectrophotometer through a HPIB interface bus.

A.1 Physical Modifications

Spectrophotometers are generally used in chemistry to measure absorbances of solutions contained in cuvettes. Therefore, the sample compartment for most spectrophotometers is about 12 cm and has an apparatus to hold cuvettes. Although some of the block widths could fit into the sample compartment, this was not feasible. Besides being awkward, the non-parallel side faces of the lead-glass blocks would have refracted the light away from the spectrophotometer detector slit. The lead-glass blocks have only two parallel faces: the front and back faces, which are 35 to 50 cm apart.

The 8451A spectrophotometer has a deuterium lamp as the source. To keep the modification of the 8451A sample compartment to a minimum, an external source has been substituted for the deuterium lamp. A Hamamatsu 75 watt Xenon arc lamp is used as the source; figure A.1 shows the spectrum. The shutter control is disconnected from the spectrophotometer's internal deuterium lamp and connected to a shutter for the Xenon light source.

A new sample compartment, 55 cm tall and 20 cm square, was built. There are holes at the top and bottom where fiber optics were mounted to the compartment. The adjustable top mount allows the distance between the fiber optic mounts to be set between 40 to 60 cm.

The source, the new sample compartment and the spectrophotometer are connected optically by two Applied Photonic Devices 2 m long quartz fiber optic cables,

Figure A.1: The xenon lamp spectrum that has been used in the modified spectrophotometer setup.

as shown in figure A.2. The connecting fiber optic cables are 660 μm core diameter, cladded and terminated SMA style. One fiber optic cable is connected to the xenon lamp source housing. The other end of the fiber optic cable is mounted in a collimating beam probe with a focal length of 19 mm, which is then mounted at the bottom of the sample compartment. Two other collimating beam probes are connected to the ends of the second optic fiber and mounted in the adjustable top mount of the sample compartment, making a collecting lens, and on a platform located in the spectrophotometer's sample compartment. Also located on the platform, a 1/4 wave adjustable mirror directs the collimated beam into a slit leading to the spectrograph, a grating which reflects the light onto a series of diodes.

The responses of the setup to different wavelengths of light have to be taken into consideration. The collimating beam probe consists of a plano-convex fused silica lens: focal length of 19 mm at wavelength 587 nm, according to the Oriel Optics Catalogue. The focal lengths at 335 and 644 nm wavelengths are 18.16 and 19.07 mm, respectively, using the refractive indices at these wavelengths from the catalogue. The finite size of the optical fiber (0.6 mm diameter) does not compensate for the 0.9 mm focal length difference for the two wavelengths. The opening angle of the optical fiber was found to be about 15°, whereas the lens from the focal point subtends an angle of 16°. Thus not all of the wavelengths will be emitted parallel to the axis of the beam probe for a fixed geometry. The light beam diverges within the sample compartment. Also, the angle of collimation is calculated to be 0.0315 (from the Oriel Catalogue, $C = d/f$ where C is the angle of collimation, d is the

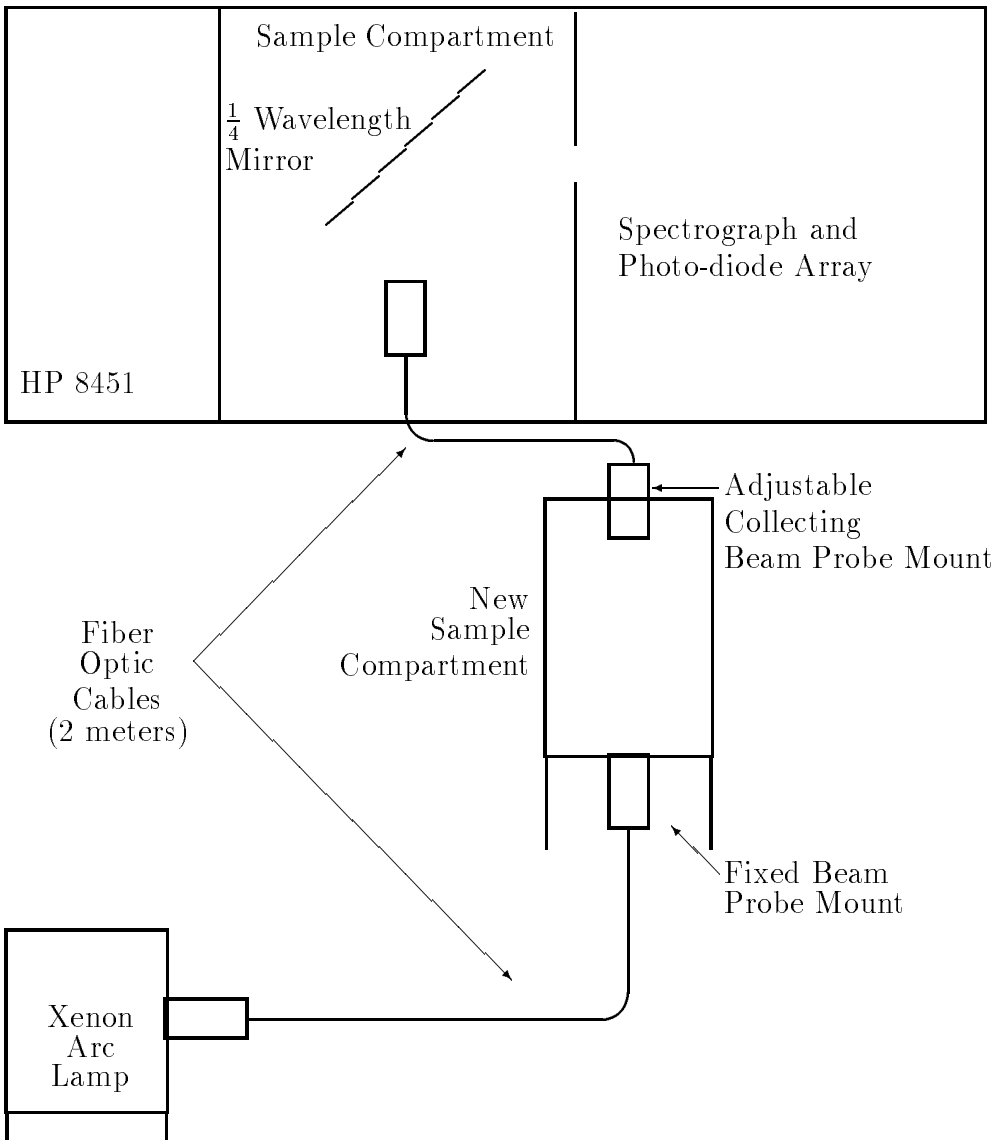

Figure A.2: The modified spectrophotometer setup (shown not to scale).

diameter and f is the focal length). Using the angle of collimation and Snell's Law, the diameter of the light spot at the collecting lens is 0.78 mm smaller for wavelength 589 nm through 40 cm of F2 lead-glass when compared to 40 cm of air. The F2 lead-glass effectively focuses the light. By the time the light reaches the collecting lens, the spot is significantly larger than the collecting lens. The ratios of the areas of the collecting lens and beam spots with 40 cm of air (F2 lead-glass) is calculated to be 0.74 (0.90).

Achromatic lenses were investigated as a possible solution to the non-parallelism of the collimated beam. Literature research showed that a commercially available achromat might be a small improvement compared to the collimating beam probes. An achromat was purchased to be used in conjunction with the collecting collimated beam probe. There, however, was no improvement and it was decided to only use the collimated beam probes.

Generally, one would like to compare the sample lead-glass blocks to a known reference. Ideally, a short piece of the same material is used as the reference, but the focusing effect is greater for the longer pieces of lead-glass when the collecting lens is a fixed distance from the emitting lens. For a reference piece of lead-glass that is 25% of the length of a lead-glass block, the collecting lens can not be moved far enough to ensure the same beam spot size for both lead-glass pieces. Air is another choice for the reference. Again, the collecting lens could not be moved far enough to compensate for the focusing effect of the lead-glass. In either case, there would need to have been a very reliable method to determine the spot size and reproduce the size

reliably at the collecting lens. Calculations suggested that the lens placement has to be accurate to 0.5 mm to be within 5% of the same spot size. The use of a set screw does not allow for the needed placement accuracy. Keeping the collecting lens fixed, corrections to the spectra are needed to compensate for the difference in light spot sizes and, therefore, intensities.

A.2 Software Modification

Transmittance is calculated in terms of the ratio of intensities through the sample, corrected for dark current, with respect to a reference. For a fixed collecting lens, *transmittance* of a 40 cm lead-glass block with respect to air is greater than 100% due to the focusing. It was decided to correct for the difference in spot sizes through software. Since the spot size differs for different wavelengths, a correction factor has to depend on wavelength.

A direct way to find a wavelength dependent factor was to change the spot size in air by moving the collecting probe, as the spot size would change between lead-glass and air measurements. While the collecting probe was moved, the intensities were recorded every 1 to 2 mm and compared to the greatest recorded intensity (the smallest spot size–smallest separation distance). A total of sixty-one air intensity spectra were recorded representing the full range of separation distances. The intensity of wavelengths 600, 450 and 350 nm were reduced over the course of travel to 54.3%, 53.4% and 52.3% ($\pm$0.5%) of their greatest values, respectively, showing

a small wavelength dependence. The intensity values of the spectra at 600 nm were divided by the 600 nm intensity value from the spectrum taken when the beam probe separation was smallest. These intensity ratios are used to correct for the focusing, see below.

The procedure to measure the transmittance of the F2 lead-glass blocks with the spectrophotometer is as follows. After the instrument has been allowed to warm up, dark current and air reference measurements are made and recorded with the sample compartment empty. A lead-glass block is then placed in the sample compartment. While the lead-glass block is rotated about its axis, intensities at several wavelengths are sampled continuously. Up to 5% fluctuations of the intensities are observed during a full rotation of a lead-glass block. The changing intensities can be explained as due to the end faces of the lead-glass block not being parallel; the light is not at normal incidence at the exit face, causing the spot not to be centered upon the collecting lens. The smaller wavelengths are affected more than the green part of the spectrum of interest. Six wavelengths' intensities are continuously monitored as the lead-glass block is rotated once and then turned to the orientation which results in the greatest intensity values. Next, an entire intensity spectrum from 300 to 600 nm is measured and recorded. The ratio of the air to lead-glass intensities at 600 nm is calculated. The closest ratio for 600 nm intensities from above (air spectra with the beam probes at different separation distances) to the air/lead-glass ratio indicates which of the sixty-one spectra is used to modify the air spectrum. The dark current (intensity) spectrum is subtracted from both the lead-glass sample and modified air reference spectrum

before taking the ratio which is defined as the transmittance for the block. A sample transmission spectrum is shown in figure 3.7. The method forces the transmittance at 600 nm to be 100% for the lead-glass.

A.3 Discussion

The HP8451A transmittance measurement is good to better than 1%. If a lead-glass block is oriented the same each time (when the intensity is greatest for all of the wavelengths), then the transmission spectrum is reproducible with less than 2% variation for all wavelengths. The modifications allow for reproducible results and have been used to compare many of the central calorimeter's lead-glass blocks. The characteristics of the the lead-glass blocks' spectra are discussed in section 3.2.2

Appendix B

Radiation Damage and Curing

The transparency of lead-glass decreases as it is irradiated. Radiation damage of lead-glass leads to a *yellowing* or *darkening* of the lead-glass. The coloring of the lead-glass is caused by creation of color centers or by the development and growth of absorption bands. The absorption bands decrease the amount of Čerenkov light which reaches the photomultiplier tube and, therefore, decrease the signal.

A spectrophotometer which measures the transmittance or absorption of materials has been used to monitor radiation damage. Several F2 lead-glass sample pieces, $\approx 10 \times 2 \times 2$ cm^3 with only the two small end faces parallel and polished, have been used to monitor the radiation damage/exposure of the central calorimeter. The calorimeter's lead-glass blocks have not been used directly since they are contained within the wedge shells and are inaccessible. Using the smaller lead-glass sample pieces, the spectrophotometer is used in its normal configuration (not as described in Appendix A). In addition to the lead-glass samples placed about the calorimeter during the running, two pieces have been placed near the debuncher ring's injection kicker magnet for a short period of time.

Placement Comment		Azimuthal Angle	Distance (cm)
Upstream	+x-axis	5°	60
Upstream	+y-axis	90°	75
Upstream	−x-axis	175°	75
Upstream	−y-axis	270°	130
Downstream	+x-axis	345°	120
Downstream	+y-axis	85°	135
Downstream	−x-axis	195°	105
Downstream	−y-axis	265°	130

Table B.1: The azimuthal angles and radial distance from beam pipe of the lead-glass samples about the calorimeter.

B.1 Placement of Lead-glass Samples

The lead-glass samples have been present constantly about the central calorimeter whenever there has been beam in the $\bar{p}$ source. Twenty-four samples have been separated into sets of three and placed at eight locations about the calorimeter. Each lead-glass sample is wrapped individually in black paper. The locations have been essentially along the experiment's positive and negative x and y axes (the z-axis is along the $\bar{p}$ direction and the y-axis is pointing upward) upstream and downstream of the calorimeter. Table B.1 shows the approximate azimuthal angles and the radial distance from the beam pipe for the eight sets. The approximate polar angles at the upstream end near the interaction point are 80° for the sets along the x-axis and between 72° and 75° for the sets along the y-axis. The downstream samples have been connected to the central calorimeter cable support apparatus located 265 cm downstream of the interaction point.

Two samples were placed near the debuncher ring's injection magnet, with no shielding, during $\bar{p}$ source studies conducted in December 1990. In between the debuncher and accumulator rings near the E760 experimental area, concrete blocks provide shielding for the detector. The placement of the shielding intercepts particles coming from the $\bar{p}$ target area via the transport line and shields against radiation produced at the nearby kicker magnets. Previous to the start of the experiment, these were the expected radiation sources for E760.

B.2 Radiation Exposure

Several radiation monitors have also been placed about the calorimeter to try to measure the radiation dosage. The radiation monitors vary in type but all are connected to a visual readout system in the E760 counting room. Only two of the radiation monitors have been continually attached to the central calorimeter. The $\bar{p}$ source has operated for three different periods over two years with the central calorimeter present; the radiation dosages received by the calorimeter according to the two monitors are shown in table B.2. The two fixed target time periods had different shielding arrangements and different injection line collimator settings; additionally, the injection line tuning improved with time. During the $\bar{p}$ source studies, the E760 detector was removed from the beam line and moved as far away as possible within the experimental area from the debuncher and accumulator beam lines, however, the shielding was also removed and the collimators were opened wide. During data taking,

Time Period	Dosage (rad)
Fixed target run 1990 (May – September)	$\approx$ 70 rad
Studies of the $\bar{p}$ source (December 1990)	$\approx$ 30 rad
Fixed target run 1991 (June – January)	$\approx$ 80 rad

Table B.2: The radiation dosages, according to monitors, that the central calorimeter received in the $\bar{p}$ source.

when the gas jet is operating, the radiation monitors showed small radiation doses as compared to doses during stacking (the collection of $\bar{p}$'s).

A separate radiation monitor was placed near the kicker magnet when the two samples were in place during the December 1990 $\bar{p}$ source studies. This monitor, a propane gas ion chamber, was operated in what is called *neutron mode*, which is a factor of ten more sensitive to charged particles than neutral particles; the neutron mode assumes that the radiation does not consist of charged particles. The nature of the radiation is unknown and therefore the dosage determined from the monitor may be an over estimate. The monitor measured a dosage of 1200 rad before failing. Estimating from other radiation monitors in the area, the two samples received an additional 1000 to 2000 rad.

B.3 Radiation Damage Analysis

The transmission spectra of the lead-glass samples were made and recorded by an HP8451A spectrophotometer before exposing them to radiation. One spectrum is shown in figure B.1 along with a spectrum from one of the 50 cm long lead-glass

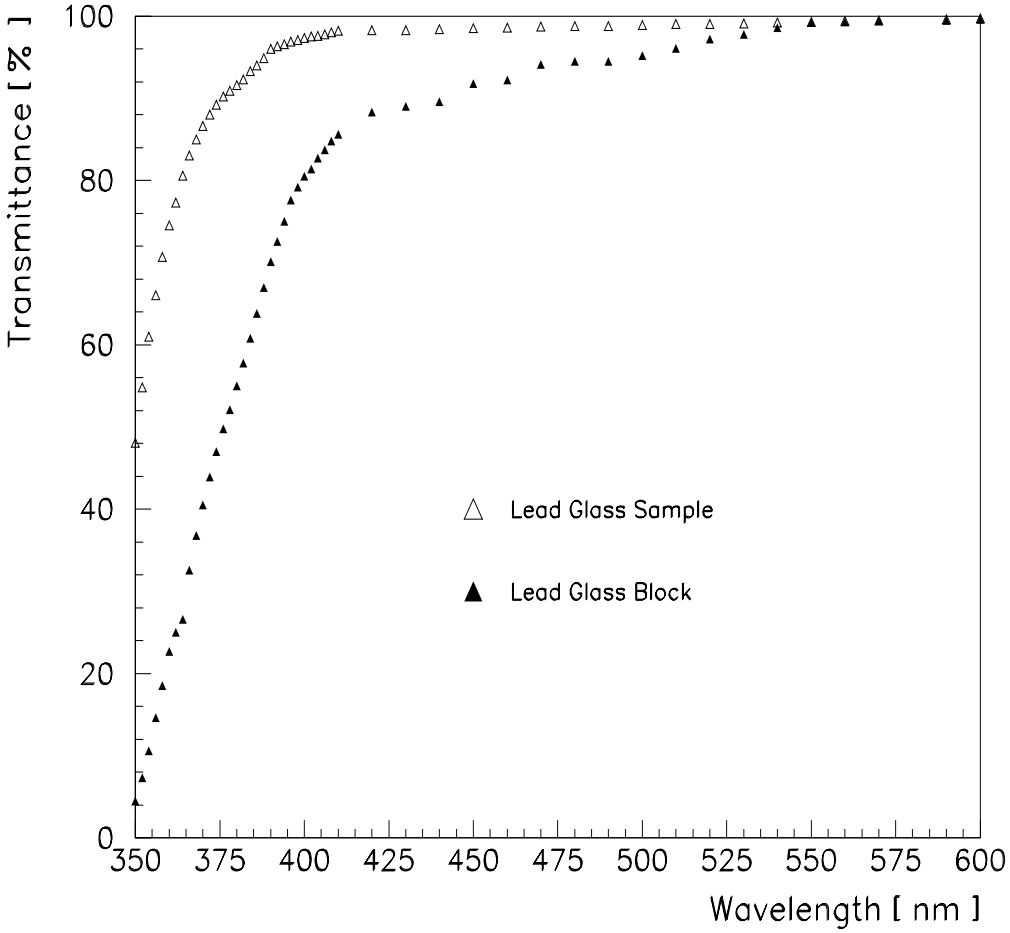

Figure B.1: A lead-glass sample's transmission spectrum and a 50 cm long lead-glass block spectrum.

blocks. The twenty-four lead-glass samples' transmittances have been re-measured after each time period as described in table B.2. None of the transmission spectra show any change, outside of the spectrophotometer's intrinsic error, from the original spectrum for the lead-glass samples that were located about the central calorimeter. The spectrophotometer's transmission measurement error for a 2 nm wavelength band interval is 2%. A 2% change in the transmittance of a small lead-glass sample

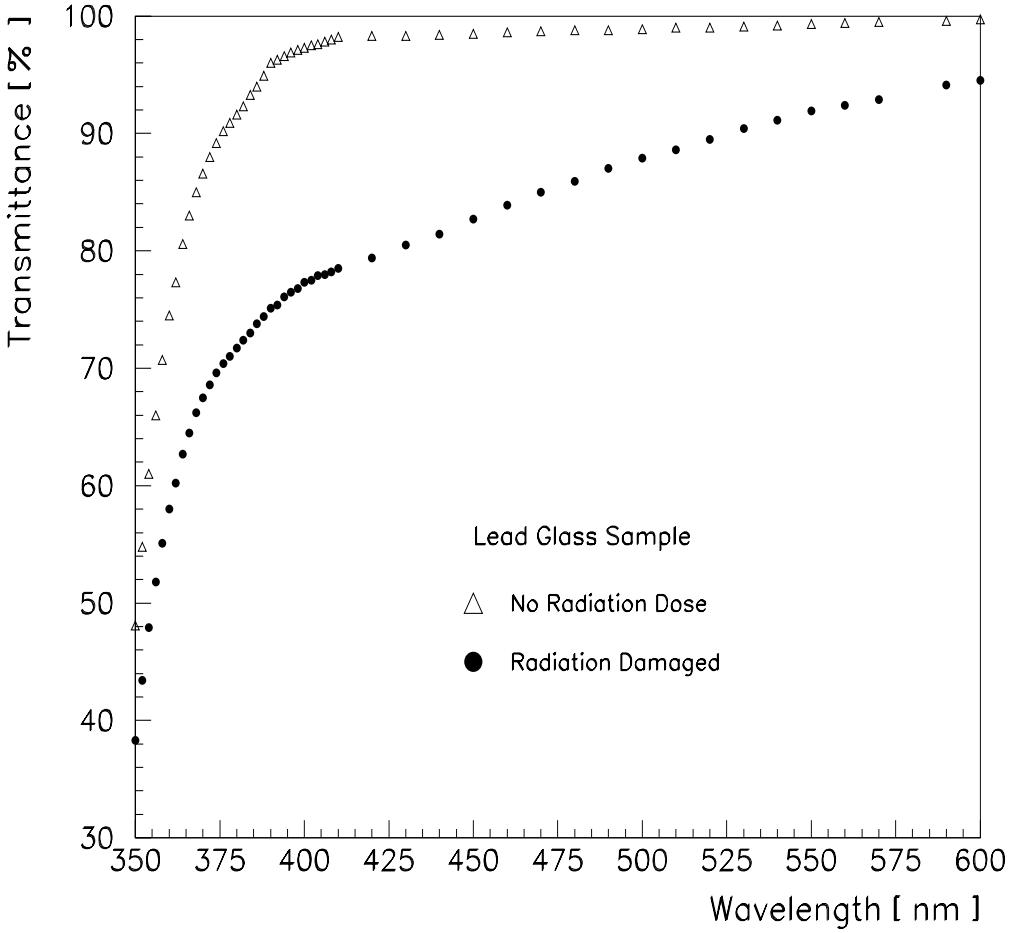

Figure B.2: The transmission spectra of one of the lead-glass samples before and after being placed near the debuncher ring's kicker magnet showing the affect of radiation damage.

corresponds to 10% change in the transmittance of a lead-glass block. The absorption of the flashlamp light would correspondingly change the flashlamp response by 20% since the light has to travel the block length twice. As stated in section 4.4.1, there has been no measureble decrease of the flashlamp response attributed to radiation damage. The lead-glass samples about the calorimeter agree with the flashlamp responses.

However, the two samples which were exposed to the larger radiation dose have shown radiation damage. Figure B.2 shows the radiation damage to the transmission spectrum; the original transmission spectrum is shown for comparison. The radiation damage affects the ultraviolet wavelengths more than the rest of the spectrum. Visually, the samples were darker and slightly brown.

The radiation dose can also be estimated another way. Kirsebom and Sollie [84] have parameterized the transmission properties of F2 lead-glass for absorbed doses, D, up to 5000 rad. The radiational absorption is defined

$$a(\lambda, D) = 1 - \frac{T(\lambda, D, x = 1\text{cm})}{T_o(\lambda)}, \tag{B.1}$$

where $T_o(\lambda)$ is the non-irradiated transmittance $T(\lambda, D = 0 \text{ rad}, x = 1 \text{ cm})$. The parameterization found by Kirsebom and Sollie is

$$a(\lambda, D) = 1 - e^{-\mu(\lambda)D}, \tag{B.2}$$

where $\mu(\lambda)$ is experimentally determined. The transmittance through x cm of lead-glass is

$$T(\lambda, D, x) = [T(\lambda, D, x = 1\text{cm})]^x \tag{B.3}$$

and substituting in appropriately the transmittance is

$$T(\lambda, D, x) = \left[T_o(\lambda)e^{-\mu(\lambda)D}\right]^x. \tag{B.4}$$

Several values of μ for several representative wavelengths have been determined by Kirsebom and Sollie. Using these values for $\mu(\lambda)$ and the transmission spectra

Wavelength (nm)	μ (10^{-6})	Calculated Dose (rad) Sample 1	Sample 2
350	40.7	434	490
400	31.8	692	622
450	21.6	782	660
500	13.3	831	670
600	5.1	652	544

Table B.3: The calculated radiation dose for the two lead-glass samples using $\mu(\lambda)$ values determined by Kiresbom and Sollie [84].

before and after irradiation, a calculated radiation dose can be determined:

$$D = \frac{1}{\mu(\lambda)x} \ln\left(\frac{T_x(\lambda)}{T(\lambda, D, x)}\right), \tag{B.5}$$

where $T_x = [T_o]^x$; the measured spectra are always for the transmittance through x cm of lead-glass. Table B.3 shows the calculated doses at the various wavelengths for the two lead-glass samples; the μ parameter is also shown. The radiation dosage appears to be between 600 and 700 rad and disagrees with the radiation monitor determination. Several explanations are possible for the discrepancy of a factor of 2 (the radiation monitor result before failure) to 5 (the largest extrapolated dosage). A basic reason could be that the F2 lead-glasses are not the same; however, one would not expect such a large difference. Another possible explanation is that the radiation monitors have overestimated the dosage since the nature of the radiation is unknown. A last possible explanation is that instant *bleaching*, or curing, of the the lead-glass occurs when exposed to light. The lead-glass samples were exposed to artificial lights while being unwrapped and placed in the spectrophotometer's sample compartment before a transmission spectrum was taken. The most reasonable explanation is that the radiation monitors have overestimated the radiation dosage.

	μ (10^{-6})					
λ		Sample 1			Sample 2	
(nm)	1200 rad	2000 rad	3000 rad	1200 rad	2000 rad	3000 rad
350	16.1	9.65	6.42	16.6	9.96	6.64
400	18.3	11.0	7.34	16.3	9.76	6.52
450	14.1	8.45	5.62	11.9	7.12	4.75
500	9.16	5.50	3.67	7.42	4.46	2.97
600	2.76	1.66	1.11	2.31	1.38	0.92

Table B.4: The calculated $\mu(\lambda)$ values for three radiation doses.

On the other hand, assuming that the radiation monitor results are correct, the two sets of spectra can be used to determine $\mu(\lambda)$. Three values of radiation dose have been used to determine $\mu(\lambda)$ and are presented in table B.4. The determined $\mu(\lambda)$ values are about a factor of three to four different than the values determined by Kirsebom and Sollie (table B.3). One does not expect the lead-glasses to be that different; the dosage determined from the radiation monitors is probably an overestimate.

Assuming that $\mu(\lambda)$ values of Kirsebom and Sollie are correct, the expected damage to the lead-glass samples on the calorimeter can be calculated. A 3% to 5% change of the transmittances for the wavelengths between 350 nm and 420 nm is expected after a 100 rad dose. The spectrophotometer is capable of showing this change in transmittance. A difference has not been seen and possible explanations, as indicated above, are either (i) the radiation monitor has overestimated the dose or (ii) instant bleaching.

Cycle Number	Exposure Time (min) Period	Cumulative
1	15	15
2	15	30
3	30	60
4	60	120
5	180	300
6	180	480
7	180	660
8	360	1020
9	360	1380

Table B.5: The exposure time periods and cumulative time that the two lead-glass samples were exposed to sunlight.

B.4 Curing

Physics practice has been to expose irradiated lead-glass to sunlight for curing. The estimated recovery time from radiation damage for lead-glass is estimated to be 50 years [85] (from measurements over a period of 1.5 years of lead-glass not exposed to light). During May 1991, the two most irradiated lead-glass samples were exposed to sunlight for different time periods. Two non-irradiated lead-glass samples were also exposed to the sunlight as controls. Table B.5 shows the exposure time periods and cumulative times; the uncertainty of the time of exposure is a few minutes. The exposure periods were scattered over a few weeks whenever there was not a threat of rain; some of the exposure periods were while the sky was overcast.

The never-irradiated lead-glass samples spectra showed no changes and continually showed that the reproducibility of the spectrophotometer results. Figure B.3 shows the radiation damaged transmission spectrum and the spectra after seven of the

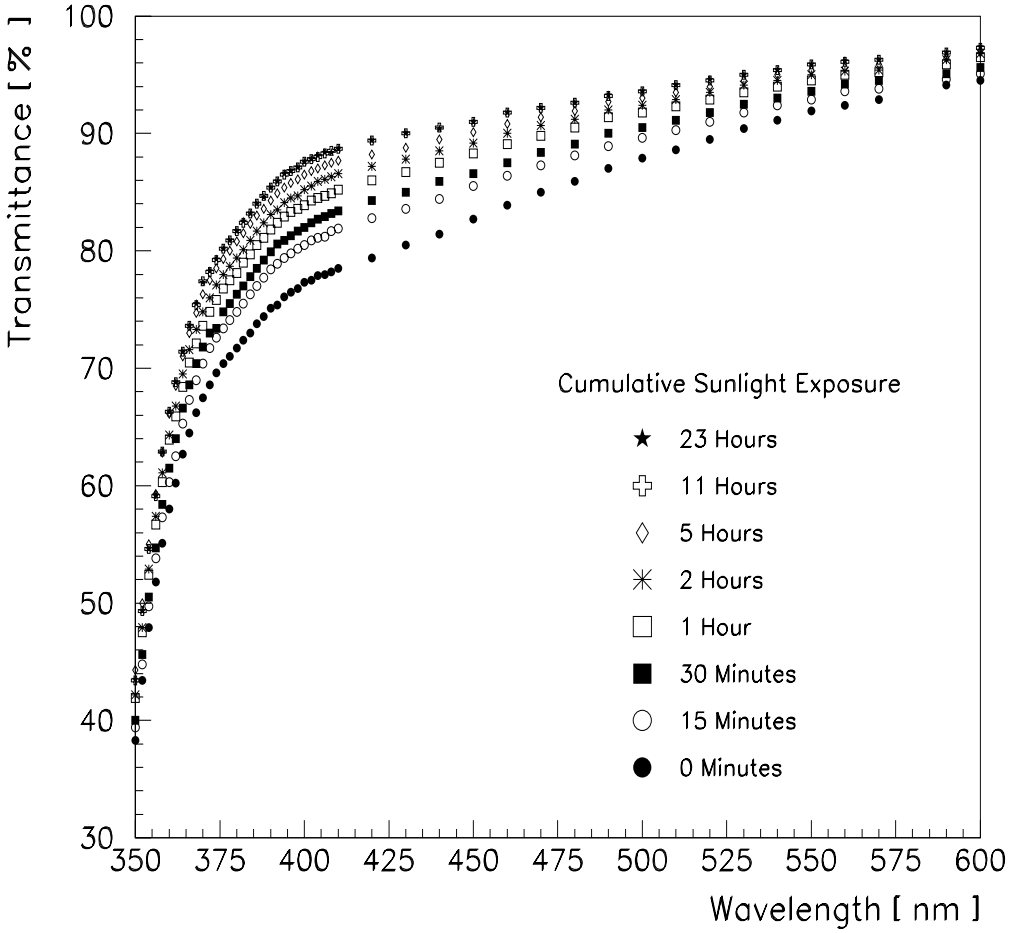

Figure B.3: The transmission spectra after different exposure periods (different cumulative times) as the lead-glass sample cures. The 11 and 23 hour cumulative time spectra are nearly the same, and the symbols are not resolved.

curing periods for one of the lead-glass samples. The spectra after 11 and 23 hours of cumulative exposure to sunlight are nearly the same. The spectra of figure B.3 have been normalized by the transmission spectrum taken before radiation exposure. These normalized spectra, as shown in figure B.4, show the loss of transmittance due to the radiation damage and the subsequent recovery due to exposure to sunlight. Complete recovery would be a value of 1.0 corresponding to no difference from

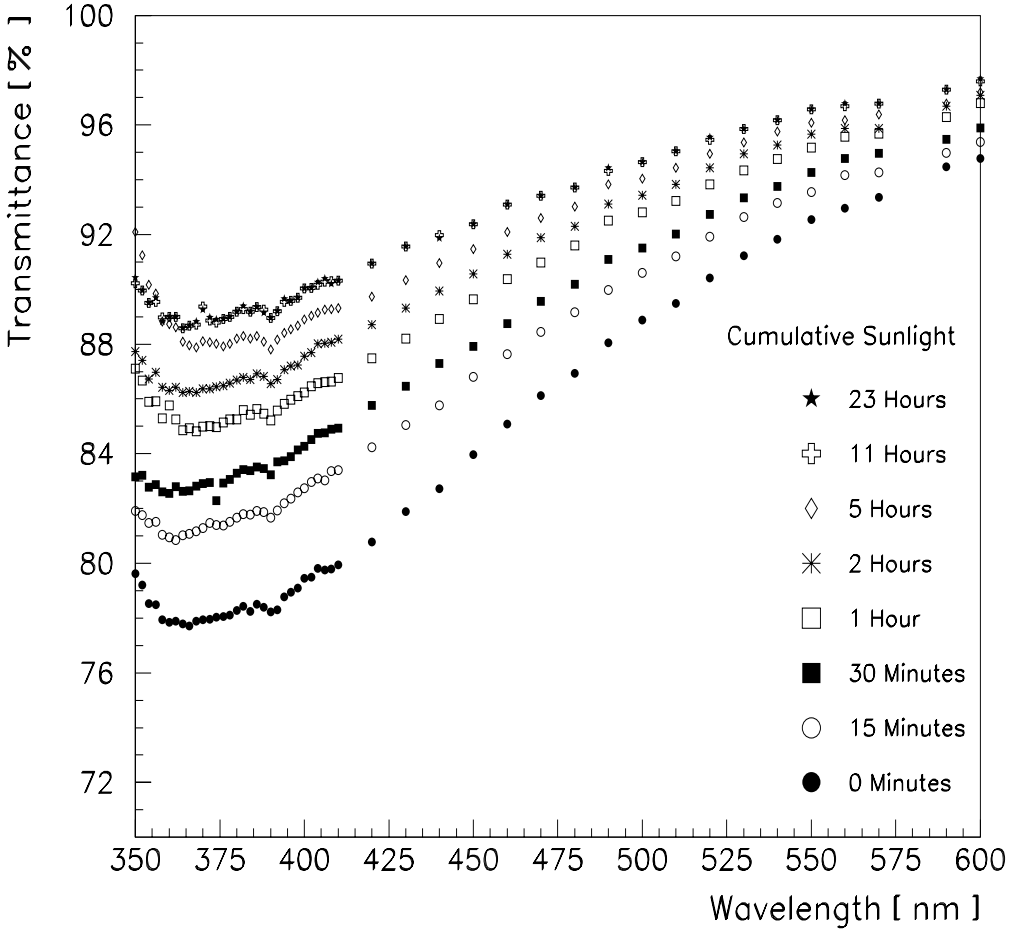

Figure B.4: The loss of transmittance due to the radiation damage and the recovery due to exposure to sunlight. The transmission spectra after different exposure periods (different cumulative times) as the lead-glass sample cures, normalized by the non-irradiated spectrum. The 11 and 23 hour cumulative time spectra are nearly the same, and the symbols are not resolved.

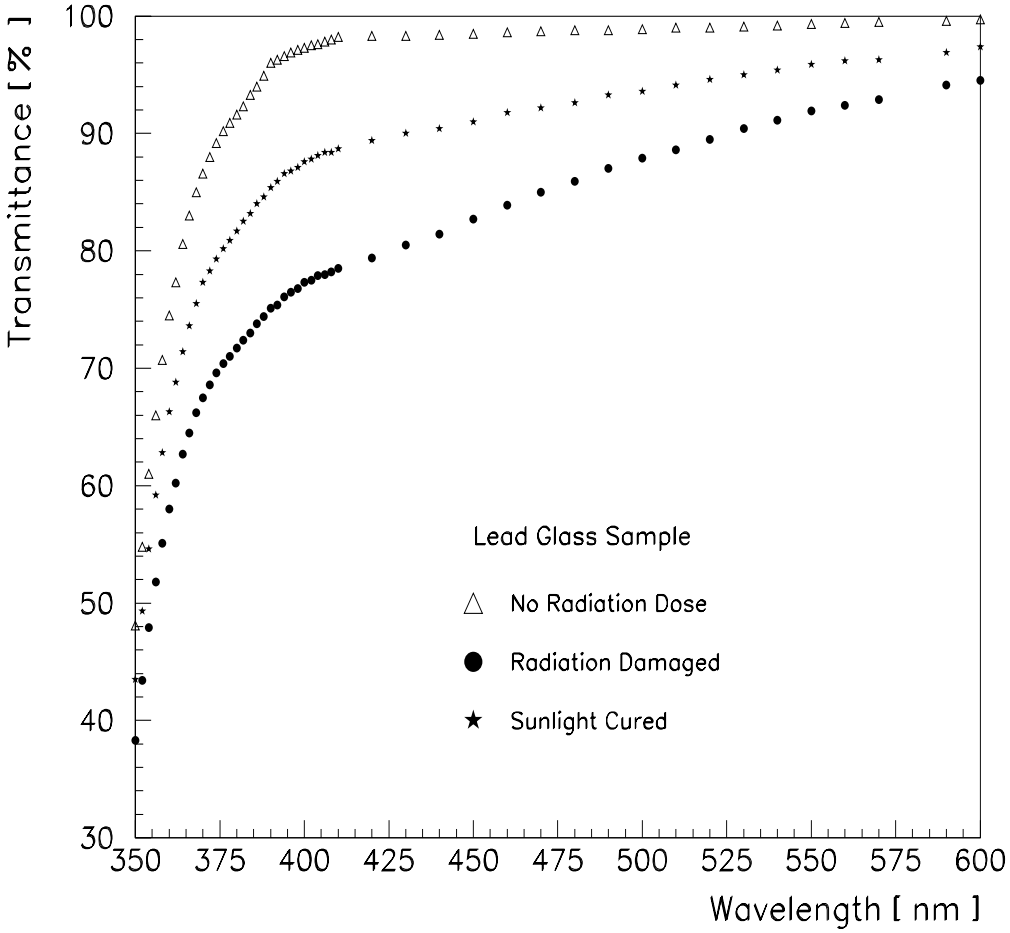

Figure B.5: The transmission spectra of a lead-glass sample before irradiation, radiation damaged and after sunlight exposure (cured).

the non-irradiated transmission spectrum. After 23 hours of exposure to sunlight, the lead-glass sample's transmittances have not shown any more recovery. The non-irradiated, radiation damaged and cured transmission spectra are shown in figure B.5. The sunlight curing does not cause a complete recovery of the transmittance.

The first hour of exposure to sunlight appears to have the greatest effect. Figure B.6 shows the transmittance normalized by the non-irradiated transmittance

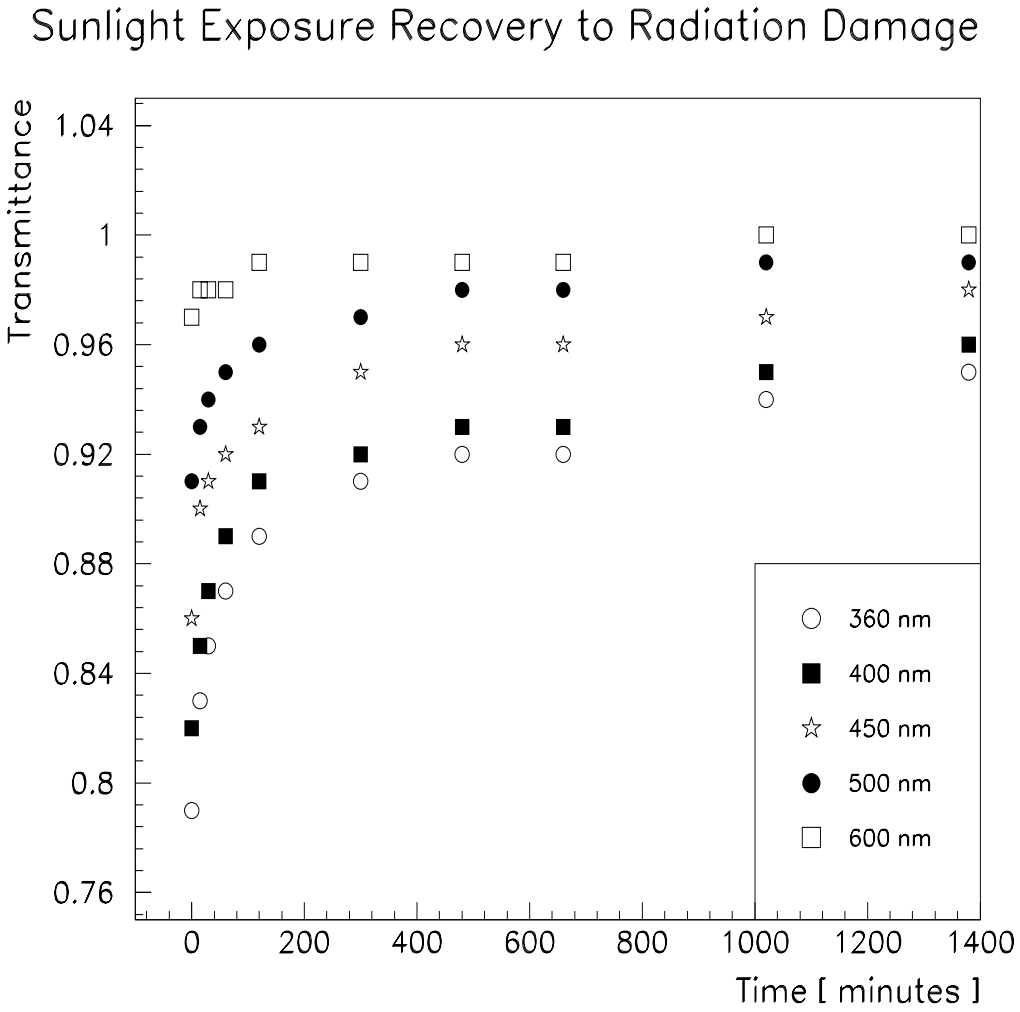

Figure B.6: The transmittance of several wavelengths while curing as a function of cumulative sunlight exposure time.

as a function of exposure time to sunlight for five wavelengths. The curing rate does not appear to be a function of wavelength.

B.5 Discussion

The spectrophotometer has been used to monitor radiation damage to the central calorimeter. The lead-glass samples placed about the central calorimeter have not shown any degradation of the transmission spectrum.

Two lead-glass samples were irradiated about a factor of 10 more than the lead-glass samples about the calorimeter. The two lead-glass samples showed radiation damage. There appears to be a discrepancy between the radiation dose received when using radiation damage parameters from a published experiment and the radiation monitors. The radiation monitors may be overestimating the dose, due to uncertainty about the type of radiation, by a factor of 2 to 5.

The two most irradiated lead-glass samples have been partially cured by exposure to sunlight. The sunlight curing does not cause the transmission spectrum to recover fully; the recovery leads to transmittances 94% of before-irradiation at ultraviolet wavelengths to nearly 100% for the green part of the spectrum. A single central calorimeter counter Monte Carlo simulation (Appendix C) shows that the photoelectron signal should decrease by 18% for a 1 GeV incident gamma ray when using Kirsebom and Sollie's parameterization of the radiation damage and assuming a 100 rad dose. Since no large decrease in signal output has been observed, it is probable that the radiation monitors associated with the central calorimeter have overestimated the radiation dose.

Appendix C

Single Counter Monte Carlo

A single lead-glass block–PMT counter Monte Carlo simulation has been developed. Some of the Monte Carlo simulation results have been described in section 4. In this appendix, a description, characteristics and results of the Monte Carlo are presented. Also included are some comparisons of the Monte Carlo results and some of the test beam studies (section 4.2).

The charged particles in the electromagnetic shower which have sufficient energy produce Čerenkov photons. The photons propagate to the PMT where photoelectrons can result. Total internal reflection is the main reason photons do not escape the block. A white paper wrapping is used to reflect photons which do not satisfy the critical angle requirement for total internal reflection. The Monte Carlo simulation tries to simulate these and other processes. The transmittance measurements through a 10 cm block of F2 lead-glass in 10 nm wavelength bands are used and are given in table C.1. The quantum efficiency as a function of wavelength for the PMTs, estimated from a data sheet provided by Hamamatsu, is also included in table C.1.

Wavelength Band (nm)		Transmittance 10 cm F2 (percent)	Quantum Efficiency (percent)
295	304	12.5	5.0
305	314	23.6	12.0
315	324	34.7	18.0
325	334	45.8	22.5
335	344	56.9	25.0
345	354	68.0	27.5
355	364	79.1	28.0
365	374	88.3	28.5
375	384	92.2	29.0
385	394	95.5	29.0
395	404	96.8	28.8
405	414	97.3	28.3
415	424	97.6	27.5
425	434	97.8	26.5
435	444	97.9	25.0
445	454	98.0	24.0
455	464	98.1	22.5
465	474	98.2	21.0
475	484	98.3	19.5
485	494	98.4	18.0
495	504	98.5	17.0
505	514	98.6	15.5
515	524	98.7	13.5
525	534	98.8	12.0
535	544	98.9	10.0
545	554	99.0	8.5
555	564	99.1	7.0
565	574	99.2	5.5
575	584	99.3	3.5
585	594	99.4	2.5
595	604	99.5	1.5

Table C.1: Transmittances and quantum efficiencies in 10 nm wavelength bands as used in the single counter Monte Carlo simulation.

C.1 Simulation

There are three parts to the Monte Carlo simulation. Since the E760 central calorimeter is designed to measure the energy of electromagnetic shower inducing particles, one part of the Monte Carlo is for the shower development. Non-showering particles require a separate simulation. Both of the above simulations pass positions and momenta of charged particles to the third part of the Monte Carlo where Čerenkov light generation and propagation of photons are simulated.

C.1.1 Electromagnetic Showers

Simulation of electromagnetic showers is done with the EGS4 code system. The radiation transport of e^+'s, e^-'s, or γ's is simulated within the proper geometries of F2 lead-glass. The EGS4 simulation includes physics processes such as Bremsstrahlung, Moliére and Compton scattering, and pair production and annihilation. All shower particles are tracked until either a particle has a position outside of the block geometry or has an energy less than 650 KeV, the Čerenkov threshold for electrons in F2 lead-glass.

Shower information about paths and energy loss per step (< 1 mm) of the particle and its secondaries is used by the Čerenkov photon generating and propagating simulation code, discussed in section C.1.3. The shower inducing particles (e^+, e^-, or γ) are assumed incident normal to the front face at a randomly chosen position in

a centered 1×1 cm^2 area. The incident energy is an input variable into the Monte Carlo.

C.1.2 Non-showering Particles

Traversing particles which do not induce electromagnetic showers are simulated: charged pions, protons and cosmic ray muons. The traversal of non-showering particles is simulated by small steps (< 1 mm) with multiple small angle scattering as well as energy loss, dE/dx. Strong nuclear reactions are not simulated. After each step, the Čerenkov photon generating and propagating code is called, section C.1.3.

A check for δ ray production (knock-on electrons) from the traversal of a non-showering particle is done each step. If a δ ray has been produced, the δ ray's energy is generated from a distribution quadratic in the reciprocal of the kinetic energy of the resulting δ ray [86]. The minimum allowed Monte Carlo energy of a δ ray is 1 MeV, while the maximum is determined by the mass and energy of the non-showering particle. The direction of the δ ray is parallel to the direction of the traversing particle. The resulting position and momentum inside the lead-glass block of the δ ray is then submitted to the EGS4 code system (section C.1.1) for transport and shower development.

Pions and protons are taken to have normal incidence upon the same area as described in the previous section. The incident energy for the pions and protons is an input variable. The cosmic ray muons are simulated to have the average energy

of cosmic ray muons at sea level, 2 GeV. The initial position and direction of a muon are set as two random variables which correspond with calibration tests performed at Fermilab using two scintillator paddles in coincidence above and below an upright counter (discussed in section 4.1.2). Therefore, the incident position and direction are taken random within the confining paddle geometry. For the smaller cross-sectional lead-glass blocks, it is possible for the muon, as in the cosmic ray tests, to enter the blocks through a side face missing the front face, thus having a shorter traversing path length through the block.

C.1.3 Čerenkov Photons

After a charged particle is stepped, the average β for the step is used to generate Čerenkov photons; the position and momentum of the charged particle is passed from the other parts of code discussed in sections C.1.1 and C.1.2. The Čerenkov photons are generated in 10 nm wavelength bands (the bands in table C.1). The first set of Monte Carlo simulations only generated Čerenkov light between 350 nm and 600 nm. The Monte Carlo was extended to include wavelengths down to 300 nm. The photons are propagated to one of three fates: the photons can be absorbed, escape the block, or hit the PMT face.

After a photon at a certain wavelength has been generated, a random number generator is used to calculate the absorption distance using the appropriate value of transmittance from table C.1 At every surface that a photon hits, the total distance

travelled by the photon is calculated. If the photon's travel distance is greater than the photon's absorption distance, the photon is considered to have been absorbed by the lead-glass.

The reflection part of the Monte Carlo has undergone some changes. Originally, only total internal reflection was used to propagate photons which hit any face. The simulation has been changed to calculate a Fresnel coefficient for a photon that does not undergo total internal reflection. Since the Fresnel coefficients depend upon the photon polarization with respect to the plane of incidence, the polarization of the incident photon is taken in accord with the Čerenkov effect: polarization is in the plane of the charged particle and photon momenta. To choose which Fresnel coefficient to calculate (parallel or perpendicular to plane of incidence), the dot product of the polarization vector and the plane of incidence is used. A random number generator is used to determine which Fresnel coefficient to calculate and then whether the photon is reflected. The Monte Carlo has been further developed by incorporating reflection from the white paper wrapped around each counter. Since paper is not a specular reflector, a cosine distribution is used for the reflected direction of the photon and the polarization is random. Another Fresnel coefficient is calculated and used to see if the photon is reflected off the the outside of the block. If reflected, the photon is considered to have escaped; otherwise, the photon is refracted and further propagated in the block. The paper is only simulated on five of the sides (not the back face).

When a photon does not get absorbed or lost, and reaches the back face, a check is made to see if the photon hits the PMT face (a circular area of the correct

size centered on the block's back face, table 3.1). If the PMT face has been hit, then the quantum efficiency for the wavelength band is used to determine whether or not a photoelectron results. If the photon does not hit the PMT face, the photon is subjected to the same treatment as described above for reflection except there is no paper. However, there exists a set of Monte Carlo simulations which includes paper reflections for the back face. There is also a set of simulations where the blocks are wrapped in aluminum foil, which has a 90% chance of specular reflection for non-internally reflected photons. The final Monte Carlo has paper on the five sides allowing for paper reflections for escaped photons.

C.2 Characteristics and Effects

Several characteristics of the Monte Carlo have been studied. All aspects of the Monte Carlo were kept in a large bookkeeping operation, split into the three areas of simulation. Below are the characteristics of each area of simulation along with the effect of different simulated physics processes on the final photoelectron results.

C.2.1 Electromagnetic Showers

A fictitious large block geometry (30 cm $\times$ 30 cm $\times$ length of a block) was used to see how an electromagnetic shower develops. In figure C.1, the radial distance from the incident axis for all generated Čerenkov photons is shown. The number of Čerenkov photons generated along a charge particle's path is dependent upon

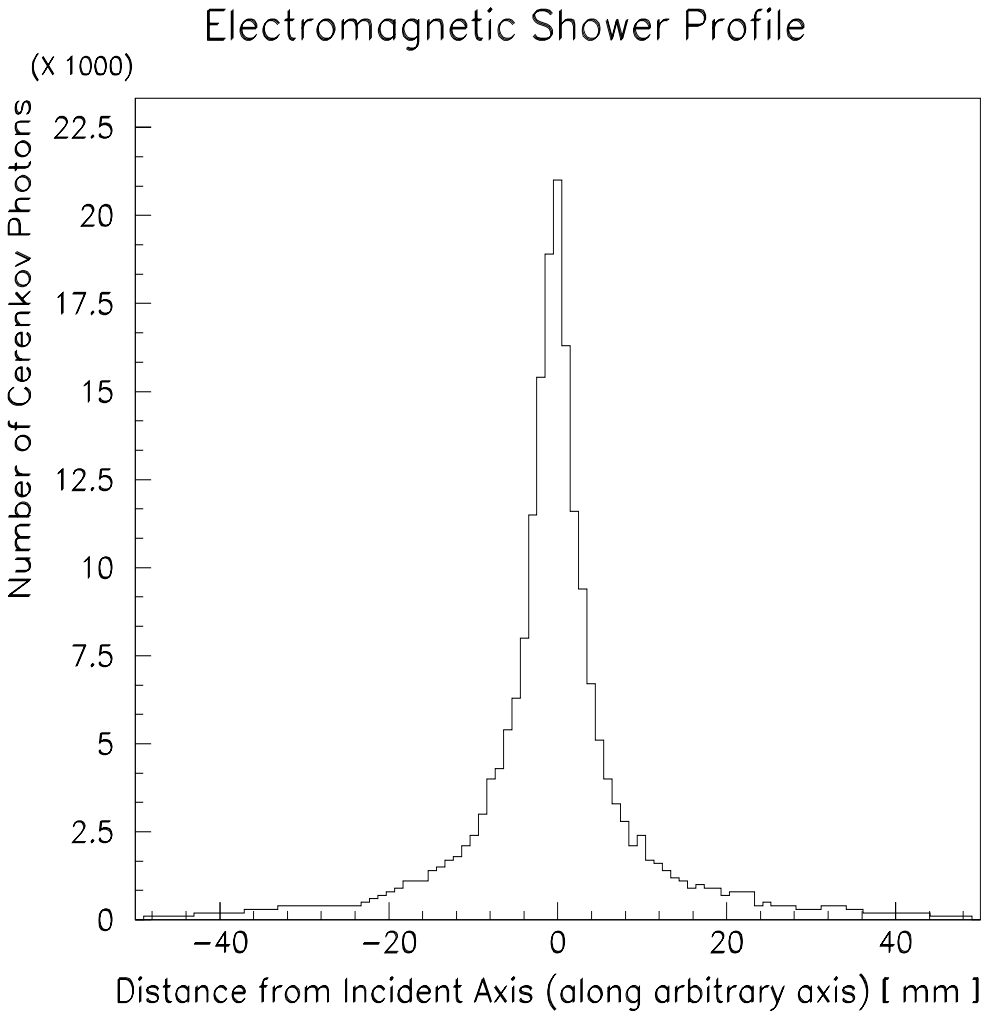

Figure C.1: The electromagnetic shower width as the number of Čerenkov photons generated as a function of distance from the incident axis along an arbitrary axis for 3 GeV incident electrons.

β. As the shower develops, the particles become less energetic, thus β becomes smaller and the particles are less efficient in producing Čerenkov light. The shower FWHM shown in figure C.1 is 7 mm which is in agreement with the Molière radius of 5 mm for F2 lead-glass. The width of the simulated shower has been determined to be independent of incident energy. The Čerenkov generation of photons along the

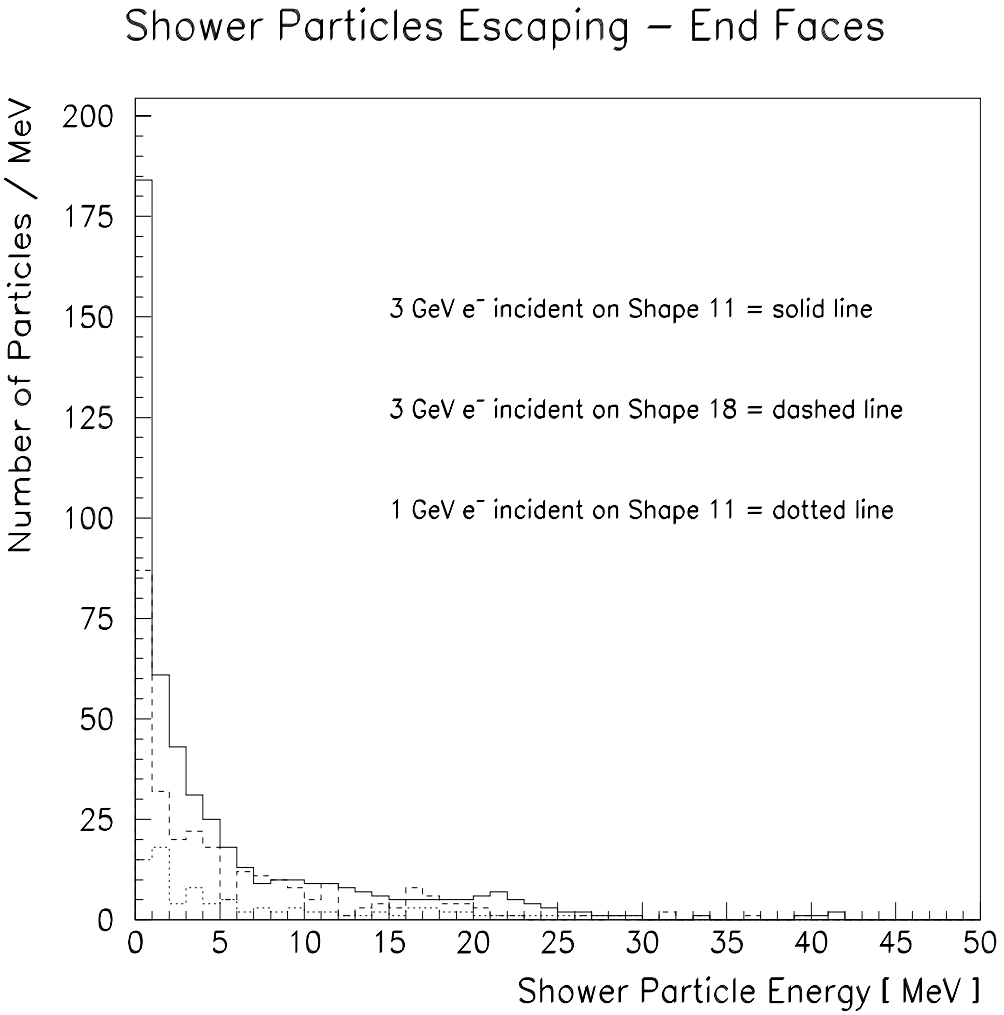

Figure C.2: The energy distribution of shower particles escaping through the end faces.

incident axis has been found to be maximum at a depth (distance from the front face) of 15.8 and 19.2 cm for 1 GeV and 3 GeV incident electrons, respectively.

For most shapes the centered electromagnetic shower is generally contained within the block. The number of Čerenkov photons generated within each shape is compared with the number generated in the large fictitious block. The larger blocks contain approximately 90% of the possible Čerenkov photons. As the cross-sectional

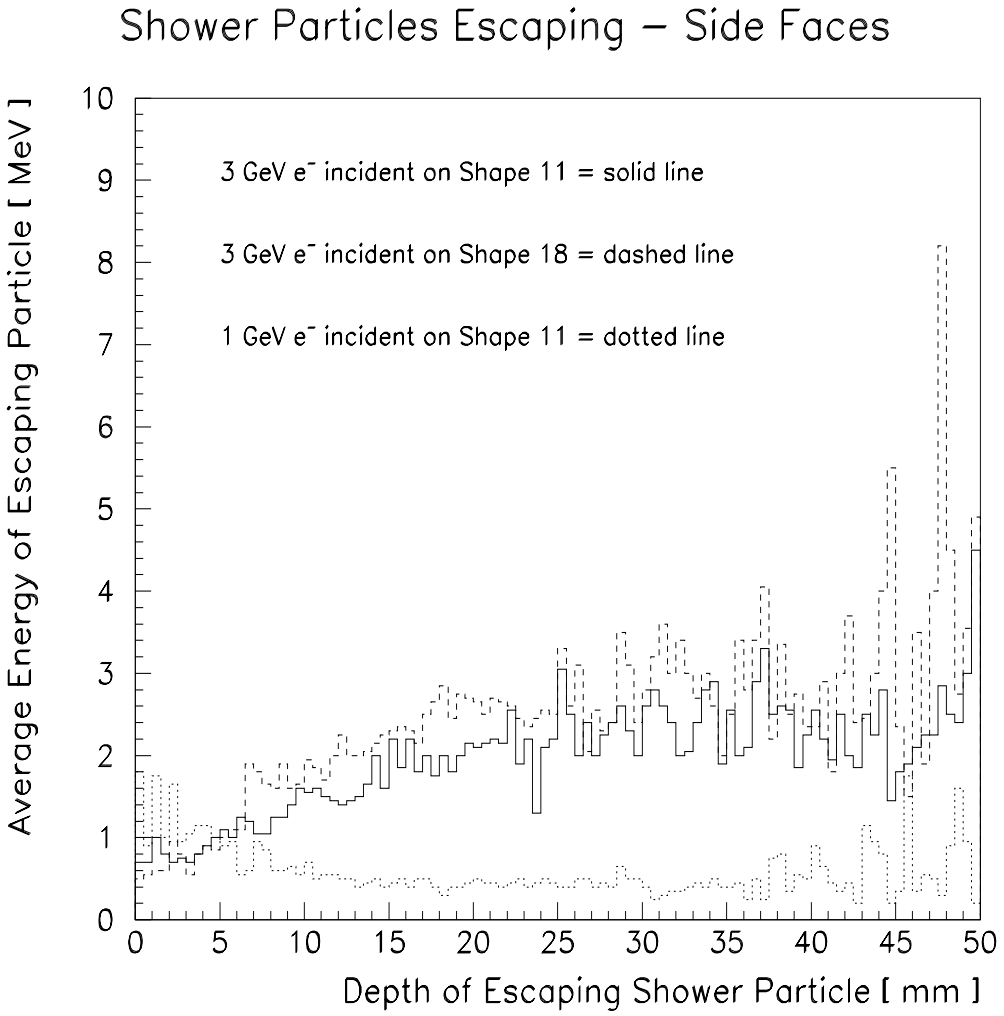

Figure C.3: The average energy of escaping shower particles through the side faces as a function of depth into a counter.

area of the blocks decreases, the percentage contained within the block decreases (see tables C.8 and C.9).

The electromagnetic shower particles which leave the blocks were investigated. Most of the particles escaping the blocks have energies less than 10 MeV. Particles escaping the end faces of shape 11 have average energies of 4.5 and 4.6 MeV for 1 and 3 GeV incident electrons. For 3 GeV electrons incident upon shape 18, the

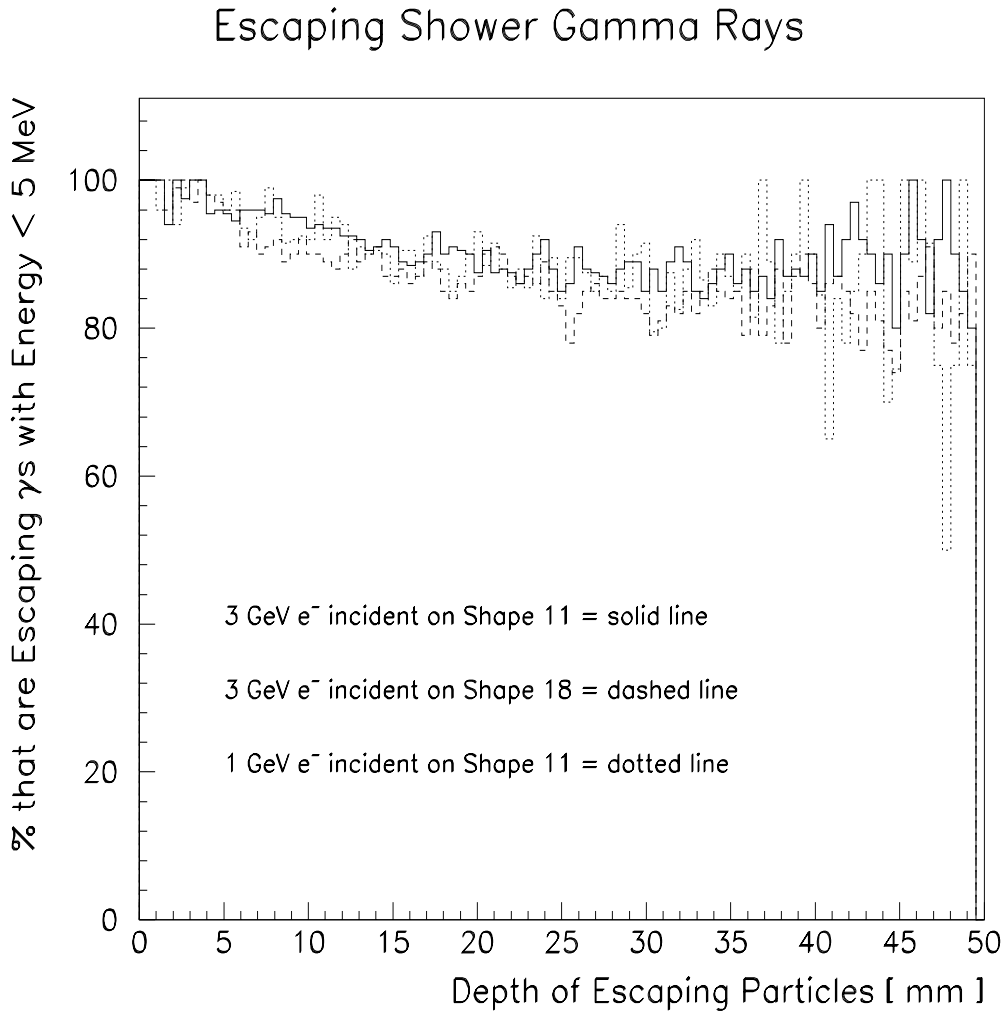

Figure C.4: The percentage of the escaping electromagnetic shower particles that are gamma rays with less than 5 MeV as a function of depth.

average shower particle escaping the end faces was found to be 6.9 MeV. Figure C.2 shows the average number of shower particles escaping the end faces for a hundred simulations of the three cases stated above. Particles leaving the side faces have smaller average energies, 1.8 and 2.0 MeV for 3 GeV incident electrons into shapes 11 and 18, respectively. For 1 GeV electrons incident upon shape 11, the average escaping particle energy decreases to 0.7 MeV. Figure C.3 shows the average shower particle energy as it leaves the block as a function of depth. Most of the escaping particles

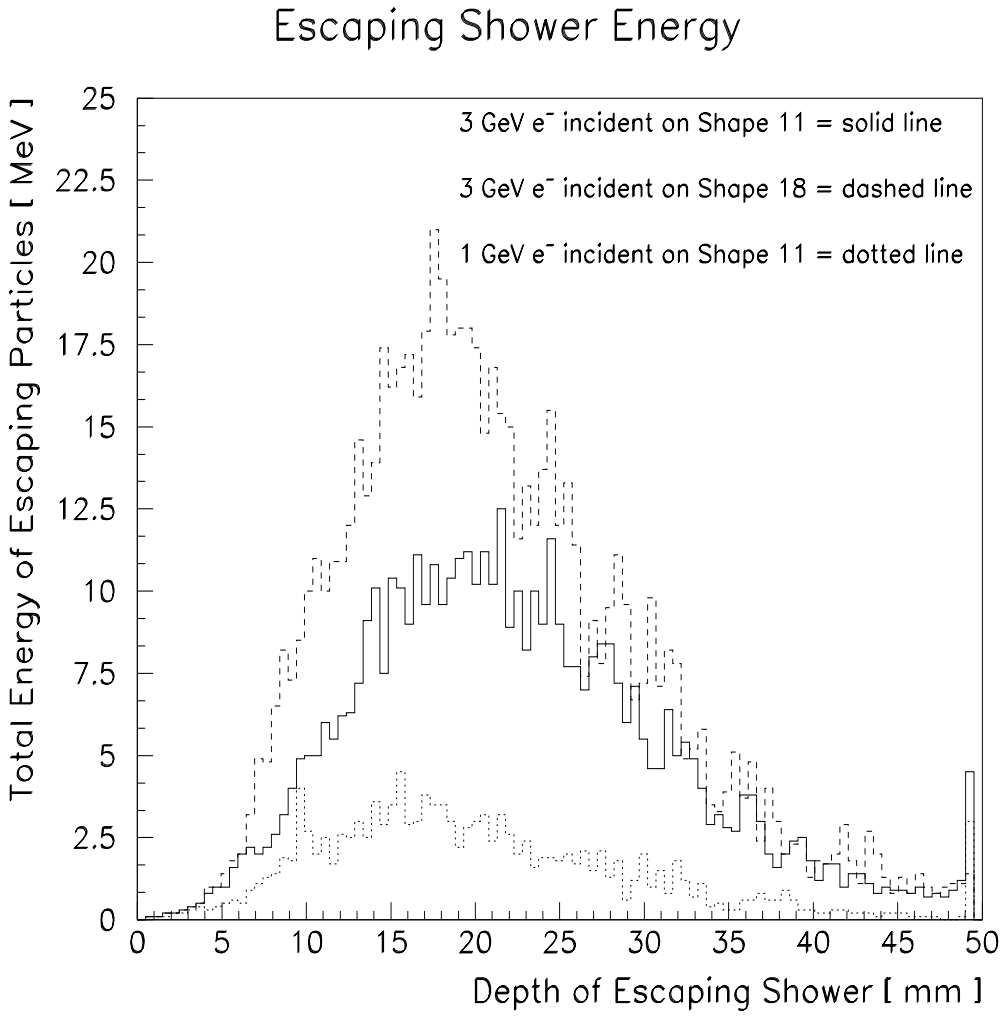

Figure C.5: The shower energy escaping through the side faces as a function of depth.

have been determined to be γ rays with energies < 5 MeV as seen in figure C.4. The total energy that leaves as a function of depth averaged over a hundred simulations is shown in figure C.5. Table C.2 shows the number of particles and the sum total of energy escaping the counters in the three simulations.

Block Number	Incident Energy (GeV)	Escaped Electromagnetic Shower Side Faces # of Particles	Side Faces Energy (MeV)	End Faces # of Particles	End Faces Energy (MeV)
11	1	71.0	169.3	0.81	3.7
11	3	247.3	484.7	3.97	18.3
18	3	312.2	726.7	2.35	16.3

Table C.2: The average number of shower particles escaping and average total energy of the escaping particles for 100 Monte Carlo simulations.

C.2.2 Non-showering Particles

The average energy lost by pions and muons traversing a 50 cm block due to dE/dx has been found to be 270 MeV. For protons, 200 MeV has been determined to be the average energy lost while passing through the longest blocks. The average distance that a non-showering particle exits the back end face of a block from the exit point calculated from a straight path, caused by multiple small angle scattering, is 1.6 and 2.6 mm for incident energies of 4 and 2.5 GeV, respectively. Of 1000 incident protons or pions with incident energies of 4 and 2.5 GeV, the largest displacements from a straight path are 5 and 8 mm. The same holds true for cosmic ray muons

Particle type	Incident Energy (GeV)	Number of δ rays	Average δ ray Energy (MeV)	Maximum δ ray Energy (MeV)	Total δ ray Energy (MeV)
Pion	2.5	12.4	4.8	286.0	61.7
Proton	2.5	7.3	2.2	6.1	4.0
Pion	4.0	12.6	6.6	686.0	72.0
Proton	4.0	10.0	2.8	17.3	13.4

Table C.3: δ ray production as a function of energy and incident particle type averaged for 1000 simulations.

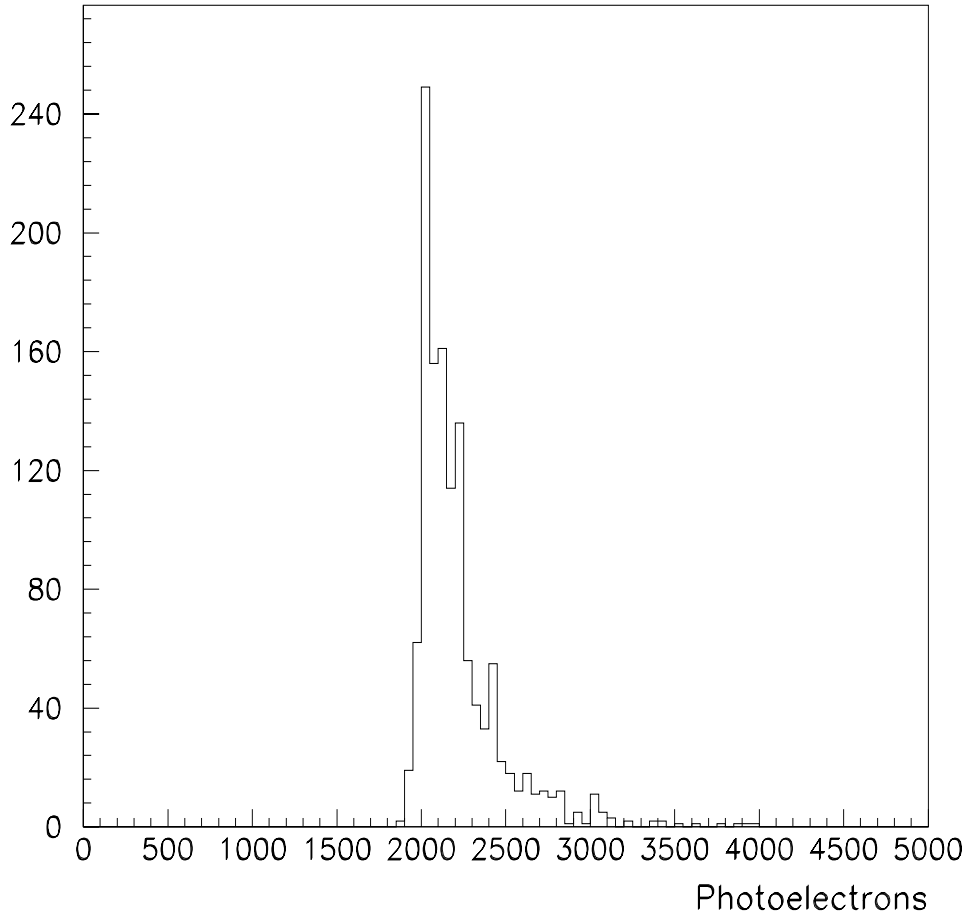

Figure C.6: The results of 1000 Monte Carlo simulations of 3 GeV incident pions into shape 11.

which intersect the front face of a block; up to 30% of cosmic ray muons do not enter through the front face of the smaller shapes.

The energy of a δ ray is a function of the incident particle's energy and mass. In table C.3, the average δ ray energy generated and the theoretical maximum energy of a δ ray are shown. Also shown is the average summed energy of all the δ rays produced from one traversing non-showering particle. The average energy of the

δ rays generated increases with increasing incident energy and decreases with heavier incident particle mass.

The total number of resulting photoelectrons is affected to some extent by the addition of the three physical processes stated above. When dE/dx is added to the simulation the photoelectron output decreases by 8%. A decrease of 2% occurs when multiple small angle scattering is included. Production of δ rays causes the resulting photoelectron spectrum to be a gaussian with a high side tail, as shown for a thousand simulations in figure C.6. The average mean number of photoelectrons increases by 8% from the δ ray production.

C.2.3 Čerenkov Photons

The simulation of the propagation of the Čerenkov photons has been developed for a period of time, allowing studies of each new simulated process. The easiest bookkeeping involved is the statistics of the fates of all Čerenkov photons generated. As an example, table C.4 shows the number of photons which suffer each fate and the resulting number of photoelectrons for shape 11. Since the photons are generated in the 10 nm wavelength bands shown in table C.1 with a $\frac{1}{\lambda^2}$ dependence, all frequency dependent processes are done within the wavelength bands.

There is at least a 40% chance that a photon will hit the PMT from any depth in the lead-glass blocks. The percentage of generated photons which hit the PMT as a function of depth at which they are generated is shown in table C.5 for shape 11.

Photon Fate	Electrons 1 GeV	Electrons 3 GeV	Cosmic Muons	Beam Pions
Generated	61650	186400	27040	26660
Absorbed	28340	84830	11450	11260
Escaped	8110	24190	1860	1450
Hit PMT	25200	77380	13730	13950
Photoelectrons	4911	15080	2724	2837

Table C.4: The fates of Čerenkov photons for a Monte Carlo event.

Depth (cm) Electrons 1 GeV	Electrons 3 GeV	Cosmic Muons	Beam Pions	Hit PMT Percentage $\geq$
0	0	0	0	40%
33	35	14	16	45%
38	41	27	20	50%
47	46	44	42	60%
49	49	48	46	70%
...	...	...	47	80%
...	...	...	49	90%

Table C.5: The Percentage of Čerenkov photons which hit the PMT as a function of the depth of generation. The data is for Monte Carlo response simulation of shape 11; the PMT is at 50 cm.

Center of 10 nm band of Wavelengths (nm)	Average Distance Propagated to PMT (cm)			
	Electrons		Cosmic	Beam
	1 GeV	3 GeV	Muons	Pions
300	8.7	8.9	4.8	4.4
320	27.4	23.6	9.7	8.9
350	45.4	41.1	22.3	21.0
370	58.3	54.7	36.4	34.6
400	76.3	74.5	55.4	52.6
450	82.0	80.1	60.6	56.9
500	84.5	83.1	63.6	60.0
550	87.6	86.5	67.1	63.3
600	90.5	89.6	70.6	65.5

Table C.6: The average distance that Čerenkov photons travel that hit the PMT

Since the pions are incident along the axis of the lead-glass block, the photons of the Čerenkov cone are within the critical angle for total internal reflection; therefore, the Čerenkov photons from pions are *focused*. The photons caused by cosmic ray muons are not as focused since the muons are not constrained to be along the axis of the lead-glass block, causing part of the cone not to be internally reflected. The generated angle of the Čerenkov photons with respect to the axis of the block (the perpendicular to the front and back faces) is shown in figure C.7 in terms of the cosine of that angle; note that $\cos\theta_C = \frac{1}{n} = 0.617$ for $\beta = 1$. The backward photons of the pion simulations are caused by δ ray induced showers.

The above focusing helps to shorten the distance that the photons travel to the PMT. In table C.6, the average distance is shown for Čerenkov photons which hit the PMT. The electromagnetic shower Čerenkov light production is spread out and is closer to the front face than the PMT. If the shower extends to near the PMT, the charged particles have low energy and are directed randomly causing the Čerenkov

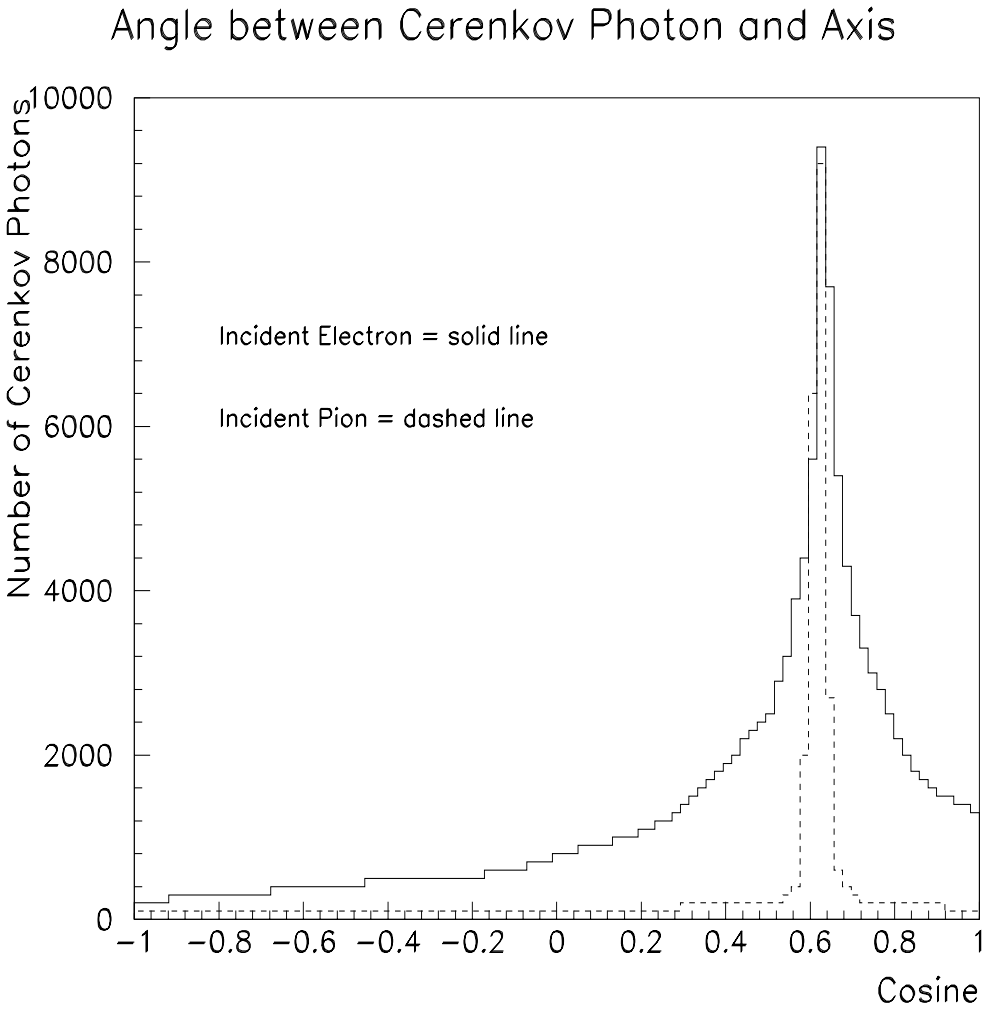

Figure C.7: The angular distribution (the angle between the Čerenkov photon momentum vector and the incident particle direction, the axis of symmetry of the lead-glass block) of Monte Carlo generated Čerenkov photons for incident electrons and pions.

Number Of Paper Reflections	Electrons 1 GeV (%)	Electrons 3 GeV (%)	Cosmic Muons (%)	Beam Pions (%)
0	70.20	69.70	87.14	89.52
1	24.70	24.50	10.03	8.33
2	4.30	4.85	2.29	1.77
3	0.66	0.79	0.44	0.32
4	0.10	0.12	0.07	0.05
5	0.02	0.02	0.01	0.01
6	small	small	small	small
7	small	small	small	small
8	none	small	small	none
9	small	small	none	none

Table C.7: The percentage of photons which hit the phototube and the number of paper reflections.

photons to be generated almost isotropically. A non-showering particles produces Čerenkov light consistently along its path.

A paper wrapping to reflect non-internally reflected photons back into the lead-glass block increases the PMT output. Table C.7 shows the percentage of the total number of photons which hit the PMT for shape 11 as a function of the number of paper reflections. As can be seen, the addition of paper affects Čerenkov photons from electromagnetic showers more than the non-showering particles. The average total number of reflections in a shape 11, internal and paper, is 12.2 for 1 and 3 GeV electrons, 8.2 for pions, and 8.8 for cosmic ray muons.

The number of photons (in the 10 nm wavelength bands) which suffer each fate has been determined. Figure C.8 shows the percentage that result in each fate for the photons created by a 3 GeV electron and a 3 GeV pion incident upon shape 11. In figure C.9, the distributions of photons generated, absorbed, hit the PMT, and which

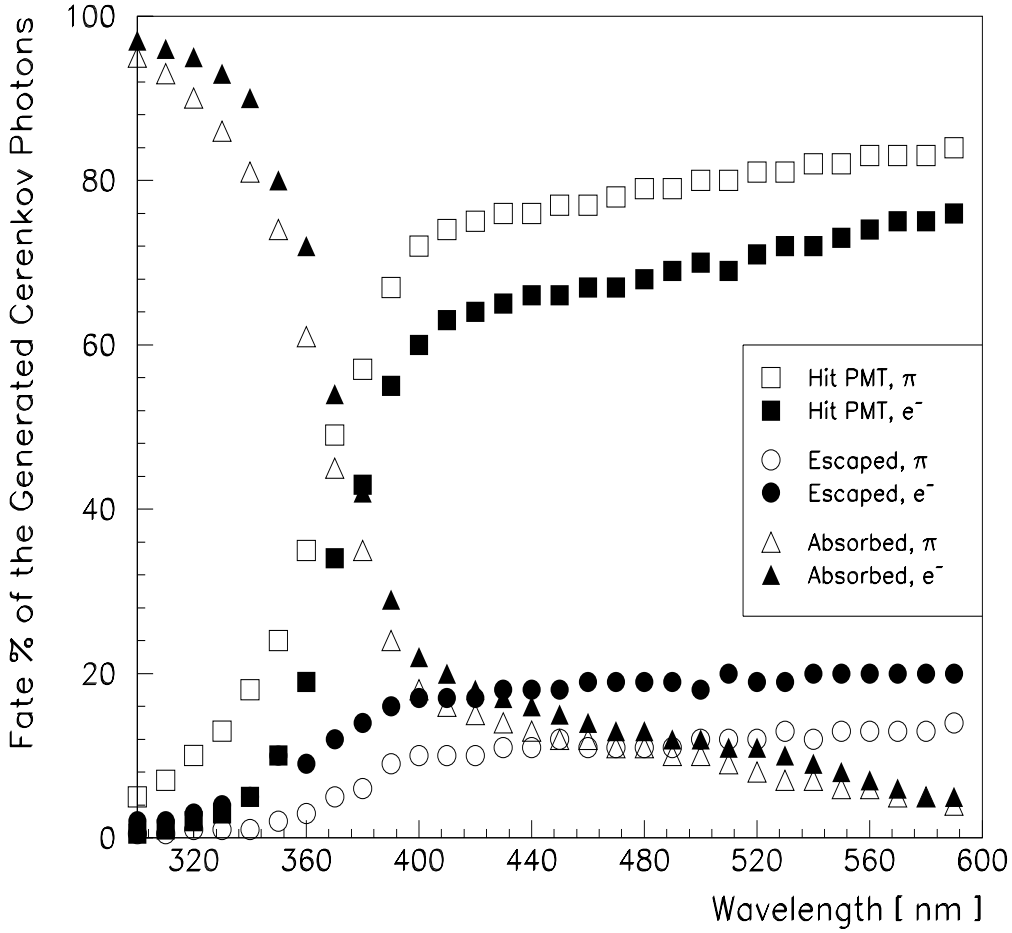

Figure C.8: The percentage of the generated Čerenkov photons which are absorbed, escape the counter, or hit the PMT.

cause photoelectrons are shown for both incident 3 GeV electrons and pions. The $\frac{1}{\lambda^2}$ Čerenkov spectrum of photons generated is apparent. The absorption of ultraviolet is shown dramatically since it is weighted by the Čerenkov spectrum for the absorbed photon distribution. The spectrum for the photons which result in the creation of photoelectrons is essentially the quantum efficiencies from table C.1 multiplied with the hit PMT photon spectrum.

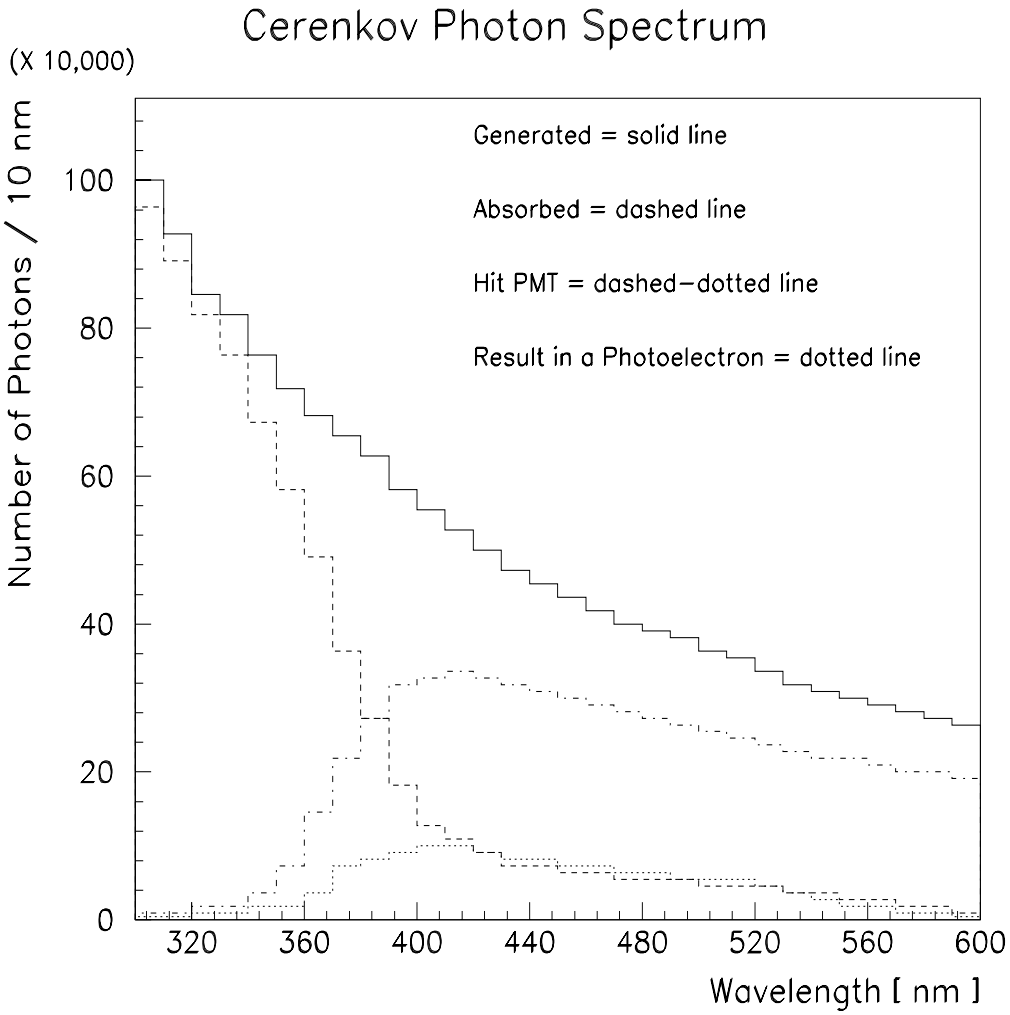

Figure C.9: The Čerenkov photon distributions for generated photons, absorbed photons, photons which hit the PMT, and photons which produce a photoelectron.

The different additions to the Monte Carlo have affected the photoelectron results differently for the shower inducing particles and the non-showering particles. The addition of the wavelengths between 300 nm and 350 nm increased the photoelectron results by 5.3% and 9.1% for 1 GeV incident electrons and cosmic ray muons, respectively, compared to Čerenkov light only being produced between 350 nm and 600 nm. The addition of ultraviolet wavelengths affected the non-showering particles

more than the electromagnetic showers. Photons which were not within the critical angle and were reflected according to the probability of reflection from Fresnel equations increased the photoelectron output by 7.5% and 1.9%, a greater effect for electromagnetic showers. The addition of paper wrapping to all sides except the back face increased the incident electron result by an additional 43.5% while the cosmic ray muon result increased by 21.4%. If paper was included on the back face (all surfaces papered except where the PMT is attached), the electron and cosmic ray muon results increased 7.4% and 3.5%, respectively. When aluminum foil was simulated as the wrapping, increases of 47% and 17% were obtained for electrons and cosmic ray muons, respectively, with respect to the internally reflected results (no Fresnel reflections).

C.3 Monte Carlo Results

Below are the results of a thousand simulations of each type of event for all the shapes. The results are for Čerenkov light generated between 300 nm and 600 nm with paper on five sides; the transmittance and quantum efficiency are in table C.1. The number of photoelectrons is directly proportional to ADC channel number; the ADC channel is the gain of the PMT multiplied by the number of liberated photoelectrons. Therefore, ratios of the number of Monte Carlo photoelectrons for different cases can be compared with ratios of ADC channels for different tests.

Block Shape Number	Energy Deposited in Block (MeV)	Energy Deposited Percent of Large Glass	Generated Photons in Block	Generated Photons Percent of Large Glass	Photo-electrons in PMT
1	850	89.6	62620	93.8	4043
2	857	90.2	63270	94.6	4073
3	860	90.4	63250	94.4	4001
4	861	90.1	63380	94.3	3953
5	865	90.2	63520	94.2	3864
6	861	89.1	63540	94.0	3774
7	862	88.6	63400	93.5	3674
8	860	88.2	63420	92.3	3753
9	858	88.0	63190	91.9	3900
10	861	88.3	63430	92.3	4090
11	859	88.1	63390	92.2	4251
12	859	88.1	63360	92.2	4450
13	859	88.1	63360	92.2	4602
14	850	87.2	62710	91.2	4697
15	831	85.2	61960	90.1	4150
16	823	84.4	61460	89.4	4691
17	799	82.0	60210	87.6	3881
18	780	80.0	59050	85.9	4356
19	756	77.6	57660	83.9	3299
20	728	74.7	55820	81.2	3667

Table C.8: Monte Carlo response of a single counter to 1 GeV incident electrons.

C.3.1 Electromagnetic Shower Inducing Particles

1 GeV incident electrons have been simulated for all twenty shapes and the results are presented in table C.8. The third and fifth columns of table C.8 compare the individual shapes to the imaginary large piece of lead-glass. The energy deposited in the first fourteen shapes is about 86% of the incident electron's energy or 89% of the energy deposited in the large block. The shower width becomes larger than the width of the smaller blocks and there is a fall off to 73% of the incident energy deposited in shape 20. A larger percentage (93% for the first fourteen shapes decreasing to 81%)

of the Čerenkov photons are generated within the shapes compared to the large piece of lead-glass. The charged shower particles outside of the shapes, but inside the large piece of lead-glass, have smaller energies and do not generate as much Čerenkov light since β approaches $\beta_{threshold} = \frac{1}{n}$. The last column shows the mean number of resulting photoelectrons. The number of photoelectrons increases with block number when the percentage of area covered by the PMT increases. The decreases occur when the blocks become smaller and a smaller sized PMT is attached covering a smaller percentage of the back face (see table 3.1).

Shower fluctuations will cause a distribution of the resulting number of photoelectrons. Defining resolution as FWHM/mean, the resolution for most of the blocks is between 0.06 and 0.12 for energy deposited in a block for 1 GeV incident electrons. The resolution is dependent upon the width of the block. This dependency is also seen in the fluctuation (FWHM/mean) of the number of Čerenkov photons generated (0.07 to 0.12) and photoelectrons observed (0.10 to 0.15).

Table C.9 has the same format as table C.8 for 3 GeV incident electrons. The percent of initial energy deposited is the same as for 1 GeV incident electrons for the longer blocks. The first five blocks are a few percent smaller since showers extend past the ends of these blocks. However, when compared to the large piece of lead-glass, the same percentage results for energy deposited as 1 GeV incident electrons. The ratios of generated photons between tables C.9 and C.8 are nearly three except for the shorter shapes which have ratios slightly less than three. The percentage of the large lead-glass Čerenkov photons generated within the shape is nearly the same

Block Shape Number	Energy Deposited in Block (MeV)	Energy Deposited Percent of Large Glass	Generated Photons in Block	Generated Photons Percent of Large Glass	Photo-electrons in PMT
1	2487	90.4	183300	92.3	12410
2	2516	92.5	185300	93.2	12460
3	2523	90.4	185900	93.3	12340
4	2531	90.7	186600	93.4	12160
5	2548	90.7	187700	93.6	12000
6	2575	90.7	189400	94.1	11710
7	2590	89.3	190400	94.4	11350
8	2591	89.2	190400	94.4	11650
9	2584	88.9	190400	94.4	12110
10	2579	88.8	190100	94.2	12630
11	2566	88.3	189400	93.9	13100
12	2561	88.1	188700	93.5	13600
13	2564	88.2	189300	93.8	14120
14	2561	88.1	189200	93.8	14450
15	2504	86.2	186400	92.3	12700
16	2461	84.7	183800	91.1	14210
17	2418	83.2	181700	90.0	11970
18	2329	80.1	176000	87.2	13260
19	2293	78.9	174600	86.5	10100
20	2203	75.8	169100	83.8	11250

Table C.9: Monte Carlo response of a single counter to 3 GeV incident electrons.

for 1 and 3 GeV incident electrons. The photoelectron results for all of the blocks have ratios slightly greater than three between tables C.9 and C.8 since the shower maximum is closer to the PMT making the travel distance for the Čerenkov photons on the average shorter.

The resolution is better for 3 GeV incident electrons when compared to 1 GeV incident electrons. The resolution of energy deposited is between 0.05 and 0.07. For Čerenkov photons generated, the resolution is between 0.05 and 0.08. The photoelectron resolution is between 0.08 and 0.10.

Incident Energy (MeV)	% Energy Deposited	Generated Photons	Photo-Electrons
50	85.4	3163	181
84	84.7	5275	306
100	85.6	6336	367
200	85.7	12610	746
300	86.6	19140	1143
400	86.1	25390	1529
500	86.1	31470	1926
600	85.8	37910	2305
800	85.6	50840	3104
1000	85.8	63190	3900
1250	86.2	79510	4936
1500	86.4	95510	5977
1750	86.1	111100	6965
2000	86.2	127000	8007
2500	86.0	158200	10030
3000	86.1	190400	12120
3500	86.5	222600	14280
4000	86.2	253800	16260

Table C.10: The Monte Carlo response of shape 9 to different incident electron energies.

Shape 9 has been studied at many different energies. Table C.10 shows the result of 18 different incident energies for electrons. The photoelectron output can be characterized by

$$\text{Photoelectrons} = \text{Energy} \times (3.1795 + 0.10735 \times \ln \text{Energy}) \qquad \text{(C.1)}$$

with Energy in MeV. The number of photoelectrons is not quite linear with respect to incident energy. The smaller incident energies have shower centers of gravity further away from the PMT, causing a greater absorption of photons of smaller wavelengths.

Block Shape Number	Pions Photo-electrons	Pions Ratio to 3GeV e^-	Cosmic Muons Photo-electrons	Cosmic Muons MeV Equivalent
1	1595	0.129	1478	366
2	1632	0.131	1526	375
3	1655	0.134	1557	389
4	1715	0.141	1613	408
5	1778	0.148	1685	436
6	1822	0.156	1733	459
7	1869	0.165	1814	494
8	1970	0.169	1881	501
9	2042	0.169	1952	501
10	2139	0.169	2046	500
11	2223	0.170	2082	490
12	2298	0.169	2197	494
13	2406	0.170	2291	498
14	2478	0.171	2325	495
15	2237	0.176	2041	492
16	2509	0.177	2193	467
17	2163	0.181	1858	479
18	2440	0.184	2028	466
19	1926	0.191	1520	461
20	2177	0.194	1684	459

Table C.11: The Monte Carlo response to punch through pions and cosmic ray muons.

C.3.2 Non-showering Particles

The non-showering particle photoelectron results all show a high tail to a gaussian distribution, see figure C.6. The results of 3 GeV incident pions and cosmic ray muons are presented in table C.11. The mean value of the distributions are in columns two and four. Column three is the ratio of photoelectrons for a 3 GeV incident pion to a 3 GeV incident electron. The ratio is dependent upon the length of the block since the number of Čerenkov photons generated is directly proportional to the path length of the pion. The ratios increase additionally when the electromagnetic shower

of the incident electron is no longer able to be contained in the smaller blocks (greater shape number). The fifth column is the equivalent energy in MeV that a cosmic ray muon appears to have when using a 1 GeV incident electron as a reference response (assuming linear response to zero energy). The pattern of increase of the equivalent energy as the block number increases is the same as for the pions mentioned above.

The photoelectron resolution for the incident pion is between 0.10 and 0.12. Resolutions of 0.12 and 0.16 for most blocks, and increasing to 0.20 for the smaller blocks due to clipping, have been obtained for cosmic ray muon Monte Carlo results. Clipping is when a muon does not enter through the front face.

Pions and protons have been run at 2.5 and 4 GeV incident energies. At 4 GeV there is an increase in the photoelectron mean of 2% and 11% for pions and protons, respectively, compared to 2.5 GeV incident particles. This increase is caused mainly by the additional available energy for δ ray production. There is also an increase in β (a greater increase for the proton) which has a small effect upon the amount of Čerenkov light production.

For the smaller shapes, the effect of a pion entering a block at non-normal incidence has been investigated. A decrease of less than a percent of the photoelectron mean has been seen for an incident angle of one degree from the normal.

C.4 Comparison to Test Beam Studies

The two test beam studies that were undertaken to calibrate the central calorimeter and study the calorimeter response are discussed in section 4.2. Discussed here is how the Monte Carlo results compare to the studies performed.

C.4.1 AGS Tests Comparison

The Monte Carlo simulates the response of one counter. The Monte Carlo does not simulate the gains of the PMTs; it is assumed that the gain of the PMTs for every shape is the same and does not depend upon incident particle type. Comparison between Monte Carlo and the data is possible by taking ratio of results on a shape by shape basis. Column three of table C.11 is the ratio of photoelectrons from 3 GeV incident pions to electrons from the Monte Carlo. Making cuts on the incident position and direction from tracking available at the AGS, a similar ratio was calculated. Figure 4.6 shows the Monte Carlo photoelectron ratios and the AGS data ratios; the explanation of the ratio as a function of shape is given in section 4.2. The Monte Carlo is in good agreement with the data.

In section C.3.2, it is mentioned that there is a slight increase in photoelectron output (2%) for 4 GeV pions when compared to 2 GeV pions. The data collected at the AGS showed an increase of 7%. Simulations were done to see what effect the paper wrapping has upon the propagation of the Čerenkov photons to the PMT. Shape 11 has been investigated since such a counter was studied at the (AGS) with

BNL-AGS or Monte Carlo	Incident Beam Particle	Energy (GeV)	Means Results Cloth	Paper	Cloth/Paper (%)
BNL-AGS	Electron	1	170	231	73.6
ADC	Electron	3	573	758	75.6
Measured	Pion	2	108	121	89.2
Means	Pion	4	116	133	87.2
Monte	Electron	1	3055	4251	71.9
Carlo	Electron	3	9312	13100	71.1
Photo-	Pion	2	2010	2223	90.4
electrons	Pion	4	2098	2361	88.9

Table C.12: Comparison of a shape 11 counter for white paper and dark cloth wrappings for Monte Carlo and AGS results.

and without paper wrapping. Table C.12 compares the measured ADC mean channel number and the Monte Carlo photoelectron results of studies of wrapping the counter in white paper or a dark cloth; there is good agreement.

Since part of the electromagnetic shower escapes the incident block, a study of sharing of energy was done on the data taken at the AGS. The eight modules' outputs that surround the hit counter were summed with the hit counter's output for a total charge collected. A Monte Carlo of nine modules with the correct block geometry would be complicated using the EGS4 code. A correction of the photoelectron results for incident electrons was made by multiplying by the ratio of Čerenkov photons generated within the large block to those within the shape. This assumes that the percentage of Čerenkov photons resulting in photoelectrons is the same for photons generated within the shape as for the photons generated outside of the shape and within the large block (i.e. the surrounding eight modules). Figure 4.7 shows the adjusted Monte Carlo results and the summed nine counter responses ratios.

Data or Monte Carlo	Shape Number	Electron Energy of 84 MeV	1 GeV	84 MeV to 1 GeV Ratio
NPL and	01	22.3	303	0.0736
BNL-AGS	09	21.6	271	0.0797
ADC	15	22.3	267	0.0835
Measured	17	24.7	265	0.0932
Means	19	17.3	232	0.0746
Monte	01	307	4043	0.0759
Carlo	09	306	3900	0.0785
Photo-	15	332	4150	0.0800
electron	17	307	3881	0.0791
Results	19	260	3299	0.0788

Table C.13: Comparision of 84 MeV and 1 GeV electron responses from the Monte Carlo and UINPL data.

C.4.2 UINPL Tests Comparison

A common light source used at both the AGS and UINPL was a bismuth source encased in scintillator plastic glued to the front face of each block. The response to incident electrons has been compared to the response to the bismuth source. The ratio of the responses to the incident 84 MeV electrons at the UINPL and 1 GeV electrons at the AGS was determined. Monte Carlo simulations of 84 MeV incident electrons have been run for the shapes that were tested at the UINPL. Table C.13 shows the ratios for the five counters. The ratio of responses to incident electrons of 84 MeV and 1 GeV is shown in the last column of table C.13 for the Monte Carlo and the two test beam studies. The Monte Carlo agrees with the data from the larger counters in which the incident electron position and electromagnetic shower size are not factors. A paper test done to one counter at the UINPL shows a decrease without the paper of 72.3% which is comparable to results shown in table C.12.

C.5 Discussion

The Monte Carlo that was developed has been useful in predicting the response of a single central calorimeter counter to different incident particles. The results of the Monte Carlo were used successfully in the initial calibration of the counters (section 4.1). Test beam results have been compared to the Monte Carlo results. The comparisons show that, for different incident particles and/or different wrappings of the counters, the Monte Carlo can accurately predict responses.